Identification and dissolution behavior of the secondary uranium minerals in the corrosion products of Depleted Uranium (DU) ammunition formed in soils

Dissertation

zur Erlangung des Grades

“Doktor der Naturwissenschaften”

im Promotionsfach Geowissenschaften

am Fachbereich Chemie, Pharmazie und Geowissenschaften

der Johannes Gutenberg-Universität Mainz

von

Mohammed Qader, M. Sc.,

Geboren im Irak

Dekan:

1. Berichterstatter:
2. Berichterstatter:

Tag der mündlichen Prüfung: 07.11.2011

Contents

List of tables……..V

List of figures……VI

List of abbreviations……..…XII

Acknowledgments……..XIII

Abstract……...XIV

Zusammenfassung……..…...XV

1 Introduction……..…1

1.1 Depleted Uranium (DU)……..…1

1.1 Definition……..1

1.1.2 DU applications……...3

1.1.3 Types of ammo and scenarios…….3

1.2 The use of DU in conflicts……....6

1.3 DU interactions with the human body…….7

1.3.1 Exposure to DU……...7

1.3.2 Behavior in the body……..7

1.3.3 Health effects……..8

1.4 Interactions of DU with the environment……..10

1.5 Description of the previous experiments……..11

1.6 Background information on U(VI) minerals……..……...15

1.6.1 Structure of U(VI) minerals……..……15

1.6.2 Chemistry of U(VI) minerals……..……17

1.6.2.1 Chemical groups of U(VI) minerals……19

1.6.2.1.1 Uranyl-oxyhydroxides group……19

1.6.2.1.2 Uranyl-carbonates group……..19

1.6.2.1.3 Uranyl-silicates group……20

1.6.2.1.4 Uranyl-phosphates and arsenates group……...20

1.6.2.1.5 Uranyl-vanadates, molybdates, and tungstates group……21

1.6.2.1.6 Uranyl-sulfates, selenites, and tellurites group……21

1.7 Corrosion of DU ammunition……..22

1.7.1 Corrosion environments for DU ammunition……...…….22

1.7.1.1 Atmospheric environment…….……22

1.7.1.2 Water environment……...25

1.7.1.3 Soil environment……25

1.7.2 Potential corrosion types of for uranium……..……26

1.7.2.1 Galvanic corrosion……...…….26

1.7.2.2 Pitting corrosion……26

1.7.2.3 Stress-Corrosion Cracking (SCC)……..……...27

1.8 Goals of study……..28

2 Materials and methods……...29

2.1 Materials……29

2.2 Methods……...29

2.2.1 Raman spectroscopy……...30

2.2.1.1 Settings and parameters……..32

2.2.2 Scanning Electron Microscope (SEM)……..34

2.2.2.1 Settings and parameters……..35

2.2.3 X-ray Photoelectron Spectroscopy (XPS)……36

2.2.3.1 Settings and parameters……37

2.2.4 Powder X-ray Diffraction (XRD)……38

2.2.4.1 Settings and parameters……..39

2.2.5 Electron Microprobe Analysis (EMA)……39

2.2.5.1 Settings and parameters……..40

2.2.6 Inductively Coupled Plasma – Optical Emission Spectrometry (ICP-OES)……42

2.2.6.1 Settings and parameters……..45

2.2.6.2 Preparation for the dissolution experiment……48

3 Results……....49

3.1 Raman spectroscopy results……..49

3.2 XRD results……...56

3.3 XPS results……...60

3.4 SEM results……63

3.5 EMA results……..65

3.6 Dissolution experiment……69

4 Discussions……..74

4.1 Transformation from U as metal to other U phases……...74

4.1.1 Structure of the formed U(VI) minerals……74

4.1.2 Paragenesis of the formed U(VI) minerals……76

4.2 Aqueous species of the formed U-minerals……78

4.2.1 Dissolution of formed U-minerals……...78

4.2.2 Dominant aqueous species……79

4.3 The role of CO_2 in the solution……84

4.4 Potential paths for DU in soils and natural water systems (case study Iraq - Basrah)……83

4.4.1 Scenarios for DU ammunition in Basrah……..88

5 Conclusions……95

6 References……...97

Appendix A……..…107

Appendix B……..…143

Appendix C……..…160

Appendix D……..…161

Curriculum vitae……..……165

List of tables

Table 1-1: Characteristics of uranium isotopes and relative isotopic abundance in natural and depleted uranium……..1

Table 1-2: Main minerals of the Uranyl-oxyhydroxides group……..….19

Table 1-3: Main minerals of the Uranyl-carbonates group……..……20

Table 1-4: Main minerals of the Uranyl-silicates group……..……..20

Table 1-5: Main minerals of the Uranyl-phosphates group…….……21

Table 1-6: Main minerals of the Uranyl-vanadates, molybdates, tungstates group…....21

Table 1-7: Main minerals of the Uranyl-sulfates, selenites, tellurites group……....21

Table 1-8: General corrosion rates for different atmospheric environments (after Craig et al., 2006 and references therein)……..23

Table 2-1: The microprobe calibration standards used for each of the selected elements……41

Table 2-2: Standard solutions for Ca and U used in the ICP-OES measurement…..….45

Table 2-3: Operating conditions of ICP-OES…….46

Table 3-1: The Raman peaks for schoepite in the literature……51

Table 3-2: The Raman peak for schoepite in the literature…….54

Table 3-3: The spin-orbit splitting parameters……...60

Table 3-4: the starting and final measured pH for samples (4, 7, & 8)…….…..71

Table 4-1: Uranyl mineral structures containing sheets based on anion topologies with triangles and pentagons…….76

Table 4-2: List of used aqueous spieces……80

List of figures

Figure 1-1: Decay chain of uranium……..2

Figure 1-2: Schematic diagram of a 30 mm DU round (after Bailey et al., 2002)……...4

Figure 1-3: Longitudinal section of a column used in the leaching experiments. (after Schimmack et al., 2005)……...12

Figure 1-4: DU penetrator used with cambisol and cleaned by nitric acid (top) at the beginning of the experiments, and after one year of corrosion (bottom) (after Schimmack et al., 2005)……..……13

Figure 1-5: DU penetrator after corroding for 3 years (after Schimmack et al., 2007)….13

Figure 1-6: Types of coordination polyhedra observed in U(VI) minerals (after Burns, 1999)…….15

Figure 1-7: The development of sheet anion topology (after Burns et al., 1996)…….17

Figure 1-8: Scheme depicts the paragenesis of major uranyl mineral groups (after Finch and Murakami, 1999)……..…64

Figure 1-9: Uranium oxidation rates in dry air, oxygen-water vapor, and water vapor as a function of temperature (after Lillard and Hanrahan 2005)……..…24

Figure 2-1: Design of a Raman spectrometer……..…..31

Figure 2-2: The different types of light scattering……..32

Figure 2-3: The prepared grains for Raman analysis from sample 4, Raman spectra have been measured for each grain……...33

Figure 2-4: The prepared grains for Raman analysis from sample 7, Raman spectra have been measured for each grain…….33

Figure 2-5: The prepared grains for Raman analysis from sample 8, Raman spectra have been measured for each grain……34

Figure 2-6: Design of a scanning electron microscope……35

Figure 2-7: The prepared grains for SEM measurements, from left to right: sample 4, 7, and 8……35

Figure 2-8: An electron is ejected due to the applied X-ray……37

Figure 2-9: The constructive interference that leads to X-ray diffraction……..38

Figure 2-10: The Jeol JXA 8900RL electron microprobe analyzer……40

Figure 2-11: The prepared resin block for the EMA analysis, each number represents a different particle (as presented in Appendix C)……..41

Figure 2-12: A Perkin Elmer Optima 5300 DV Inductively Coupled Plasma – Optical Emission Spectrometry instrument……42

Figure 2-13: Scheme of an ICP torch (after Manning and Grow 1997)……43

Figure 2-14: Minuteman scanning monochromator (after Skoog et al., 1998)……44

Figure 2-15: Calibration curve for Ca by ICP-OES……..……46

Figure 2-16: Calibration curve for U by ICP-OES……..…..47

Figure 3-1: The comparison between reference schoepite Raman spectrum (on top) and some of the acquired spectra from the samples…….....……..…..50

Figure 3-2: The comparison between reference billietite Raman spectrum (balck) and a measured spectrum from the sample 8 (blue)…….....52

Figure 3-3: The comparison between the measured becquerelite Raman spectrum (balck) and the reference spectrum of billietite (blue)……53

Figure 3-4: The comparison between reference becquerelite Raman spectrum (on top) and some of the acquired spectra from the samples……..…..54

Figure 3-5: The comparison between a measured spectrum (black) of sample 4, and reference spectra of meta-autunite (blue) & sabugalite (green)……55

Figure 3-6: The three acquired X-ray diffraction spectra of samples 4 (black), 7 (blue), and 8 (green)……..…56

Figure 3-7: The acquired X-ray diffraction spectra of samples 7 (blue) and the reference meta-schoepite……..57

Figure 3-8: The acquired X-ray diffraction spectra of samples 7 (blue) and the reference becquerelite……58

Figure 3-9: The acquired X-ray diffraction spectra of samples 4 (blue) and the reference autunite……...58

Figure 3-10: The acquired X-ray diffraction spectra of samples 8 (blue) and the reference sabugalite……59

Firgure 3-11: The two main photoelectron peaks of U (U $4f_{5/2}$ and U $4f_{7/2}$) along with the two maller satellite peaks of sample 7……....61

Firgure 3-12: The main photoelectron peaks of O1s of sample 7……62

Figure 3-13: The BSE image of a location on sample 4 acquired by SEM……..64

Figure 3-14: The EDS spectrum by SEM of the location showed in Fig. 3-13…….64

Figure 3-15: The BSE images taken by EPMA; A, B, & C represent 3 distinguishable regions with different mineralogy; an elemental map was made for the area inside red rectangle in (I); Images I-III taken for grain # 9, and IV for grain # 5 as shown if Fig. 2-11……..…..65

Figure 3-16: An elemental map made by EPMA showing the relations among U, Ca, Mg, Ti, Al, & Si for the area inside the red rectangle in Fig. 3-15 (I)……..66

Figure 3-17: An elemental map made by EPMA showing the relations among U, Ca, Mg, Ti, Al, & Si……67

Figure 3-18: An elemental map made by EPMA showing the relations among U, Ca, Mg, Ti, Al, & Si for the area represented in Fig 3-15 (III)……68

Figure 3-19: Modeled dissolution curves for U & Ca, assuming the presence of schoepite or becquerelite, with and without atmospheric CO_2……70

Figure 3-20: Modeled dissolution curves for U (curves), assuming the presence of schoepite or becquerelite, with and without atmospheric CO_2, plus the measured U data (points)……....72

Figure 3-21: Modeled dissolution curves for Ca (curves), assuming the presence of becquerelite, with and without atmospheric CO_2, plus the measured Ca data (points)……73

Figure 3-22: Measured points and modeled dissolution curves for U, assuming the presence of schoepite, with different amounts of atmospheric CO_2; numbers like 0.05, 0.1 etc refer to values that are multiplied by 3.8×10^{-4} to calculate the amount of the CO2 partial pressure……...…61

Figure 4-1: Sheets bases upon anion topology that contains only triangles and pentagons: (a) the sheet that occur in the structure of schoepite;(b) the sheet anion topology that correspond to the sheet shown in (a) (modified after Burns et al., 1996)……74

Figure 4-2: Sheets bases upon anion topology that contains only triangles and pentagons: (a) the sheet that occur in the structure of becquerelite, billietite, compreignacite, richetite, protasite;(b) the sheet anion topology that correspond to the sheets shown in (a) and (c); (c) the sheet that occur in the structure of $Mg[(UO_2)(SO_4)_2]$ H_2O_{11} (after Burns, 1999)……75

Figure 4-3: Sequence of paragenetic mineral formation during oxidative alteration of UO_2 as observed experimentally by Wronkiewicz et al. 1996 (after Amme et al. 2006)……77

Figure 4-6: Uranium oxidation rates in dry air, oxygen-water vapor, and water vapor as a function of temperature (after Lillard and Hanrahan 2005)……74

Figure 4-4: The dominant uranium aqueous species for dissolving schoepite in 0.01M $NaClO_4$ in the absence of atmospheric CO_2……..82

Figure 4-5: The dominant uranium aqueous species for dissolving schoepite in 0.01M $NaClO_4$ in the presence of atmospheric CO_2……..82

Figure 4-6: The dominant uranium aqueous species for dissolving becquerelite in 0.01M $NaClO_4$ in the absence of atmospheric CO_2…….83

Figure 4-7: The dominant uranium aqueous species for dissolving becquerelite in 0.01M $NaClO_4$ in the presence of atmospheric CO_2……83

Figure 4-8: Measured points and modeled dissolution curves for U, assuming the presence of schoepite, with different amounts of atmospheric CO_2; numbers like 0.1, 1 etc refer to values that are multiplied by 3.8×10^{-4} to calculate the amount of the CO_2 partial pressure……..85

Figure 4-9: Measured points and modeled dissolution curves for U, assuming the presence of becquerelite, with different amounts of atmospheric CO_2; numbers like 0.1, 1 etc refer to values that are multiplied by 3.8×10^{-4} to calculate the amount of the CO_2 partial pressure……..85

Figure 4-10: Basrah map with the showing the targeted locations with DU ammunition in 1991 war (stars) and 2003 war (triangles)……...87

Figure 4-11: Wind rose diagrams for Basrah from June to December 2005……..……..89

Figure 4-12: Wind rose diagrams from Basrah in 2006…….……..……90

Figure 4-13: Wind rose diagrams for Basrah from January to June 2007……..…..91

Figure 4-14: Soil map of Basrah (modified after Buringh, 1960)……93

Figure 4-15: Ground water depth for Basrah (modified after Jassim and Goff, 2006)…94

List of abbreviations

BWRs	Boiling Water Reactors
DU	Depleted Uranium
EMA	Electron Microprobe Analysis
IAEA	International Atomic Emission Agency
ICP-OES	Inductively Coupled Plasma – Optical Emission Spectrometry
ICRP	International Commission on Radiological Protection
pCO_2	Partial pressure of carbon dioxide
PWRs	Pressurized Water Reactors
SEM	Scanning Electron Microscope
TRLSFs	Time-Resolved Laser-Induced Fluorescence Spectroscopy
UK MOD	United Kingdom Ministry of Defense
UNEP	United Nations Environment Programme
USNRC	United States Nuclear Regulatory Commission
XPS	X-ray Photoelectron Spectroscopy
XRD	X-ray Diffraction

Acknowledgements

This section has been deleted in conformity with the rules stipulated by the internet publisher (ArchiMed). I am thankful to all the people for their help, discussions, and support. Their names are listed in the print-version of this dissertation.

Abstract

Several techniques were used to analyze 3 samples (4, 7, and 8) which represent the corrosion products of DU ammunition rounds that have been taken originally from the Kosovo war battle fields. At first, the results obtained from using the Raman spectroscopy showed that schoepite $(UO_2)_8O_2(OH)_{12}(H_2O)_{12}$ is present in the samples and it is characterized by its double peak. The first and second peaks were in the range of 840.3-842.5 cm^{-1} and 853.6-855.8 cm^{-1} respectively. These values agree with the reported Raman peaks for schoepite in the literature. The other mineral that has been identified by Raman spectroscopy is becquerelite $Ca(UO_2)_6O_4(OH)_6(H_2O)_8$ with a peak ranged between 829 to 836 cm^{-1}. Due to the lack of becquerelite spectrum in the spectral library, a natural becquerelite specimen was analyzed, and yielded a peak at 829 cm^{-1}, which is what to be expected for becquerelite. The powder X-ray diffraction analysis gave similar spectrum for each sample, indicating that the powdered material is similar in all of the samples. They all showed very good match with schoepite and/or meta-schoepite $(UO_2)_8O_2(OH)_{12}(H_2O)_{10}$, and also becquerelite. No autunite nor sabugalite nor any uranyl phosphate phase was detected, which disproves a former study on the same material. Only uranium and oxygen were detected by the X-ray photoelectron spectroscopy. No P, C, nor Ca was detected, although, the absence of Ca and presence of U could be due to their atomic ratio in becquerelite (1:6). The two main peaks for U were U 4f 7/2 at 382.0 eV and U 4f 5/2 at 392 eV. The oxygen peak was O 1s at 531.6 eV. These values agree with measured values for schoepite and meta-schoepite in the literature. The results obtained from the scanning electron microscope showed that U is dominant in all the measurements, as well as, O, Ca, Ti. Elements like Si, Al, Fe, S, Na, and C were also detected, yet they could be from the soil which surrounded the DU rounds. Au was also detected but this was due to the necessary gold coating in the sample preparation. According to the electron microprobe analysis, there were spots where metal U and soil minerals were detected as well as the secondary uranium minerals. The elemental maps showed a direct relation between U and Ca, and at the same time, no relation between U and Si, or Mg. On the other hand, Si was related to Al where both represent the constituents of the soil minerals. A quantitative analysis was done by the electron microprobe showed that the majority of U mass percentages were around 78-80%, which agrees with 78.2% and 79.47% for becquerelite and schoepite respectively according to their chemical formulas. Also the Ca mass percentage was about 2% which is expected to be found in becquerelite (2.19%). Ti mass percentage reached in some occasions 0.77%, which represent a DU alloy that has not yet been corroded. A dissolution experiment has been performed for the remaining powder amount of the corrosion products with a background 0.01 M $NaClO_4$ solution; the use of sodium perchlorate was to adjust the ionic strength at 0.01. All of the 15 vessels prepared for the 3 main samples were purged with nitrogen gas in order to remove the atmospheric CO_2. A model for the same experiment was calculated by Visual MINTEQ v.3.0 for the minerals that have been already identified by the earlier techniques to specify the pH range of interest, which is 6-10 in this case for becquerelite and schoepite and/or meta-schoepite. The modeled dissolution curves were calculated with and without the presence of atmospheric CO_2. After performing the dissolution experiment for about 6 months, the concentrations of dissolved U measured by ICP-OES showed a good match with both schoepite and becquerelite modeled curves. Nevertheless, it was not possible to distinguish between the two minerals due to their similar dissolution behavior. Schoepite was found to be the uranium solubility controlling phase in the acidic region, while becquerelite was the least soluble U mineral in the basic region. The measured data showed that some amounts of CO_2 were able to penetrate the sealed vessels; these amounts could be predicted by comparison with the modeled data. The solubility of U in the solutions as a function of pH showed the following pattern: the dissolved U concentrations were decreased to their lowest values as pH increased from 5 to 7 (about 5.1 E-6 mole/l); and up to pH of 8 (about 1.5 E-6 mole/l). After these points any further rise of pH would increase the dissolved U in solution. The solutions pH as well as their pCO_2 is controlling the amounts of dissolved U. The Ca concentrations on the other hand showed that they represent values more than that expected for becquerelite, and probably their source is the soils that were mixed with the samples. A case study of Basrah-Iraq was discussed for undergoing two major conflicts were DU ammunition have been used (1991 & 2003) in two regions with different environmental characteristics.

Zusammenfassung

In der vorliegenden Studie wurden verschiedene Techniken eingesetzt um drei Proben (4, 7, and 8) die aus den Korrosionsprodukten von aus dem Kosovo Krieg stammenden Munitionskugeln, bestehend aus abgereichertem Uran (Depleted Uranium - DU), zu untersuchen. Als erstes Verfahren wurde die Raman-Spektroskopie eingesetzt. Hierbei zeigte sichin den Proben, charakterisiert durch einen Doppelpeak, die Anwesenheit von Schoepit $(UO_2)_8O_2(OH)_{12}(H_2O)_{12}$. Der erste und zweite Peakzeigte sich im Spektralbereich von 840,3-842,5 cm^{-1} beziehungsweise 853,6-855,8 cm^{-1}. Diese Werte stimmen mit den Literaturwerten für Raman-Peaks für Schoepit überein. Des Weiteren wurde bei dieser Untersuchungsmethode Becquerelite $Ca(UO_2)_6O_4(OH)_6(H_2O)_8$ mit einem Peak im Bereich zwischen 829 to 836 cm^{-1} gefunden. Aufgrund des Fehlens des Becquerelitespektrums in der Spektralbibliothek wurde eine in der Natur vorkommende Variante analysiert und deren Peak bei 829 cm^{-1} bestimmt, was mit den Ergebnissen in den Proben korrespondiert. Mittels Röntgenbeugung (X-Ray Diffraction, XRD) zeigten sich in allen Proben ähnliche Spektren. Das lässt darauf schließen, dass das pulverisierte Material in allen Proben das gleiche ist. Hierbei zeigte sich eine sehr gute Übereinstimmung mit Schoepit und/oder meta-Schoepit$(UO_2)_8O_2(OH)_{12}(H_2O)_{10}$, sowie Becquerelite. Weiterhin war weder Autunit, Sabugalit noch Uranylphosphat anwesend, was die Ergebnisse einer anderen Studie, durchgeführt an denselben Proben, wiederlegt. Die Anwesenheit von P, C oder Ca im Probenmaterial konnte ausgeschlossen werden. Im Falle von Calciumkann dies mit der Anwesenheit von Uran erklärt werden, welches aufgrund seines Atomradius bevorzugt in Becquerelite (1:6) eingebaut wird. Die beiden Hauptpeaks für Uran lagen im Falle von U 4f 7/2 bei 382.0 eV und im Falle von U 4f 5/2 bei 392 eV. Diese Werte mit den Literaturwerten für Schoepit und meta-Schoepitüberein. Die Ergebnisse elektronenmikroskopischen Untersuchung zeigen U, O, Ca, Ti als dominante Komponenten in allen Messungen. Elemente wie Si, Al, Fe, S, Na, und C wurden ebenfalls detektiert; allerdings kann nicht ausgeschlossen werden, dass diese Elemente aus dem Boden in der unmittelbaren Umgebung der Munitionsgeschosse stammen. Gold wurde ebenfalls gemessen, was aber auf die Goldarmierung in den Probenaufbereitungsbehältern zurückgeführt werden kann. Die Elektronenmikroskopie zeigte außerdem einige Stellen in denen elementares Uran und Bodenminerale sowie sekundäre Uranminerale auftraten. Die Elementübersicht zeigt einen direkten Zusammenhang zwischen U and Ca und gleichzeitig keine Korrelation zwischen U und Si, oder Mg. Auf der anderen Seite zeigte sich aber ein Zusammenhang zwischen Si und Al da beide Konstituenten von Bodenmineralen darstellen. Eine mit Hilfe der Elektronenstrahlmikroanalyse durchgeführte quantitative Analyse zeigte den Massenanteil von Uran bei ca. 78 - 80%, was mit den 78,2% and 79,47% für Becquerelite beziehungsweise Schoepit aufgrund ihrer Summenformel korrespondiert. Zusätzlich zeigt sich für Calcium ein Massenanteil von 2% was mit dem Wert in Becquerelite (2.19%) recht gut übereinstimmt. Der Massenanteil von Ti lag in einigen Fällen bei 0,77%, was auf eine noch nicht korrodierte DU-Legierung zurückzuführen ist. Ein Lösungsexperiment wurde weiterhin durchgeführt, wobei eine 0,01 M $NaClO_4$-Lösung zum Einsatz kam in der die verbliebene Probensubstanz der Korrosionsprodukte gelöst wurde; Natriumperchlorate wurde hierbei genutzt um die Ionenstärke bei 0,01 zu halten. Um Verunreinigungen durch atmosphärisches CO_2 zu vermeiden wurden die im Versuch für die drei Hauptproben genutzten 15 Probenbehälter mit Stickstoffgas gespült. Eine Modelkalkulation für den beschriebenen Versuchsaufbau wurde mit Visual MINTEQ v.3.0 für die mittels vorgenannten Analysemethoden beschriebenen Mineralphasen im pH-Bereich von 6 – 10 im Falle von Becquerelite, und Schoepit berechnet. Die modellierten Lösungskurven wurden unter An- und Abwesenheit von atmosphärischem CO_2 kalkuliert. Nach dem Ende des Lösungsexperiments (Dauer ca. 6 Monate) zeigten die Konzentrationen des gelösten Urans, gemessen mittels ICP-OES, gute Übereinstimmung mit den modellierten Schoepit und Becquerelite Kurven. Auf Grund des ähnlichen Löslichkeitverhaltens war es nicht möglich zwichen den beiden Mineralen zu unterscheiden. Schoepit kontrolliert im sauren Bereich die Löslichkeit des Urans, während becquerelit im basichen am wenigsten gelöst wird. Des Weiteren bleibt festzuhalten, dass ein Anteil an CO_2 in die verschlossenen Probenbehälter eingedrungen ist, was sich mit der Vorhersage der Modeldaten deckt. Die Löslichkeit von Uran in der Lösung als Funktion des pH-Wertes zeigte die niedrigsten Konzentrationen im Falle einer Zunahme des pH-Wertes von 5 auf 7 (ungefähr 5,1 x 10^{-6} mol/l) und einer Zunahme des pH-Wertes auf 8 (ungefähr 1,5 x 10^{-6} mol/l bei). Oberhalb dieses Bereichs resultiert jeder weitere Anstieg des pH-Wertes in einer Zunahme gelösten Urans in der Lösung. Der ph-Wert der Lösung wie auch deren pCO_2-Wert kontrollieren hier die Menge des gelösten Urans. Auf der anderen Seite zeigten im Falle von Becquerelite die Ca-Konzentrationen höhere Werte als erwartet, wobei wahrscheinlich auf eine Vermischung der Proben mit Bodensubstanz zurückgeführt werden kann. Abschließend wurde, unter Berücksichtigung der oben genannten Ergebnisse, eine Fallstudie aus Basrah (Irak) diskutiert, wo in zwei militärischen Konflikten Uranmunition in zwei Regionen unter verschiedenen Umweltbedingungen eingesetzt wurden.

1 Introduction

1.1 Depleted Uranium (DU)

1.1.1 Definition

The term “Depleted Uranium” (DU) refers to the waste product of the uranium enrichment process, or the remaining uranium after the removal of the enriched fraction. Natural uranium consists of a mixture of three radioactive isotopes which are identified by the mass numbers U-238 (99.27% by mass), U-235 (0.72%) and U-234 (0.0054%) (WHO, 2003). The process of uranium enrichment takes place when uranium is to be used as fuel in light water reactors. The percentage of U-235 has to be raised from 0.72% in natural uranium to a reactor grade of 3.2% and 3.6% for Boiling Water Reactors BWRs and Pressurized Water Reactors PWRs (Diehl, 1999). The depleted or exhausted uranium has U-238 (99.8%), U-235 (0.2%), and U-234 (0.001) by mass, it can be distinguished from natural uranium by lower relative concentrations of U-235 and U-234 (at least three time less 235U than the natural uranium) as shown in Table 1-1. Therefore, the activity of DU is about 60% of the activity of natural uranium with the same mass. Another source for DU is the recycling or reprocessing of uranium and it can be distinguished from the DU produced as a byproduct of the uranium enrichment by the presence of reactor-created radioisotopes U-236 and U-232. The specific activity, which is the activity per unit mass of a particular radionuclide and is used as a measure of how radioactive a radionuclide is (L’Annunziata, 2007) of uranium in natural uranium is 25.4Bq mg^{-1}, lower than that in DU which is 14.8 Bq mg^{-1}.

Table 1-1: Characteristics of uranium isotopes and relative isotopic abundance in natural and depleted uranium.

Isotope	Relative isotopic abundance by weight		Specific Activity (Bq mg^{-1})	Half life (years)
	Natural	Depleted		
U-238	99.28%	99.8%	12.4	4510000000
U-235	0.72%	0.2%	80	710000000
U-234	0.0057%	0.001%	231000	257000

Uranium isotopes emit mainly alpha particles, which are particles emitted as a result of the disintegration of a parent nucleus to a daughter through the emission of the helium atom. It consists of 2 protons and 2 neutrons (Das and Ferbel, 2003) as shown in Equation 1-1. The disintegration of U-238 to Th-234 is located at the beginning of the uranium decay chain that ends up with stable lead Pb-206 (Fig. 1-1).

$$^{238}_{92}U \rightarrow {}^{234}_{90}Th + {}^{2}_{2}He^{2+}$$ Equation 1-1

The range of these alpha particles in air is of the order of one centimeter, and concerning tissues, they can barely penetrate the external dead layer of the skin. On the other hand, the beta-particles (electrons) are capable of penetrating about a centimeter of the tissue, while gamma-radiation (high energy photons) can pass through the body (Eisenbud and Gesell, 1997).

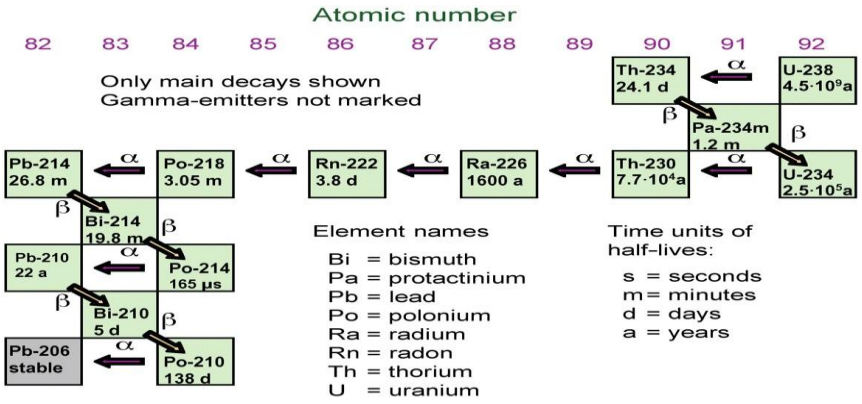

Figure 1-1: Decay chain of uranium.

1.1.2 DU Applications

DU has several civilian and military applications. It can be used for civilian purposes as a cladding material in fast-breeder reactors, as a fluorescent additive in dental porcelain crowns (not anymore), as X-ray radiation shielding in hospitals, as counterweights for rudders and flaps in commercial aircraft and forklifts (U.S. Department of Transportation, 1984), and in the keels of sailing yachts. Its main military application would be as ammunition (WHO, 2003). The DU ammunition is favored as an armor-

piercing weapon due to its high density (19 gm/cm^3), pyrophoricity (the capability of igniting spontaneously in air after hitting a hard surface), and the large amounts left at the end of the uranium enrichment process. It can also be used in tank armor, sandwiched between sheets of steel armor plate. DU is used as a tamper in fission bombs and as a nuclear explosive in hydrogen bombs (U.S. Office of the Secretary of Defense, 2000; and Miller, 2006).

1.1.3 Types of Ammo and Scenarios

The DU armor piercing rounds represent most of the military use of DU. This incendiary ammunition varies in size depending on the firing platform. 20 mm, 25 mm, 30 mm, and 120 mm different caliber ordnance can be fired from helicopters, fighting vehicles, aircrafts, and tanks respectively. In the production process of DU rounds, the material is alloyed with 0.75% titanium in order to make it harder. The alloying will eventually reduce the potential corrosion rate making it more resistant to corrosion than unalloyed uranium (Lillard and Hanrahan, 2005). Due to the relatively low melting point of uranium (1132 C) and the high temperature generated on impact of DU rounds on hard surfaces, the impact will lead to the ignition of the DU rounds (Bleise et al., 2003; Miller, 2006). One of the reasons that DU is used in armor piercing ammunition rather than tungsten is that, it undergoes self-sharpening as it pierces heavy armor, unlike the tungsten rounds, which blunt on impact with heavy armor (Bailey et al., 2002). The 30 mm DU rounds can pierce steel armor up to a thickness of 9 cm. A DU 30 mm round consists of a conical DU penetrator of 95 mm length, a diameter at the base of 16 mm and a weight of approximately 280 g. The penetrator is fixed in aluminum casing called “the jacket”. This has a diameter of 30 mm and a length of 60 mm (Bleise et al., 2003 and references therein) as shown in Fig. 1-2.

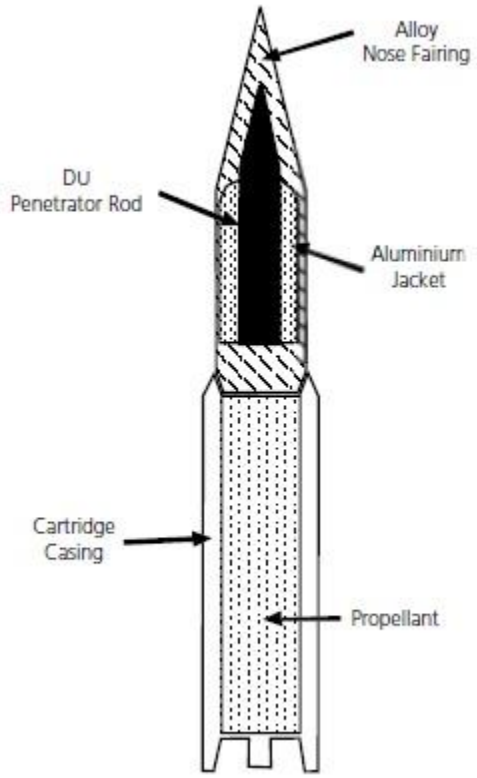

Figure 1-2: Schematic diagram of a 30 mm DU round (after Bailey et al., 2002).

One of the common platforms used for firing DU rounds is the A-10 aircrafts. The A-10 aircraft is equipped with one gun firing 3900 rounds per minute. A typical burst of fire of 2-3 s involves 120-195 rounds. Normally the DU ammunition is present in about 75% of the rounds; the rest consists of non-DU ammunition. The shots hit the ground in a straight line and, depending on the angle of approach, it can hit the ground 1-3 m apart and cover an area of about 500 m^2. The number of penetrators hitting a target depends upon the type of target. In most cases not more than 10% of the penetrators hit the target (CHPPM, 2000; Bleise et al., 2003). On impact with a hard surface, like a tank, the penetrator pierces the metal of the tank, causing the round to ignite and eventually form what so called the DU dust or aerosols. These aerosols can either precipitate in and around the targets in the battle fields or can travel for long distances depending on properties like the aerosol's size, shape, & weight; wind speed & direction; and the topography of the area. 10-35% (and a maximum of 70%) of the DU penetrator becomes an aerosol on impact (Harley et al., 1999). The other and more probable

scenario for the DU rounds is when they miss their target and hit the ground. In this case the rounds would penetrate the soil to a depth of more than 50 cm depending on the aircraft speed, and firing angel. Eventually the buried round will undergo corrosion and oxidation leading to the formation of different secondary uranium minerals depending on properties like the chemistry and pH soil and water involved in the local environment.

1.2 The use of DU in conflicts

Depleted uranium ammunition has been used in four conflicts:

1- 1991, Iraq and Kuwait.
2- 1995, Bosnia-Herzegovina.
3- 1999, Kosovo.
4- 2003 Iraq.

DU ammunition was used for the first time in conflicts during the first gulf war in Iraq and Kuwait in 1991, only the forces of the United States and the United Kingdom used the DU ammunition in this war. Large DU projectiles were fired from tanks. The air force fired 783514 rounds of 30 mm DU ammunition corresponding to 259 tons of DU. The army fired 9552 DU tank rounds, corresponding to approximately 50 tons of DU and the Marine aviation expended DU ammunition corresponding to about 11 tons of DU. The UK Ministry of Defense estimates that its tanks fired less than one hundred 120 mm rounds, corresponding to about one ton of DU(Bleise et al., 2003 and references therein). The DU ammunition was used for the second time in Iraq in 2003. The total amount is unknown, but speculative figures from various studies range between 170 and 1700 metric tons. The United Kingdom Ministry of Defense (UK MOD) has indicated that approximately 1.9 tons were fired in that this conflict. They stated that no airplanes were used to fire DU ammunition and it was fired only from tanks. The UK MOD provided the UNEP with the coordinates of DU firing points for the UK Challenger II tanks (UNEP, 2007). No information was provided by the American army despite the fact that they used DU ammunition much more than the UK army.

As for Europe, there are two conflicts were DU ammunition has been used. The first conflict was In Bosnia-Herzegovina in 1994 and 1995 where About 10800 rounds (approximately 3 tons of DU) were fired, mainly around Sarajevo. The second conflict was in Kosovo 1999, 30000 rounds of DU (approximately 10 tons of DU) were fired from the A-10 planes (Bleise et al., 2003 and references therein). The samples used in this study are from the Kosovo conflict, they represent the DU rounds which missed their targets and hit the ground.

1.3 DU interactions with human body

1.3.1 Exposure to DU

Exposure to DU can be either external or internal. The external exposure involves beta and gamma particles, since the alpha particles cannot penetrate the human skin. It happens mainly during battles where the DU aerosols are formed and can be in excessive concentrations in the air, where they move until they precipitate on the ground or on people (soldiers) and/or animals. Because they emit mainly alpha particles, the potential risk from external exposure to DU ammunition is exceedingly low, unless the uranium is introduced directly into the body (e.g. through wounds) (International Atomic Energy Agency IAEA Fact sheet). On the other hand, the internal exposure can take one of the three pathways: Ingestion (in food and water); Inhalation (DU aerosols); and through contaminated wounds. The DU can enter the body either as uranium metal or as uranium oxides that have relatively low solubilities. It could be carried by the body fluids for years or at some point dissolve forming the uranyl ion (UO_2^{2+}), which may react and absorbed on body tissues and organs (Stevens et al. 1980). The major concern in ingestion is through water. That is when the DU aerosols precipitate in surface waters like lakes, and rivers, perhaps leading to contamination of ground water as well. The contamination is dependent on various local environmental properties, but strongly on the pH and chemistry of the water and the surrounding soil. The other pathways that lead to contamination with DU (inhalation and contaminated wounds) concern mostly the soldiers, people or animals that were in or close to the battle fields, while inhalation is the most likely route of intake of DU (EPA, 2006).

1.3.2 Behavior in the body

When inhaled, uranium is attached to particles of different sizes. The size of the uranium aerosols and the solubility of the uranium compounds in the lungs and gut influence the transport of uranium inside the body. Coarse particles are caught in the upper part of the respiratory system (nose, sinuses, and upper part of the lungs) from where they are exhaled or transferred to the throat and then swallowed. Fine particles reach the lower part of the lungs (alveolar region). If the uranium compounds are not

easily soluble, the uranium aerosols will tend to remain in the lungs for a longer period of time (up to 16 years), and deliver most of the radiation dose to the lungs. They will gradually dissolve and be transported into the blood stream. For more soluble compounds, uranium is absorbed more quickly from the lungs into the blood stream. About 10% of it will initially concentrate in the kidneys. Most of the uranium ingested is excreted in feces within a few days and never reaches the blood stream. The remaining fraction will be transferred into the blood stream. Most of the uranium in the blood stream is excreted through urine in a few days, but a small fraction remains in the kidneys and bones and other soft tissue (IAEA: http://www.iaea.org/newscenter/features/du/du_qaa.shtml; USNRC, 2011).

1.3.3 Health Effects

In sufficient amounts, uranium that is ingested or inhaled can be harmful because of its chemical toxicity. Like mercury, cadmium, and other heavy-metal ions, excess uranyl ions depress renal function (e.g. affect the kidneys). High concentrations in the kidney can cause damage and in extreme cases a renal failure. The general medical and scientific consensus is that in cases of high intake, uranium is likely to become a chemical toxicological problem before it is a radiological problem. Since uranium is mildly radioactive, once inside the body it also irradiates the organs, but the primary health effect is associated with its chemical action on body functions. In many countries, current occupational exposure limits for soluble uranium compounds are related to a maximum concentration of 3 µg uranium per gram of kidney tissue. Any effects caused by exposure of the kidneys at these levels are considered to be minor and transient. Current practices, based on these limits, appear to protect workers in the uranium industry adequately. In order to ensure that this kidney concentration is not exceeded, legislation restricts long term (8 hour) workplace air concentrations of soluble uranium to 0.2 mg per cubic meter and short term (15 minute) to 0.6 mg per cubic meter. Like any radioactive material, there is a risk of developing cancer from exposure to radiation emitted by natural and depleted uranium. This risk is assumed to be proportional to the dose received. Limits for radiation exposure are recommended by the International Commission on Radiological Protection (ICRP) and have been adopted in the IAEA's

Basic Safety Standards. The annual dose limit for a member of the public is 1 mSv, while the corresponding limit for a radiation worker is 20 mSv. The additional risk of fatal cancer associated with a dose of 1 mSv is assumed to be about 1 in 20,000. This small increase in lifetime risk should be considered in light of the risk of 1 in 5 that everyone has of developing a fatal cancer. It must also be noted that cancer may not become apparent until many years after exposure to a radioactive material (Craft et al., 2004; IAEA: http://www.iaea.org/newscenter/features/du/du_qaa.shtml; USNRC, 2011). The contact dose rate from a DU penetrator is about 2 mSv per hour, primarily from beta particle decay from DU progeny. At this dose rate it is unlikely that prolonged contact with a DU penetrator would lead to skin burns (erythema) or any other acute radiation effect (IAEA Fact sheet; Bleise et al. 2003).

1.4 Interactions of DU with the environment

The use of DU ammunition in the conflicts has lead to the increase of the uranium levels in the environment. Depending on several factors characterizing the local environment, the impact will be different in each case. The DU rounds have two possibilities, either hitting the target (normally hard surfaces) generating DU aerosols that might precipitate in or close to the battle fields, or travel for short distances away from the conflict zone carried by the wind until they precipitate. After settling on the ground, the re-suspension of the DU aerosols by the wind or by human activities would decrease the concentration of DU in the soil with time. The environmental factors controlling this phase are: the aerosols' weight, size, & shape; wind speed & direction; the topography of the area, and seasonal weather patterns & climatic factors like rain and sand storms. It is expected that the DU aerosol would travel for longer distances when carried by strong winds in flat areas (e.g. no mountains or dams or any other barriers) with no rain fall periods.

The second possibility is when the DU rounds miss their targets or precipitate after having been carried by the wind and settle in the soil, or into rivers or lakes if any existed close to the battle fields. The DU fragments settling on the soil surface or down to one meter (or less) in the soil profile will be oxidized and corrode with time, and the uranium's oxidization state will be U^{6+} in this case, while U^{4+} is the oxidation state for uranium in the reduced environments. The DU ammunition corrosion products are the result of the uranium metal alteration to different secondary uranium minerals. They represent at least one or most likely a mixture of minerals. The types of these secondary minerals depend highly on the soil and water characteristics. Notably under oxidizing conditions, uranyl oxy-hydroxide mineral(s) are formed at the beginning of the alteration sequence. In addition, uranyl carbonates, silicates, sulfates, phosphates etc could form depending on the available ligand and pH. Eventually these minerals will dissolve sparingly in water and migrate. The distance or scale of migration depends on the local hydrological situation until they meet the suitable conditions to precipitate as mineral again (e.g. change in pH or reacting with a specific ligand or cation). The aqueous speciation of uranium and eventually the uranium mobility depends on the oxidation-reduction conditions and pH of the solution. Under reducing conditions like in

deep aquifers, uranium is present as U^{4+}; $U(OH)_4$ ion is dominant under pH conditions typical of most natural waters. It would precipitate to form relatively insoluble minerals like uraninite UO_2 and coffinite $U(SiO_4)_{1-x}(OH)_{4x}$. The minerals formed have high tendencies to be adsorbed onto mineral surfaces, and partitioned into organic matter (EPA, 2006 and references therein). Under oxidizing conditions, the U^{6+} always bonds to two O atoms forming the uranyl ion UO_2^{2+}. The speciation will change as pH changes, positively charged species are expected to dominate under acidic conditions, while neutral and negatively charged species will dominate under neutral and alkaline conditions respectively like UO_2CO_3 (aq) and $UO_2(CO_3)_2^{2-}$. The minerals formed in this environment have greater solubilities than of those formed in the reduced environment. Thus the uranium is expected to be more mobile under oxidizing conditions than under reducing conditions.

1.5 Description of the Previous Experiments

This research adds to two previous works. The early works were performed by scientists in the GSF- National Research Center for Environment and Health, Institute of Radiation and Protection; and the Research Center Rosendorf, Institute of Radiochemistry in 2005 and 2007 (Schimmack et al., 2005 ; 2007). Both studies involved leaching of depleted uranium in soil as determined by column experiments, also in the second study uranium species in the effluent of soil columns and in the corroded material have been identified.

The soil material that has been used for these experiments was taken from the plough horizon of two fields with different soil types at the Klostergut Scheyern Experimental Station, Germany, about 40 km north of Munich. The first soil was a sandy-loamy brownearth (FAO system: cambisol) with a pH value of 5.6 (clay content: 13%; silt content: 32%; organic content: 2.1%; natural uranium content: 2.5% mg kg^{-1}). The second soil was a silty-loamy parabrownearth (FAO: luvisol) with a pH value of 5.8 (clay content: 22%; silt content: 60%; organic content: 2.1%; natural uranium content: 3.9 mg kg^{-1}) (Schimmack et al., 2005 ; 2007).

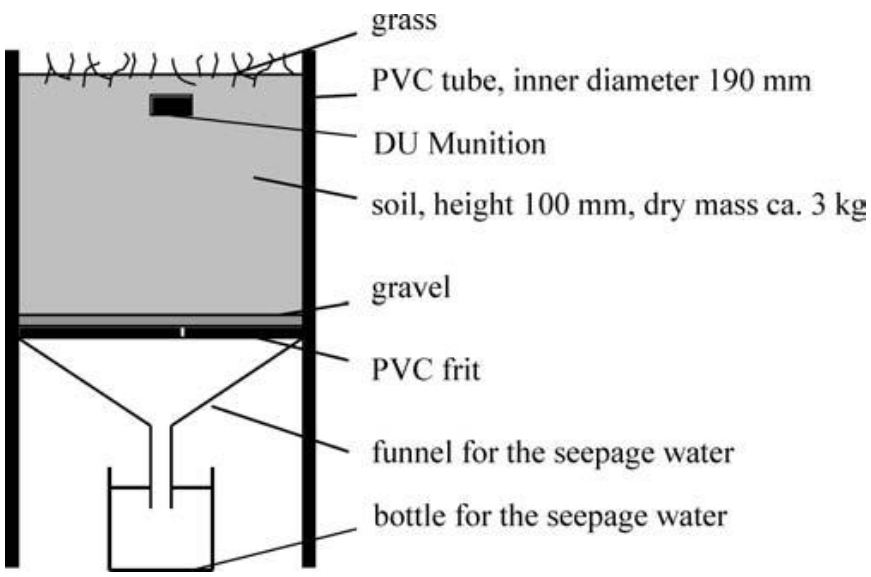

Figure 1-3: Longitudinal section of a column used in the leaching experiments. (after Schimmack et al., 2005).

The columns (Fig. 1-3) were plastic tubes 190 mm in diameter and 400 mm in height. About 3.3 kg of dry soil resulting in a height of about 10 cm, as well as 1 kg of gravel was filled on a plastic frit for better drainage. The columns were installed in a laboratory with controlled temperature (21±1) °C and a relative humidity of (55±10) %. The columns were irrigated weekly with 16 mm of synthetic rainwater that has a pH value of 6, consisting mainly of 0.09 mM NH_4NO_3, 0.08 mM $(NH_4)_2SO_4$ and 0.05 mM $CaSO_4$. The rainwater dropped through about 80 cannulae of a rain simulator distributed over the cross section of 283 cm^2 of the column. To establish a vegetated area, a mixture of grass species suitable for shady sites was selected and grown on the soil in the column. After about 1 year, moss had spread over the soil surface and a fern (*Dryopteris cathusiance (Vill.) H.P. Fuchs s.l.*) grew (Schimmack et al., 2005 ; 2007).

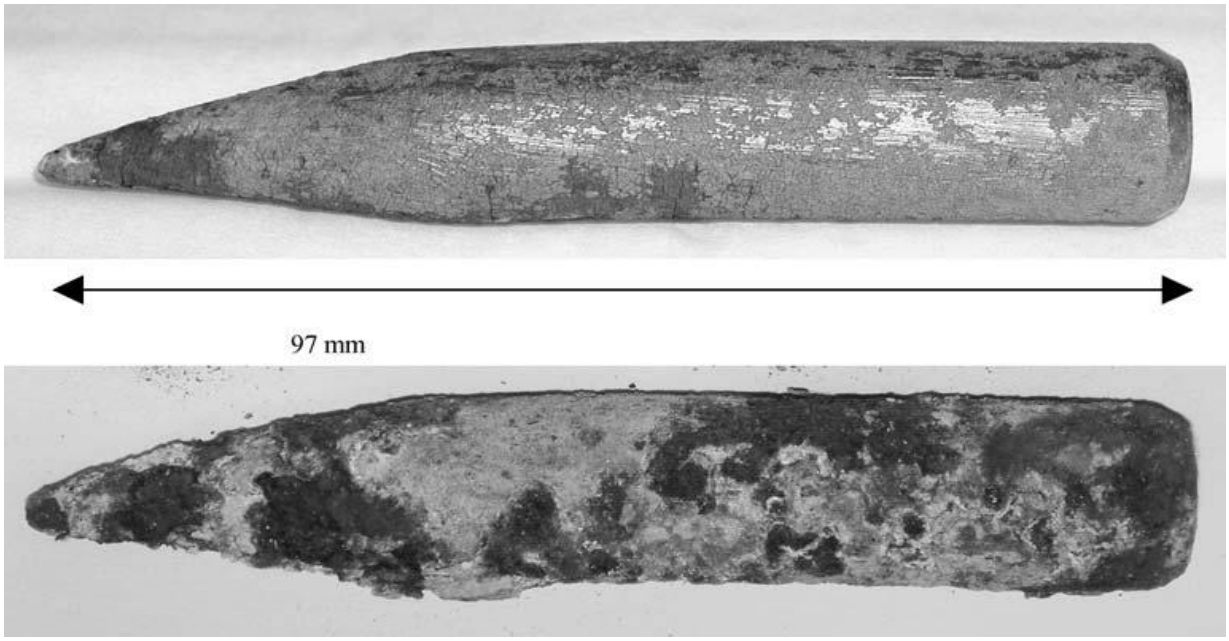

Figure 1-4: DU penetrator used with cambisol and cleaned by nitric acid (top) at the beginning of the experiments, and after one year of corrosion (bottom) (after Schimmack et al., 2005).

Figure 1-5: DU penetrator after corroding for 3 years (after Schimmack et al., 2007).

Sixteen columns, eight for each soil type were installed in June and July 2003. DU penetrators and fragments have been placed in the columns; the penetrators had length of about 97 mm and a diameter of about 16 mm (Fig. 1-4). Their masses varied between 264 and 294 g, while the fragments had masses ranging between 145 and 195 g. All penetrators and fragments were found in Kosovo in 2001, this implies 1-2 years of corrosion. Each DU round was cleaned by nitric acid and aqua dest, before it was put into the columns to achieve uniform conditions for the corrosion in the soil (Schimmack et al., 2005 ; 2007). The uranium concentrations in the effluent have been analyzed by ICP-MS to determine the leaching rate of uranium after 1 year. Also 6 of the 12 columns were dismantled, the mass loss of the DU ammunition was determined as the difference between the initial mass and the final mass. As for the other 6 soil columns (the second study 2007), the experiment continued, and the same measurements mentioned above were performed, also the speciation of uranium has been determined by time-resolved laser-induced fluorescence spectroscopy (TRLFS). After the 1st year, the leaching rate of U-238 from the DU munitions was 0.03 mg. After year 3 it was increased to 13 mg. 14.5 g corresponding to 7.9% of the initial DU mass was corroded after 3 years (Fig. 1-5), compared to 1.6% corroded mass after 1 year. Uranium species in the seepage water were mainly hydroxo and carbonate compounds, while those in the corroded material were phosphate compounds (Schimmack et al., 2007).

1.6 Background information on U(VI) minerals

The uranium has four possible positive oxidation states (from 3 to 6) but in nature only two states exist. These two states are uranium tetravalent U(IV) and hexavalent U(VI), which occur in reduced and oxidized environments respectively. The uranium minerals can be generally classified into 2 categories: the U(IV) minerals, and the U(VI) minerals. In this research, it is expected to have oxidizing conditions more than reducing conditions, because the previous experiments done by Schimmack et al. 2005 & 2007 were simulated under aerobic conditions. For this reason, it is useful to focus on the structure and chemistry of the U(VI) minerals, which are the minerals formed in an oxidized environment.

1.6.1 Structure of U(VI) minerals

In minerals the U^{6+} cation is present as part of the nearly linear uranyl ion $(U^{6+}O_2)^{2+}$ (Evans, 1963), which is the main constituent in all U(VI) phases. In the uranyl ion, the U^{6+} - O bond lengths are ~ 1.8 Å, corresponding to very strong covalent bonds. The U^{6+} - O boding mechanism is primarily through donation of electrons from the p orbitals of the O atoms into the empty d and f orbitals of the U^{6+} cation (Craw et al., 1995).The uranyl ion has a formal valence of 2+, and as such it must be coordinated by ligands in a crystal structure. The uranyl ion can be coordinated by four, five, or six ligands arranged at the equatorial corners, forming square bipyramids, pentagonal bipyramids, and hexagonal bipyramids, respectively. These ligands are O^{2-}, OH^-, and H_2O (Fig. 1-6). The O atoms of the uranyl ions are located at the apices of the bipyramids. The equatorial bonds are longer than the U^{6+}- O bonds and therefore weaker (Burns et al., 1996; Burns, 1999).

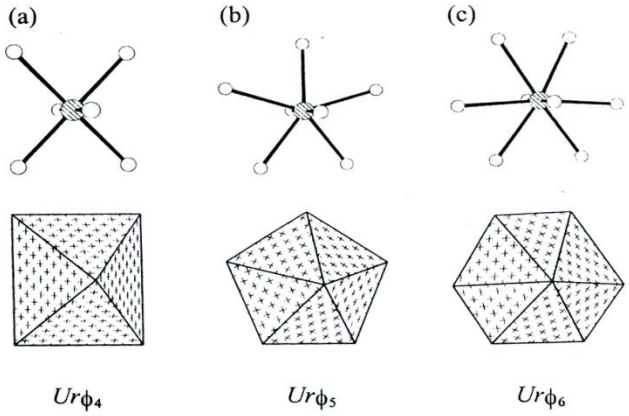

Figure 1-6: Types of coordination polyhedra observed in U(VI) minerals (after Burns, 1999).

The U(VI) minerals can be classified structurally according to their sheet anion topologies, which is a hierarchy suggested by Burns et al. 1996. The sheet anion topology contains triangles, squares, pentagons, and hexagons. It can be derived as follows (Fig. 1-7):

1) Each anion that is not bonded to at least 2 anions within the sheet, and is not an equatorial anion of a bipyramid or pyramid within the sheet, is not considered a constituent of the sheet anion topology (Fig. 7c).
2) Cations are ignored, also the cation-anion bond, leaving an array of unconnected anions (Fig. 1-7d).
3) Anions are joined by lines, such that only anions that may be realistically considered as part of the same coordination polyhedron are connected (Fig. 7e).
4) Anions are removed from further consideration, leaving only a series of lines that represent the sheet anion topology (Fig. 7f).

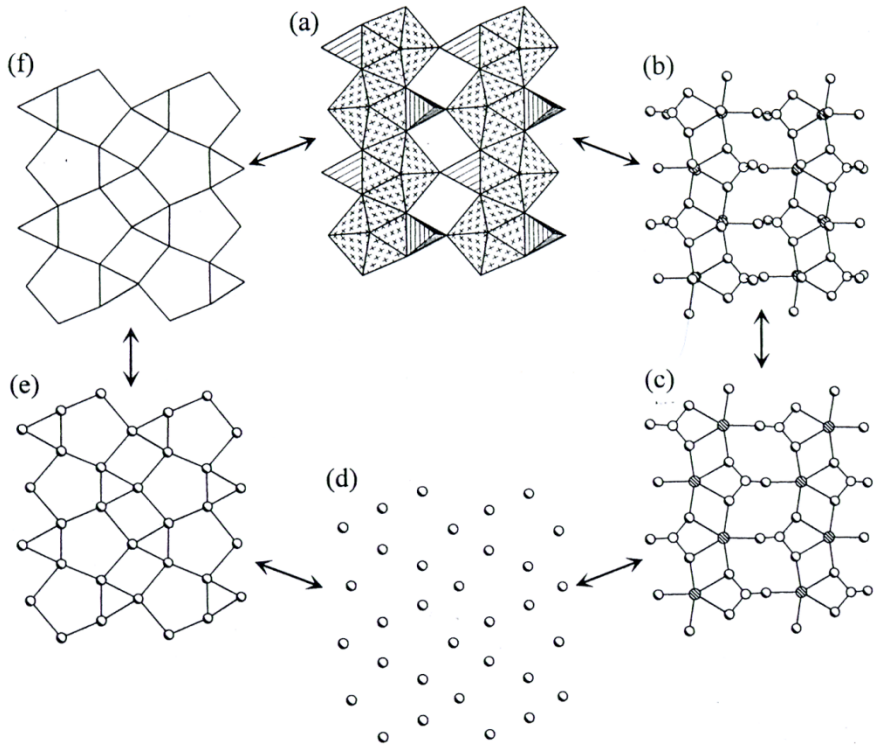

Figure 1-7: The development of sheet anion topology (after Burns et al. 1996).

The different minerals will be categorized when applying the concept of the hierarchy to the U(VI) minerals. For example, minerals like uranophane $Ca(UO_2)_2(SiO_3OH)_2(H_2O)_5$ and ulrichite $CaCu(UO_2)(PO_4)_2(H_2O)_4$ have the same sheets that are based on anion topologies with triangles, squares, and pentagons, despite the fact that these minerals have different ligands.

1.6.2 Chemistry of U(VI) minerals

The dissolved U in solution and the simulated oxidizing laboratory conditions (like in our case) would give the U the most common oxidized state in nature, which is U^{6+}. Consequently these conditions would lead to the formation of the uranyl ion UO_2^{2+}. The uranyl ion is the dominant aqueous species in most waters below a pH of 5. At higher pH, the uranyl ion hydrolyzes, forming a number of aqueous hydroxide complexes (Finch and Murakami, 1999), according to the general hydrolysis reaction:

$$UO_2^{2+} + yH_2O \rightarrow UO_2(OH)_y + yH^+$$ Equation 1-2

In more U-rich solutions, polymeric U complexes could be formed:

$$xUO_2^{2+} + yH_2O \rightarrow (UO_2)_x(OH)_y^{2x-y} + yH^+$$ Equation 1-3

Consequently, the precipitation of these solutions with dissolved U concentrations, would lead to the formation of many uranyl minerals depending mainly on the pH and the chemistry of water. Fig. 1-8 shows the paragenesis of the main uranyl minerals groups.

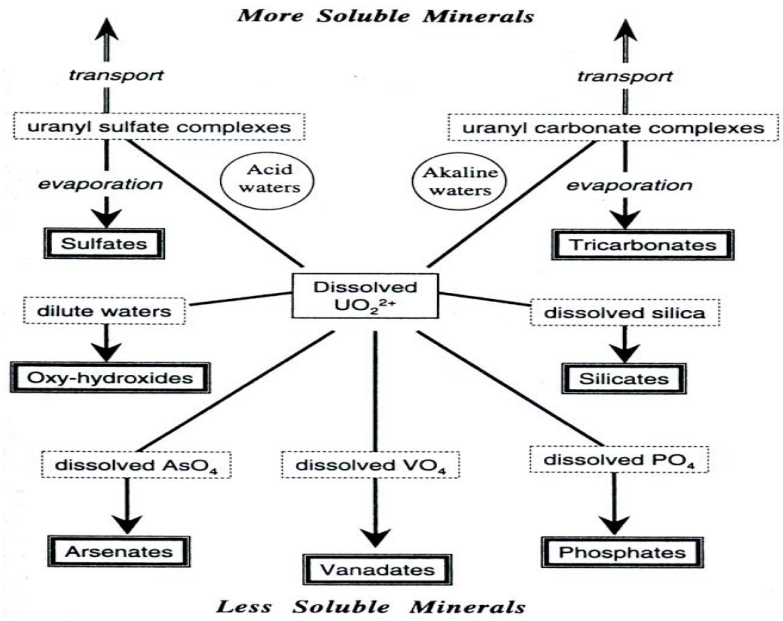

Figure 1-8: Scheme depicts the paragenesis of major uranyl minerals groups (after Finch and Murakami, 1999).

The uranyl or U(VI) minerals belong to different chemical groups. These minerals display remarkable structure and chemical diversity. This diversity results from different chemical conditions under which U minerals are formed. Therefore, the U minerals are excellent indicators of the geochemical environment (Finch and Murakami, 1999). The chemical groups can be classified as follows:

1.6.2.1 Chemical groups of U(VI) minerals

The differences among these groups are defined by the different ligands attached in their structures. In general, the ligands can be oxy-hydroxides, carbonates, silicates, phosphates, arsenates, vanadates, molybdates, tungstates, sulfates, selenites, or tellurites.

1.6.2.1.1 Uranyl-oxyhydroxides group

This group can be presented by the general formula:
$M_n[(UO_2)_xO_y(OH)_z](H_2O)_m$

Where M is the divalent cation, commonly Ca^{2+}, $Pb^{2+,}$, Ba^{2+}, Sr^{2+}, and even K^+ is also known. They form in U-rich aqueous solutions and develop early during the oxidation and corrosion of uraninite-bearing ore deposits. Table 1-2 shows some of the common minerals from this group. No Na or Mg bearing uranyl oxyhydroxides were found in nature, but they were synthesized.

Table 1-2: Main minerals in the Uranyl-oxyhydroxides group.

Name	Formula
Agrinierite	$(K_2,Ca,Sr)(UO_2)_3O_2(OH)_3(H_2O)_4$
Becquerelite	$Ca(UO_2)_6O_4(OH)_6(H_2O)_8$
Billietite	$Ba(UO_2)_6O_4(OH)_6(H_2O)_8$
Compreignacite	$K_2(UO_2)_6O_4(OH)_6(H_2O)_7$
Scheopite	$(UO_2)_8O_2(OH)_{12}(H_2O)_{12}$
Metaschoepite	$(UO_2)_8O_2(OH)_{12}(H_2O)_{10}$
Fourmarierite	$Pb(UO_2)_4O_3(OH)_4(H_2O)_4$
Vandendriesscheite	$Pb_{1.57}(UO_2)_{10}O_6(OH)_{11}(H_2O)_{11}$

1.6.2.1.2 Uranyl-carbonates group

They may precipitate where evaporation is significant or where the fugacity of CO_2 is greater than the atmospheric pressure. Mono- di- and tricarbonates can precipitate from acidic to alkaline waters respectively. The monocarbonates are relatively insoluble while the di- and tricarbonates are soluble when re-exposed to fresh water. Table 1-3 shows some of the minerals from this group.

Table 1-3: Main minerals in the Uranyl-carbonates group.

Name	Formula
Blatonite	$UO_2CO_3.H_2O$
Rutherfordine	UO_2CO_3
Voglite	$Ca_2Cu(UO_2)(CO_3)_4(H_2O)_6$
Fontanite	$Ca(UO_2)_3(CO_3)_4(H_2O)_3$
Rabbittite	$Ca_3Mg_3(UO_2)_2(CO_3)_6(OH)_4(H_2O)_{18}$
Liebigite	$Ca_2(UO_2)(CO_3)_3(H_2O)_{11}$

1.6.2.1.1.3 Uranyl-silicates group

They are the most abundant group of uranyl minerals because of the ubiquity of dissolved Si in most groundwaters. Uranophane is the most common uranyl mineral, precipitating from near neutral to alkaline groundwaters that contain dissolved Si and Ca. These minerals might lose some Ca and Si when exposed to carbonate-free waters, altering to more U-rich minerals such as uranophane and Soddyite. In more alkaline carbonate-rich waters, they may lose U preferentially, altering to amorphous or microcrystalline silica. Table 1-4 shows some of the minerals from this group.

Table 1-4: Main minerals in the Uranyl-silicates group.

Name	Formula
Uranophane	$Ca(UO_2)_2(SiO_3OH)_2(H_2O)_5$
Boltwoodite	$K(UO_2)(SiO_3OH)(H_2O)_{1.5}$
Kasolite	$Pb(UO_2)(SiO_4)(H_2O)$
Sklodowskite	$Mg(UO_2)_2(SiO_3OH)_2(H_2O)_6$
Soddyite	$(UO_2)_2SiO_4(H_2O)_2$
Weeksite	$K_2[(UO_2)_2(Si_5O_{13})] \cdot 1.4(H_2O)$

1.6.2.1.1.4 Uranyl-phosphates and arsenates group

Dissolved phosphate is a common constituent of many groundwaters. Uranyl phosphates and arsenates precipitate from waters when dissolved phosphate and AsO_4 are available and they show low solubilities. This group has approximately 70 species. Table 1-5 shows some of the minerals from this group.

Table 1-5: Main minerals in the Uranyl-phosphates group.

Name	Formula
Autunite	$Ca[(UO_2)(PO_4)]_2(H_2O)_{10\text{-}12}$
Sabugalite	$Al[(UO_2)_4(HPO_4)(PO_4)_3](H_2O)_{16}$
Saleeite	$Mg[(UO_2)(PO_4)]_2(H_2O)_{10}$
Bassetite	$Fe[(UO_2)(PO_4)]_2(H_2O)_8$
Meta-autunite	$Ca[(UO_2)(PO_4)]_2(H_2O)_6$
Metatorbernite	$Cu[(UO_2)(PO_4)]_2(H_2O)_6$
Dewindtite	$Pb_3[(UO_2)_3O(OH)(PO_4)_2]_2(H_2O)_{12}$
Ulrichite	$CaCu(UO_2)(PO_4)_2(H_2O)_4$

1.6.2.1.1.5 Uranyl-vanadates, molybdates, and tungstates group

This group comprises the most insoluble uranyl minerals. Table 1-6 shows some of the minerals from this group.

Table 1-6: Main minerals in the Uranyl-vanadates, molybdates, tungstates group.

Name	Formula
Carnotite	$K_2(UO_2)_2(V_2O_8)(H_2O)_3$
Tyuyamunite	$Ca(UO_2)(V_2O_8)(H_2O)_8$
Iriginite	$(UO_2)Mo_2O_7(H_2O)_3$
Uranotungstite	$(Ba,Pb,Fe^{2+})(UO_2)_2(WO_4)(OH)_4(H_2O)_{12}$

1.6.2.1.1.6 Uranyl-sulfates, selenites, tellurites group

Dissolved sulfate in groundwater can combine with UO_2^{2+} to form stable uranyl phosphate complexes in solution. Afterwards, evaporation is required to precipitate uranyl sulfates. They can precipitate from waters with less than 6 pH. Uranyl sulfates occur where uranyl carbonates are absent (and vice versa). This might reflect the different pH ranges over which uranyl sulfate and uranyl carbonate complexes are important. Table 1-7 shows some of the minerals from this group.

Table 1-7: Main minerals in the Uranyl-sulfates, selenites, tellurites group.

Name	Formula
Johannite	$Cu(UO_2)_2(SO_4)_2(OH)_2(H_2O)_{6\text{-}8}$
Uranopilite	$(UO_2)_6(SO_4)(OH)_{10}(HO)_{12}$
Meta-uranopilite	$(UO_2)_6(SO_4)(OH)_{10}(HO)_5$
Haynesite	$(UO_2)_3(OH)_2(SeO_3)_3(H_2O)_5$
Cliffordite	UTe_3O_9

1.7 Corrosion of DU ammunition

Corrosion can be defined as a chemical or electrochemical reaction between a material, usually a metal, and its environment that produces a deterioration of the material and its properties (Davis, 2000). It involves the disintegration of material into its constituent atoms by chemical interactions with their surroundings. Eventually this would cause the cracking of material producing corrosion products leading to loss of mass of metal. The unalloyed uranium and the different U alloys, for example, U-0.75Ti (referring to an alloy with 99.25%U and 0.75Ti, which is what was used in the DU ammunition) can undergo different types of corrosion depending on their environment. The alloy is more resistant to corrosion than unalloyed uranium, but still it can suffer corrosion.

1.7.1 Corrosion environments for DU ammunition

The DU ammunition can corrode in atmospheric, aqueous (fresh & salt water), and soil environments. The corrosion process is controlled by several factors with different impacts for each environment.

1.7.1.1 Atmospheric environment

Atmospheric corrosion can vary widely depending on the contaminants present, humidity & rainfall, wind, and temperature. The studies that have been conducted to compute the corrosion rates led to the categorization of environments into rural, urban, industrial, marine, and combination of them (ordered from least to highest corrosivity). In addition, deviations of corrosion rates have led to a further subcategorization based upon weather and climate as shown in Table 1-8 (Craig et al., 2006). The corrosion rate is normally expressed either by weight loss per unit area per unit time, usually mdd (milligrams per square decimeter per day), or by the rate of penetration mmpy (millimeters per year).

Table 1-8: General corrosion rates for different atmospheric environments (after Craig et al., 2006 and references therein).

Rate of Corrosion	Type of Environment		
High	Tropical	Industrial	Marine
Moderate	Temperate	Suburban	Inland
Low	Arctic	Rural	

Increasing humidity can increase the corrosion rate, as moisture provides the electrolyte, which is required for corrosion reactions to take place. Rainfall can increase or decrease corrosion rates. In areas where stagnant water may accumulate, a localized corrosion cell will most likely be the result. However, rain may also wash corrosive deposits off from metal surfaces decreasing corrosivity. Corrosion rates can increase with increasing temperature. Changing temperature may change the corrosion mechanism from uniform to pitting. It can also evaporate condensed moisture on metallic surfaces leaving behind corrosive contaminants (Craig et al., 2006).

Atmospheric corrosion of uranium is commonly divided into oxidation in dry air or oxygen, water vapor, and oxygen-water vapor mixtures (Lillard and Hanrahan, 2005). The reaction of uranium with oxygen can be described as:

$$U + \frac{2+x}{2} O_2 \rightarrow UO_{2+x}$$ Equation 1-4

The value of x is a product of the atmosphere (oxygen activity), temperature, and time. The value of x therefore varies as a function of the particular oxidizing species (oxygen, CO_2, and CO mixtures). As the oxide scale grows, the outer layer in contact with the oxide/gas interface gradually increases in the oxygen content. The oxide spalls off of the surface at a thickness of about 1 µm, leading to a reinitialization of the process (Lillard and Hanrahan, 2005). The reaction of uranium with water vapor is much faster than that of dry air or oxygen (Fig. 1-9).

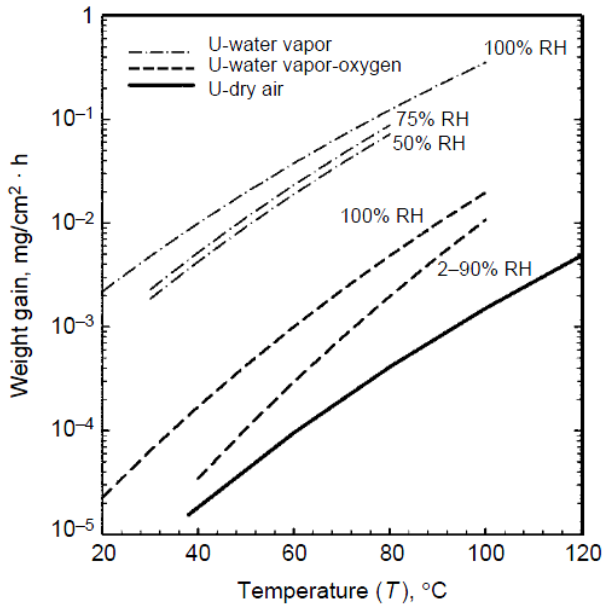

Figure 1-9: Uranium oxidation rates in dry air, oxygen-water vapor, and water vapor as a function of temperature (after Lillard and Hanrahan, 2005).

In humid environments, a thin layer of water forms on a material surface and sets up an electrochemical cell. Therefore, uranium oxidation in water vapor environments is electrochemical corrosion, which is governed by anodic and cathodic reaction. The anodic reaction is the oxidation of uranium whereby uranium gives up electrons and UO_{2+x} is formed. To maintain charge neutrality, the cathodic reaction (Eq. 1-5) must consume the electrons generated by oxidation (Lillard and Hanrahan 2005 and references therein). The overall reaction is expressed in Eq. 1-6.

$$O_2 + 2H_2O + 4e^- \rightarrow 4OH^- \qquad \text{Equation 1-5}$$

$$U + O_2 + 3H_2O \rightarrow UO_2 + 3OH^- + 3H^+ \qquad \text{Equation 1-6}$$

These equations could be applied to the environment in which the corrosion of the DU ammunition took place, because of the presence of water (the synthetic rain water used for irrigation) and the DU ammunition's location near the soil surface (1-2 & 8-9 cm deep) assuming the presence of oxygen as well.

1.7.1.2 Water environment

Water corrosivity is related to water composition, dissolved gases, pH, temperature, water velocity, and biological organisms. The presence of oxygen and sulfurous gases can increase the corrosion rate. In addition, the ions from dissolved salts most responsible for increased water corrosivity are chlorides and sulfates (Craig et al., 2006). This can be relevant for the corrosion of DU ammunition that has been used in this study due to the synthetic rain water used for irrigation, which included sulfates (0.08 mM $(NH_4)_2SO_4$, & 0.05 mM $CaSO_4$). pH also affects the corrosion of uranium in water. It controls the type of oxide that would be formed above the metal surface. As in the atmospheric environments, increasing temperature leads to increasing in corrosion rate. The effects of changes in temperature on corrosion is not of concern in this case, because the temperature was controlled in the laboratory at (21 ± 1)°C. There is no information about the water velocity in the original column experiment, but it is unlikely to have a major effect on the corrosion in this case.

1.7.1.3 Soil environment

The factors controlling corrosivity in soils are water, degree of aeration, pH, temperature, salt content and biological activity. Small soil particle sizes would hold water, and have less oxygen, while large particle sizes and loose soil will also have greater oxygen content (Craig et al., 2006). The pH values for the soils used in the column experiment were 5.6 and 5.8 for cambisol and luvisol soils respectively. In general, the acidic soils can increase the corrosion rates of metals.

1.7.2 Potential corrosion types for uranium

The uranium is susceptible to galvanic corrosion, pitting corrosion, and stress-corrosion cracking (SCC). The corrosion that the DU ammunition experienced could be a mixture of these types.

1.7.2.1 Galvanic corrosion

Galvanic corrosion occurs when two dissimilar metals are in physical (and electrical) contact in an aqueous electrolyte (Mccafferty, 2010). This system forms an electrochemical cell that will conduct electricity. The induced electrical current can attract electrons away from one of the metals, which thus acts as the anode in the electrochemical cell. This would accelerate the corrosion rate of the anode. Galvanic corrosion can happen within the same metal, the metal has both an active and passive state. For example, one part is covered with an oxide film (passive), while another part is exposed (active). This condition would create a potential difference causing the unpassivated area of the metal to galvanically corrode (Craig et al., 2006).

1.7.2.2 Pitting corrosion

Pitting corrosion is a localized form of corrosion that occur when a corrosive medium attacks a metal at specific points causing small holes or pits to form. This usually happens when a protective coating or oxide film is perforated, due to mechanical damage or chemical degradation. Pitting begins at a specific area of a passivated metal where there is a break in the passivation layer, which acts as the anodic area, while the rest of the metal acts as the cathodic area. With a potential difference between the anode and the cathode, extremely localized corrosion initiates. Due to the small area of the anode, the corrosion continues at a rapid speed (Craig et al., 2006).
The DU ammunition shows a clear pitting corrosion after 3 years of performing the column experiment (Fig. 1-5). It is also shows how the pits were developed and in some cases reached other pits.

1.7.2.3 Stress-Corrosion Cracking (SCC)

SCC is an environmentally assisted corrosion that can occur when a metal is under the rule of a tensile stress and a corrosive environment at the same time. In this type, the metal undergoes an internal propagation of cracking without being detected on the surface. Pitting corrosion can be one of the causes to initiate SCC. The U-0.75 Ti alloy (the alloy used in the DU ammunition) has the highest susceptibility to SCC (Craig et al., 2006).

1.8 Goals of Study

The firing mechanism and intensity of DU ammunition used in relatively recent conflicts (officially since 1991 in Iraq war – until 2003 in Iraq as well) had left sometimes thousands of tons of the ammunition in the battle fields as well as in the testing sites used for training proposes. DU rounds have been analyzed by performing various studies that dealt with the potential chemical weathering that metallic DU would suffer with time, oxidation and corrosion of the metal, leaching of DU rounds in soil, speciation and solubility of the formed secondary uranium minerals, behavior of DU in the human body, in animals and in plants. The motivation for such studies always concerns the potential paths or mobility and solubility of DU in the environment and whether it's possible to enter the food chain through plants and animals. Another main concern is how it reacts with the different organs in the human body which, because of the material's radioactivity and toxicity, affects the human health. For these reasons it was important to carry out a research to analyze and investigate the corrosion products of DU ammunition acquired from the 1999 Kosovo war, the goals of the study are:

1- To identify the different secondary uranium minerals formed due the corrosion of real depleted uranium rounds.
2- To validate of several spectroscopic techniques in analyzing corroded DU fragments.
3- To perform a dissolution experiment for the material under different solution pH values in order to study the solubility and dissolution behavior of the DU corrosion products. And modeling the dissolution behavior for the same material and under same conditions to compare with the measured behavior, and also to have an idea about the potential dominant uranium aqueous species.
4- To identify the secondary uranium minerals by dissolving them.

2 Materials and Methods

2.1 Materials

The samples in this study represent some of the corrosion products of the DU ammunition. This ammunition was originally found in 2001 in Kosovo and underwent 1 or 2 years of corrosion since the 1999 Kosovo war (Schimmack et al., 2005). The corrosion products were gleaned after performing leaching experiments in the soil columns for about 3 years. They have been provided by the GSF- National Research Center for Environment and Health, Institute of Radiation and Protection. The previous work is described in 1.5 (more about these experiments in Schimmack et al., 2005 ; 2007). The total amount of the samples was 5.27 g: 1.9 g for sample 4, 1.7 g for sample 7, and 1.68 g for sample 8. They represent debris from the DU penetrators attached by a small amount of soil and very small amount of vegetation residue.

2.2 Methods

Several different techniques have been used in this study; these techniques can be categorized into two groups:
The first group is the one that dealt with the samples as solid material in order to identify the solid phases or minerals qualitatively and quantitatively, these are:

1- Raman Spectroscopy.
2- SEM (Scanning Electron Microscope).
3- XPS (X-ray photoelectron Spectroscopy).
4- Powder X-ray Diffraction.
5- EPMA (Electron Probe Micro-Analysis).

The second group is the one that dealt with the samples as solutions in order to measure the dissolved uranium and calcium concentrations after performing a dissolution experiment of the solid material; this was done by ICP-OES (Inductively Coupled Plasma Optical Emission Spectroscopy).

2.2.1 Raman Spectroscopy

This is a spectroscopic technique named after C.V. Raman (Indian physicist), it studies vibrational, rotational, and other low-frequency modes in a system (Gardiner and Bowley, 1989; McCreery, 2000). Since vibrational information is specific for the chemical bonds in molecules, it provides a fingerprint by which the molecule can be identified. When monochromatic radiation is incident upon a sample then this light will interact with the sample in some fashion. It may be reflected, absorbed or scattered in some manner. It is the scattering of the radiation that occurs which can tell the Raman spectroscopist something about the samples molecular structure (Fig. 2-1). If the frequency (wavelength) of the scattered radiation is analyzed, not only is the incident radiation wavelength seen (Rayleigh scattering) but also, a small amount of radiation that is scattered at some different wavelength (Stokes and Anti-Stokes Raman scattering). Approximately only 1 x 10^{-7} of the scattered light is Raman (Pelletier, 1999). It is the change in wavelength of the scattered photon that provides the chemical and structural information. If a molecule interacts with an electromagnetic field, a transfer of energy from the field to the molecule can occur only when Bohr's frequency condition is satisfied according to Equation 2-1:

$$\Delta E = h\nu = h\frac{c}{\lambda} = hc\bar{\nu} \qquad \text{Equation 2-1}$$

Where ΔE: $(E_2\text{-}E_1)$: Represent the energies of the excited and ground states of a molecule, respectively.

h: Planck's constant (6.62 10^{-27} erg. s)

v: wave frequency, the number of waves in the distance light travels in one second.

c: speed of light (3 x 10^{10} cm/s)

λ: wavelength Hz

$\bar{\nu}$: wavenumber cm^{-1}

Light scattered from a molecule has several components - the Rayleigh scatter and the Stokes and Anti-Stokes Raman scatter (Fig.2-2). The scattering process without a change of frequency is called Rayleigh scattering. It is the same process described by Lord Rayleigh and which accounts for the blue color of the sky. A change in the frequency (wavelength) of the light is called Raman scattering. Raman shifted photons of light can be either of higher or lower energy, depending upon the vibrational state of the molecule. The molecule absorbs Δ*E* when it is excited from $E_1$to E_2, and emits Δ*E* when it reverts from E_2 to E_1 (Ferraro et al., 2003).

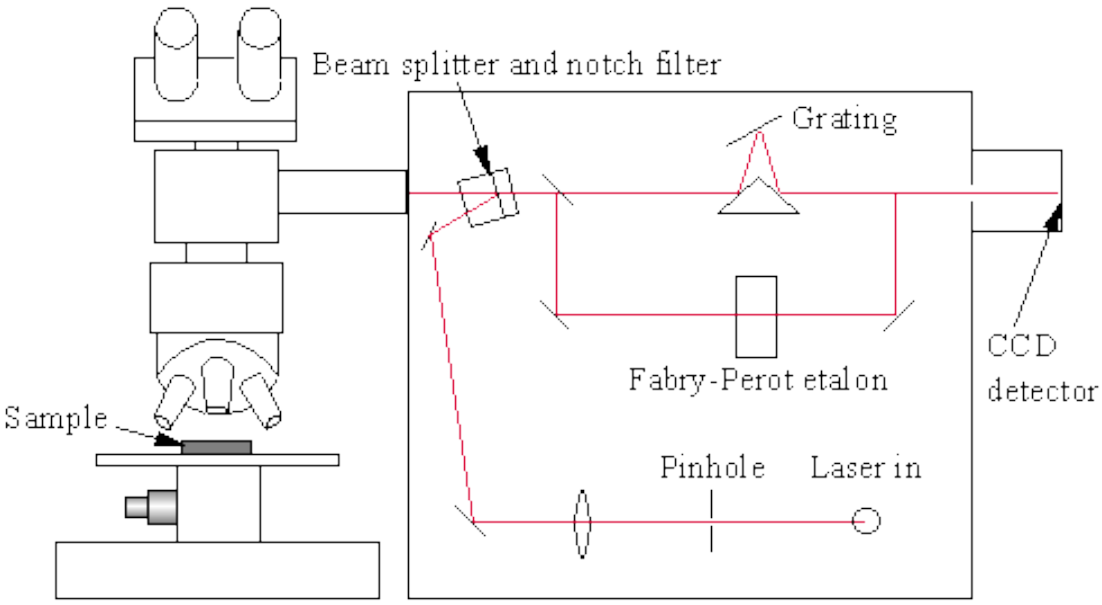

Figure 2-1: Design of a Raman spectrometer.

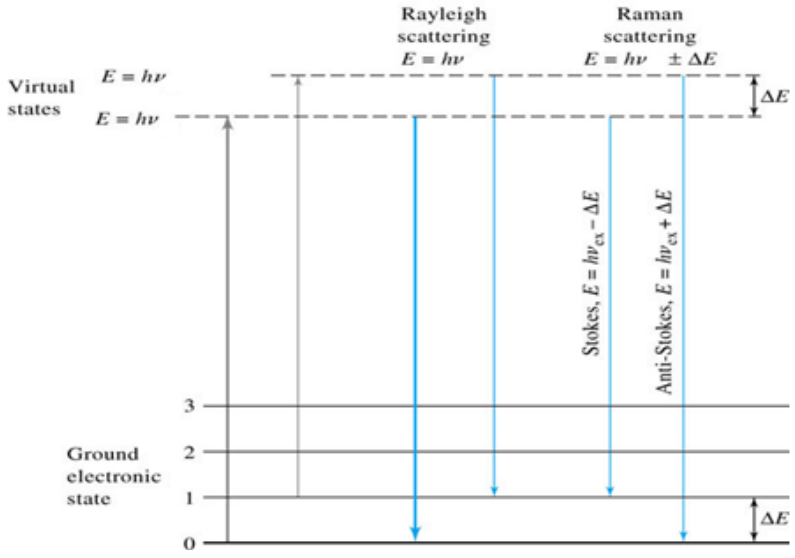

Figure 2-2: The different types of light scattering.

2.2.1.1Settings and parameters

The used Raman spectroscopy model is Jobin Yvon Horiba HR800, located at the Institute for Geosciences, Mainz University. The biggest four grains were taken from each tube (the samples come in 3 tubes labeled 4, 7, and 8). Then the selected grains were kept in a cuvette due to their radioactivity, and sealed with a teflon cap (the cuvettes are originally designed for UV photometry) (Figs. 2-3, 2-4, & 2-5). In addition a becquerelite sample provided by the Harvard mineralogical museum (#10902) was analyzed as well. This specimen represents a natural sample of becquerelite from the Shinkolobwe mine, Zaire.

The Raman spectra were excited by a spectra-physics model 127 He-Ne laser (632.816 nm) using other energies or wavelengths would yield luminescence. The calibration was done using a 520.5 cm^{-1} line of silicon. The samples were scanned at a nominal resolution of 2 cm^{-1} in the range between 250 and 1500 cm^{-1}. The working magnification is 50 times, and the imaging magnification is 10 times. The acquisition time for some scans as well as the number of accumulations varied in order to provide a better signal-to-noise ratio. The spectral database and the software used (CrystalSleuth) for processing and matching the Raman spectra for the samples was provided by the

RRUFF project for integrating database of Raman spectra and X-ray diffraction done by Arizona University.

Figure 2-3: The prepared grains for Raman analysis from sample 4, Raman spectra have been measured for each of the grains A, B, C, and D as shown in Appendix A.

Figure 2-4: The prepared grains for Raman analysis from sample 7, Raman spectra have been measured for each of the grains A, B, C, and D as shown in Appendix A.

Figure 2-5: The prepared grains for Raman analysis from sample 8, Raman spectra have been measured for each of the grains A, B, C, and D as shown in Appendix A.

2.2.2 Scanning Electron Microscope (SEM)

The SEM permits the observation and characterization of heterogeneous organic and inorganic materials on a nanometer (nm) to micrometer (µm) scale (Goldstein et al., 2003). It is a type of microscope (Fig. 2-6) that images the sample surface by scanning it with a high-energy beam of electrons in a raster scan pattern. The electrons interact with the atoms that make up the sample producing signals that contain information about the sample's surface topography, composition, and electrical conductivity (Flewitt and Wild, 1994; Reimer, 1998). Depending on the integrated detectors in the instrument, different types of signals could be detected by the SEM, for example: secondary electrons, Back-scattered electrons BSE, characteristic X-rays, light (cathodoluminescence), specimen current and transmitted electrons. A characteristic X-ray detector was used in this research. This type of signal is emitted as a result of electrons bombardment. The analysis of such signals can yield both qualitative identification and quantitative elemental information.

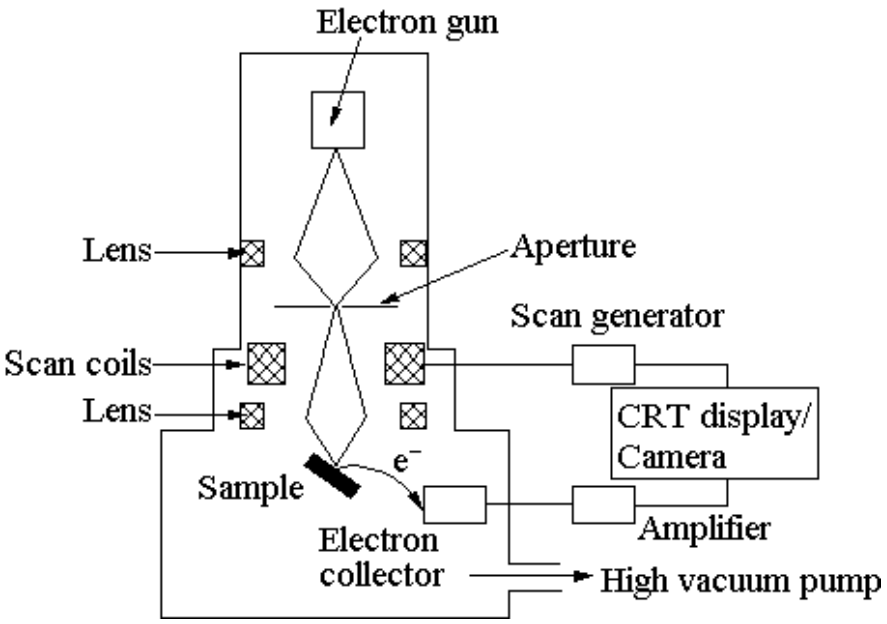

Figure 2-6: Design of a scanning electron microscope.

2.2.2.1 Settings and parameters

The analysis was performed on a Zeiss DSM 962 Scanning Electron Microscope located at the Institute for Geosciences, Mainz University. The microscope is equipped with an Oxford energy dispersive electron detector (accelerating voltage 15 KeV). One grain has been taken from each of the 3 tubes (4, 7, & 8), the grains have been attached to the carbon disc and coated with liquid silver, exactly between the grain and the carbon disc. The top of the samples were coated with gold. The coatings are necessary to increase the conductivity of the samples (Echlin, 2009).

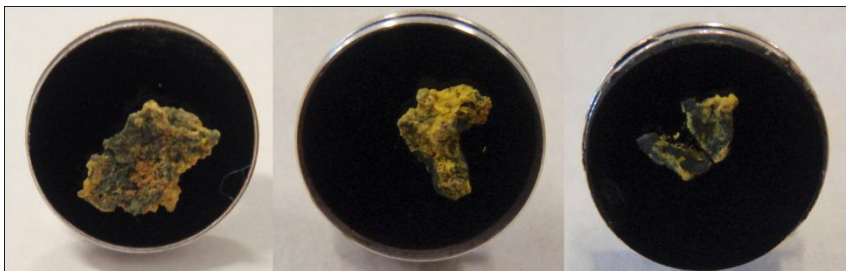

Figure 2-7. The prepared grains for SEM measurements, from left to right: sample 4, 7, and 8.

2.2.3 X-ray Photoelectron Spectroscopy (XPS)

Also known as ESCA (Electron Spectroscopy for Chemical Analysis), this is a quantitative technique that measures the elemental composition at the surface of material (usually top 1-10 nm), as well as: the empirical formula, chemical state, and electronic state of the elements that exist within a material. The basic experiment involves the bombardment of a material in vacuo with (usually) soft X-rays, capable of penetrating many micrometers into the bulk. The X-ray adsorption by an atom in the solid leads to the ejection of an electron (photoionisation) either from the tightly-bound core level or from the weakly-bound valence levels (Fig. 2-8). A fraction of these electrons, generated close to the surface, escape into the vacuum system (photoemission). The overall process is known as the photoelectric effect. The photoelectron emission is analyzed to produce a spectrum of electron intensity as a function of energy (Briggs, 2003).

The concept of the technique is based on the Equation 2-2:

$$E_{\text{binding}} = E_{\text{photon}} - (E_{\text{kinetic}} + \Phi) \qquad \text{Equation 2-2}$$

E_{binding}: The binding energy (BE) of the electron
E_{photon}: The energy of the X-ray photons being used
E_{kinetic}: The kinetic energy of the electron as measured by the instrument
Φ : The work function of the spectrometer

XPS spectra are obtained by irradiating a material with a monoenergetic X-ray beam (Al Ka 1486.6 eV or Mg Ka 1253.6 eV) which represent the E_{photon} in (Eq. 2-2). After measuring the kinetic energy of the electrons that have escaped from the material, the binding energy of these electrons can be calculated. This is a sensitive characteristic of the chemical bonds in a compound and it is related to the energy of ionization (Nefedov, 1988; Verma, 2007).

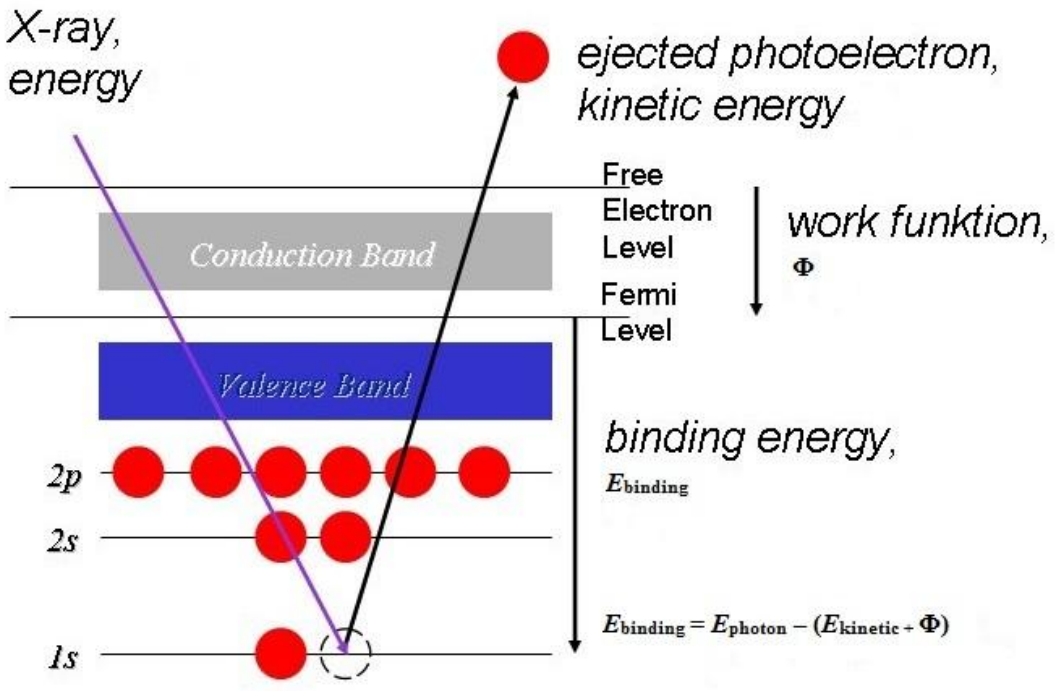

Figure 2-8: An electron is ejected due to the application of the X-ray.

2.2.3.1 Settings and parameters

The samples were prepared for measurement by grinding small portions with an agate mortar from each of the 3 tubes (4, 7, & 8). The resulting powder was pressed into an indium foil and transferred into the spectrometer. Sample 8 was measured as a 4x4 mm piece as well (not powder). The photoelectron spectra were measured at room temperature under a vacuum of 7 x 10^{-9} mbar using a custom-built XPS system (SPECS) located at the institute of nuclear chemistry, Mainz University. The spectrometer has an ion source (IQE 11/35 LP) to remove the surface contamination by bombardment with Ar^+ ions. The photoelectron spectra were excited using the non-monochromatic k_α radiation from a high-intensity anode (Mg) X-ray source XR-50. The photoelectron spectra were recorded with Mgk_α (1253.6 eV) radiation. The photoelectrons were recorded with constant analyzer pass energy of 13 eV using the hemispherical energy analyzer PHOIBOS 100. The spectral evaluation was done by CasaXPS program.

2.2.4 Powder X-ray Diffraction (XRD)

This analytical technique is primarily used for phase identification of a crystalline material and can provide information on unit cell dimensions. When applying an X-ray source to the investigated crystalline material, a constructive interference will happen or when the bragg's law is satisfied (Eq. 2-3) as shown in Figure 2-9. A beam will be diffracted generating characteristic XRD spectra, which give information about the structure of the investigated materials (Warren, 1990; Suryanarayana and Norton, 1998; Cullity & Stock, 2001).

Bragg's Law: $n\lambda = 2d\sin\theta$ Equation 2-3

Where n: An integer determined by the order given
- λ: Wave length of the X-rays
- d: Spacing between the planes in the atomic lattice
- θ: Angle between the incident ray and the scattering planes

In a powder diffraction it is important to have a sample with a smooth plane surface, in order to have a random distribution of all possible h, k, l planes (indices cutting the axes a,b, & c forming the unit cell), so that the crystallites having reflecting planes parallel to the specimen surface will contribute to the reflected intensities.

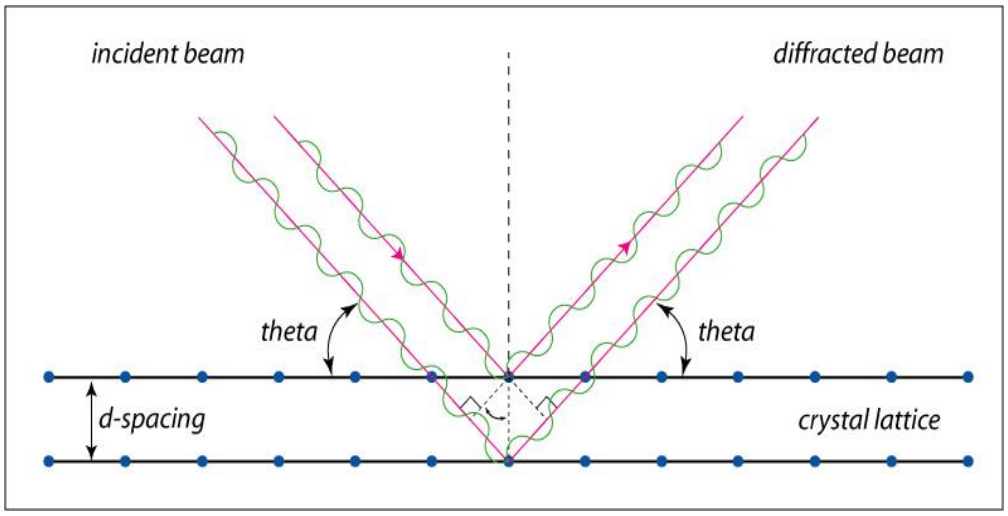

Figure 2-9: The constructive interference that leads to X-ray diffraction.

2.2.4.1 Settings and parameters

The rest of the samples were ground by a mortar to be prepared for the XRD measurement. The powder was pressed into 1 mm deep steel and brass holders for samples 4 & 7, and another holder size (0.5 mm depth) was chosen for sample 8 due to the small amount of the material available. X-ray diffraction patterns were collected using a Seifert XRD 3000 TT diffractometer located at the Institute for Geosciences, Mainz University, operating at 40 kV and 30 mA in step scan mode, with CuK_α radiation (1.540598 Å). Patterns were collected in the range 1 to 90° 2θ with a step size of 0.03° and a rate of 2 seconds per step. Finally the acquired XRD patterns were processed and matched using RAYFLEX v. 2.370 program.

2.2.5 Electron Microprobe Analysis (EMA)

This is a microbeam instrument used primarily for the non-destructive chemical analysis of minute solid samples. An electron microprobe (Fig. 2-10) operates under the principle that if a solid material is bombarded by an accelerated and focused electron beam, the incident electron beam has sufficient energy to liberate both matter and energy from the sample. These electron-sample interactions yield characteristic X-rays, secondary and backscattered electrons, which can be used for imaging a surface or obtaining an average composition of the material (Reed, 1997; 2005). The polished surfaces of samples are excited with an electron beam, accelerated to a voltage between 15 and 30 kV and focusable to a diameter of less than 1 µm. The electron probe is arranged to strike the sample at right angles to its surface, therefore, the specimen must be prepared as flat polished (to avoid topographic effects) geological thin section mounted on a glass slide backing, or as samples polished in a resin block (Potts, 1987). The characteristic X-rays generated within the sample are detected using wavelength dispersive or energy dispersive spectrometers for quantitative analysis of volumes a few microns across.

Figure 2-10: The Jeol JXA 8900RL electron microprobe analyzer.

2.2.5.1 Settings and parameters

The same grain sample (4) that has been used for the SEM analysis was broken into smaller pieces, and then polished in a resin block to be prepared for the microprobe analysis (Fig. 2-11). A Jeol JXA 8900RL electron probe microanalyzer was used. It is located at the Institute for Geosciences, Mainz University. The qualitative and quantitative analyses were performed with 15 kV accelerating voltage, 12 nA beam current, and 1 µm beam diameter. Backscattered electron images (BSE) have been acquired as well as three elemental maps. The accelerating voltage was 20 kV, the beam current 30 nA, and the beam diameter 1 µm. The maps were produced with a dwell time 180-250 ms per pixel and have the dimensions 200 x 200, 300 x 300, and 300 x 160 pixels respectively. The calibration standards used for the selected elements are listed in (Table 2-1).

Table 2-1: The microprobe calibration standards used for the selected elements.

Element	Calibration Standard
Mg	MgO
Al	Al_2O_3
Ca & Si	Wollastonite $CaSiO_3$
U	UO_2
P	Apatite $Ca_5(PO_4)_3(OH,F,Cl)$
K	Orthoclase $KAlSi_3O_8$
Ti	$MnTiO_3$

Figure 2-11: The prepared resin block for the EMA analysis, each number represents a different particle (as presented in Appendix C).

2.2.6 Inductively Coupled Plasma-Optical Emission Spectrometry (ICP-OES)

Also referred to as ICP-AES (Inductively Coupled Plasma-Atomic Emission Spectroscopy) (Fig. 2-12), this is an analytical spectroscopic technique that consists of two facilities (the inductively coupled plasma, and the optical emission spectrometer). It is used to determine the concentrations of elements in a sample, through atomizing and exciting the elements under investigation. The atoms as a result will emit an electromagnetic radiation at specific wavelengths. These wavelengths are then measured to give an indication of the concentration of the elements (Potts, 1987; Winge et al., 1989; Neikov et al., 2009).

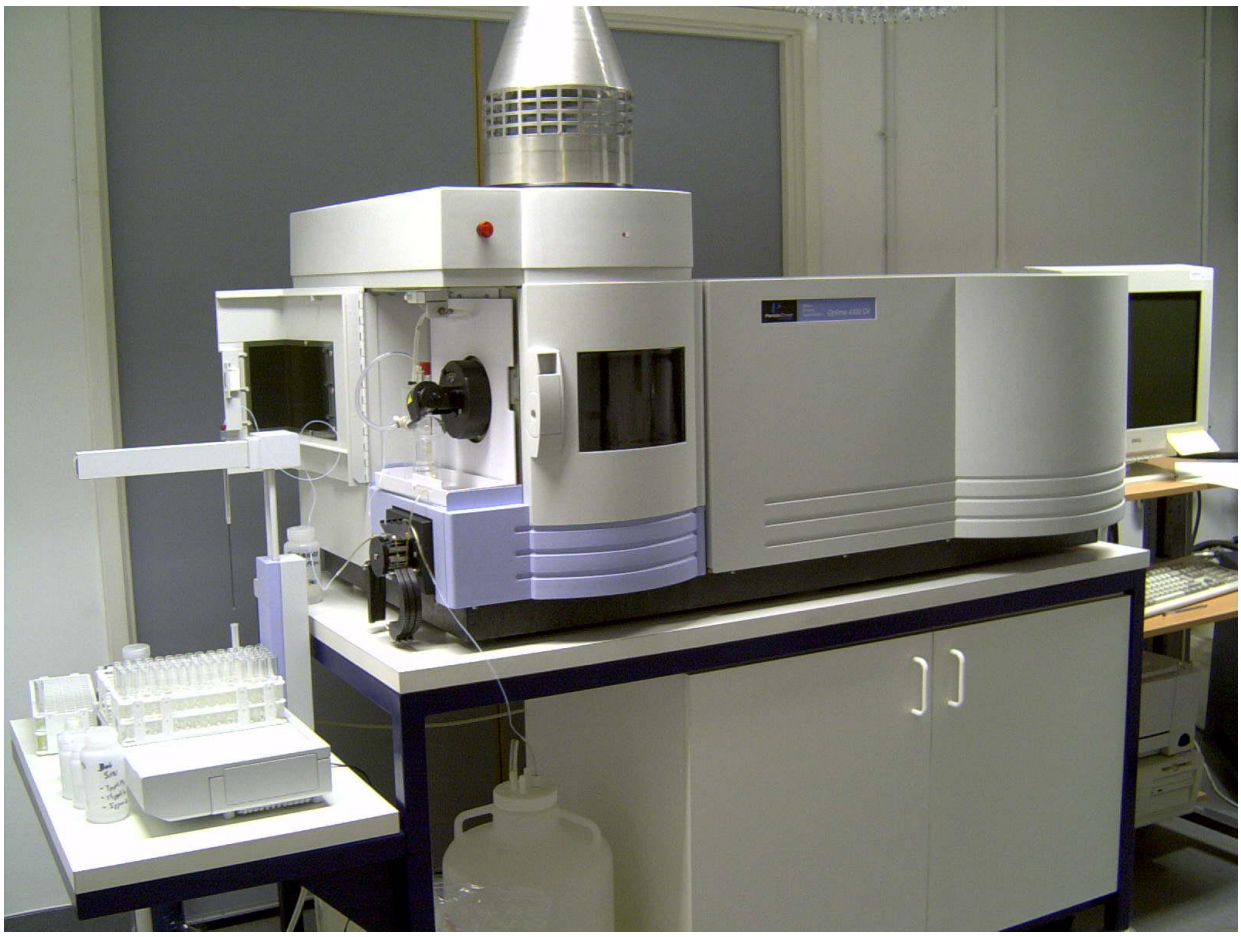

Figure 2-12: A Perkin Elmer Optima 5300 DV Inductively Coupled Plasma – Optical Emission Spectrometry instrument.

The first part of the instrument is the ICP, which is a high temperature source used primarily for generating atomic vapor from an aqueous sample. It consists of 3 concentric quartz glass tubes. The quartz torch is partly surrounded by the output coil of a Radio Frequency (RF) generator. Argon gas used to create the plasma, which is an electrically neutral, highly ionized gas that consists of ions, electrons, and atoms. In the ICP torch (Figure 2-13) an induction coil is used to produce a high magnetic field inside the quartz tube. Argon is flowing inside this quartz tube. To start plasma, a Tesla discharge (a source of electrons) provides "seed" electrons to the argon stream. The electrons are accelerated by the magnetic field, which is oscillating at a high frequency (*i.e.*, 27 MHz). Upon colliding with argon atoms the electrons produce argon ions and more electrons. The ionization and collision processes continue to produce more ions and electrons in a cascade manner. After the initial Tesla discharge which created the seed electrons, the plasma is self-propagating; *i.e.*, no more external source of electrons is required. The argon plasma adsorbs high amounts of energy from the oscillating field, causing the plasma to have a temperature ranging between 5725 and 9725 °C (Manning and Grow, 1997; Winge et al., 1989).

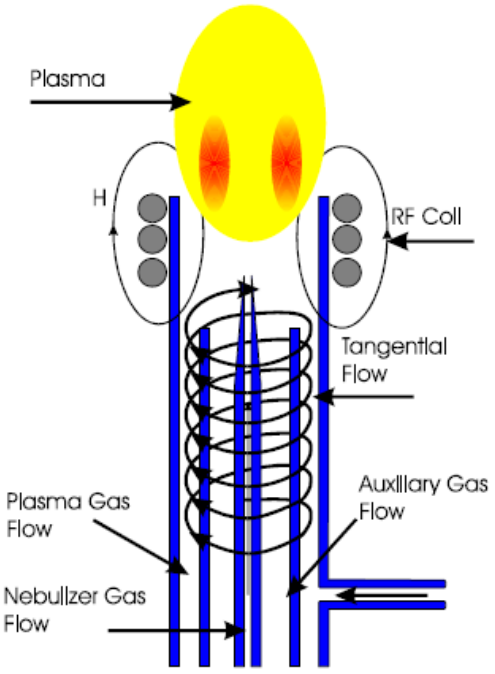

Figure 2-13: Scheme of an ICP torch (after Manning and Grow 1997).

A peristaltic pump delivers an aqueous sample into a nebulizer where it is changed into mist or fine aerosols and introduced directly inside the plasma flame. The sample immediately collides with the electrons and charged ions in the plasma and breaks down into charged ions. The various molecules break up into their respective atoms which then lose electrons and recombine repeatedly in the plasma, giving off radiation at the characteristic wavelengths of the elements involved. A Minuteman scanning monochromator (in early models) with a focal length of one meter is used to separate the emission lines from the ICP source. It is placed along the optical viewing region of the ICP (Fig. 2-14). The emission radiation enters the monochromator or polychromator and is separated by a diffraction grating. The separated radiation is then reflected into a photomultiplier detector. In these detectors, the separated wavelengths or colors fall upon an array of semiconductor photo-detectors like Charge Coupled Devices (CCDs). The intensities of all wavelengths can be measured simultaneously. In other words, the analysis can be performed for more than one element at the same time. The intensity of each line is then compared to previously measured intensities of known concentrations of the elements, and their concentrations are then computed by interpolation along the calibration lines (Manning and Grow, 1997; Skoog et al., 1998).

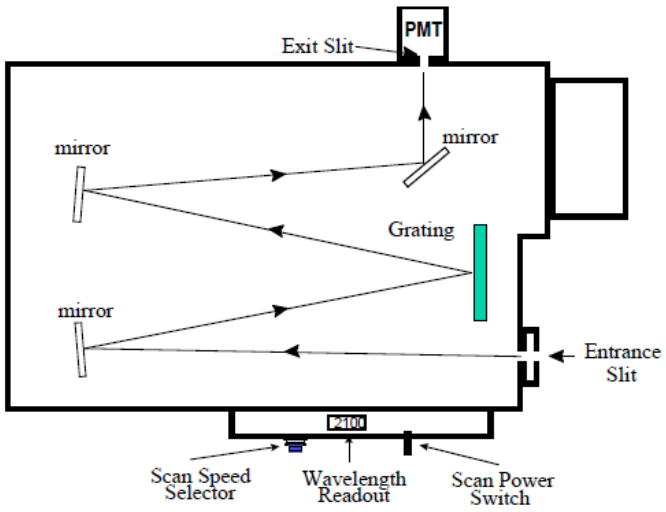

Figure 2-14: Minuteman scanning monochromator (after Skoog et al. 1998).

2.2.6 Settings and parameters

A Perkin Elmer Optima 5300 DV model equipped with a Perkin Elmer AS 90 Auto sampler located at the Central Laboratory of Hessen Water, Darmstadt was used to determine the dissolved uranium and calcium concentrations after performing a dissolution experiment of the DU powder. Different standard solutions were used for calibration and controlling purposes for Ca and U as shown in (Table 2-2). The filtered solutions were diluted 5- folds with H_2O.

Table 2-2: Standard solutions for Ca and U used in the ICP-OES measurement.

Element		Ca	U
Calibration Standard	Company	Merck	Perkin Elmer Life and Analytical Sciences
	Name	Certipur Calcium Standard solution	Multi-Element Standard 3
	Number	1.19778.0500	Catt#N9300233
	Concentration	1000 mg/l	10 mg/l
Controlling Standard	Company	Bernd Kraft	Merck
	Name	Calcium ICP Standard	Certipur Uranium ICP Standard
	Number	03832.0000	1.70360.0100
	Concentration	1000 mg/l	10 mg/l

The operating conditions of the measurement are shown in (Table 2-3). The wavelengths for Ca are 315.887, 317.933, & 396.847 nm, and for U are 367.007, 385.958, & 409.014 nm. The limit of quantification (sensitivity) of the instrument is 0.5 mg/l and the error for Ca & U is 3%.

Table 2-3: Operating conditions of ICP-OES.

Element	All
Plasma flow (L/min)	15
Auxiliar flow (L/min)	0.4
Nebulizer flow (L/min)	0.7
Power (watts)	1450
Plasma view	Axial
Axial Position (mm)	15.0
Sample flow rate (mL/min)	1.3
Number of replicates	3

All the solutions were measured in ICP-OES calibration curves (Figures 2-15 & 2-16) prepared in the range of 0 to 10 mg/l and wavelengths of 317 & 385 nm for Ca and U respectively (Appendix D-1 & D-2). The correlation coefficients for four-point linear calibration curves were 1 for Ca and 0.99 for U.

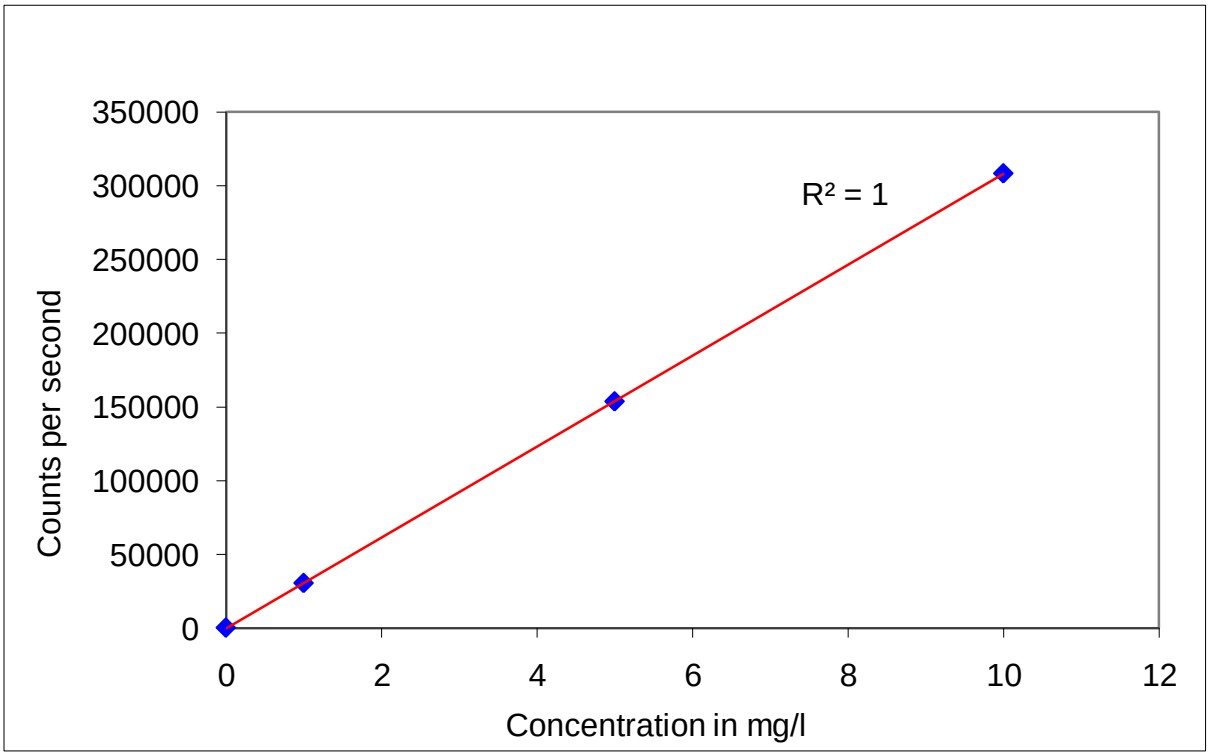

Figure 2-15: Calibration curve for Ca by ICP-OES.

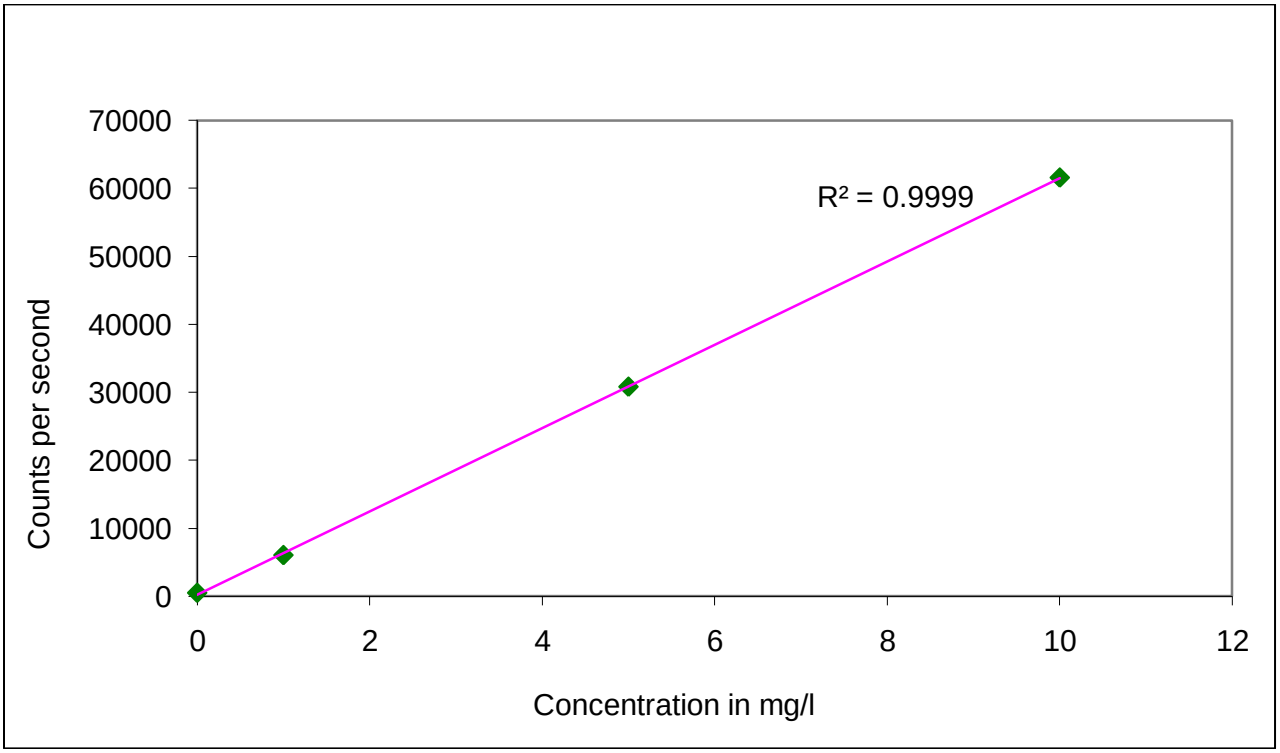

Figure 2-16: Calibration curve for U by ICP-OES.

2.2.6.2 Preparations for the dissolution experiment

In order to fix the ionic strength at 0.01, a 0.01M $NaClO_4$ solution was prepared for use as an ionic adjuster. 1.4046 g of sodium perchlorate monohydrate (zur Analyse, Merck 1.06564.0100) with a molar weight of 140.46 g/mol was dissolved in 1 liter of deionized water with 0.005 µsiemens/cm conductivity in a 1 L glass flask. Five 45 ml polypropylene vessels were prepared for each of the three samples (4, 7, & 8). The samples were grinded by mortar. An amount of 50 mg of the powdered material was added to each of the 15 vessels plus 35ml of 0.01M $NaClO_4$. The solutions in the vessels of each sample had pH values ranging from 6 to 10, which were obtained by adding either HNO_3 or KOH to the solution. While adjusting the pH, each vessel was purged by nitrogen gas to remove the CO_2 from the solution. After purging, the vessels were sealed by cap and parafilm, and finally put inside two plastic bags (for safety reasons to minimize the risk of potential leakage). Then the vessels were placed on a shaker to obtain equilibrium. The sampling at the end of experiment involved: measuring the final pH, leaving the vessels in a stand position for about 2-3 hours in order for the solid material to settle down, followed by centrifuging the vessels for 20 minutes at 3500 rpm, then using a syringe connected to a disposable 0.2 µ filter paper to separate the sampled solution from the solid residue. The sampled solutions were kept after that in acidified polyethylene bottles and were ready for the ICP-OES analysis. The experiment was performed under laboratory temperature (22.38 ± 0.45). The duration of the whole shaking process took about 6 months.

3 Results

3.1 Raman Spectroscopy Results

Using a microscopic, spatially resolving scanning application combined with software-based identification of numerous secondary phases that can be formed seems especially promising for investigating the complex, heterogeneous chemical system present in spent nuclear fuel corrosion processes (Amme et. al., 2002). The use of Raman spectroscopy to investigate the aqueous species and minerals of different materials has been approved widely by many works e.g. (Bukalov et al., 1970; Hoekstra and Siegel, 1973; Toth and Begun, 1980; Maya and Begun, 1981; Biwer et al., 1990; Morris et al., 1996; Tsushima et al., 1998; Quile`s and Burneau, 2000; Amme et al., 2002; Frost 2004; Frost et al., 2006; 2009).

More than one secondary uranium mineral is expected to be found in the corrosion products of DU ammunition, originally transformed from the uranium alloy penetrator. It is the Raman signal of the uranyl ion (UO_2^{2+}) known as the symmetric axial stretching vibration of the uranyl ion v1 that gives a general feature for most of the U(VI) minerals and/or aqueous species shifting the beam around 800 cm^{-1}. The first uranium mineral that has been found is schoepite $(UO_2)_8O_2(OH)_{12}(H_2O)_{12}$ which is a uranyl oxy-hydroxide. Matching the schoepite Raman spectrum in the spectral library with several spectra from different locations on the samples showed very good agreements (Fig. 3-1).

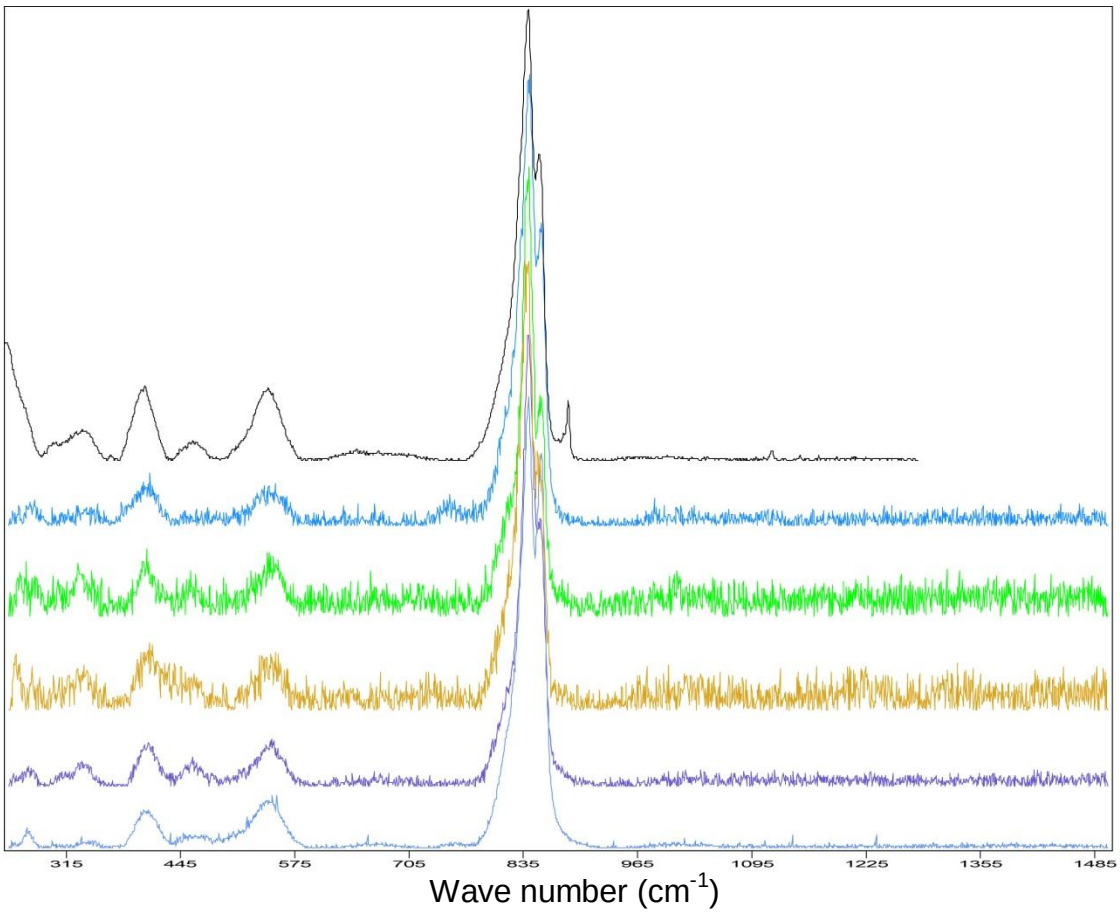

Figure 3-1: The comparison between reference schoepite Raman spectrum (on top) and some of the acquired spectra from the samples.

The characteristic double peak in schoepite makes it relatively easy to match with other spectra. The presence of the double peak may refer to the existence of the uranyl ion in two different environments within the crystal lattice (Maya and Begun, 1981; Biwer et al., 1990; Amme et al., 2002). The schoepite measured double peak was in the range of 840.3-842.5/853.6-855.8 cm^{-1} for the first and second peaks respectively. Which are in good agreements with previous works (Table 3-1).

Table 3-1: The Raman peaks for schoepite in the literature.

Measured wave numbers (cm^{-1})	References
838/855	Frost et al. 2006
843/855	Amme et al. 2002
840/860	Biwer et al. 1990
846/870	Hoekstra and Siegel 1973
844	Maya and Begun 1981
840/860	Sobry 1973

The different environments around the uranyl ion are caused by the differences in ligands closest to each site. These ligands could be O^{2-}, OH^- and H_2O. No clear distinction could be made in order to choose a given set of two ligands unless the effect of two different ligands on the v1 signal is the same (Maya and Begun, 1981). In all cases the first peak is stronger in intensity than the second peak, except for Hoekstra and Siegel 1973. They stated that the first peak at 846 cm^{-1} is the weak peak, and the second peak at 870 cm^{-1} is the strong peak. In addition to these strong signals, schoepite spectrum has also weak signals between 300 and 500 cm^{-1}, which can be attributed to the v (U-O) at the equator of the uranyl ion (UO_2^{2+}). These signals are not as well identifiable as the strong symmetric stretch of v1 of the uranyl ion.

As for the second uranium mineral that has been found in the corrosion products, at the beginning the spectra showed a good match with another uranyl oxy-hydroxide mineral named billietite $Ba(UO_2)_6O_4(OH)_6(H_2O)_8$ as shown in Fig. 3-2. However, this mineral is probably not present in the corrosion products because Ba is a trace element in the soil and therefore it's not probable to interact with the uranium alloy to form a Ba-uranyl mineral in this case.

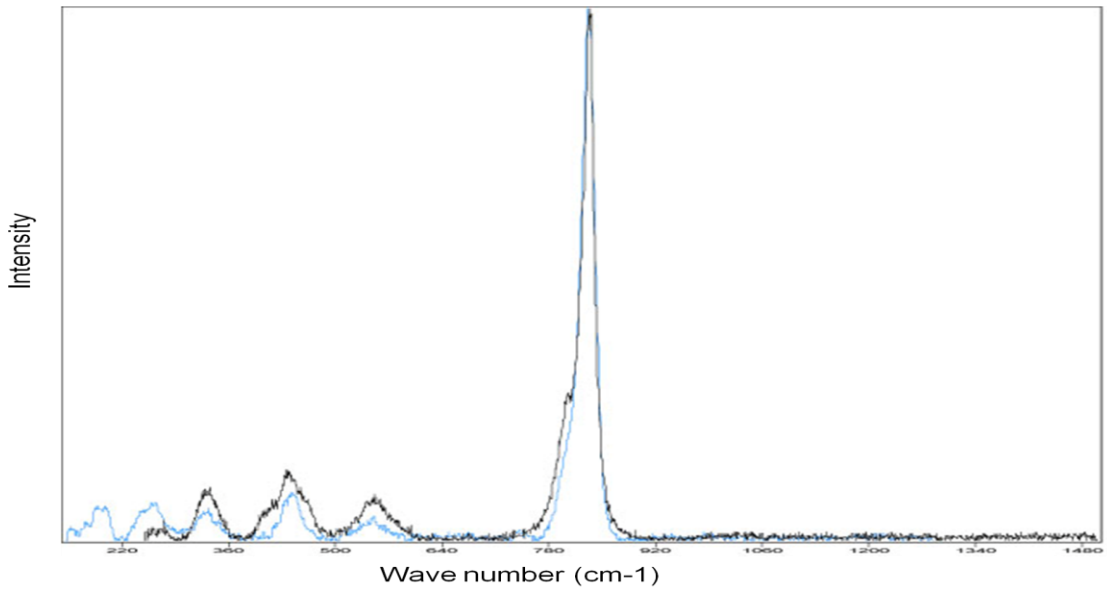

Figure 3-2: The comparison between reference billietite Raman spectrum (black) and a measured spectrum from the sample 8 (blue).

It was necessary to analyze a becquerelite sample due to the similarity in the chemical composition between billietite and becquerelite $Ca(UO_2)_6O_4(OH)_6(H_2O)_8$ (a more common uranyl oxy-hydroxide mineral), and the lack of a becquerelite Raman spectrum to match with the measured spectra of the samples. A natural becquerelite specimen has been provided by the mineralogical museum at Harvard University and measured. The resulted spectra showed a very good match between the billietite and becquerelite (Fig. 3-3). Both becquerelite and billietite belong to the same group in the structural hierarchy of uranyl minerals suggested by Burns et al. 1996 & 1997, and Burns 1999, which is the sheet anion topology with triangles and pentagons.

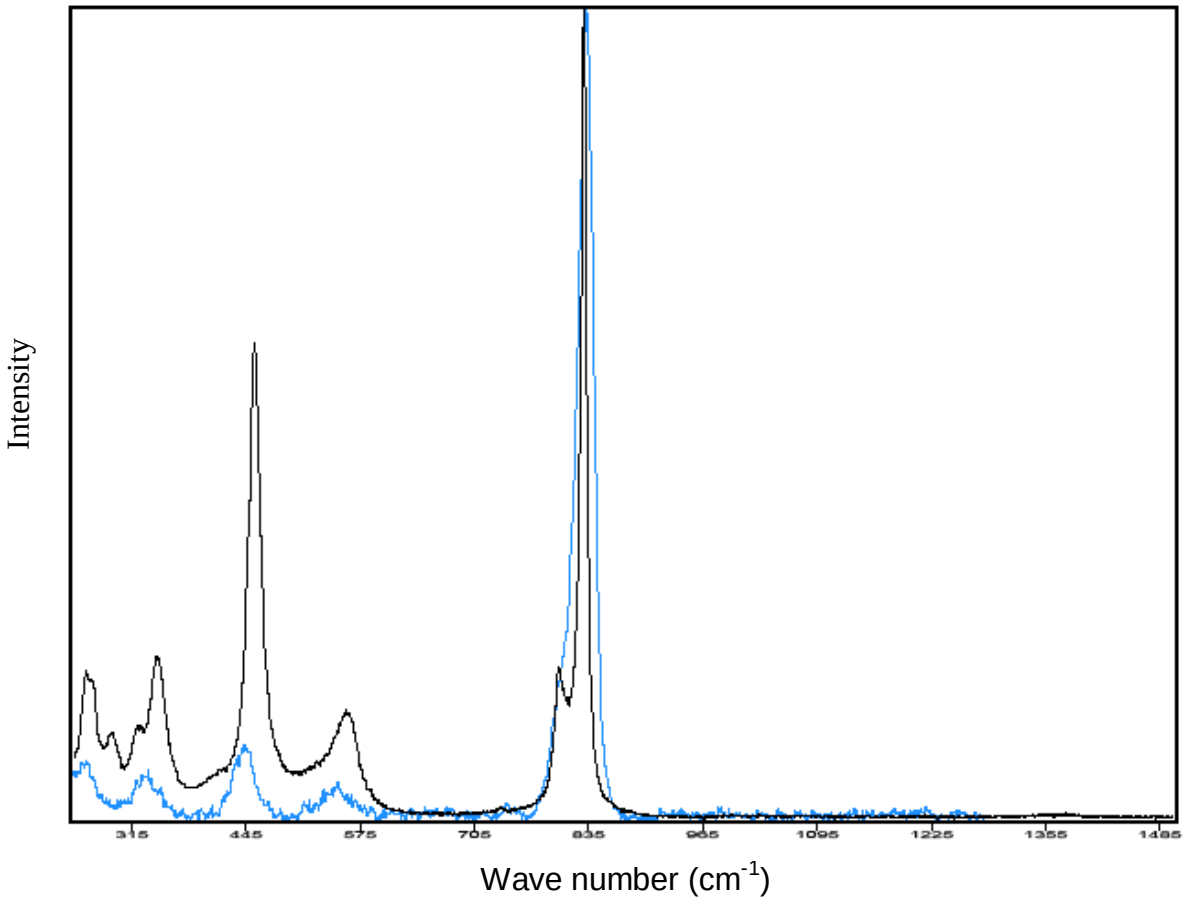

Figure 3-3: The comparison between the measured becquerelite Raman spectrum (black) and the reference spectrum of billietite (blue).

The measured spectra of different locations of the samples showed a very good match with the acquired becquerelite spectrum as shown in Fig. 3-4. The measured v1 (UO_2^{2+}) Raman shift was at 829 cm^{-1} for becquerelite in the natural specimen, and it was in the range of 829-836 cm^{-1} in the corrosion products of DU ammunition. Recorded becquerelite peak from other works is shown in Table 3-2.

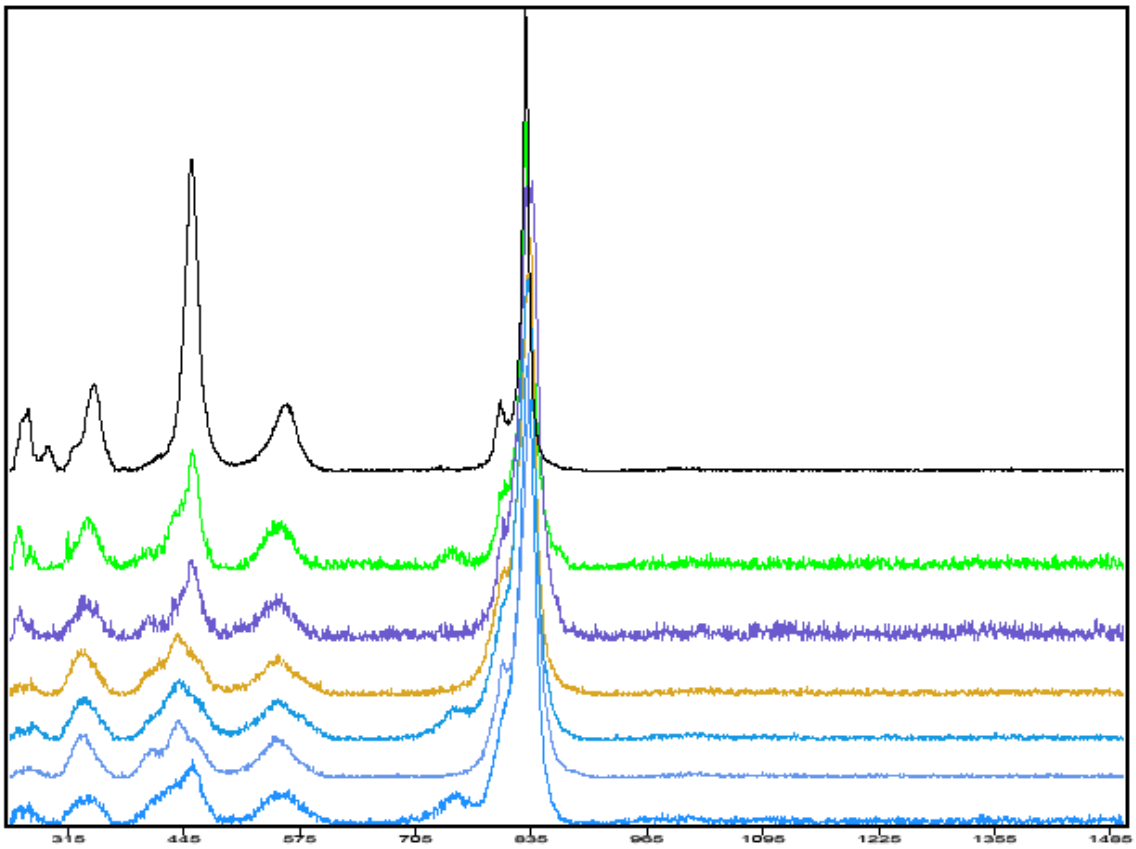

Figure 3-4: The comparison between reference becquerelite Raman spectrum (on top) and some of the acquired spectra from the samples.

Table 3-2: The Raman peaks for becquerelite in the literature.

Measured wave numbers (cm^{-1})	References
838	Frost et al. 2006
828	Amme et al. 2002
841	Sobry 1973

The previous works by Schimmack et al. 2007 suggested that these corrosion products represent phosphate uranyl minerals which are autunite $Ca[(UO_2)(PO_4)]_2(H_2O)_{10\text{-}12}$ and sabugalite $Al[(UO_2)_4(HPO_4)(PO_4)_3](H_2O)_{16}$. As for this work, there is no good match between the acquired spectra and the uranyl phosphate minerals (Fig. 3-5). It shows that both of the uranyl phosphate minerals have a v1 $(UO_2)^{2+}$ symmetrical stretching at about 810 cm^{-1}.

This difference in the symmetrical stretching (810 cm^{-1} for the uranyl phosphate minerals and 828-855 cm^{-1} from the acquired spectra) proves that the secondary uranium minerals presented in the corrosion products do not contain phosphate, and that they are chemically and structurally different from the uranyl phosphate minerals. The corrosion products can have more than one single mineral, and not all of them contain uranium as a main constituent. This is the reason some spectra are not easy to read. The acquired spectra can be found in Appendix A.

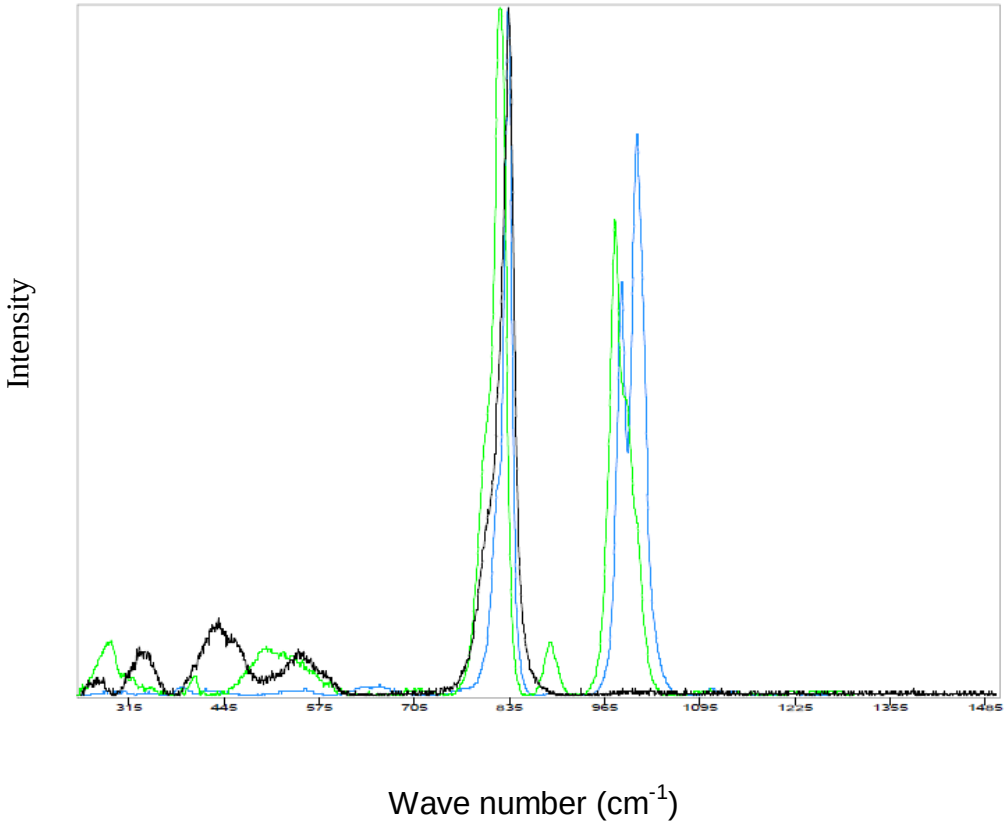

Figure 3-5: The comparison between a measured spectrum (black) of sample 4, and reference spectra of meta-autunite (blue) & sabugalite (green).

3.2 XRD Results

XRD is a common analytical technique that reveals information about the crystallographic structure and chemical composition. It is a simple, accurate, and relatively cheap tool to identify major and minor components (Dinnebier and Billinge, 2008). The three samples (4, 7, & 8) were grounded and the resulting powder was analyzed. Three XRD spectra were collected (Fig. 3-6). These spectra are very similar to each other, meaning that the material or mineral(s) in these samples are similar.

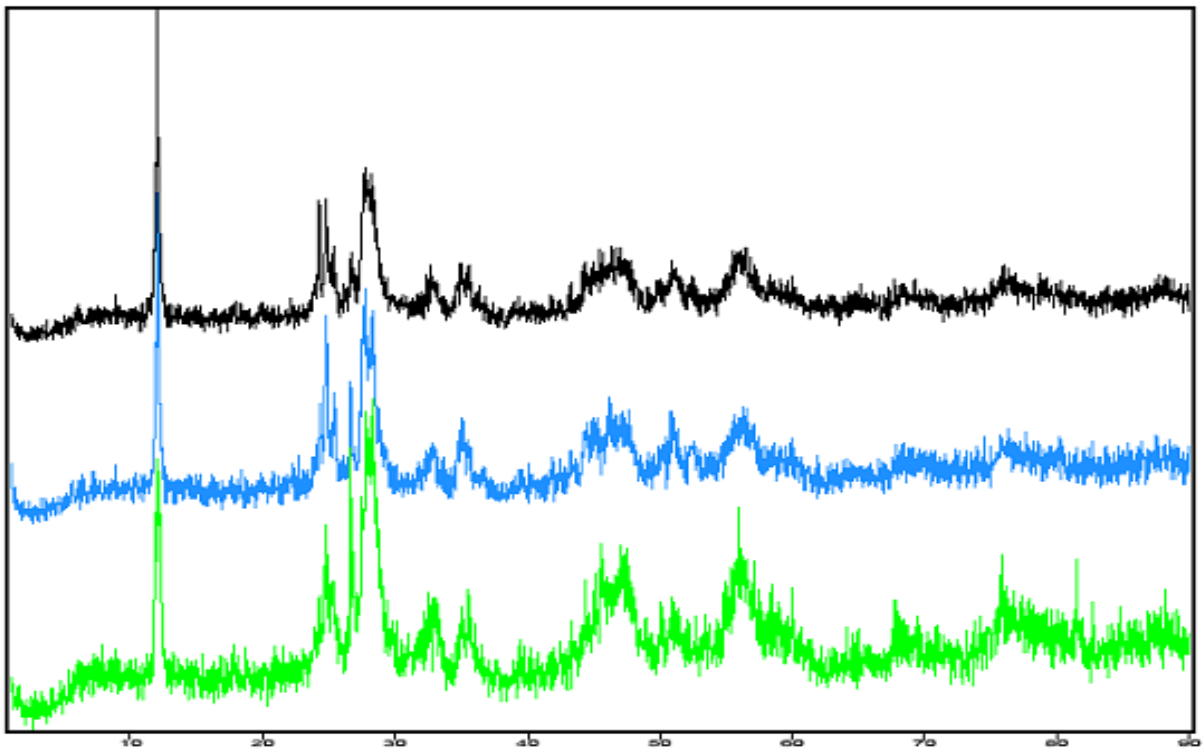

Figure 3-6: The three acquired X-ray diffraction spectra of samples 4 (black), 7 (blue), and 8 (green).

Matching the acquired spectra with the spectral database showed a very good match with two uranyl oxy-hydroxides (Figs. 3-7 & 3-8). The first one is schoepite and/or meta-schoepite$(UO_2)_8O_2(OH)_{12}(H_2O)_{10}$, which has 2 fewer water molecules in the interlayer. The crystal system of schoepite is orthorhombic, class (H-M) mm2 –pyramidal, space

group $P2_1ca$, cell parameters a=14.33 b=16.813 c=14.73 Å, ration= a:b:c= 0.8534:1:0.8773, Z=4. (Pagoaga et al., 1987).

The second uranyl oxy-hydroxide phase which showed a good agreement with the acquired spectra is becquerelite, The crystal system of becquerelite is orthorhombic, class (H-M) mm2 –pyramidal, space group Pna21, cell parameters a=13.8378 b=12.3781 c=14.9238 Å, ration= a:b:c= 1.118:1:1.206, Z=4 (Finch et al., 1996). The matching with the spectral library confirms the findings from the Raman spectra.

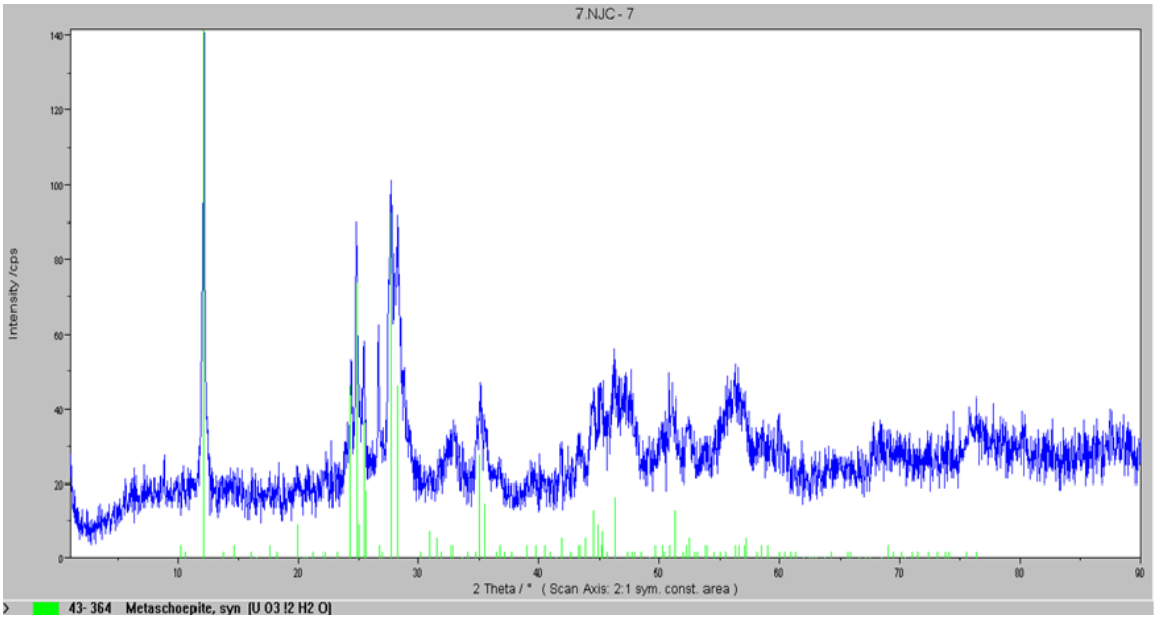

Figure 3-7: The acquired X-ray diffraction spectra of samples 7 (blue) and the reference meta-schoepite (green).

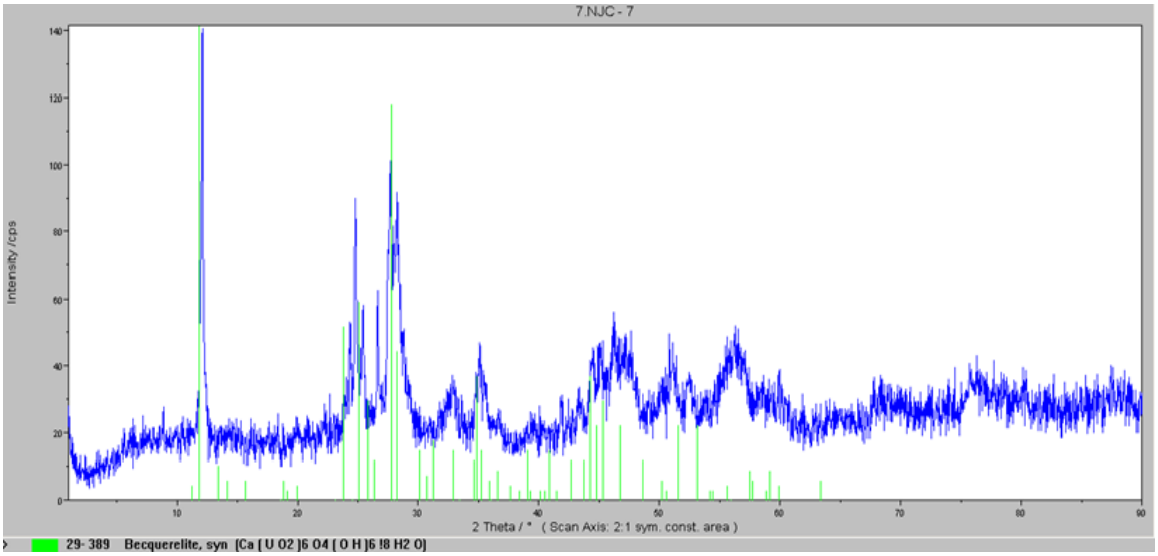

Figure 3-8: The acquired X-ray diffraction spectra of samples 7 (blue) and the reference becquerelite (green).

It was necessary to match the acquired spectra with uranium phosphate phases (Figs. 3-9 & 3-10) because of the findings from the experiment done by Schimmack et al. (2005 & 2007), where they found that the secondary uranium minerals have phosphates e.g. autunite and sabugalite. No good match was found at any point and only uranium oxy-hydroxides were detected by the powder XRD analysis.

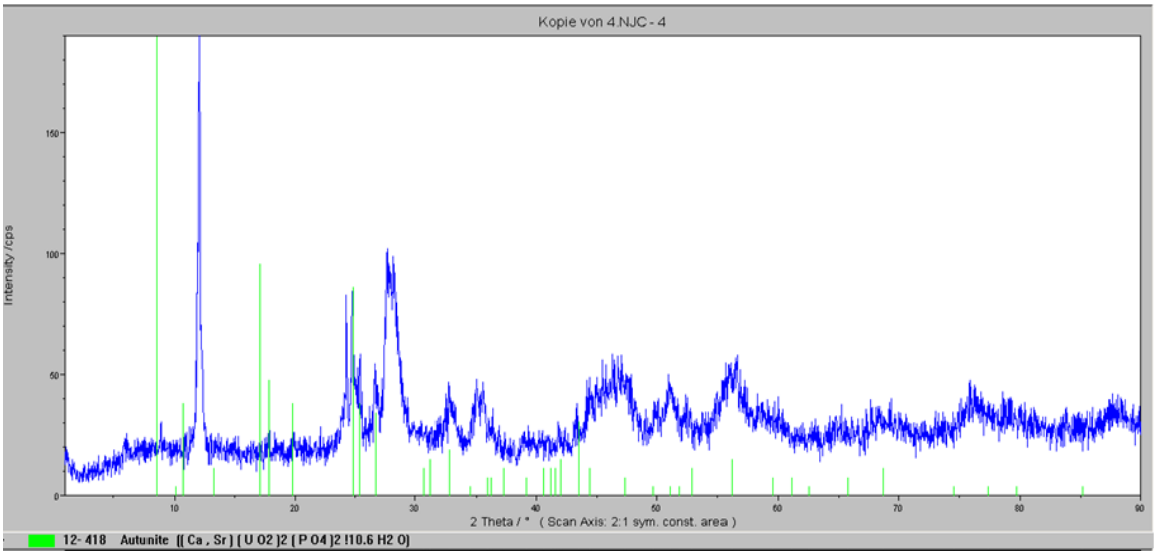

Figure 3-9: The acquired X-ray diffraction spectra of samples 4 (blue) and the reference autunite (green).

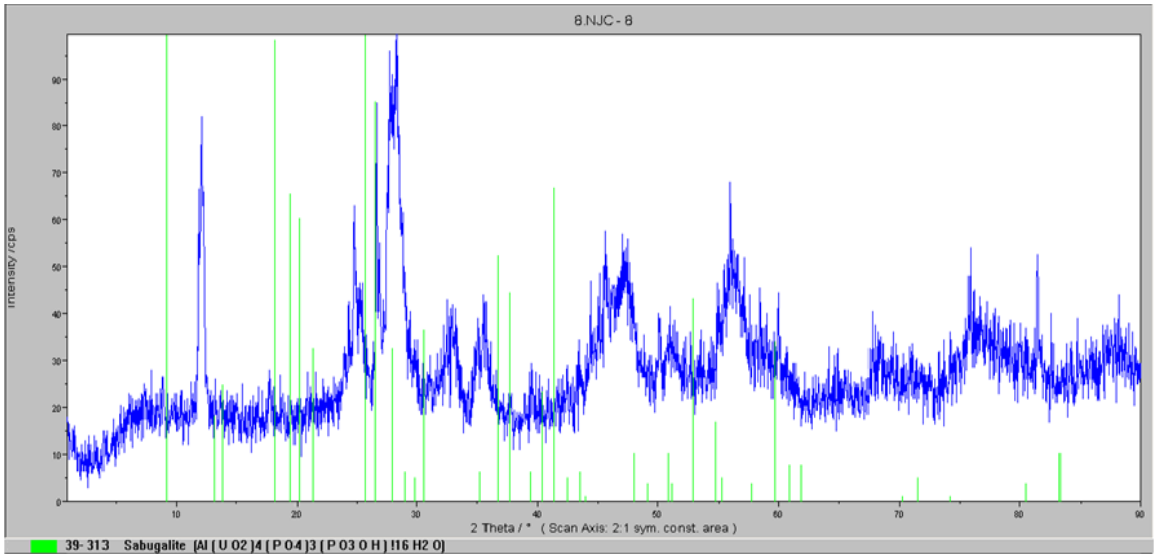

Figure 3-10: The acquired X-ray diffraction spectra of samples 8 (blue) and the reference sabugalite (green).

3.3 XPS Results

X-Ray Photoelectron Spectroscopy is a method to characterize the surface region of materials by analyzing the energy distribution of electrons ejected from the material when it is exposed to X-Rays of a well-defined energy. Samples 4, 7, and 8 were analyzed and their XPS spectra were measured. Also sample 4 was grounded and the spectrum of the powder was measured. Only uranium and oxygen were identified in the samples as shown in (Figs. 3-11 & 3-12). The U 4f peaks are the strongest and most resolved peaks in the XPS spectrum of U (Schindler et al., 2009a and references therein). Due to the spin-orbit splitting parameters in the f orbital of U, two typical main peaks in (Fig. 3-11) are detected. These are U $4f_{5/2}$ and U $4f_{7/2}$.

Table (3-3) shows the spin-orbit splitting parameter, for example, in orbital f the angular momentum (l) has a principle quantum number which is 3, the electron spin (s) ±1/2, and because the total angular momentum quantum number (j) can be calculated as follows:

$j = l \pm s$

Table 3-3: The spin-orbit splitting parameters.

(l) angular momentum	(n) principal quantum number	(s) electron spin	(j) total angular momentum quantum number
s	0	±1/2	±1/2
p	1	±1/2	1/2, 3/2
d	2	±1/2	3/2, 5/2
f	3	±1/2	5/2, 7/2

The U $4f_{7/2}$ occurs at 382.0 eV and the U $4f_{5/2}$ at about 392 eV which is the typical value for uranium (VI) minerals. In this case about 10 eV is the separation between the two peaks. In addition, Weller et al. 2000 and Schindler et al. 2009a measured natural meta-schoepite samples and the U $4f_{7/2}$ was 382.0 eV. This also agrees well with the reported binding energy of 382.0 eV for a synthetic schoepite sample by Froideval et al. 2003.

There are smaller peaks called satellite peaks (Fig. 3-11). These peaks are formed after the expulsion of the core-level electron. Subsequently, an electrostatic potential is experienced by the valences electrons and then they are excited to a higher unfilled level (Briggs, 2003). The other detected photoelectron peak is the O 1s at 531.6 eV. This is in line with the measured O 1s peak for meta-schoepite by both Weller et al. 2000 and Taylor 1971 which is 531.4 eV. However, the O 1s peak in the vicinity of 531 e.V. can be found in more than one uranyl mineral (Schindler et al., 2009b). The XPS couldn't detect any Ca or P.

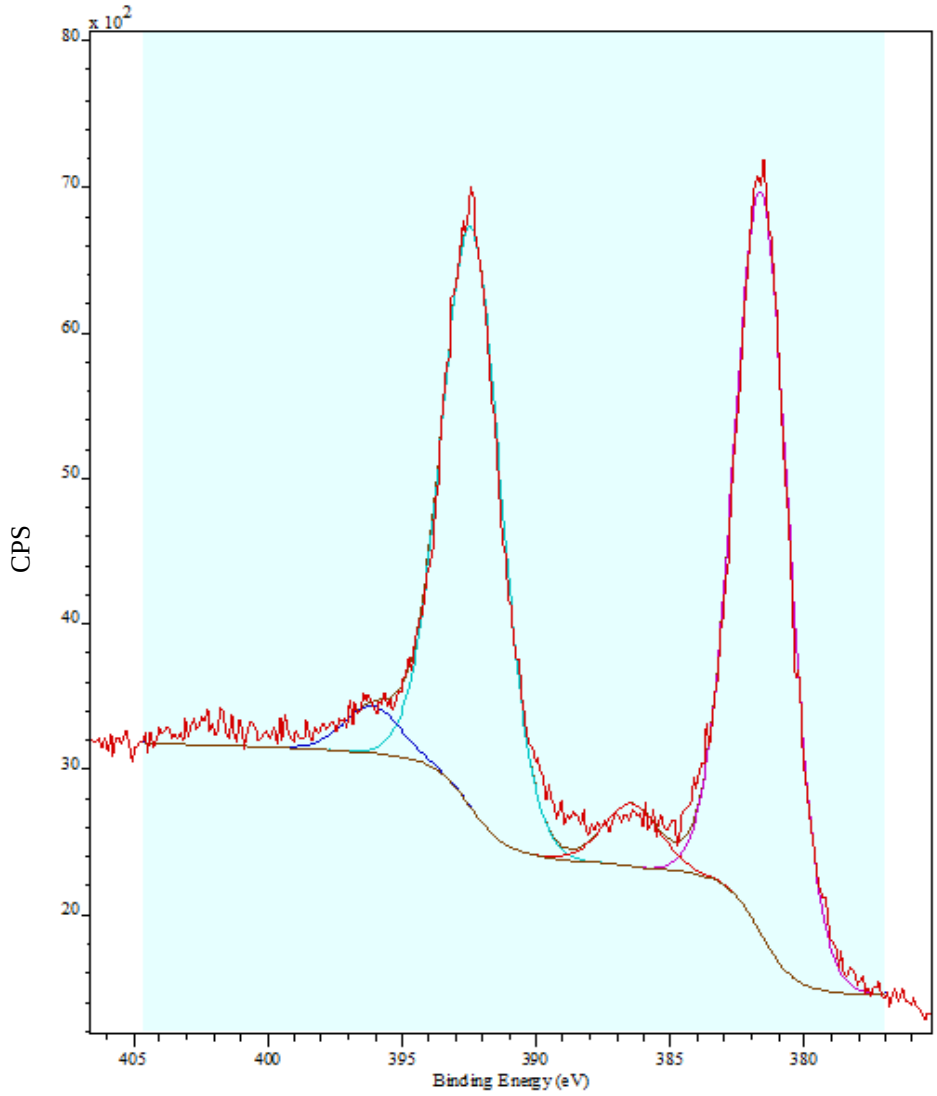

Firgure 3-11: The two main photoelectron peaks of U (U $4f_{5/2}$ and U $4f_{7/2}$) along with the two smaller satellite peaks of sample 7.

Neither Ca nor P was detected with the XPS analysis, although the reason for not detecting Ca could be due to its atomic ration with U in becquerelite which is (1:6). As for P, the atomic ratio P:U is only 1:2 in autunite and still could not be detected.

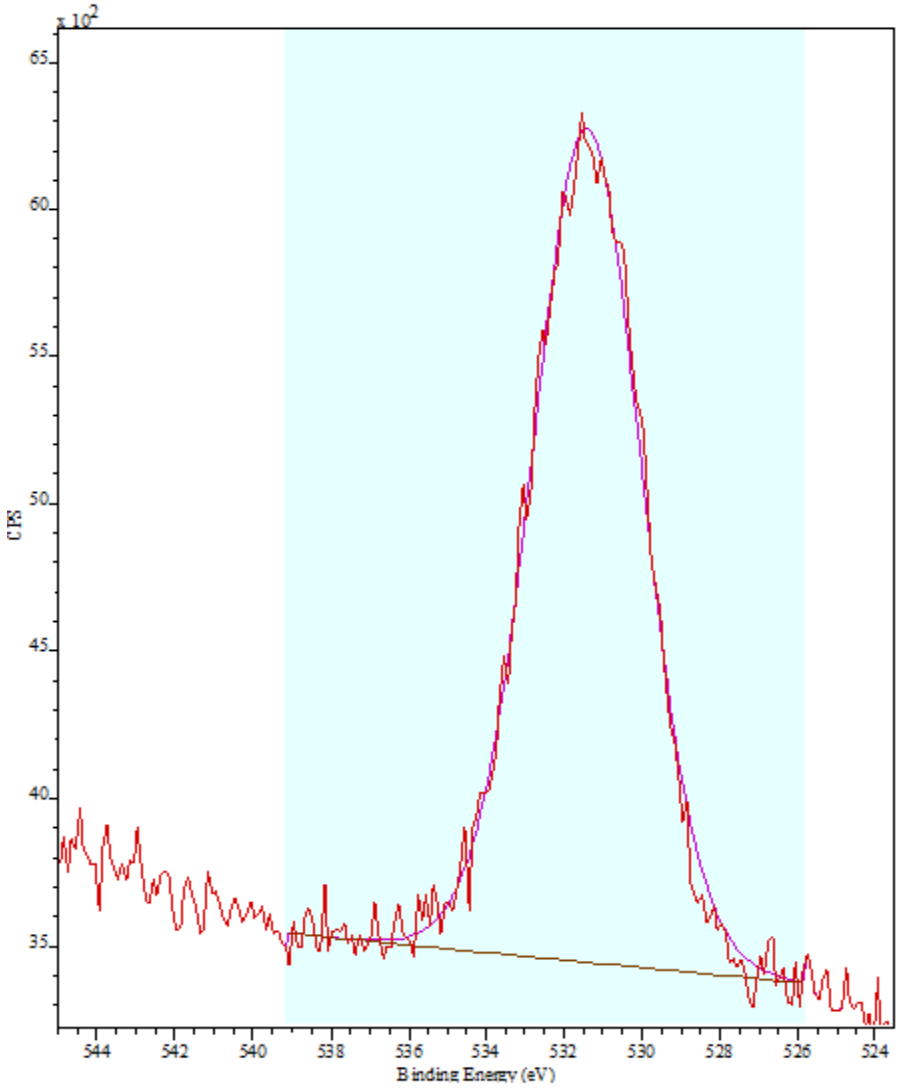

Firgure 3-12: The main photoelectron peaks of O1s of sample 7.

3.4 SEM Results

Three samples (4, 7, & 8) have been prepared for the SEM analysis. 17 SEM spectra and their associated backscattered electron (BSE) images were gained (Appendix B). In general, all the acquired spectra showed the same major elements. U is dominant in all cases, which is expected, because the DU projectile or alloy is made of 99.25% depleted uranium, and 0.75 titanium (Sajih et al., 2010; Bleise et al., 2003 and references therein). O peak is also strong in all spectra. This is likely because the secondary minerals formed due to the corrosion process are uranyl oxy-hydroxides. Ca peak appeared several times. This finding supports the conclusion that becquerelite $Ca(UO_2)_6O_4(OH)_6(H_2O)$ is also formed after the reaction with uranium from the DU alloy and the calcium from the synthetic rain water (0.05M $CaSO_4$) that had been used for irrigation or from the soil itself in the previous leaching experiment by Schimmack et al. 2005 and 2007. Si as well as smaller Mg peaks were detected. This could be from the surrounding soil. Ti is present and it is from the alloy itself. Fe and S were detected but only in 2-3 measurements. Au is found, but this is due to sample preparation after coating with gold. Al is found also, however it is not sure whether it comes from the sample or from the sample chamber in the SEM. The same case also for C, it has been detected and it could be either from the sample or contamination i.e. from the carbon disk which the sample is placed on. Na peak appeared twice on one sample, which can be seen on the “black spots” on sample 4 (App. B-5). These spots represent soil. A common feature from the BSE images is the desiccation cracks e.g. (Fig. 3-13). These desiccation cracks support the conclusion that the metal uranium was transformed to schoepite first $(UO_2)_8O_2(OH)_{12}.(H_2O)_{12}$ then the later underwent dehydration and lost some of its crystallization water (which caused the desiccation) forming the meta-schoepite $(UO_2)_8O_2(OH)_{12}.(H_2O)_{10}$. A similar case can be found in Buck 2004. Both schoepite and meta-schoepite were identified via Raman spectroscopy and XRD.

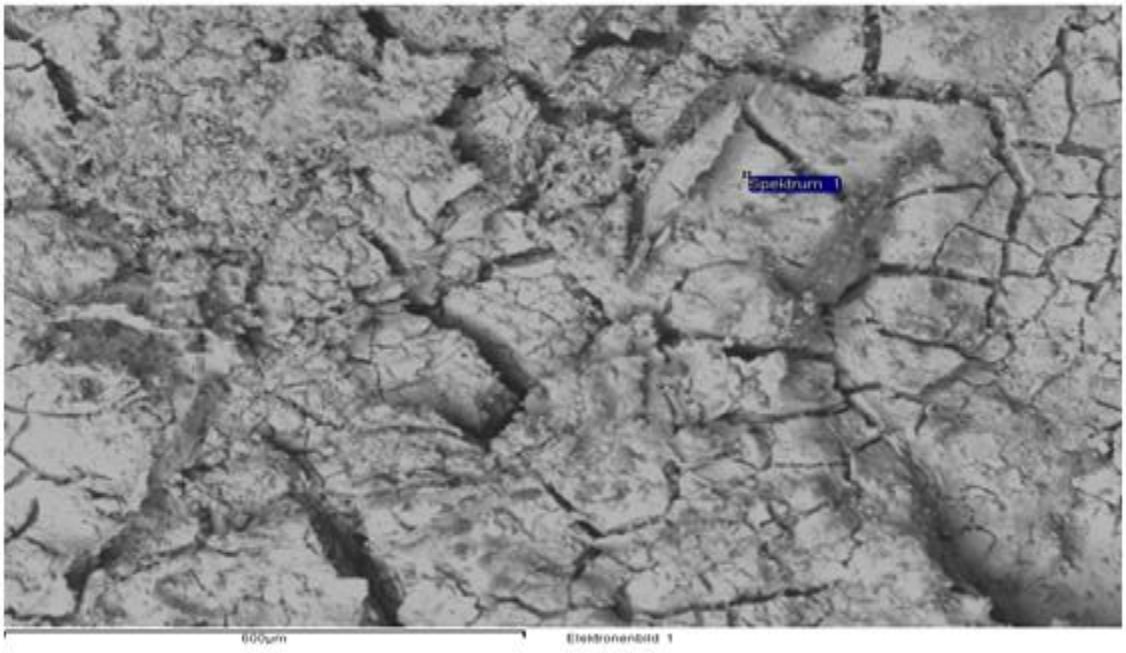

Figure 3-13: A BSE image of a location on sample 4 acquired by SEM.

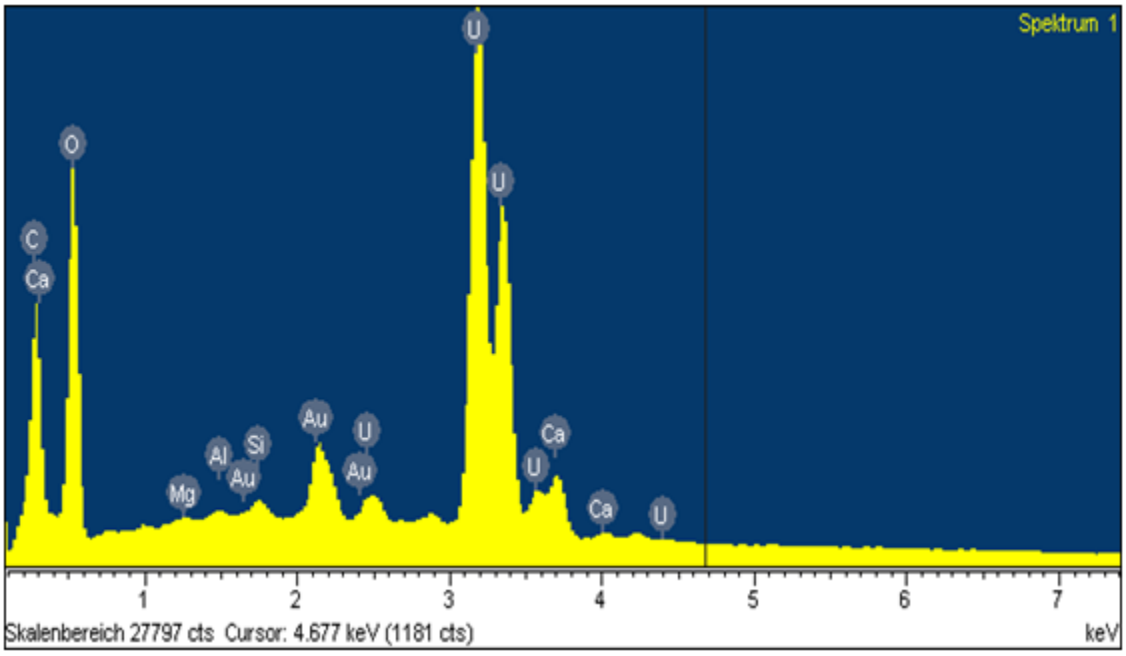

Figure 3-14: The EDS spectrum by SEM of the location showed in Fig. 3-13.

3.5 EMA Results

Performing an electron microprobe analysis on a single prepared resin block yielded useful information about the chemical composition, chemical relationships, and grains shape & morphologies of sample 4. BSE images were taken by the EMA (Fig. 3-15). Three different regions can be distinguished from these images: the white parts (A) region, which represent the metal uranium ,the light grey (B) region, which represents the secondary uranium minerals meta-schoepite and/or becquerelite, , and the darker & bigger crystals (C) region, which represents the soil minerals.

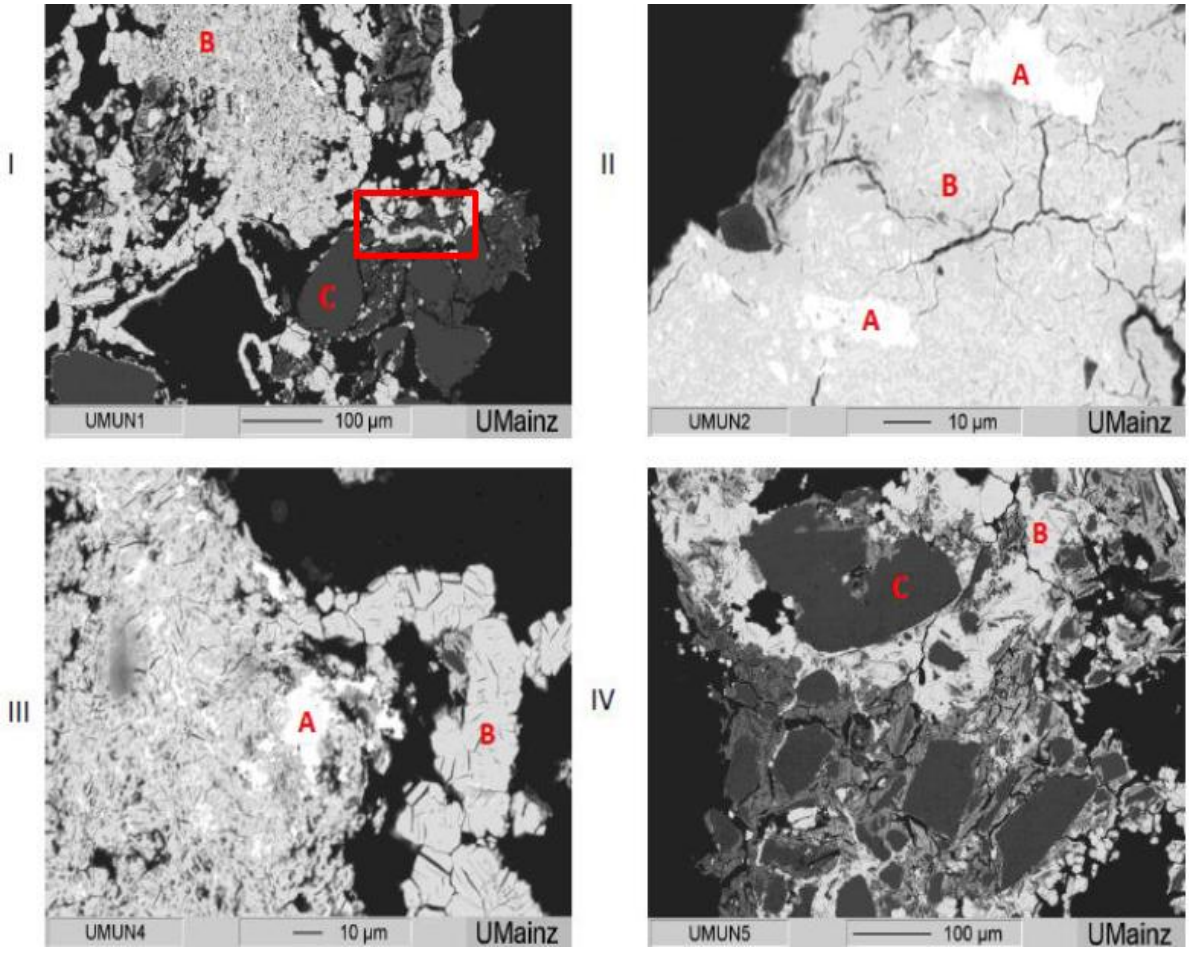

Figure 3-15: The BSE images taken by EMA; A, B, & C represent 3 distinguishable regions with different mineralogy; an elemental map was made for the area inside red rectangle in (I); Images I-III taken for grain # 9, and IV for grain # 5 as shown in Fig. 2-11.

Three elemental maps were implemented for U, Ca, Si, Al, Mg, and Ti (Figs. 3-16, 3-17, & 3-18). A clear direct relation between U and Ca that can be seen on these maps, which also supports the opinion that says becquerelite was formed after bonding between uranium from the DU alloy and Ca from the irrigation water used in the previous experiment. This can be seen very well in Figs. 3-16 & 3-17, where Ca is increasing with increasing U. Meanwhile, Fig. 3-18 shows dominance of U, especially at the highly concentrated spot in the middle representing the DU alloy. There was no association between U and Si. Instead Si is sometimes related with Al to form clay minerals. Mg from the soil was detected and it is not related to U, which means, no Mg uranyl oxy-hydroxide is present. Ti is present sometimes, which comes from the alloy itself.

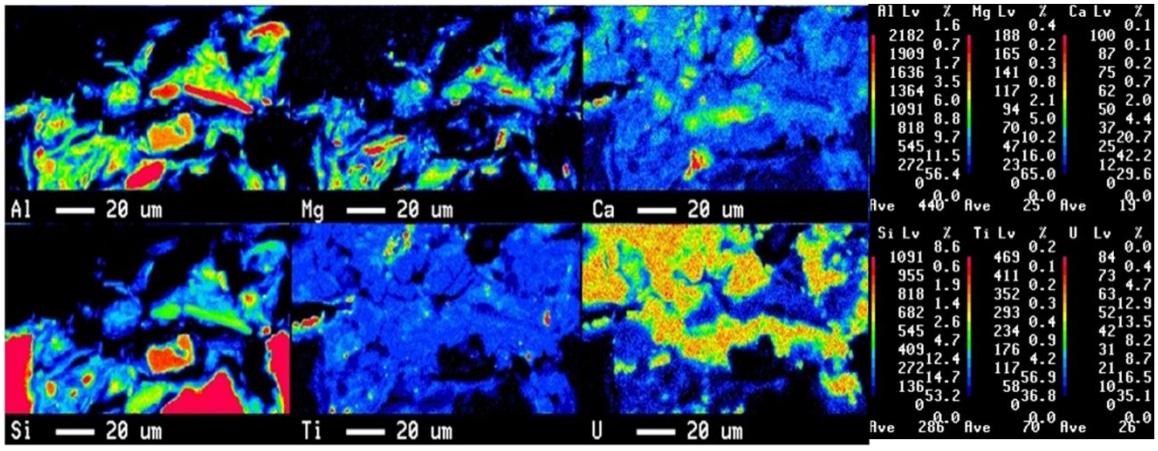

Figure 3-16: An elemental map made by EMA showing the relations among U, Ca, Mg, Ti, Al, & Si for the area inside the red rectangle in Fig. 3-15 (I).

A quantitative analysis was performed for U, Ca, Mg, K, Al, Si, P, & Ti for the different grains in the prepared resin block Fig. 2-11. All 41 readings are listed in Appendix C. The elements were measured as oxides, after which the mass percentage was calculated for each element. As for the uranium, the majority of readings were around 78-80% by mass. According to the chemical formulas of becquerelite $Ca(UO_2)_6O_4(OH)_6.(H_2O)_8$ and schoepite $(UO_2)_8O_2(OH)_{12}.(H_2O)_{12}$, the mass percentage of U should be 78.2% and 79.47% respectively, which is in line with the acquired

readings. Some of the Ca readings were about 2%, which is also expected in becquerelite (2.19% by mass). The very high U readings represent the DU alloy. The same readings have Ti about 0.77% by mass, which is expected for a DU alloy. Other readings gave much lower U mass percentage and higher Ca, Al, and Si, which represent a mix of soil and uranium minerals.

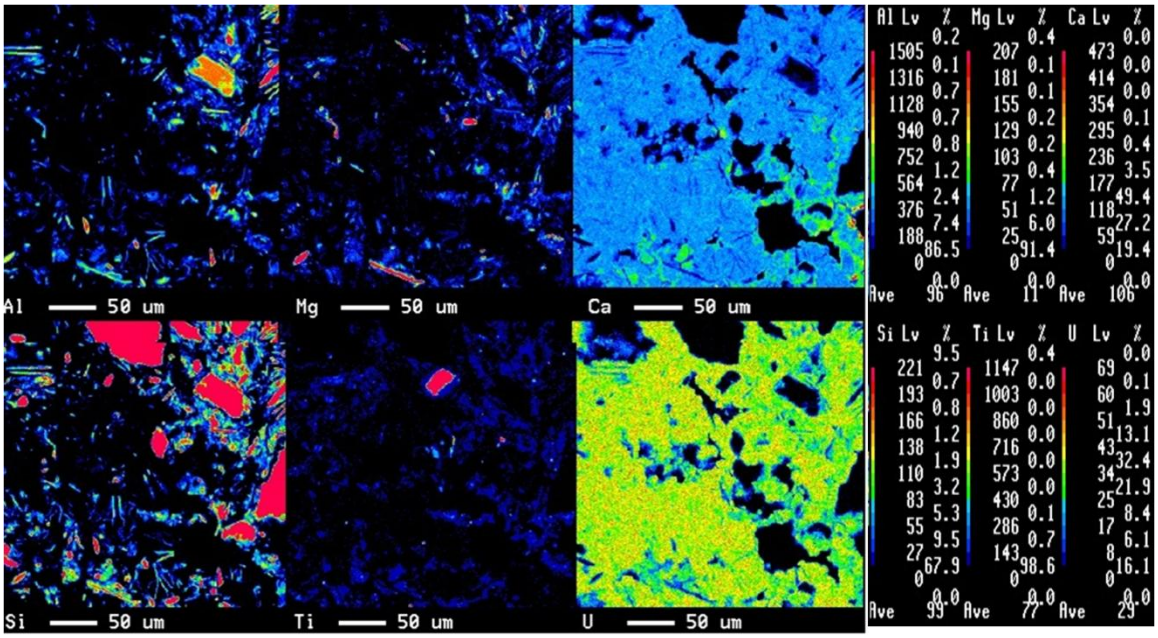

Figure 3-17: An elemental map made by EMA showing the relations among U, Ca, Mg, Ti, Al, & Si for a location in grain #4 in Fig. 2-11.

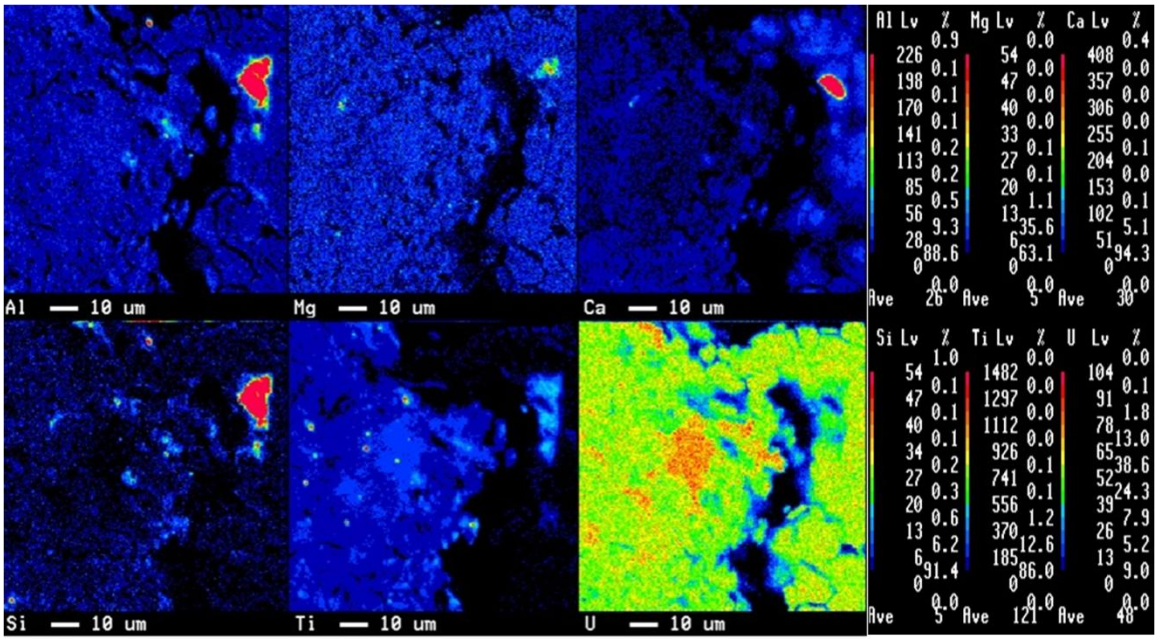

Figure 3-18: An elemental map made by EMA showing the relations among U, Ca, Mg, Ti, Al, & Si for the area represented in Fig 3-15 (III).

3.6 Dissolution Experiment

A dissolution experiment was performed for the remaining amount of the DU ammunition corrosion products powder in order to determine the dissolution behavior of the secondary uranium minerals in the corrosion products as a function of pH. Another reason for the experiment was to compare the experimental data with the modeled dissolution curves of relevant phases which may control the solubility and consequently, the mobility of uranium in the soil.

The modeling of the dissolution curves for uranium and calcium needed to be compared with the measured data. It was also useful to determine the pH range of interest for the lab experiment. The environment or conditions were simulated using the geochemical computer code VISUAL MINTEQ v.3.0. According to the data acquired from the different analyses of the solid material, the two main identified uranium phases were schoepite /or meta-schoepite and becquerelite. Schoepite and meta-schoepite can be considered as one mineral in this case, because the only difference between them is in the number of molecules of the crystallization water attached, and that Visual MINTEQ does not differ between the two minerals in this situation. Therefore schoepite and becquerelite were assumed to be present as solid phases in the 0.01M $NaClO_4$:H_2O solution. The dissolution curves for U and Ca were calculated for each phase with and without the presence of the atmospheric CO_2 (Fig. 3-19).

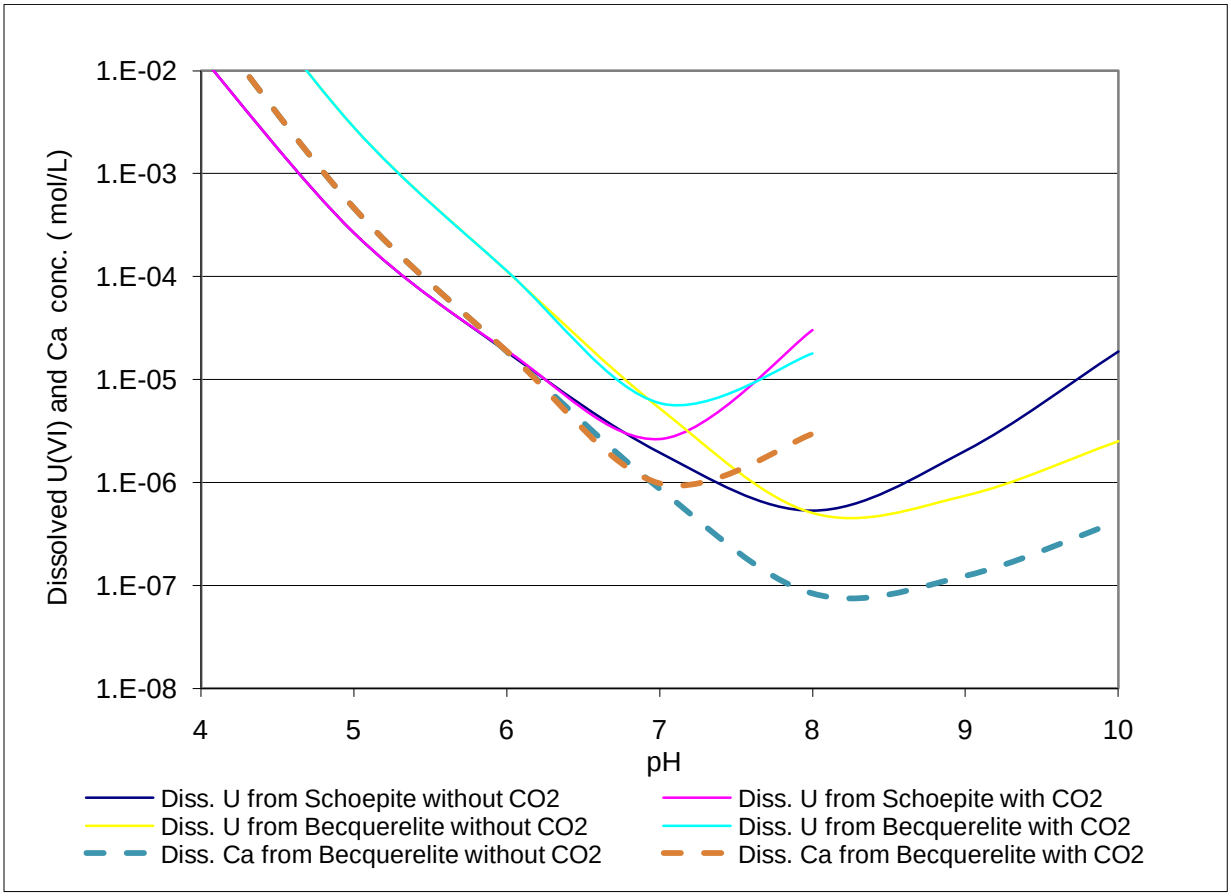

Figure 3-19: Modeled dissolution curves for U & Ca, assuming the presence of schoepite or becquerelite, with and without atmospheric CO_2.

The area of interest was set to be between pH 6 and 10. It was chosen after checking the modeled curves in figure 3-19. The final pH was always less than the initial pH (Table3- 5); this might be due to the dissolution of atmospheric CO_2 and/or the solid phases in the solution. According to the modeled curves, the uranium solubility controlling phase is schoepite in the acidic region (specifically until ph of 8 and 7.6 in the absence and presence of CO_2 respectively), after that becquerelite is the less soluble phase.

Table 3-5: The starting and final measured pH for samples (4, 7, and 8).

Sample	Starting pH	Final pH
4-1	6.16±0.14	5.71±0.19
4-2	7.2±0.03	6.15±0.23
4-3	8.27±0.07	7.71±0.18
4-4	8.86±0.04	7.49±0.21
4-5	9.89±0.06	8.39±0.16
7-1	7.01±0.1	6.39±0.17
7-2	6.19±0.11	5.84±0.22
7-3	8.01±0.1	5.74±0.16
7-4	9.03±0.11	6.59±0.16
7-5	10.13±0.2	8.55±0.18
8-1	7.25±0.05	7.07±0.26
8-2	8.34±0.055	7.60±0.15
8-3	6.3±0.1	5.82±0.09
8-4	9.03±0.07	8.04±0.22
8-5	10.18±0.65	8.55±0.23

The measured uranium concentrations for samples (4, 7, and 8) showed a good agreement with the modeled data (Fig. 3-20). The uranium results show that, the measured points are in good agreement with the modeled schoepite curve as well as the becquerelite curve, and it is not possible to tell which mineral is in equilibrium with the solution from this figure only. This is due to the similarity in the dissolution behavior for both minerals.

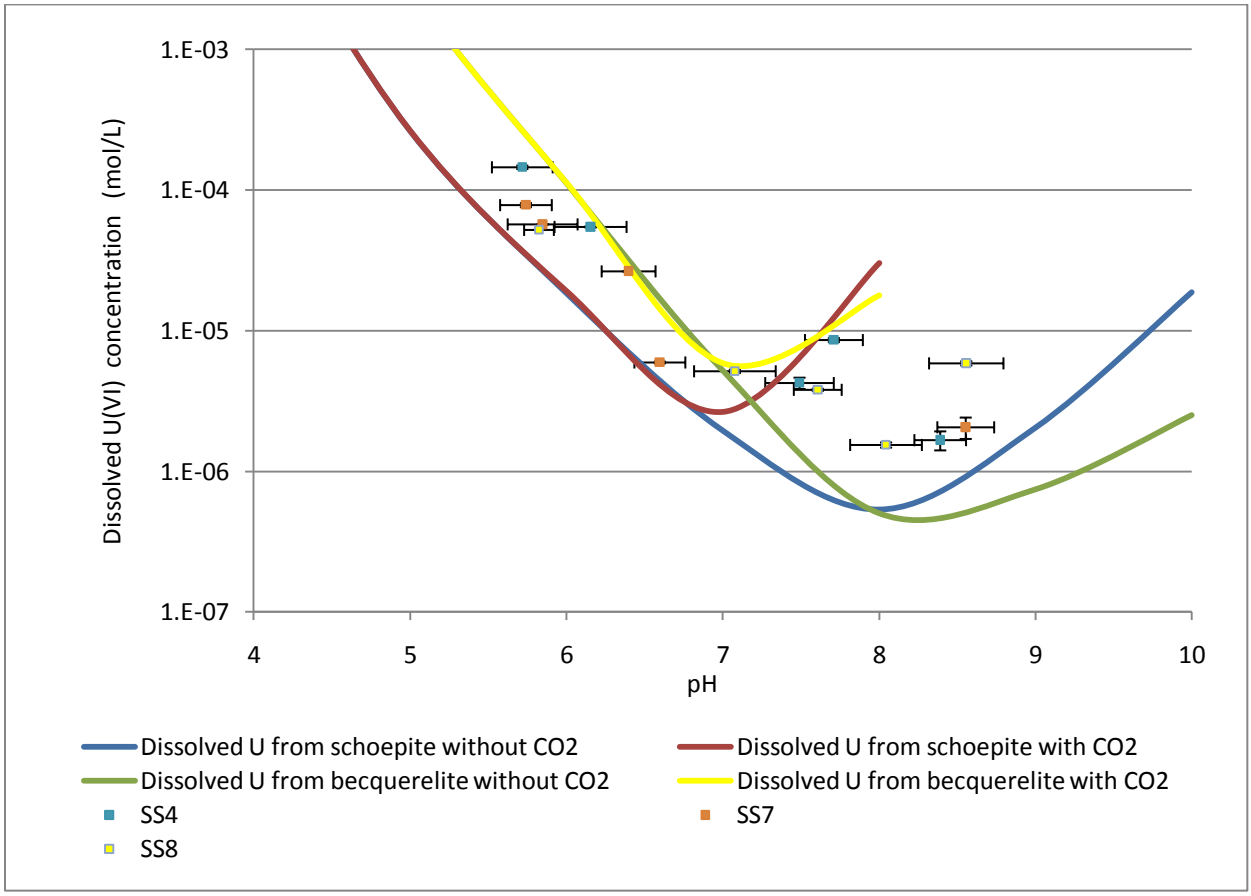

Figure 3-20: Modeled dissolution curves for U (curves), assuming the presence of schoepite or becquerelite, with and without atmospheric CO_2, plus the measured U data (points).

The measured calcium concentrations show no relation to the modeled dissolution curve of becquerelite (Fig. 3-21). This means that the source for the dissolved calcium in the solution does not come from becquerelite and it could be from any mineral in the soil, especially after reacting with the calcium from the irrigation water used in the previous column experiment done by Schimmack et al. 2005 & 2007.

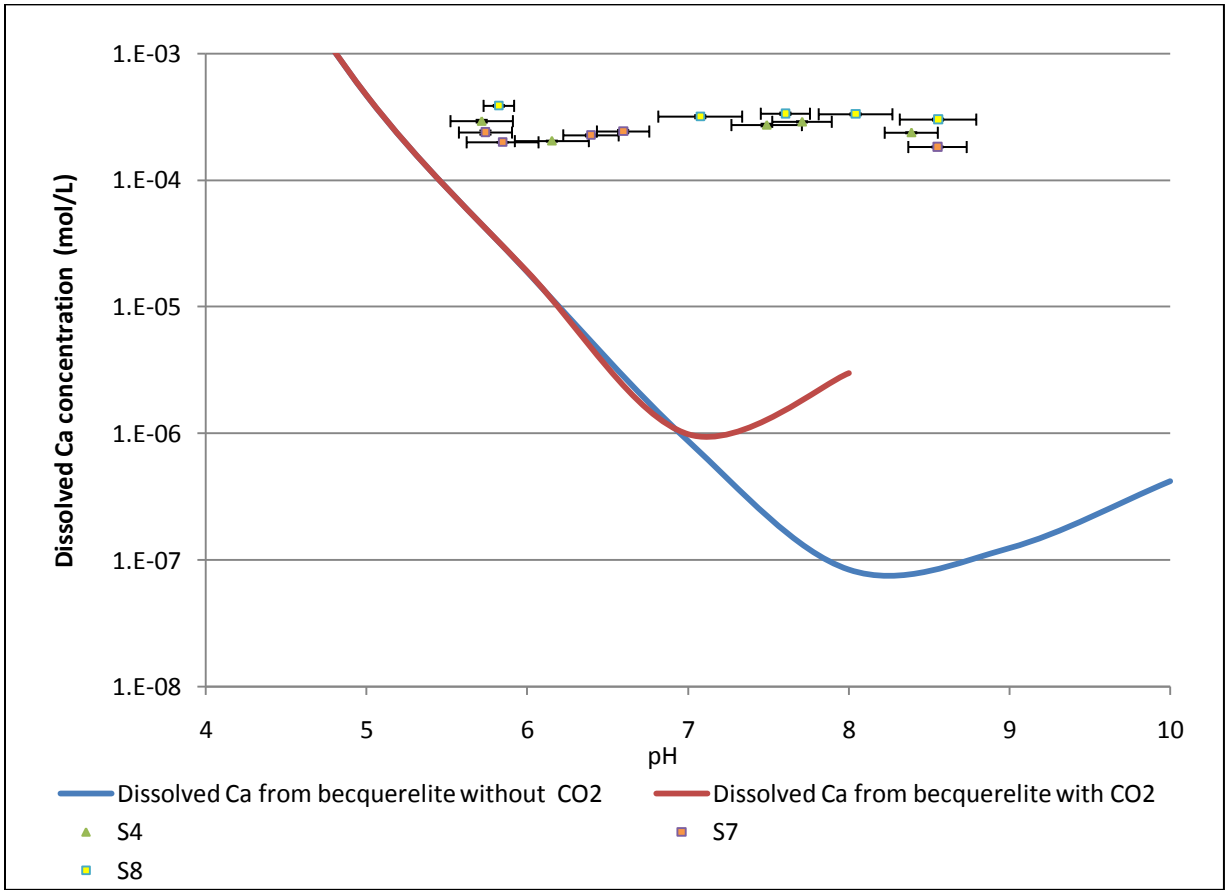

Figure 3-21: Modeled dissolution curves for Ca (curves), assuming the presence of becquerelite, with and without atmospheric CO_2, plus the measured Ca data (points).

4 Discussion

4.1 Transformation from U metal to other U phases

As mentioned before, the DU round is an alloy made of 99.25% metallic depleted uranium, and 0.75% Ti. In the case where the rounds miss their targets, as in our case, the metallic uranium will undergo oxidation under all earth surface conditions (Bailey et al., 2002).Eventually the uranium will transform or alter from its metal form to other U phases or minerals with time.

4.1.1 Structure of the formed U(VI) minerals

The first mineral formed from the metallic U is schoepite. All of the identified U(VI) minerals (schoepite, meta-schoepite, and becquerelite) structurally belong to the same group or have the same anion topologies, according to the hierarchy of uranyl mineral structures of Burns et al. 1996. The anion topologies of these minerals are made of triangles and pentagons (Figs. 4-1 & 4-2).

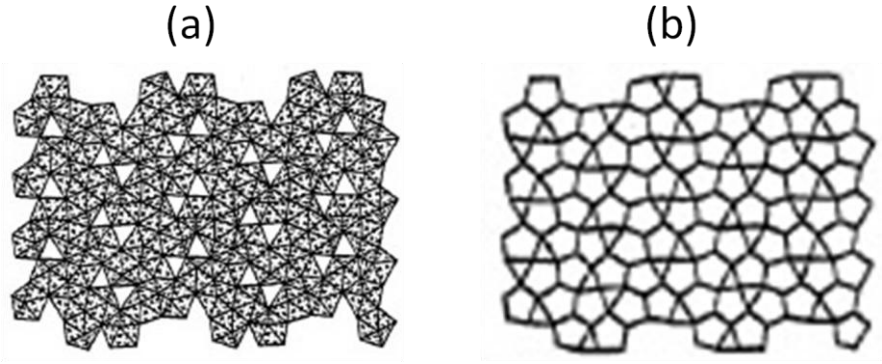

Figure 4-1: Sheets bases upon anion topology that contains only triangles and pentagons: (a) the sheet that occur in the structure of schoepite, (b) the sheet anion topology that correspond to the sheet shown in (a) (modified after Burns et al., 1996).

The structure of schoepite contains sheets with underlying anion topology (Fig. 4-1). It contains chains of edge-sharing pentagons that are separated by two adjacent arrowhead chains of pentagons and triangles, with the arrowheads of adjacent chains pointing in opposite directions. The sheets are connected via hydrogen bonding to intersheet H_2O groups only (Burns et al. 1996). Schoepite is not a stable U mineral. It tends to lose its water of crystallization forming a more stable meta-schoepite phase. This phenomenon is clear with the desiccation cracks due to the dehydration in Fig. 3-13. Becquerelite has a slightly different structure from schoepite. It has an anion topology that contains a chain of edge-sharing pentagons. Each of these chains is separated by a chain containing pentagons and triangles, arranged so that each triangle shares an edge with one pentagon and a corner with another pentagon within the same chain (Fig. 4-2). The sheets are linked through intersheet cations and hydrogen bonds (Burns et al., 1996).

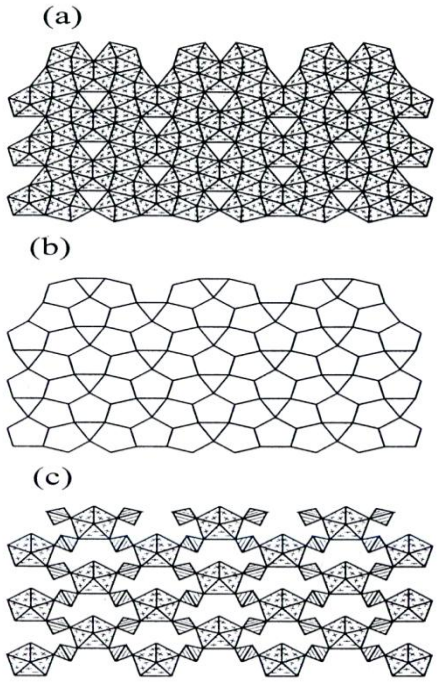

Figure 4-2: Sheets bases upon anion topology that contains only triangles and pentagons: (a) the sheet that occur in the structure of becquerelite, billietite, compreignacite, richetite, protasite;(b) the sheet anion topology that correspond to the sheets shown in (a) and (c); (c) the sheet that occur in the structure of $Mg[(UO_2)(SO_4)_2]$ H_2O_{11} (after Burns et al. 1996).

Table 4-1: Uranyl mineral structures containing sheets based on anion topologies with triangles and pentagons.

Name	Formula
Billietite	$Ba(UO_2)_6O_4(OH)_6(H_2O)_8$
Becquerelite	$Ca(UO_2)_6O_4(OH)_6(H_2O)_8$
Compreignacite	$K_2(UO_2)_6O_4(OH)_6(H_2O)_7$
Schoepite	$(UO_2)_8O_2(OH)_{12}(H_2O)_{12}$
Fourmarierite	$Pb(UO_2)_4O_3(OH)_4(H_2O)_4$

Billietite $Ba(UO_2)_6O_4(OH)_6(H_2O)_8$ has a chemical composition and structure very close to becquerelite $Ca(UO_2)_6O_4(OH)_6(H_2O)_8$ (Table 4-1). The only difference is the divalent cation here. There was no becquerelite spectrum in the database to be used for matching with the acquired Raman spectra, therefore, the natural becquerelite specimen was brought to measure and analyze its Raman spectrum. The recorded spectrum showed high similarity with the billietite spectrum (Fig. 2-3), which agrees with our theory. The uranyl ions in all of the identified minerals are coordinated with 5 ligands (pentagonal bipyramids).

4.1.2 Paragenesis of the formed U(VI) minerals

Only uranyl oxyhydroxides were detected in this study (schoepite and/or meta-schoepite, becquerelite). They are likely to be formed at the beginning of an oxidative alteration process. This could be because the oxidative alteration of the DU ammunition is at the beginning of the alteration sequence. This agrees with another study made by Wronkiewicz 1996, in which the author studied the paragenetic sequence of alteration phases for UO_2 under oxic atmosphere for about 10 years (Fig. 4-3).

The uranyl oxyhydroxides could be precipitated from the waters that had U content. They could then be developed during the oxidation and corrosion of DU ammunition, most likely at or near the surface of the corroded DU rounds, or even in the corroded pits.

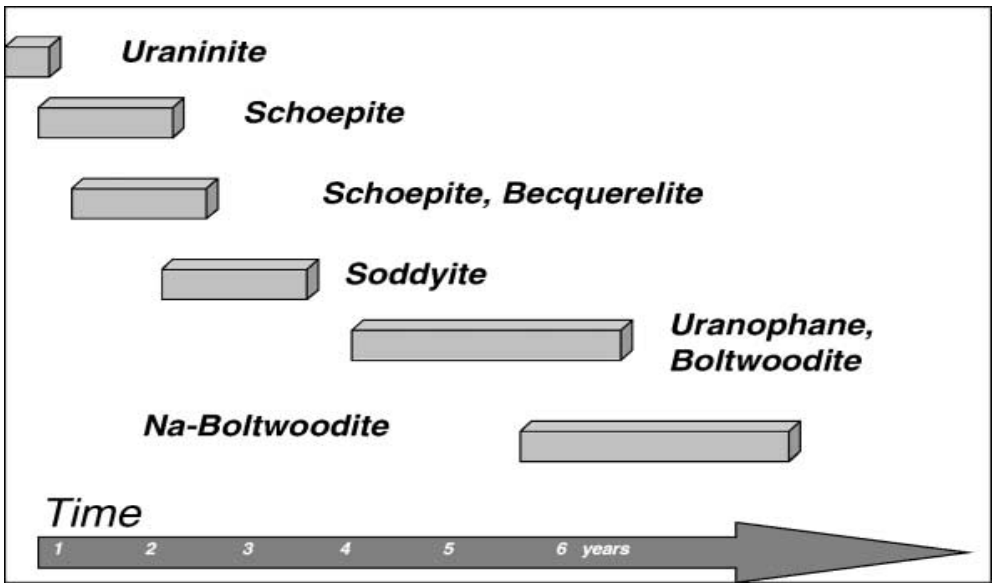

Figure 4-3: Sequence of paragenetic mineral formation during oxidative alteration of UO_2 as observed experimentally by Wronkiewicz et al. 1996 (after Amme et al., 2006).

Schoepite $(UO_2)_8O_2(OH)_{12.}(H_2O)_{12}$ might be formed at the beginning of the alteration process. This phase is unstable and tends to lose some of the interlayer water (two molecules) to form a more stable meta-schoepite phase $(UO_2)_8O_2(OH)_{12.}(H_2O)_{10}$. The alteration includes the removal of 2 of the 12 water molecules in schoepite. These 2 molecules are more weakly bonded than the remaining 10 (Finch et al., 1996). The structural sheets will not collapse as a result of the transformation and relatively minor changes to H-bonding are induced (Finch et al., 1998). Christ and Clark (1960) mentioned that the spontaneous dehydration of schoepite is irreversible at any temperature.

The other phase which could be formed after the formation of schoepite is becquerelite $Ca(UO_2)_6O_4(OH)_6(H_2O)_8$ due to the presence of Ca in the irrigation water used in the original experiment by Schimmack et al. 2005 & 2007. Such phase alteration (the reaction of Ca^{2+} with schoepite to form becquerelite) has been experimentally proven by Vochten and Haverbeke 1990 as well.

4.2 Aqueous Species of Formed U minerals

After the dissolution of DU ammunition corrosion products, several aqueous species are expected to exist depending on the secondary uranyl minerals that have been formed due to corrosion or alteration of the DU alloy. Also the dissolution behavior of these formed minerals is expected to be different, because each mineral has a different composition and solubility product Ksp. Analyzing the dissolution behavior under different pH values shows how the pH is affecting the process. In addition, the concentration of dissolved U and/or Ca could give information about the original solid material.

4.2.1 Dissolution of Formed U-minerals

Meta-schoepite has a similar structure as schoepite but with some sheet rearrangement and contraction of the interlayer water molecules (Finch et al., 1996). Therefore, the dissolution of schoepite/meta-schoepite can be expressed by the following equation:

$$2H^+ + UO_3(H_2O)_2 \rightarrow UO_2^{2+} + 3H_2O$$ Equation 4-6

And the solubility product Ksp:

$$K_{sp} = \frac{\{UO_2^{2+}\}}{\{H^+\}^2}$$ Equation 4-7

The used log Ksp in the modeling is taken from NIST 46.7, which is the same value as that of Langmuir 1978 (5.39). For becquerelite, the dissolution reaction is:

$$Ca(UO_2)_6O_4(OH)_6.8H_2O + 14H^+ \rightarrow 6UO_2^{2+} + Ca^{2+} + 18H_2O$$ Equation 4-8

And the used log Ksp was taken from Rai et al 2002 (41) and can be written as follows:

$$K_{sp} = \frac{\{UO_2^{2+}\}^6.\{Ca^{2+}\}}{\{H^+\}^{14}}$$ Equation 4-9

Normally, schoepite is not a long-term solubility controlling phase in natural waters (Finch and Ewing, 1992). It has a tendency to incorporate cations into the interlayer spacings of the lattice. In natural environments, the cation most commonly incorporated is calcium, leading to the formation of becquerelite (Finch and Murakami, 1999). It has been reported that schoepite can be experimentally transformed to becquerelite within a month when in contact with a calcium solution of 10 mM or more (Giammar, 2001 and references therein). On the other hand, comparing the modeled dissolution curves for schoepite and becquerelite led to the conclusion that schoepite /or meta-schoepite could be the uranium solubility controlling phase in the acidic region, while becquerelite will become the least soluble phase in the basic region.

4.2.3 Dominant Aqueous Species

The speciation was modeled using the geochemical code Visual MINTEQ 3.0. This code uses several thermodynamic databases. The involved aqueous species in the modeling of dissolving schoepite are listed in Table 4-2 with their constants and sources.

Table 4-2: List of used aqueous spieces.

Aqueous Species	Log *K* Formation	Reference
(UO2)2(OH)2+2	-5.62	NEA 2003
(UO2)2OH+3	-2.7	NEA 2003
(UO2)3(OH)4+2	-11.9	NEA 2003
(UO2)3(OH)5+	-15.55	NEA 2003
(UO2)3(OH)7-	-32.2	NEA 2003
(UO2)4(OH)7+	-21.9	NEA 2003
UO2(OH)2	-12.15	NEA 2003
UO2(OH)3-	-20.25	NEA 2003
UO2(OH)4-2	-32.4	NEA 2003
UO2OH+	-5.25	NEA 2003
(UO2)2CO3(OH)3-	-0.86	NEA 2003
(UO2)3O(OH)2(HCO3)+	0.65	NEA 2003
(UO2)11(CO3)6(OH)12-2	36.4	NEA 2003
UO2(CO3)2-2	16.61	NEA 2003
UO2(CO3)3-4	21.84	NEA 2003
UO2CO3	9.94	NEA 2003
(UO2)3(CO3)6-6	54	NEA 2003
Ca2UO2(CO3)3	30.7	DonBro07
CaUO2(CO3)3-2	27.18	DonBro06
H2CO3	16.681	PlumBus82
HCO3-	10.329	PlumBus82
OH-	-13.997	NIST 46.7
NaCO3-	1.27	NIST 46.7
NaClO4	-0.7	NIST 46.7
NaHCO3	10.029	NIST 46.7
NaOH (aq)	-13.897	NIST 46.7
CaOH+	-12.697	NIST 46.7
CaCO3	3.22	PlumBus82
CaHCO3+	11.434	PlumBus82

The modeling involved the dissolving of schoepite in the same electrolyte as in the performed experiment (0.01 M $NaClO_4$) at room temperature with and without the presence of atmospheric CO_2 (Figs. 4-8 and 4-9). Then the same modeling was done for becquerelite.

The modeled aqueous species of schoepite (Figs. 4-4 and 4-5) and becquerelite (Figs. 4-6 and 4-7) show a pH increase from 4 to 8 (until 7 in the presence of CO_2) corresponding to the decrease in the dissolved uranium concentrations. After that they tend to increase with increasing pH as the solution is becoming more basic.

Only the dominating species were plotted. In the acidic region, it shows that positively charged species are dominating: UO_2^{2+} until about pH of 5 (for schoepite only), $(UO_2)_3(OH)_5^+$ in the acidic to near neutral region in both cases (in the absence and presence of atmospheric CO_2). In the neutral region, neutral species are dominating $UO_2(OH)_2$ and UO_2CO_3. In the basic region the dominating species are the negatively charged $UO2(OH)_3^-$ with no CO_2 and $UO_2(CO_3)_2^{2-}$ & $UO_2(CO_3)_3^{4-}$ with CO_2.

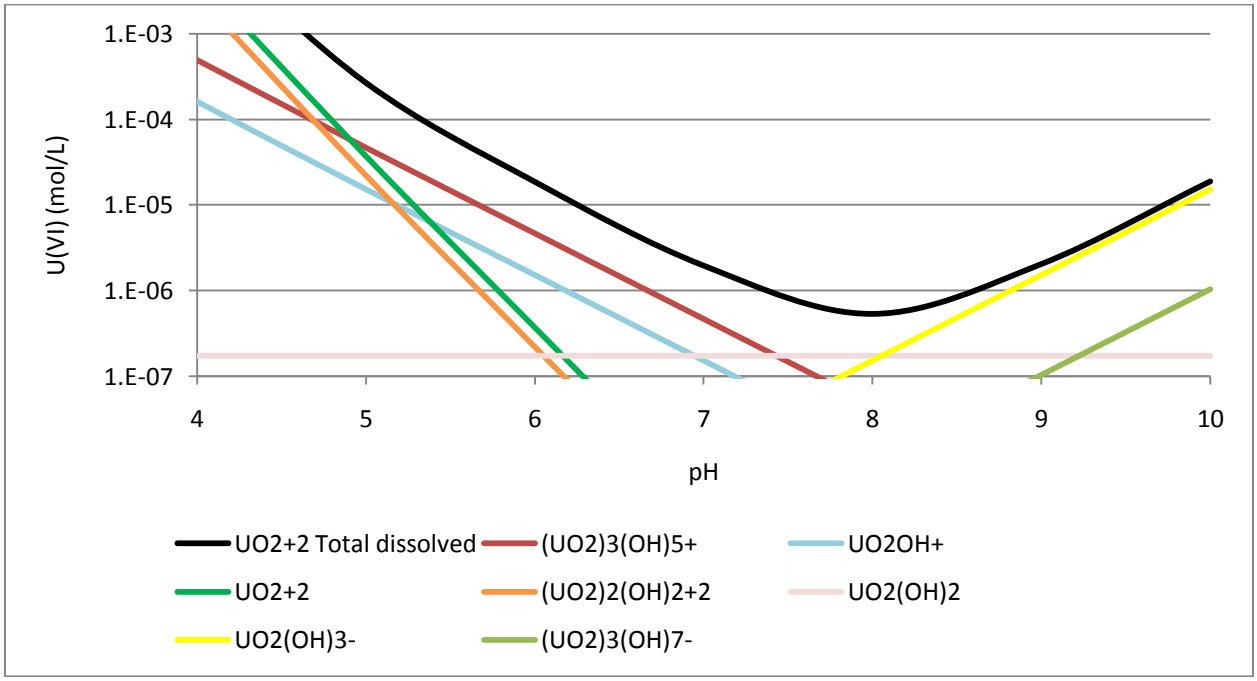

Figure 4-4: The dominant uranium aqueous species for dissolving schoepite in 0.01M $NaClO_4$ in the absence of atmospheric CO_2.

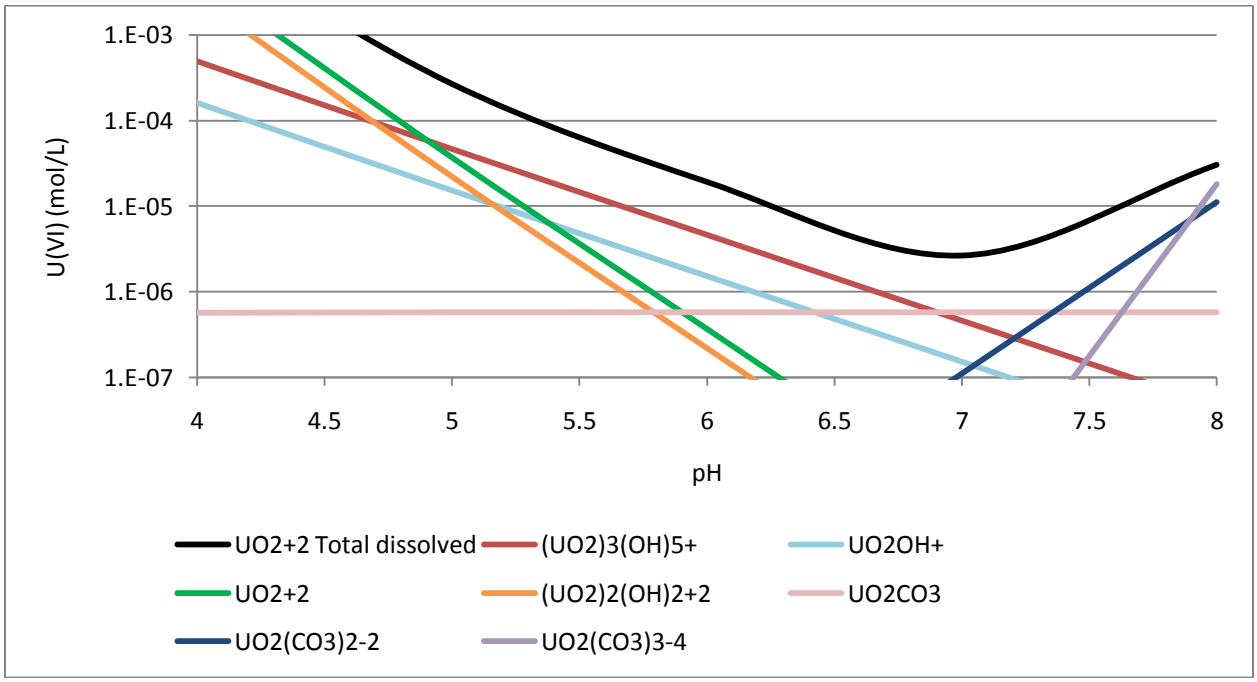

Figure 4-5: The dominant uranium aqueous species for dissolving schoepite in 0.01M $NaClO_4$ in the presence of atmospheric CO_2.

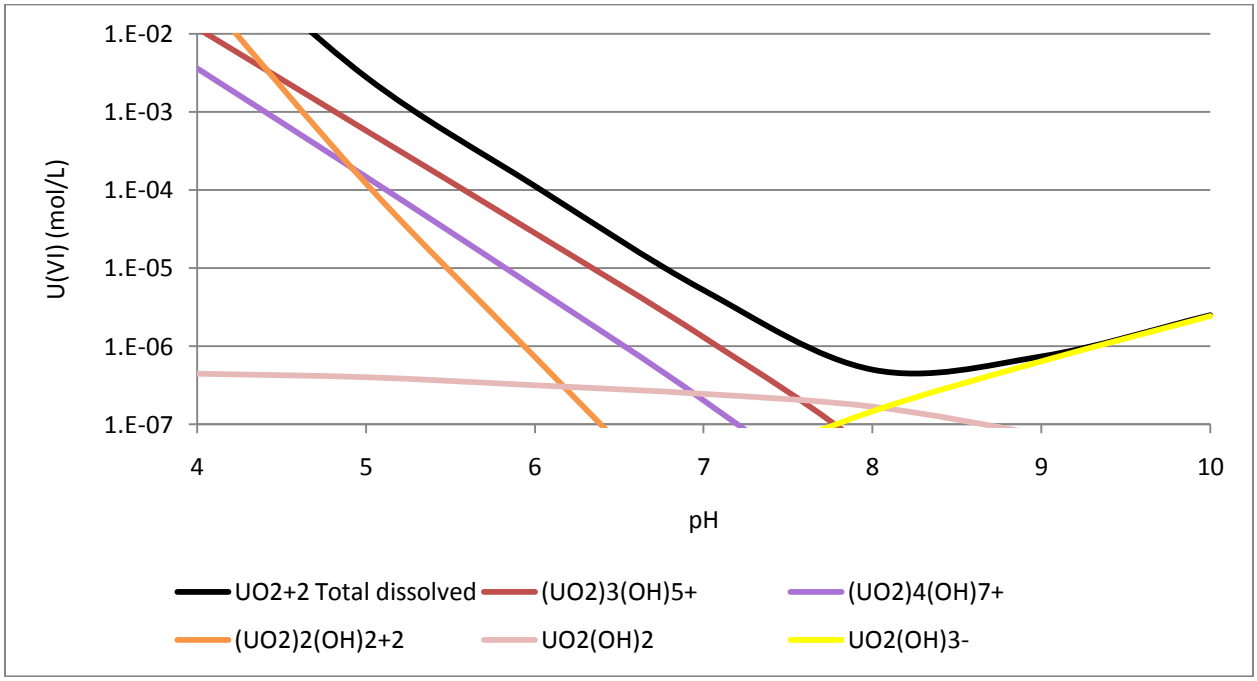

Figure 4-6: The dominant uranium aqueous species for dissolving becquerelite in 0.01M $NaClO_4$ in the absence of atmospheric CO_2.

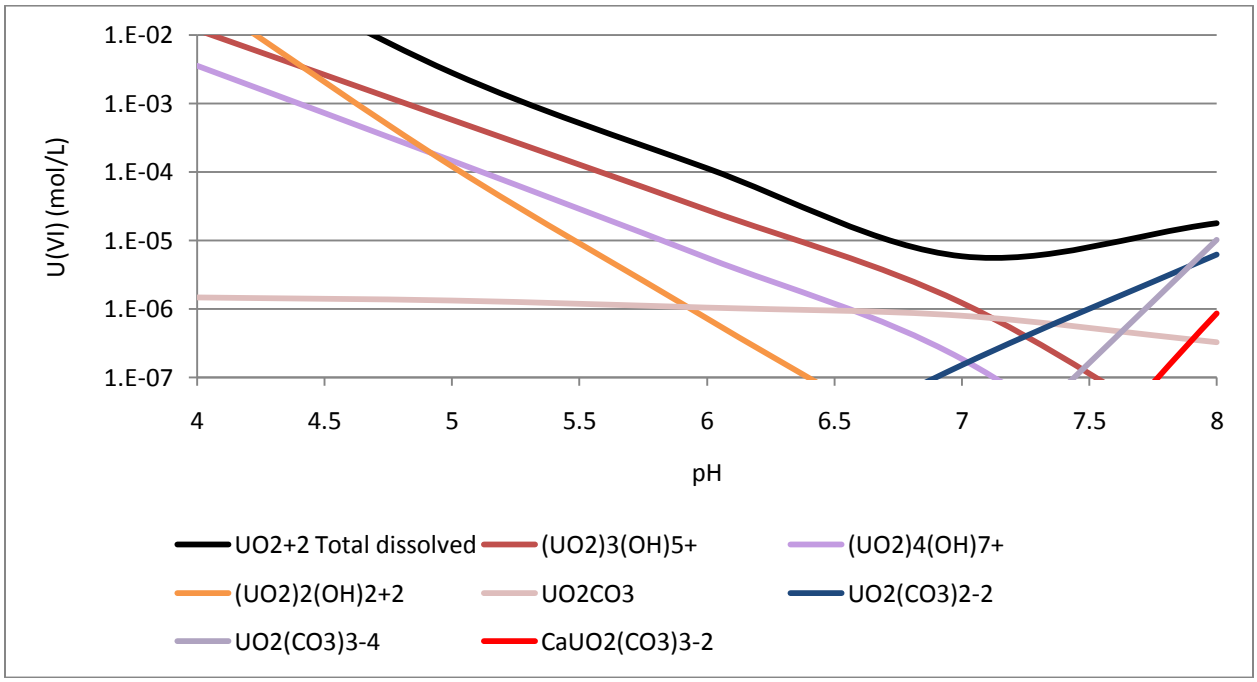

Figure 4-7: The dominant uranium aqueous species for dissolving becquerelite in 0.01M $NaClO_4$ in the presence of atmospheric CO_2.

4.3 The role of CO_2 in the solution

Whether the mineral is schoepite or becquerelite, the measured U points in Fig. 3-20 were at some point in the area between the two curves that represent the dissolution of the mineral in the absence and presence of CO_2, suggesting that different amounts of atmospheric CO_2 were able to penetrate and reach the solution. This led to the modeling of more schoepite and becquerelite dissolution curves with different amounts of partial pressure of CO_2 (pCO_2). The atmospheric pCO_2 is assumed to be 3.8×10^{-4} atm, while the pCO_2 in the soils could be 100 times higher than that in the atmosphere due to the respiration of plant roots and the associated soil microorganisms (Berthelin, 1988; Bohn et al. 2001; Karberg et al. 2005). The average pCO_2 in the pores of agricultural soils is probably 0.003 to 0.03, 10 to 100 times that of the atmosphere (Bohn et al. 2001).

The modeled pCO_2 amounts were: 0 or no CO_2 (without CO_2 curve), 3.8×10^{-5} atm (0.1 CO_2 curve), 3.8×10^{-4} atm (1 CO_2 curve), 3.8×10^{-3} atm (10 CO_2 curve), and 3.8×10^{-2} atm (100 CO_2 curve) as shown in Figs. 4-8 and 4-9. The numbers 0, 0.1, 1, 10, and 100 represent the values that are multiplied by 3.8×10^{-4} to calculate the amount of the CO_2 partial pressure. From these curves, the dissolution of the same mineral varies depending on its pCO_2 and eventually its CO_2 concentration (according to Henry's Law i.e. the amount of gas that dissolves in a liquid is proportional to the partial pressure of the gas over the liquid). The amount of CO_2 presented in the solution along with its pH play a key role in deciding the dissolution behavior and the amount of the dissolved U concentration in the solution. The more dissolved CO_2 in the solution, the more dissolved U concentration is expected at the same ph value. For example, the U concentration at pH 7.5 in Figs. 4-8 and 4-9 would be more if the CO_2 partial pressure was 3.8×10^{-4} that is the "1 CO_2" curve rather than the "no CO_2 or 0.1 CO_2" curves for the same point.

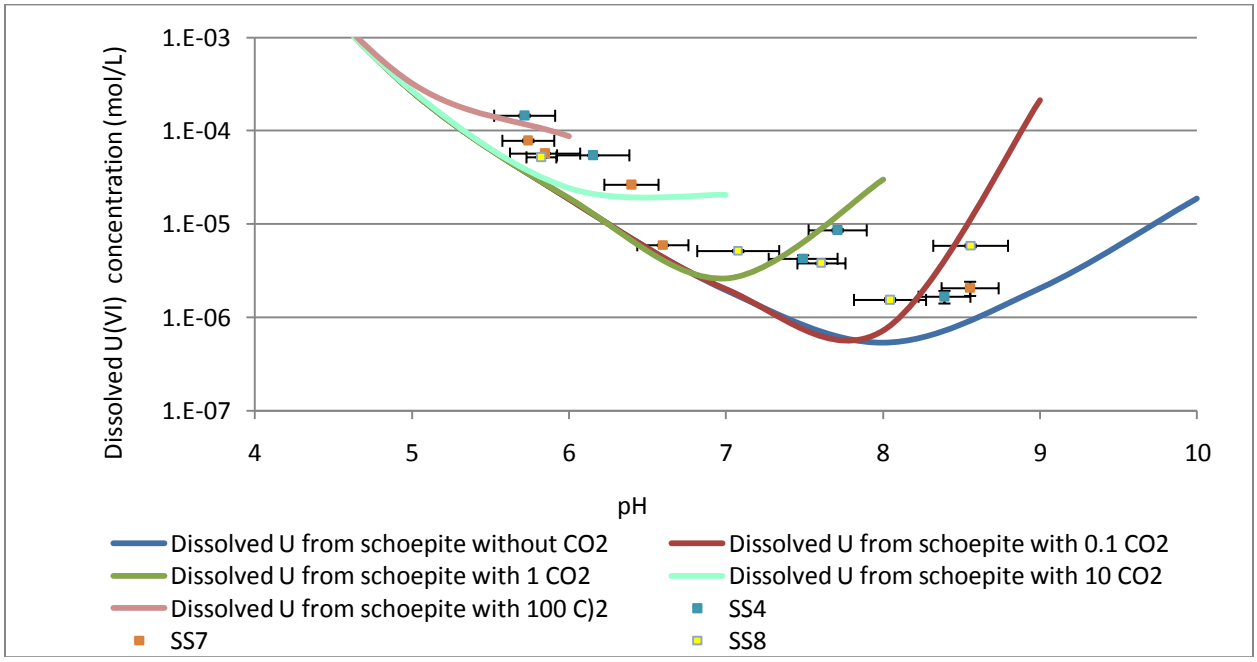

Figure 4-8: Measured points and modeled dissolution curves for U, assuming the presence of schoepite, with different amounts of atmospheric CO_2; numbers like 0.1, 1 etc refer to values that are multiplied by 3.8×10^{-4} to calculate the amount of the CO_2 partial pressure.

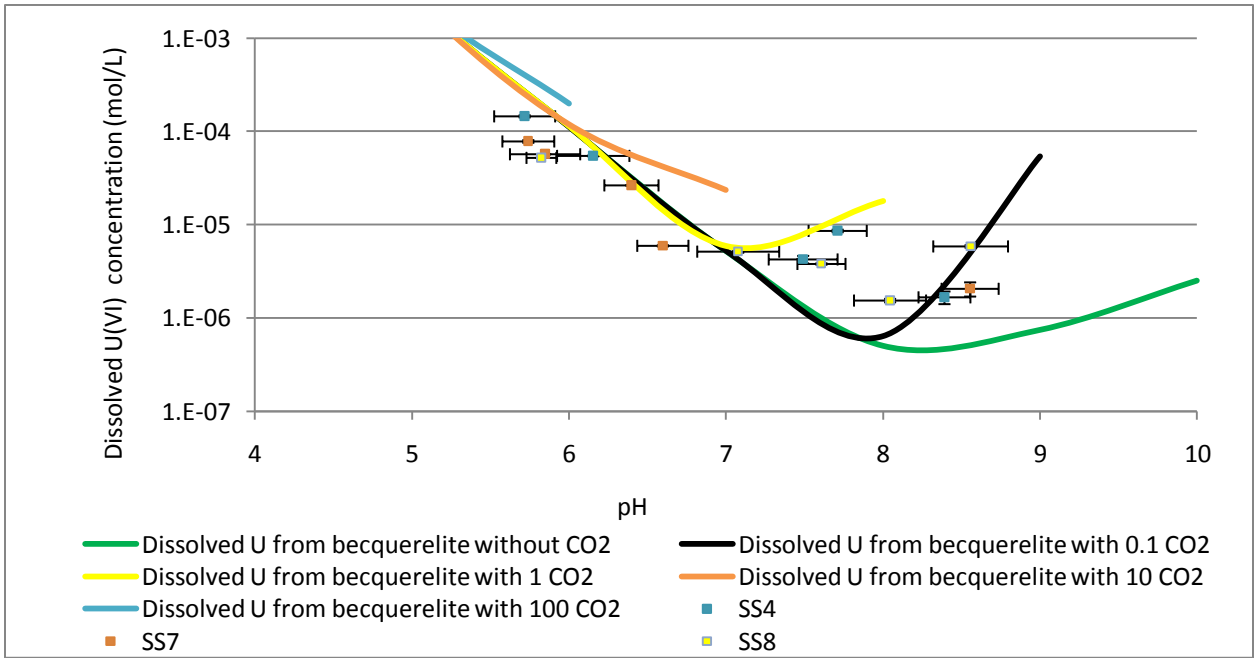

Figure 4-9: Measured points and modeled dissolution curves for U, assuming the presence of becquerelite, with different amounts of atmospheric CO_2; numbers like 0.1, 1 etc refer to values that are multiplied by 3.8×10^{-4} to calculate the amount of the CO_2 partial pressure.

4.4 Potential paths for DU in soils and natural water systems (case study Iraq - Basrah)

The DU ammunition was used in Iraq in the 1991 and 2003 wars throughout the North, Middle, and South of the country. The large amounts of DU ammunition fired from the different platforms (e.g. guns installed on airplanes, helicopters, and tanks) and their low accuracy led to the increase of the DU levels in the local and probably regional environment. One of the major cities that were severely damaged in Iraq is Basrah, which is a strategic governorate (about 550 km south of Baghdad) with a population of almost 2 million; it borders Kuwait and Iran, and has its own shore on the gulf (Fig. 4-10). Due to its location, Basrah was the scene of many battles and therefore was a common target during all major conflicts.

The majority of the battle fields in Basrah during the 1991 war are located at the southern Iraqi-Kuwaiti-Saudi Arabian borders. Famous tank battles using DU ammunition took place in these areas as shown in the targeted locations map. In the 2003 war the DU ammunition was used widely within the highly populated urban areas in and around the center of the main city, where the Shatt-al-Arab River (the confluence of the Tigris and the Euphrates in the town of Al-Qurna) flows into the city. The targets are shown in Fig. 4-10 for both wars.

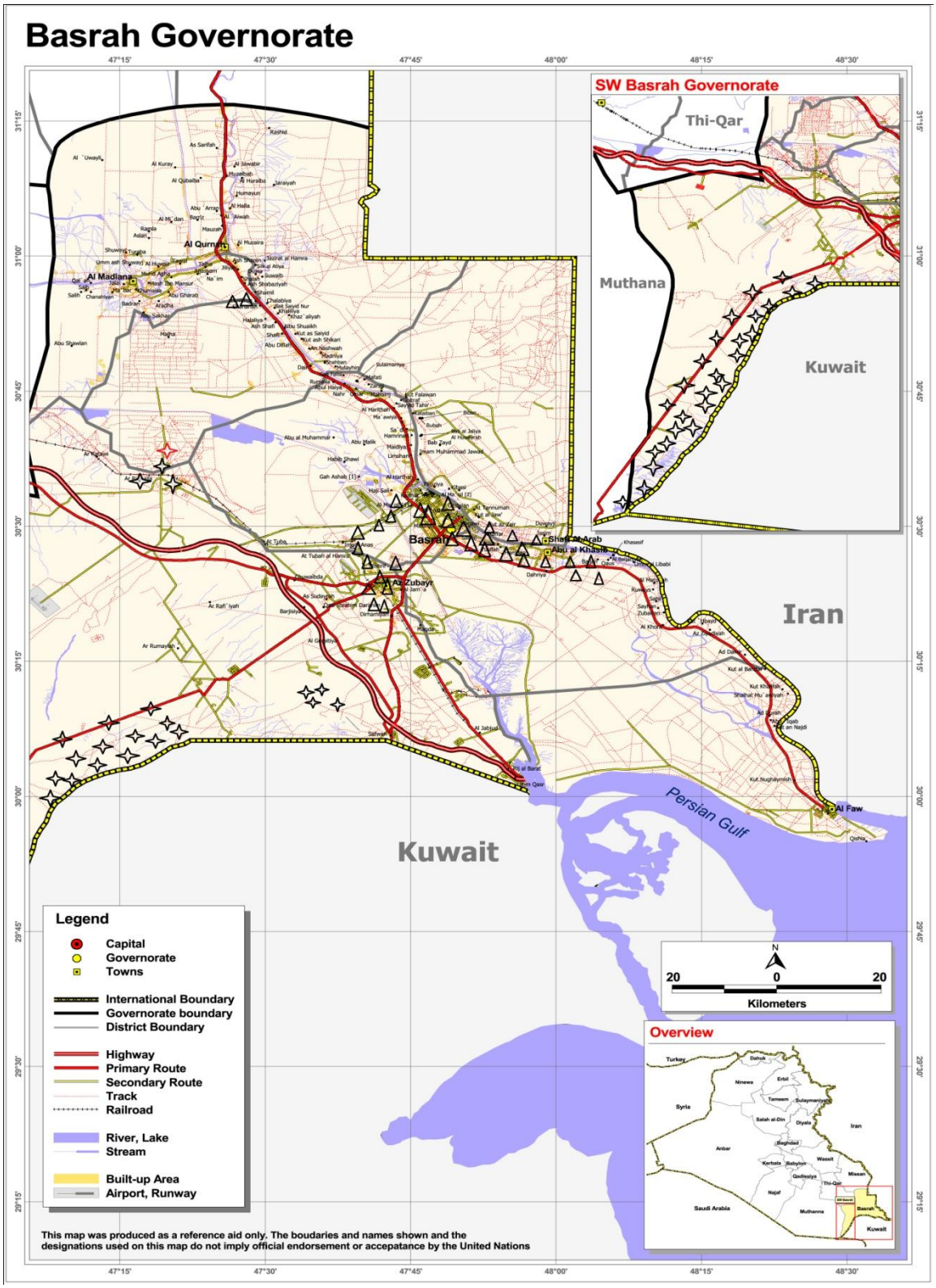

Figure 4-10: Basrah map with the showing the targeted locations with DU ammunition in 1991 war (stars) and 2003 war (triangles).

4.4.1 Scenarios for DU ammunition in Basrah

1- When DU hit their targets

This is when the DU rounds hit their targets (normally hard surfaces) leading to the formation of DU aerosols. These aerosols will be carried by the wind. Determining how long it would take for the aerosols to precipitate or settle down depends mainly on physical parameters like particle size & density, wind speed & direction, and temperature. The precipitation could be either onto soil or surface water, or directly onto the leaves of plants (depending on the type of plant, geometry and surface area of the leaf). To have an idea about the potential pathways for DU aerosols formed after the 1991 and 2003 wars, weather data were used for stations in and around Basrah for the period June 2005 – June 2007.

Wind rose diagrams have been plotted to check the wind speed and direction in that area (Figs. 4-11 to 4-13). According to these diagrams, most of the DU aerosols could have been carried away from the region in a southeasterly direction. According to several works that dealt with the DU aerosols modeling (e.g. Glissmeyer and Mishima, 1979; Mitsakou et., al 2002 and references therein), the aerosols would precipitate very close to the release point(s), and the deposition flux at a couple of kilometers from the release point is more than one order of magnitude lower than the one a few meters near the release point. Those scholars also concluded that the controlling parameters are the atmospheric stability, height of release, and wind speed. At the same time, the aerosol size distribution is less significant.

In addition, there is a possibility for the DU particles to be re-suspended by the wind after precipitating on the ground. The continuation of re-suspension and dragging of the DU particles by the wind would decrease the DU concentrations in the area with time. This is more expected in the open desert area with higher wind velocities.

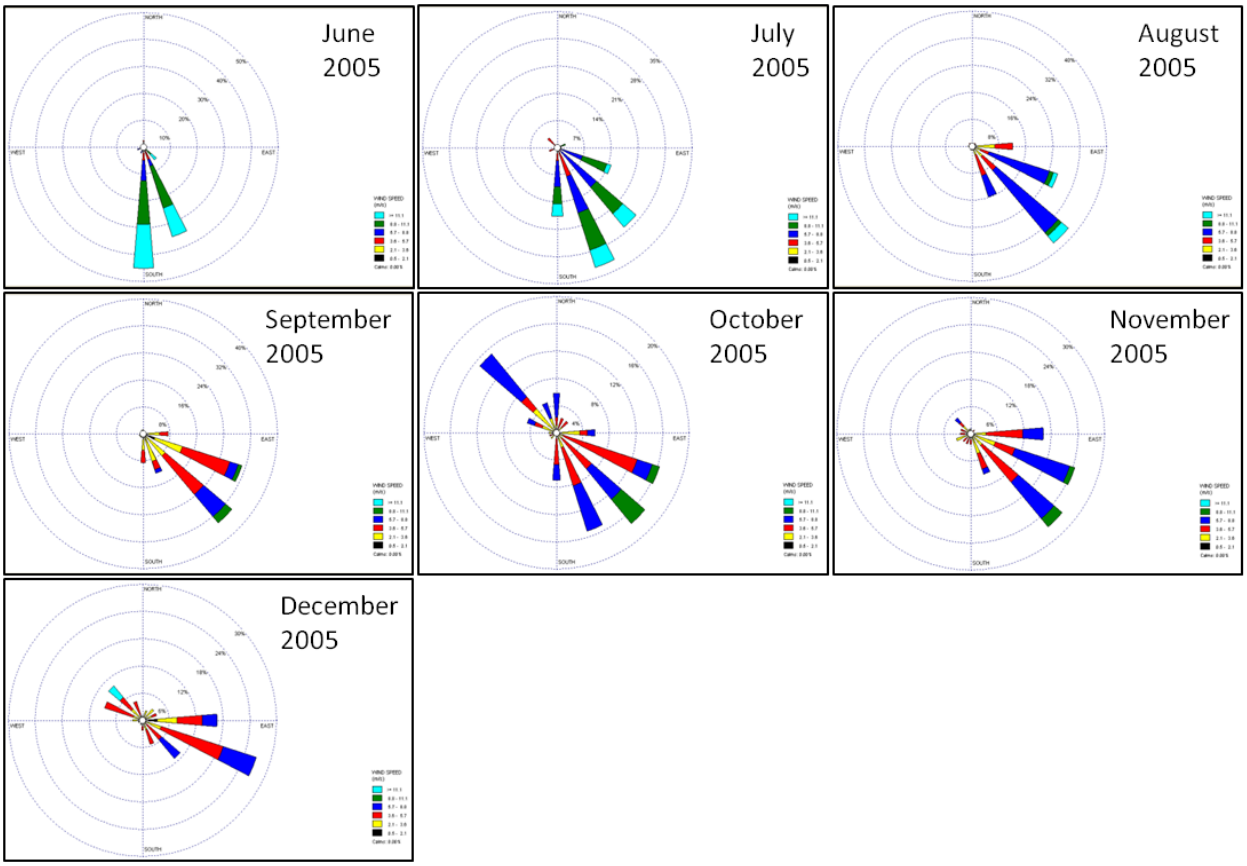

Figure 4-11: Wind rose diagrams for Basrah from June to December 2005.

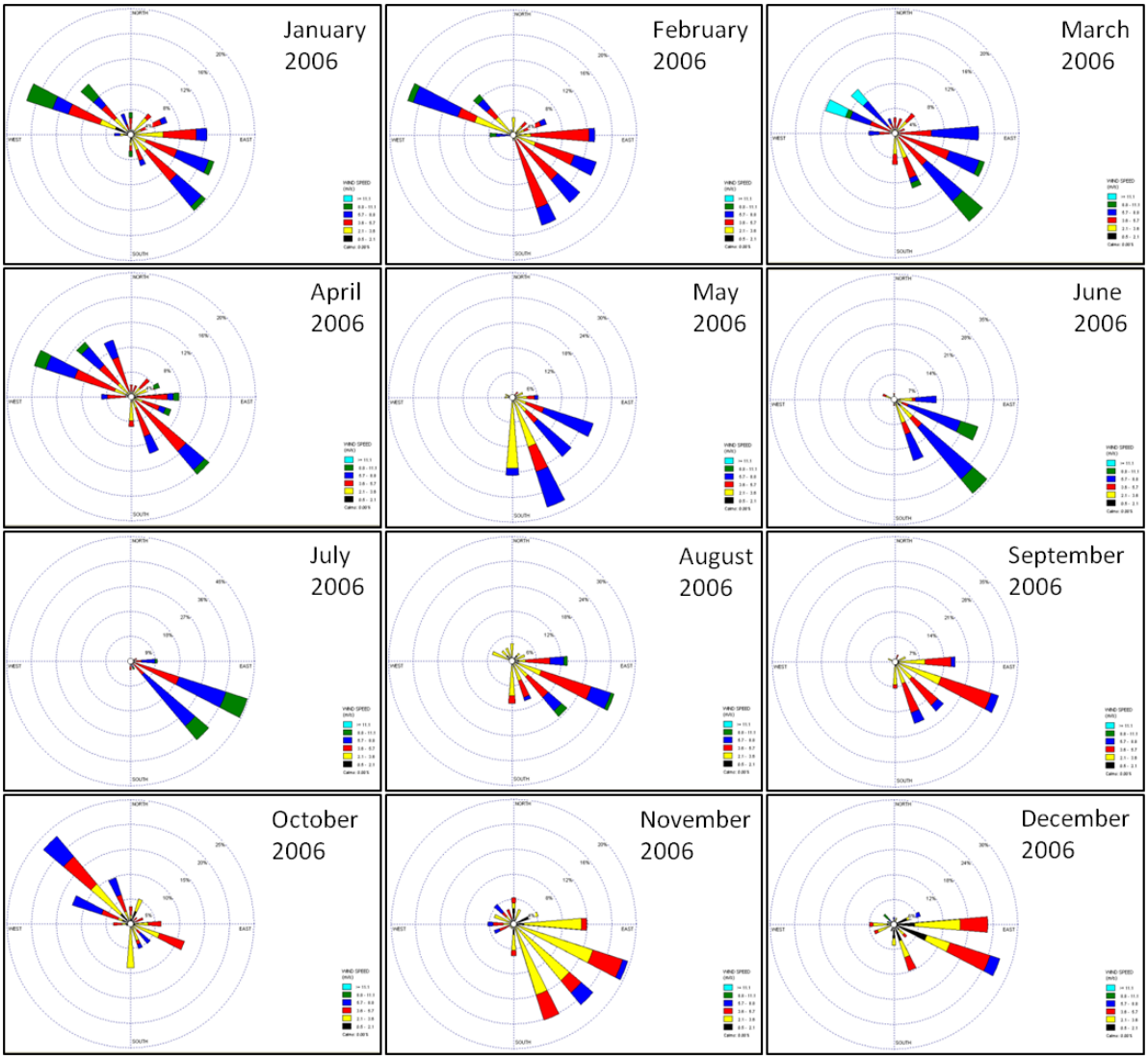

Figure 4-12: Wind rose diagrams for Basrah in 2006.

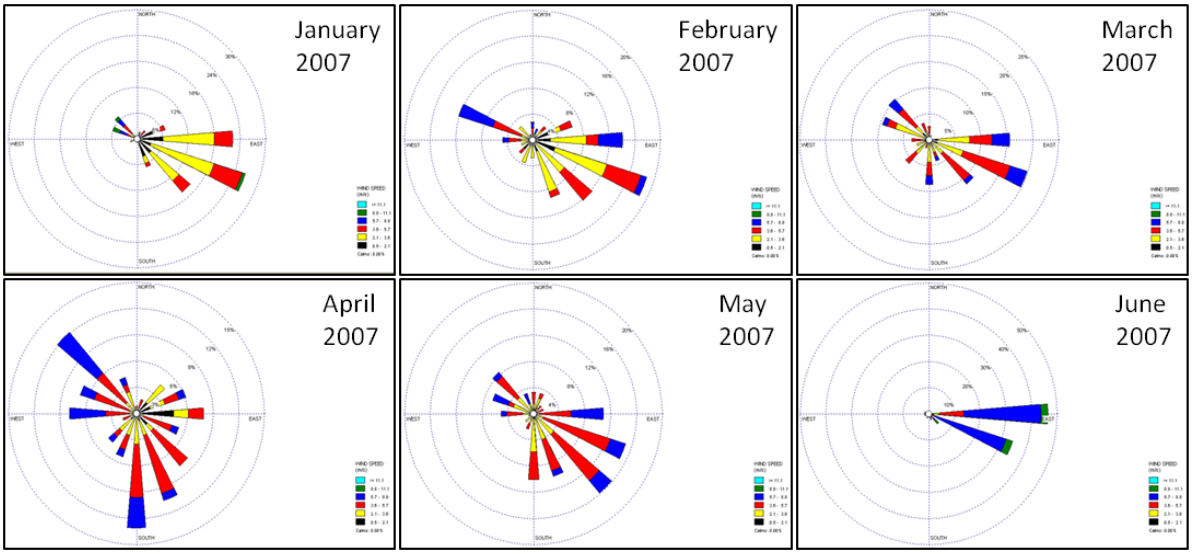

Figure 4-13: Wind rose diagrams for Basrah from January to June 2007.

2- When DU missed their targets

This is when the DU rounds miss their targets and penetrate and rest in the soil. With time, the DU rounds will start to react with their hosting soil and water. The types and rates of such reactions are mainly controlled by the local chemical characteristics for each environment, such as the chemical composition and pH of soil & water, as well as whether it is an oxidized or reduced environment.

In the 1991 war most of the battle fields in Basrah targeted with DU rounds were in the desert. This part of the region in Basrah is characterized by pebbly and sandy desert land (Fig. 4-14). The ground water levels vary from 20 to 100 m in depth (Fig. 4-15), and the dominant ground waters are sulfates and chlorides, with Total Dissolved Solids (TDS) mostly 3-5, 5-10, 1-3 g/l. The main aquifers are the Mio-Pliocene Dibdibba sandstone & Al-Batin fan sand (Buringh, 1960; Jassim and Goff, 2006).

Different locations were targeted in Basrah during the second war in 2003, mainly in and around urban areas. These areas have estuary levee soils along the river and tidal flats on the river banks; In addition, shallow ground waters are available at about 1-2 m deep. These ground waters are mostly chlorides, with TDS values that vary from more than 50 g/l in the areas close to and along the river and hitting 10 g/l in the other areas. The main aquifer in this region is the Mesopotamian plain silt with some Al-Batin fan sand (Buringh, 1960; Jassim and Goff, 2006).

It is expected that the environments in both areas are under oxidized conditions more than reduced due to the shallow depths of penetration of the DU rounds in soil. In the desert region, the role of the ground water is of lesser concern because of its high depths. While in the urban area it can play a bigger role due to its shallow depths. In the presence of atmospheric CO_2, the DU rounds or fragments would undergo a series of corrosion and oxidation reactions. These reactions will eventually lead to the transformation of the DU metal to uranyl mineral oxy-hydroxides (e.g. schoepite /or meta-schoepite) at the beginning of the process, and with time it can react with a divalent cation (e.g. Ca^{2+}, Mg^{2+}, and even Ba^{2+} if available) to form different secondary uranium minerals with a more complicated structure. As the transformation process

proceeds with time, different ligands would form other uranyl minerals (e.g. uranyl silicates, uranyl phosphates, uranyl carbonates). In addition, pH values of the ground water in this area range between 7 and 7.6 (Al-Kubaisi, 1996). Under such pH's the dominant uranium aqueous species would be mainly neutral and negatively charged carbonates like UO_2CO_3 and $UO_2(CO_3)_2^{2-}$. The dissolved uranium in this case is considered to be more mobile and unlikely to be adsorbed on the soil, this is because of the negative charge of the aqueous species and the negative charge of most of the natural surfaces. Therefore, it is likely for the dissolved U to reach the ground water system in the urban areas. The crucial question still to be answered is what are the concentrations of U in these waters?

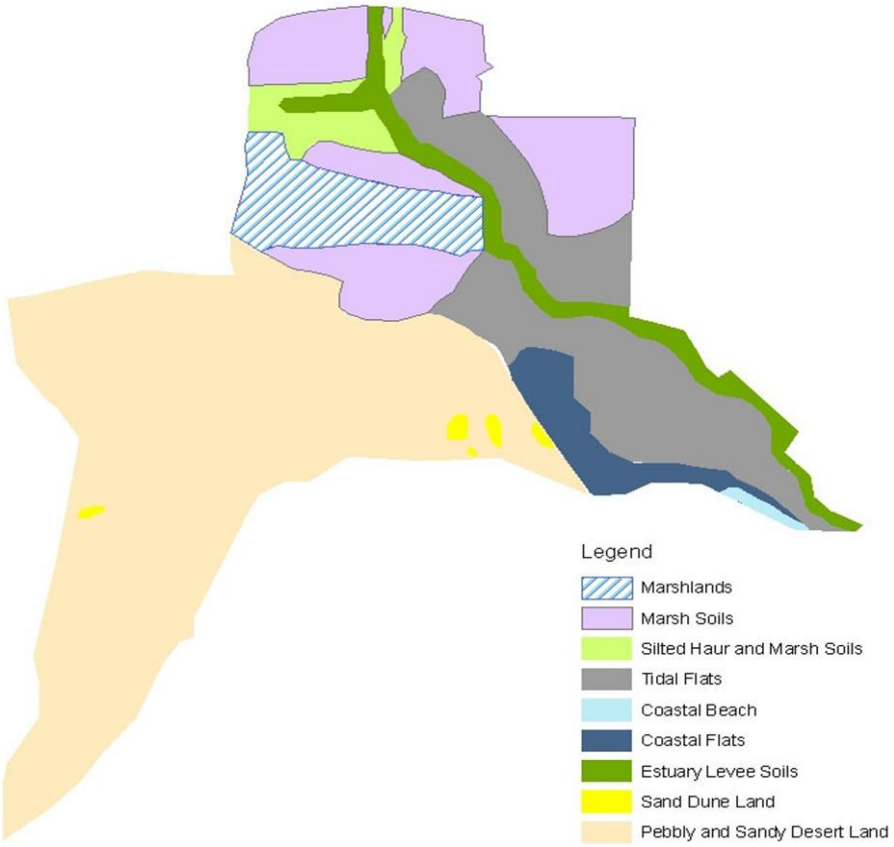

Figure 4-14: Soil map of Basrah (modified after Buringh 1960).

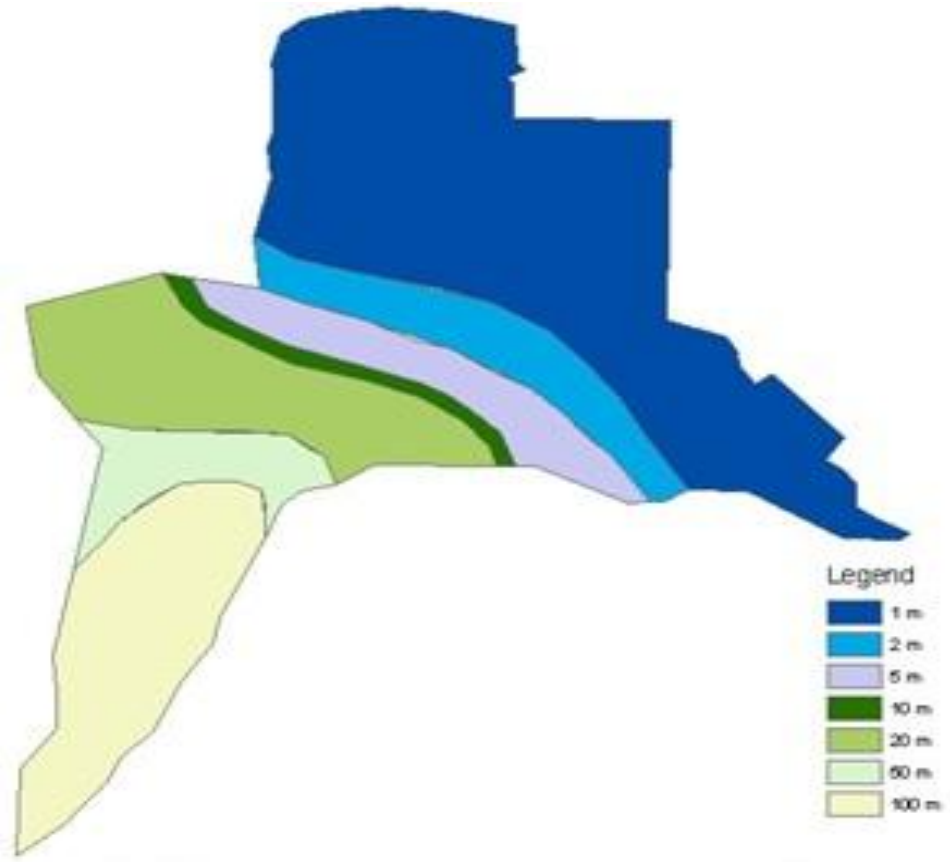

Figure 4-15: Ground water depth for Basrah (modified after Jassim and Goff, 2006).

5 Conclusions

All of the used spectroscopic techniques were valid and efficient in analyzing the corrosion products of DU ammunition. The qualitative and quantitative analyses were able to identify the elemental and molecular composition of the secondary uranium minerals that have been formed due to the corrosion of the DU rounds. 3 uranium minerals have been identified: schoepite $(UO_2)_8O_2(OH)_{12}(H_2O)_{12}$, meta-schoepite $(UO_2)_8O_2(OH)_{12}(H_2O)_{10}$, and becquerelite $Ca(UO_2)_6O_4(OH)_6(H_2O)_8$. The first mineral to be formed after the corrosion and oxidation of the U metal is schoepite. After undergoing dehydration and losing some of its water of crystallization, this mineral transforms after a short time (due to its instability) to a more stable phase, which is meta-schoepite. The presence of Ca in the synthetic rain water used in the previous experiments, plus the used soils (luvisols and cambisols) made it possible for becquerelite to be formed eventually. The finding of U as a metal in some areas in the samples showed that the transformation of U metal into secondary uranium minerals is an ongoing process and that the metal is not yet fully corroded. Due to the chemical and structural similarity between becquerelite and billietite $Ba(UO_2)_6O_4(OH)_6(H_2O)_8$, the Raman spectra for these minerals were almost identical. Yet no Ba was detected in the samples by any means. Also no uranyl phosphate phase(s) was detected disproving a former study concerning the same samples. Through the dissolution of the solid material, Schoepite /or meta-schoepite or becquerelite were identified. The change in pH affected the U solubility in a pattern similar to the modeled data for dissolving schoepite and becquerelite. The U concentrations were at the minimum at pH 8 and 7 in the absence and presence of atmospheric CO_2 respectively. However, it is not possible to distinguish between these minerals from the dissolution curves only due to its similarity. It has been found that schoepite is the uranium solubility controlling phase in the acidic region, while becquerelite is the least soluble uranium phase in the basic region. The U concentrations tend to increase away from these pH points in both acidic and basic directions. Apparently some CO_2 was being able to penetrate the sealed vessels and

that its presence in the solution could have been increased the dissolved uranium concentrations.

6 References

AL-Kubaisi, Q. Y., 1996, Hydrogeology of Dibdiba aquifer in Safwan-Zubair area (south Iraq), Ph.D. dissertation, University of Baghdad, Baghdad, Iraq.

Amme, M., Renker, B., Schmid, B, Feth, M. P., Bertagnolli, H., Döbelin, W., 2002. Raman microscpectrometric identification of corrosion products formed on UO_2 nuclear fuel during leaching experiments, Journal of Nuclear Materials, Vol. 306, Iss. 2-3, pp. 202-212.

Arbuthnot, F., Bertell, R., Bristow, R., Diehl, P., Fahey, D., Van der Keur, H., Robicheau, D., 1999. Depleted uranium: a post-war disaster for environment and health, Laka Foundation.

Bailey, M. R., Beral, V., Clayton, B., Darby, S. C., Goodhead, D. T., Hendry, J. H., Marsh, C., Murray, V., Smith, B., Spratt, B., Stoneham, M., 2002. The health of hazards of depleted uranium munitions Part II, The Royal Society, London.

Berthelin, J. 1988, Microbial weathering processes in natural environments. In: Lerman, A. Meybeck, M. (eds) Physical and chemical weathering in geochemical cycles. Kluwer, Dordrecht, pp. 33-59.

Biwer, B. M., Ebert, W. L., Bates, J. K., 1990. The Raman spectra of several uranyl-containing minerals using a microprobe, Journal of Nuclear Materials, Vol. 175, Iss. 3, pp. 188-193.

Bleise, A., Danesi, P.R., Burkart, W., 2003. Properties, use and health effects of depleted uranium (DU): a general overview, Journal of Environmental Radioactivity, Vol. 64, pp. 93-112.

Bohn, H. L., McNeal, B. L., O'Conner, G. A., 2001, Soil chemistry, Wiley, 3rd edition, 320 p.

Briggs, D., 2003. Surface analysis by Auger and X-ray photoelectron spectroscopy, Manchester, UK: Surface Spectra, 899 p.

Buck, B. J., Brock, A. L., Johnson, W. H., Ulery, A. L., 2004. Corrosion of depleted uranium in an arid environment: Soil-Geomorphology, SEM/EDS, XRD, and electron microprobe analyses, Soil & Sediment Contamination, Vol. 13, pp. 545-561.

Bukalov, S. S., Vdovenko, V. M., Ladygin, I. N., Suglobov, D. N., 1970. Raman spectra of anionic uranium complexes, Journal of Applied Spectroscopy, Vol. 12, Iss. 2, pp. 263-265.

Buringh, P., 1960. Soils and soil conditions in Iraq, Ministry of agriculture, Republic of Iraq. 322 p.

Burns, P. C., Miller, M. L., Ewing, R. C., 1996. U^{6+} Minerals and inorganic phases: A comparison and hierarchy of crystal structures, The Canadian Mineralogist, Vol. 34, pp. 845-880.

Burns, P. C., Ewing, R. C., Hawthorne, F. C., 1997. The crystal chemistry of hexavalent uranium: Polyhedral geometries, bond-valence parameters, and polymerization of polyhedra, The Canadian Mineralogist, Vol. 35, pp. 1551-1570.

Burns, Peter C., 1999. The crystal chemistry of uranium (in Uranium: mineralogy, geochemistry and the environment), Reviews in Mineralogy, Vol. 38, pp. 23-90.

CHPPM. 2000. Health risk assessment consultation No. 26-MF-7555-00D, Depleted uranium – Human exposure assessment and health risk characterization in support of the environmental exposure report “Depleted uranium in the Gulf” of the Office of the Special Assistant to the Secretary of Defence for Gulf War Illnesses, Medical Readiness, and Military Deployments (OSAGWI), OSAGWI Levels I, II, and III Scenarios.

Christ C. L., Clark, J. R., 1960. Crystal chemical studies of some uranyl oxide hydrate, Amer. Mineral., Vol. 45, pp. 1026-1061.

Craft, E. S., Abu-Qare, A. W., Flaherty, M. M., Garofolo, M. C., Rincavage, H. L., Abou-Donia, M. B., 2004. Depleted and natural uranium: Chemistry and toxicological effects, Journal of Toxicology and Environmental Health, Part B, Vol. 7, Iss. 4, pp. 297-317.

Craig, B. D., Lane, R. A., Rose, D. H., 2006. Handbook of corrosion and prevention control: A program management guide for selecting materials, Advanced Materials, Manufacturing, and Testing Information Analysis Center (AMMTIAC), Alion Science & Technology, New York, 2nd edition, 276 p.

Craw, J. S., Vincent, M. A., Hillier, I. H., Wallwork, A. L., 1995. Ab initio quantum chemical calculations on uranyl UO_2^{2+}, plutonyl PO_2^{2+}, and their nitrates and sulfates, Journal of Physical Chemistry, Vol. 99, pp. 10181-10185.

Cullity, B. D., Stock, S. R., 2001, Elements of X-ray diffraction, Prentice Hall, 3rd edition, 664 p.

Das, A., Ferbel, T., 2003. Introduction to nuclear and particle physicse, World Scientific Publishing Company, New Jersey, 2nd edition, 416 p.

Davis, Joseph R., 2000. Corrosion: Understanding the basics, ASM International, 563 p.

Diehl, P., 1999, Depleted uranium: A by-product of the nuclear chain (in Depleted uranium : A post-war disaster for the environment and health), Laka Foundation.

Dinnebier, R. E. (Ed.), Billinge, S. L. (Ed.), 2008. Powder diffraction: Theory and practice, The Royal Society of Chemistry, Cambridge, 1st edition, 604 p.

Echlin, Patrick, 2009. Handbook of sample preparation for scanning electron microscopy and X-ray microanalysis, Springer, New York, 330 p.

Eisenbud, M., Gesell, T., 1997. Environmental radioactivity: From natural, industrial, and military sources, Academic Press, 4th edition, San Diego:, 656 p.

EPA 402-R-06-011, 2006. Depleted Uranium Technical Brief, Environmental Protection Agency, Office of Radiation and Indoor Air, Radiation Protection Division, United States.

Evans, H. T., Jr. 1963. Uranyl ion coordination, Science, Vol. 141, pp. 154-158.

Ferraro, J. R., Nakamoto, K., Brown, C. W., 2003. Introductory Raman spectroscopy, Academic Press, 2nd edition, 434 p.

Finch, R. J., Cooper, M. A., Hawthorne, F. C., Ewing, R. C., 1996. The crystal structure of schoepite, $[(UO_2)_8O_2(OH)]_{12}(H_2O)_{12}$, The Canadian Mineralogist, Vol. 34, pp. 1071-1088.

Finch, R. J., Ewing, R. C., 1992. The corrosion of uraninite under oxidizing conditions, Journal of Nuclear Materials, Vol. 190, pp. 133-156.

Finch, R. J. Hawthorne, F. C., Ewing, R. C., 1998. Structural relations among schoepite, metaschoepite, and “dehydrated schoepite”, The Canadian Mineralogist, Vol. 36, pp. 831-845.

Finch, R., Murakami, T., 1999. Systematic and paragenesis of uranium minerals (in Uranium: mineralogy, geochemistry and the environment), Reviews in Mineralogy, Vol. 38, pp. 91-179.

Frost, R. L., 2004. An infrared and Raman spectroscopic study of the uranyl micas, Spectrochimica Acta Part A: Molecular and Bimolecular Spectroscopy, Vol. 60, Iss. 7, pp. 1469-1480.

Frost, R. L., Weier, M. L., Ayoko, G. A., Martens, W., Cejka, J., 2006. An XRD, SEM, and TG study of uranopilite from Australia, Mineralogical Magazine, Vol. 70, Iss. 3, pp. 301-309.

Frost, R. L., Stefaniak, E. A., Alsecz, A., Mathe, Zoltan, Sajo, Istvan E., Torok, Szabina, Worobiec, Anna, van Grieken, Rene, 2009. The combined application of SEM/EDX and micro-Raman spectroscopy to analyse uranium minerals from a

former uranium mine. Journal of Hazardous Materials, Vol. 168, Iss. 1, pp. 416-423.

Froideval, A., Del Nero, M., Barillon, R., Hommet, J. Mignot, G., 2003. PH dependence of uranyl retention in a quartz/solution system: an XPS study. Journal of Colloid and Interface Science, Vol. 266, Iss. 2, pp. 221–235.

Flewitt, P. E. J., Wild, R. K., 1994, Physical Methods for Materials Characterization, Institute of Physics Publishing, 2nd edition, Bristol, 602 p.

Gardiner, D. J., Bowley, H. J., 1989. Practical Raman spectroscopy, Springer-Verlag, 1st ed. 157 p.

Giammar, D., 2001. Geochemistry of uranium at mineral-water interfaces: Rates of sorption-desorption and dissolution-precipitation reactions, Ph.D. dissertation, California Institute of Technology.

Glissmeyer, J.A., Mishima, J., 1979. Characterization of airborne uranium from test firings of XM774 ammunition. Richland, WA: Pacific Northwest Laboratory; PNL-2944.

Goldstein, J., Newbury, D. E., Joy, D. C., Lyman, C. E., Echlin, P., Lifshin, E., Sawyer, L., Michael, J. R., 2003. Scanning electron microscopy and X-ray microanalysis, Plenum Publishing Corp., 3rd edition, 586 p.

Harley, N. H., Foulkes, E. C., Hilborne, L. H., Hudson, A., Anthony, C. R., 1999. A review of the scientific literature as it pertains to Gulf war illnesses, Vol. 7, Depleted Uranium. RAND, Corporation National Defense Research Institute, Washington, USA.

Hoekstra, H. R., Siegel, S., 1973. The uranium trioxide-water system, Journal of Inorganic and Nuclear Chemistry, Vol. 35, No. 3, pp. 761-779.

IAEA Fact sheet: Features: Depleted Uranium, International Atomic Energy Agency: http://www.iaea.org/newscenter/features/du/du_qaa.shtml.

Jassim, S. Z., Goff, J. C., 2006. Geology of Iraq, DOLIN, 341 p.

Karberg, N. J., Pregitzer, K. S., King, J. S., Friend, A. L., Wood, J. R., 2005, Soil carbon dioxide partial pressure and dissolved inorganic carbonate chemistry under elevated carbon dioxide and ozone, Oecologia, Vol. 142, pp 296-306.

Langmuir, D., 1978. Uranium solution-mineral equilibria at low temperatures with applications to sedimentary ore deposits, Geochim. Cosmochim. Acta, Vol. 42, pp. 547-569.

L'Annunziata, M. F., 2007. Radioactivity: Introduction and history, Amsterdam: Elsevier, 1st edition, 632 p.

Lillard, J.A., and Hanrahan, R.J., 2005. Corrosion of uranium and uranium alloys (in ASM Handbook, Volume 13B: Corrosion: Materials, ASM International, pp. 370-384.

Manning, T. J., Grow, W. R, 1997. Inductively Coupled Plasma – Atomic Emission Spectrometry, The Chemical Educator, Springer – Verlag New York, INC, Vol. 2, No. 1, pp. 1-19.

Maya, L., Begun, G. M.. 1981. A Raman spectroscopy study of hydroxo and carbonato species of the uranyl (VI) ion, Journal of Inorganic and Nuclear Chemistry, Vol. 43, No. 11, pp. 2827-2832.

Mccafferty, E., 2010. Introduction to corrosion science, Springer, New York, 1st edition, 302 p.

McCreery, R. L., 2000. Raman spectroscopy for chemical analysis, Wiley, New York, 1st edition, 452 p.

Miller, A. C., 2006. Depleted uranium: Properties, uses, and health consequences, CRC Press, Boca Raton, 1st edition, 288 p.

Mitsakou, C., Eleftheriadis, K., Housiadas, C., Lazaridis, M., 2002. Modeling of the dispersion of depleted uranium aerosols, Health Physics, Vol. 84, No. 4, pp. 583-344.

Morris, D. E., Allen, P. G., Berg, J. M., Chisholm-Brause, C. J., Conradson, S. D., Donohoe, R. J., Hess, N. J., Musgrave, J. A., Drew Tait C., 1996. Speciation of uranium in Fernals soils by molecular spectroscopic methods: Characterization of untreated soils, Environ. Sci. Technol., Vol. 30, pp. 2322-2331.

Nefedov, V. I., 1988. X-ray photoelectron spectroscopy of solid surfaces, VSP Books, Utrecht, 1st edition, 200 p.

Neikov, O. D., Naboychenko, S. S., Murashova, I. V., Gopienko, V. G., Frishberg, I. V., Lotsko, D. V., 2009. Handbook of non-ferrous metal powders: Technologies and applications, Elsevier, Amsterdam 1st edition, 634p.

Pelletier, Michael J., 1999. Analytical applications of Raman spectroscopy, Oxford, Blackwell, 1st Edition, 478 p.

Potts, P. J., 1987. A handbook of silicate rock analysis, Blackie, 622 p.

Quiles, F., Burneau, A., 2000. Infrared and Raman spectra of uranyl(VI) oxo-hydroxo complexes in acid aqueous solutions: a chemometric study, Vibrational Spectroscopy, Vol. 23, Iss. 2, pp. 231-241.

Rai, D., Felmy, A. R., Hess, N. J., LeGore, V. L., McCready, D. E., 2002, Thermodynamics of the U(VI)-Ca^{2+}-$Cl^{-}$$OH^{-}$$H_2O$ system: Solubility product of becquerelite, Radiochim. Acta., Vol. 90, pp. 495-503.

Reed, S. J. B.,1997. Electron microprobe analysis, Cambridge, Cambridge Univ. Press, 2nd edition, 350 p.

Reed, S. J., 2005. Electron microprobe analysis and scanning electron microscopy in geology, Cambridge: Cambridge Univ. Press, 2005, 2nd edition, 189 p.

Reimer, L., 1998. Scanning electron microscopy: physics of image formation and microanalysis, Springer series in optical sciences Vol. 45, Berlin, Springer,. 2nd edition, 527 p.

Sajih, M., Livens, F. R., Alvarez, R., Morgan, M., 2010. Physicochemical characterization of depleted uranium (DU) particles at a UK firing test range, Science of the Totoal Environement, Vol. 408, Iss. 23, pp. 5990-5996.

Schimmack, W., Gerstmann, U., Oeh, U., Schultz W., Schramel, P., 2005. Leaching of depleted uranium in soil as determined by column experiments. Radiat Environ Biophys, Vol. 44, pp. 183-191.

Schimmack, W., Gerstmann, U., Schultz, W., Geipel, G., 2007. Long-term corrosion and leaching of depleted uranium (DU) in soil. Radiat Environ Biophys, Vol. 46, pp. 221-227.

Schindler, M., Hawthorne, F. C., Freund, M. S., Burns, P. C., 2009a. XPS spectra of uranyl minerals and synthetic uranyl compounds. I: The U 4f spectrum, Geochimica et Cosmochimica Acta, Vol. 73, Iss. 9, pp. 2471-2487.

Schindler, M., Hawthorne, F. C., Freund, M. S., Burns, P. C., 2009b. . XPS spectra of uranyl minerals and synthetic uranyl compounds. II: The O 1s spectrum, Geochimica et Cosmochimica Acta, Vol. 73, Iss. 9, pp. 2488-2509.

Skoog, D. A., Holler, F. J., Nieman, T. A., 1998. Principles of instrumental analysis, Boston, MA., Thomson Learning, 5th edition, 960 p.

Stevens, W., Bruenger, F. W., Atherton, D. R., Smith, J. M., Taylor, G. N., 1980. The distribution and retention of hexavalent 233 U in the beagle. Radiation Research, Vol. 83, Iss. 1, 109-126.

Suryanarayana, C., Norton, M. G., 1998. X-ray diffraction: A practical approach, Springer, 292 p.

Taylor, J. C., 1971. The structure of the a-form of uranyl hydroxide. Acta Crystallographica, Section B, Vol. 27, pp. 1088–1091.

The U.S. office of the Secretary of Defense, 2000. Depleted uranium in the Gulf war II, Environmental exposure report.

Toth, L. M., Begun, G. M., 1980. Raman spectra of uranyl ion and its hydrolysis products in aqueous HNO_3, Journal of Physical Chemistry, Vol. 85, pp. 547-549.

Tsushima, S., Nagasaki, S., Tanaka, S., Suzuki, A., 1998. A Raman Spectroscopic Study of Uranyl Species Adsorbed onto Colloidal Particles, Journal of Physical Chemistry, Section B, Vol. 102, pp. 9029-9032.

UNEP, 2007. Technical report on Capacity-building for the assessment of depleted uranium in Iraq, Technical report, United Nations Environment Programme, Geneva.

U.S. Department of Transportation, 1984. Federal Aviation Administration, Advisory Circular.

USNRC, 2011. Background information on depleted uranium, United States Nuclear Regulatory Commission: http://www.nrc.gov/about-nrc/regulatory/rulemaking/potential-rulemaking/uw-streams/bg-info-du.html.

U.S. Office of the Secretary of Defense, 2000, Environmental exposure report: Depleted uranium in the gulf (II).

Verma, H. R., 2007. Atomic and nuclear analytical methods: XRF, Mössbauer, XPS, NAA and ion-beam spectroscopic techniques, Springer, 376 p.

Vochten, R., Van Haverbeke, L., 1990. Transformation of schoepite into the uranyl oxide hydrates: becquerelite, billietite, and wölsendorfite, Mineralogy and Petrology, Vol. 43, pp. 65-72.

Warren, B. E., 1990. X-ray diffraction, New York, Dover Publications, 381p.

Weller, M. T., Light, M. E., Gelbrich, T., 2000. Structure of uranium (VI) oxide dihydrate, UO3.2H2O; synthetic meta-schoepite (UO2)4O(OH)6.5H2O, Acta Crystallographica, Section B, Vol. 56, pp. 577–583.

WHO, 2003. Fact sheet N° 257, World Health Organization: http://www.who.int/mediacentre/factsheets/fs257/en/

Winge, R. K., Fassel, V. A., Peterson, V. J., Floyd, M. A.. 1989. Inductively coupled plasma-atomic emission spectroscopy: An atlas of spectral information, Elsevier, 584 p.

Wronkiewicz, D., Bates, J., Wolf, S., Buck, E., 1996. Ten-year results from unsaturated drip tests with UO_2 at 90°C: implications for the corrosion of spent nuclear fuel, Journal of Nuclear Materials, Vol. 238, Iss. 1, pp. 78-95.

Appendix A: Raman spectroscopy results, the measurements' symbols e.g. (4A-1) refer to sample 4, grain A as shown in figures 2-3 till 2-5, and the last number represent the number of measurement.

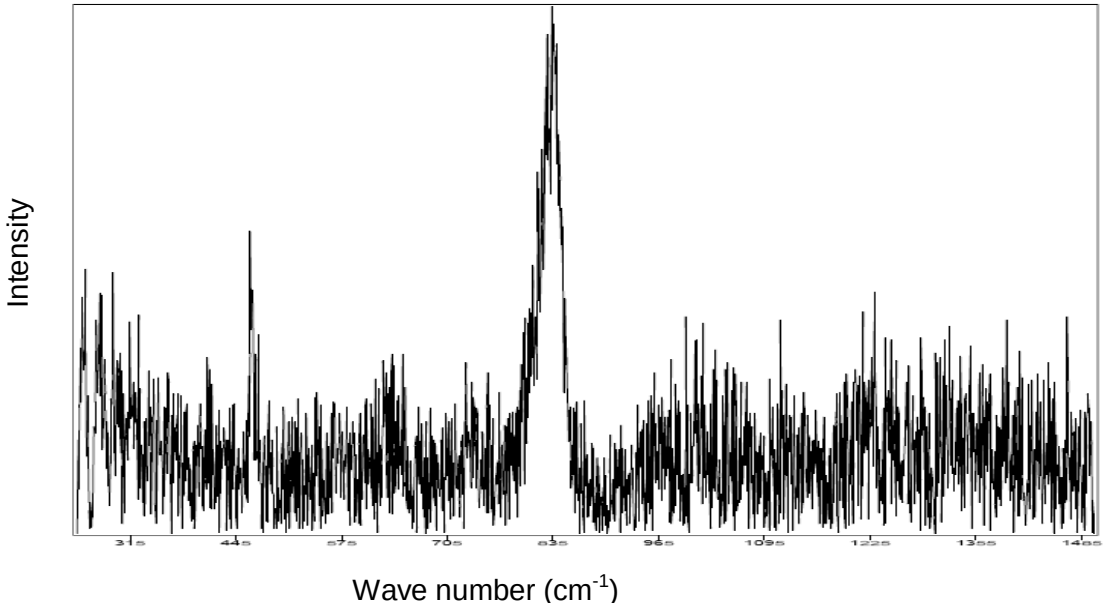

Figure A-1: Raman spectrum of sample (4A-1).

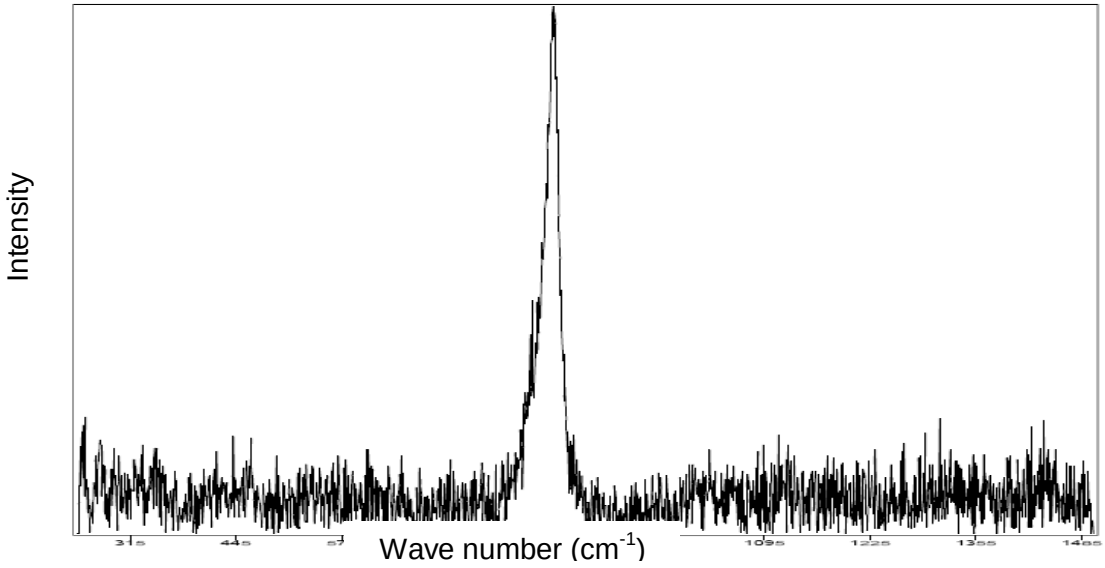

Figure A-2: Raman spectrum of sample (4A-2).

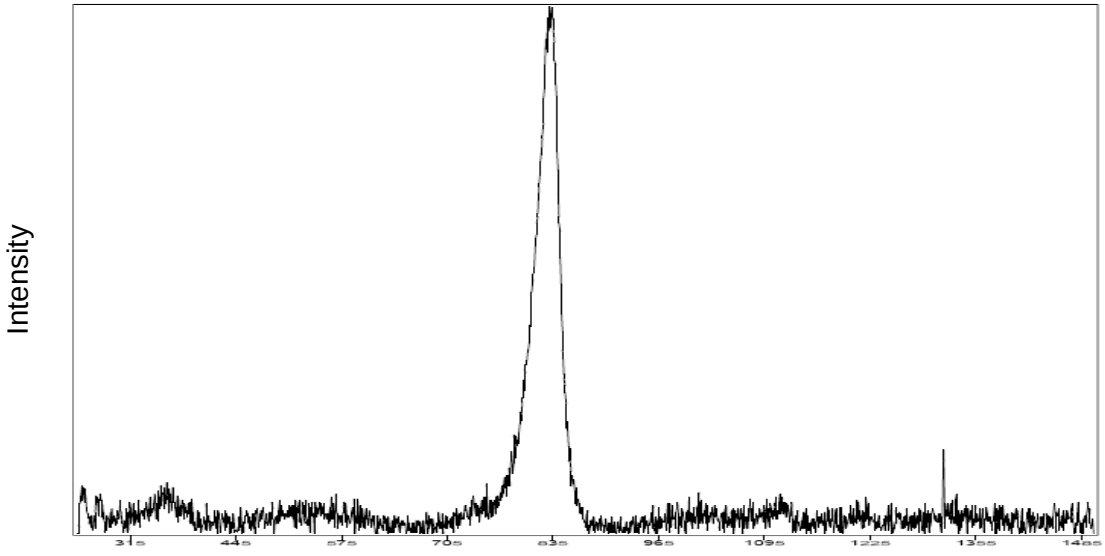

Figure A-3: Raman spectrum of sample (4A-3).

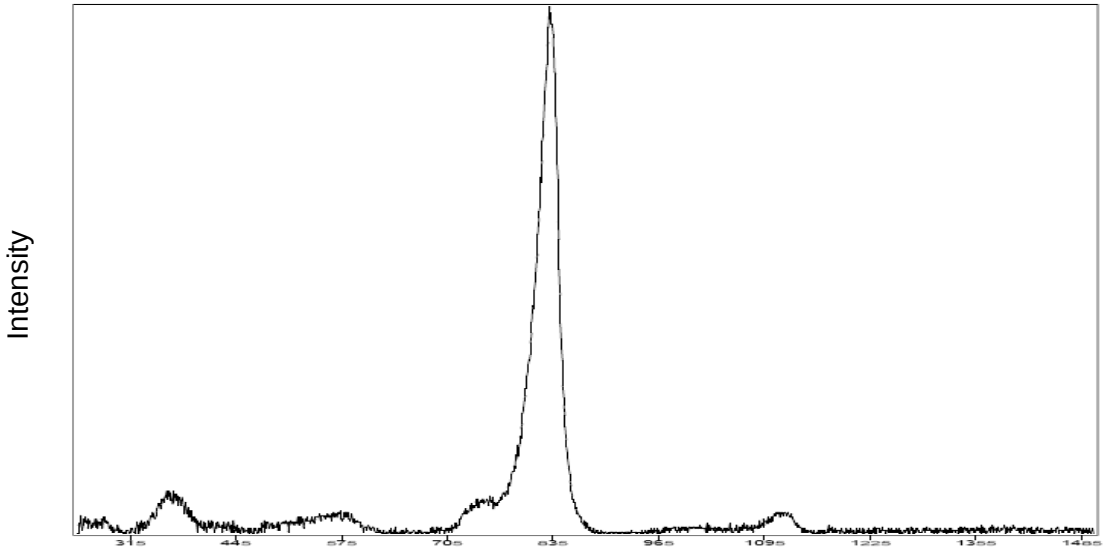

Figure A-4: Raman spectrum of sample (4A-4).

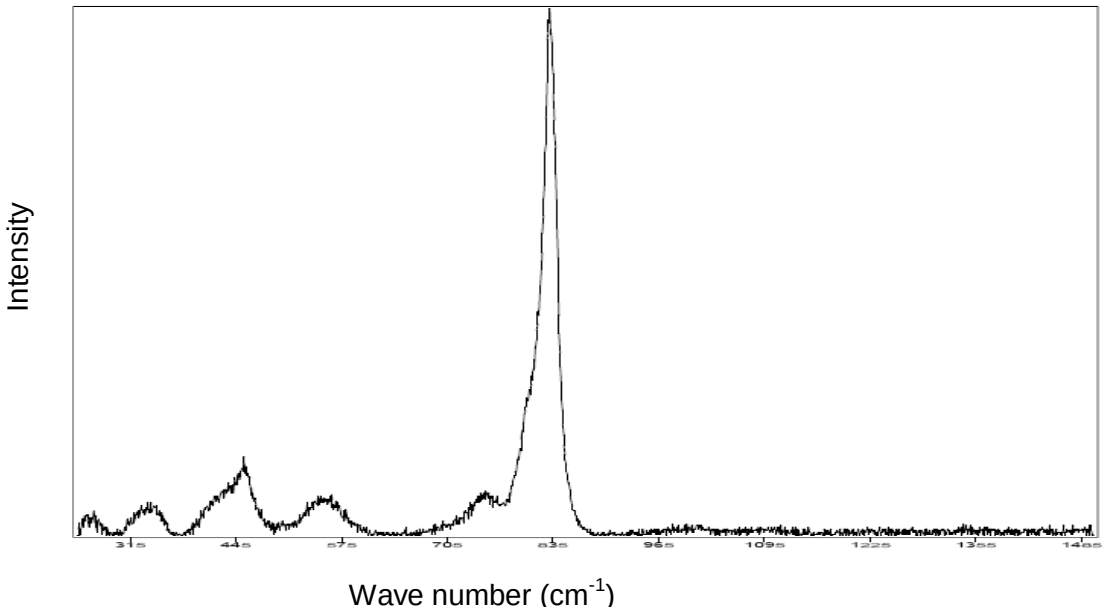

Figure A-5: Raman spectrum of sample (4A-5).

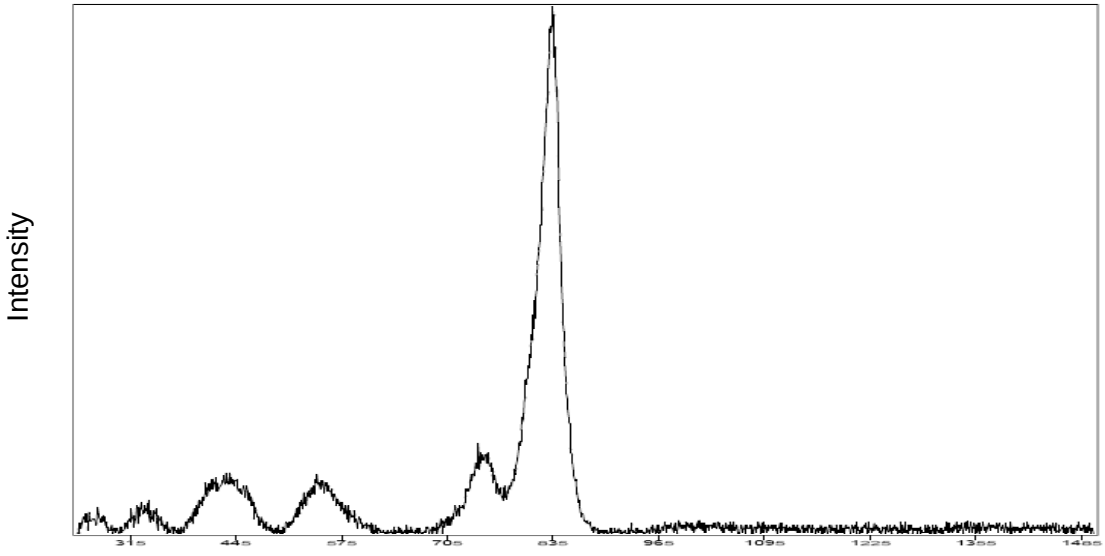

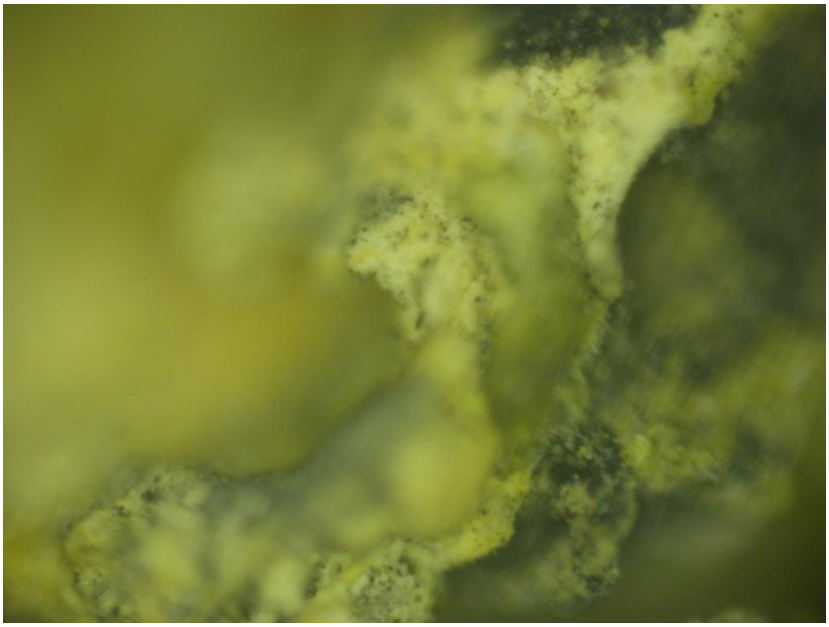

Figure A-6: Raman spectrum of sample (4A-6) above, and its image below.

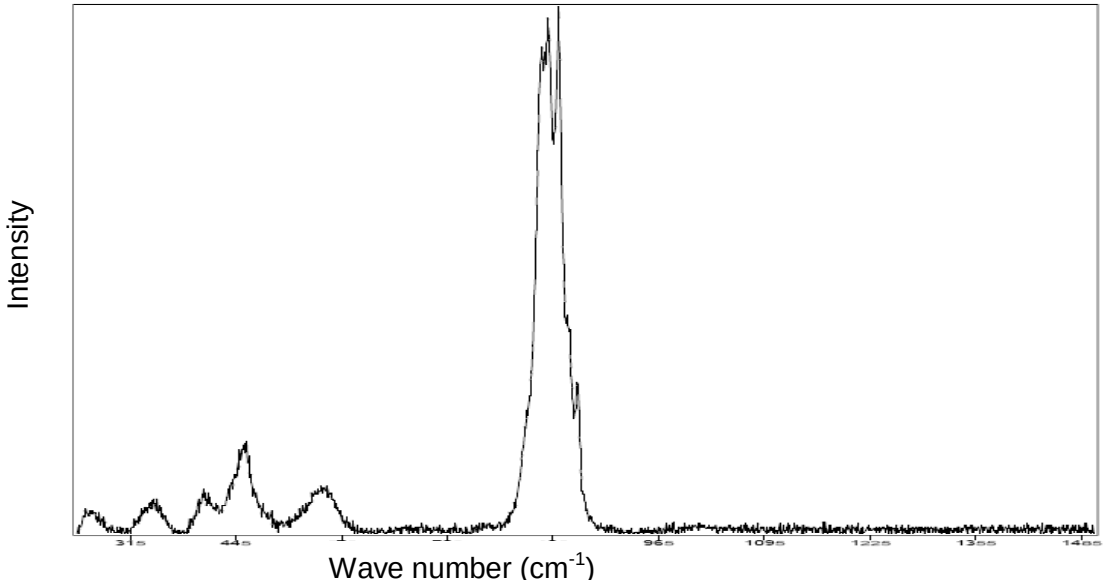

Figure A-7: Raman spectrum of sample (4A-7).

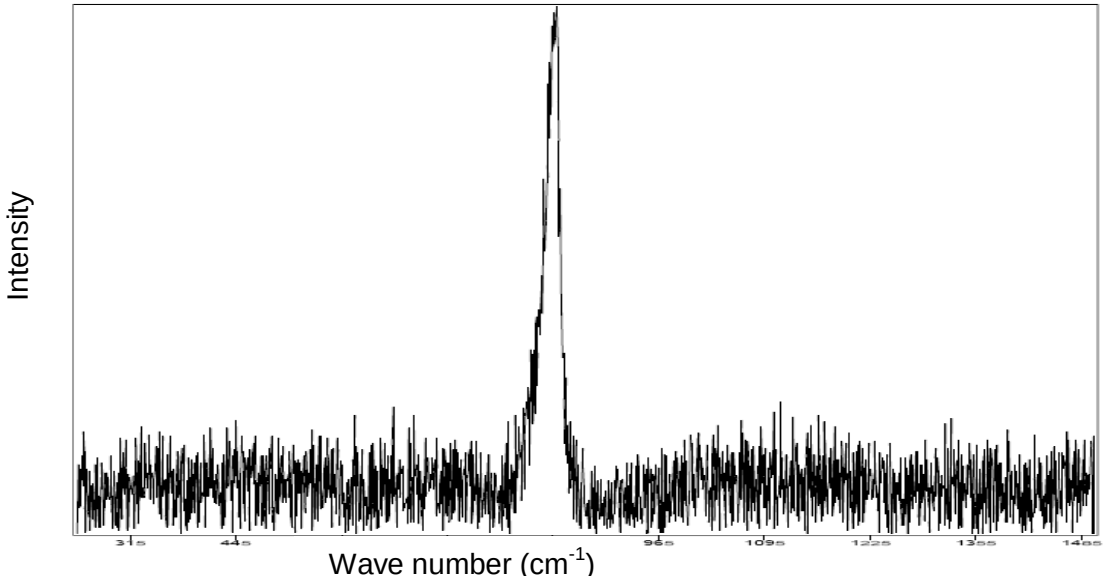

Figure A-8: Raman spectrum of sample (4B-1).

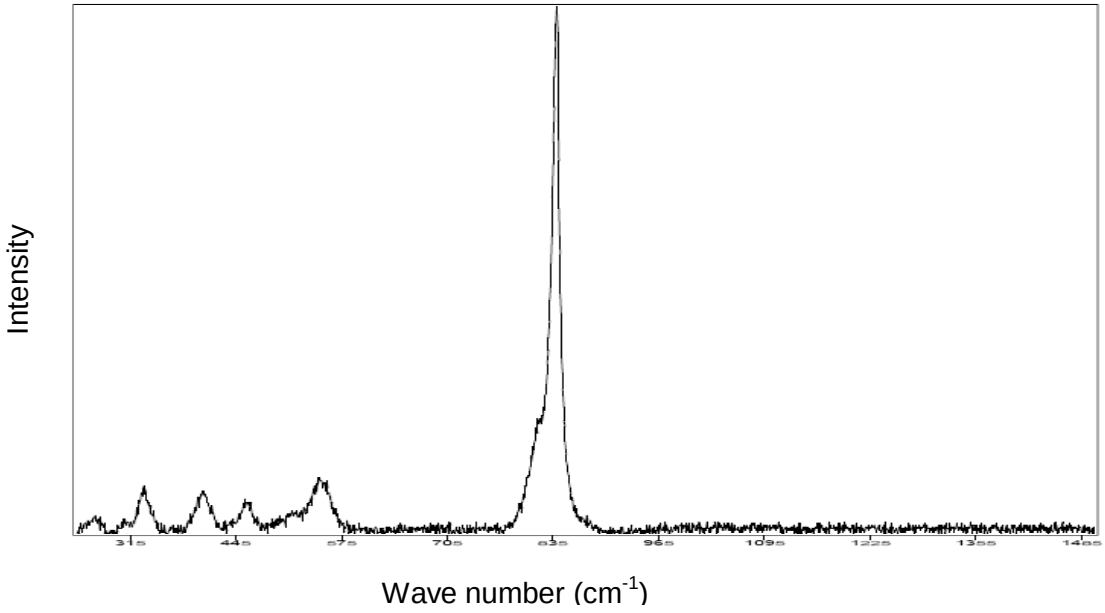

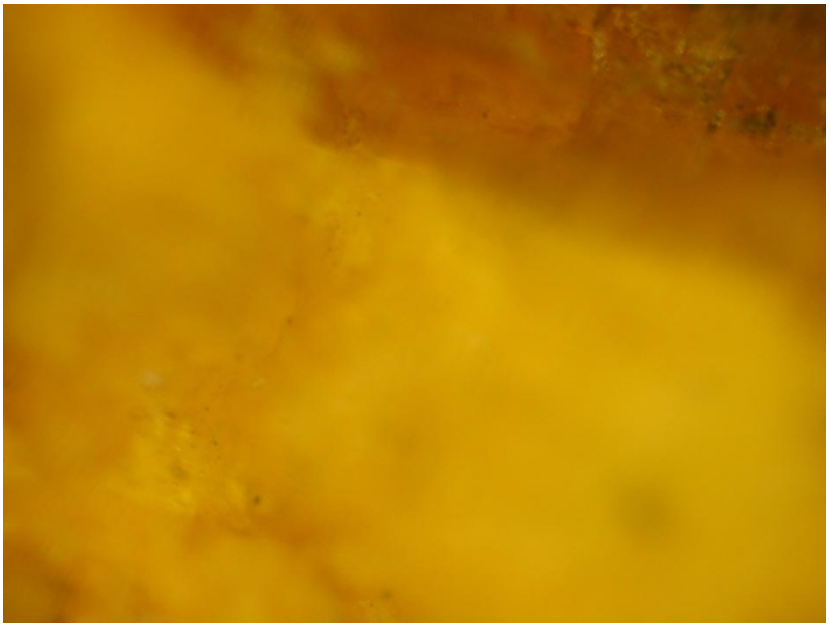

Figure A-9: Raman spectrum of sample (4B-2) above, and its image below.

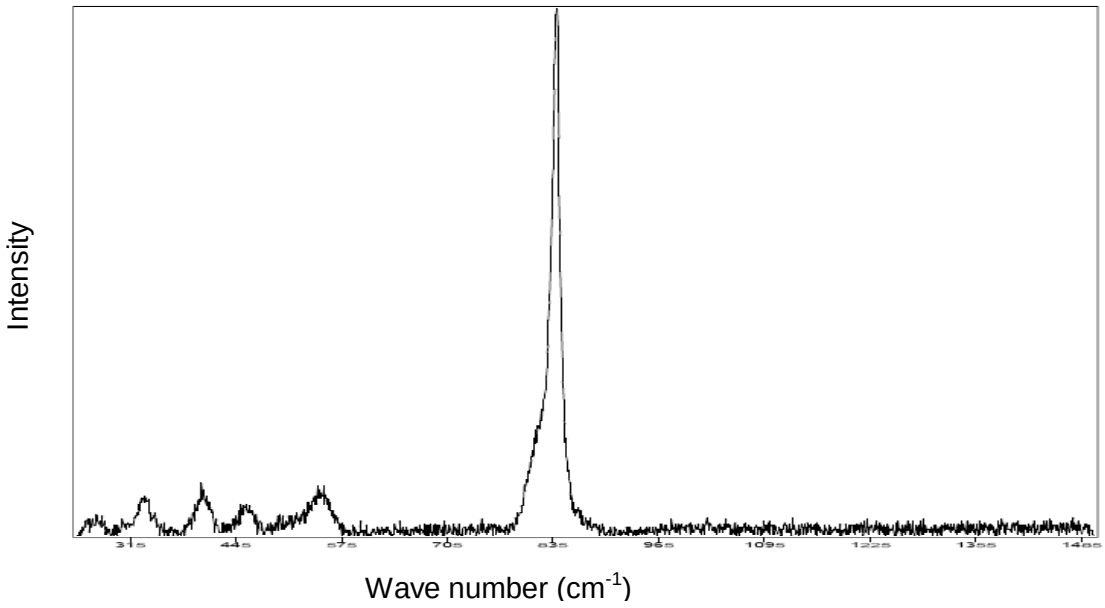

Figure A-10: Raman spectrum of sample (4B-3).

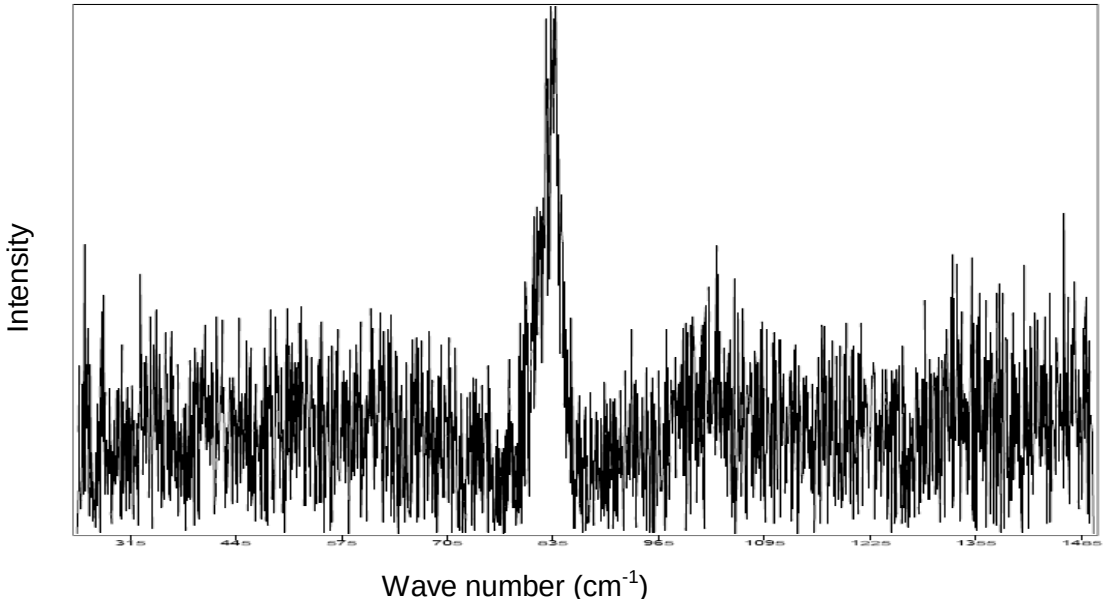

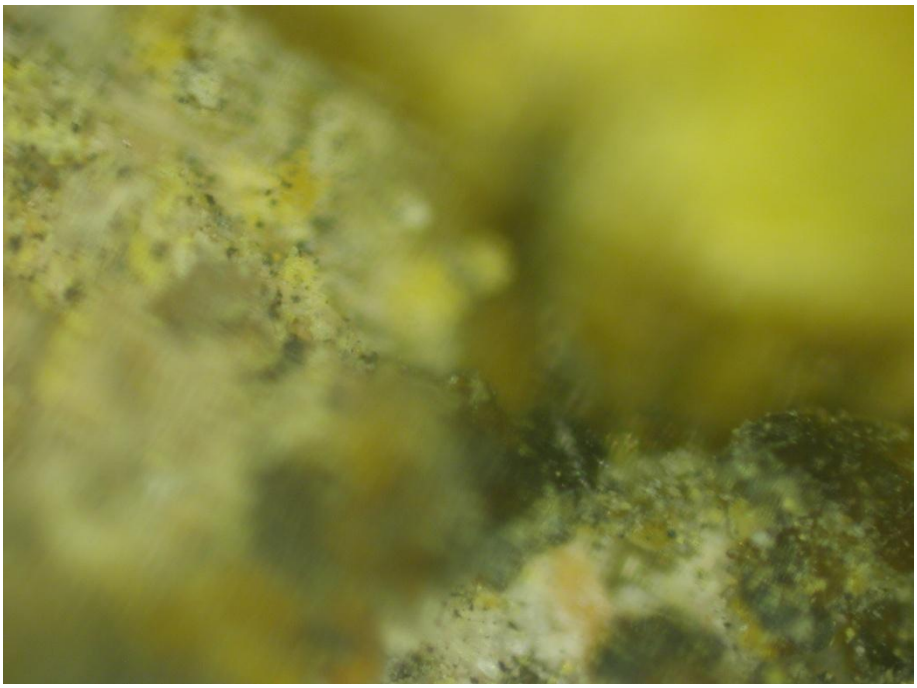

Figure A-11: Raman spectrum of sample (4B-4) above, and its image below.

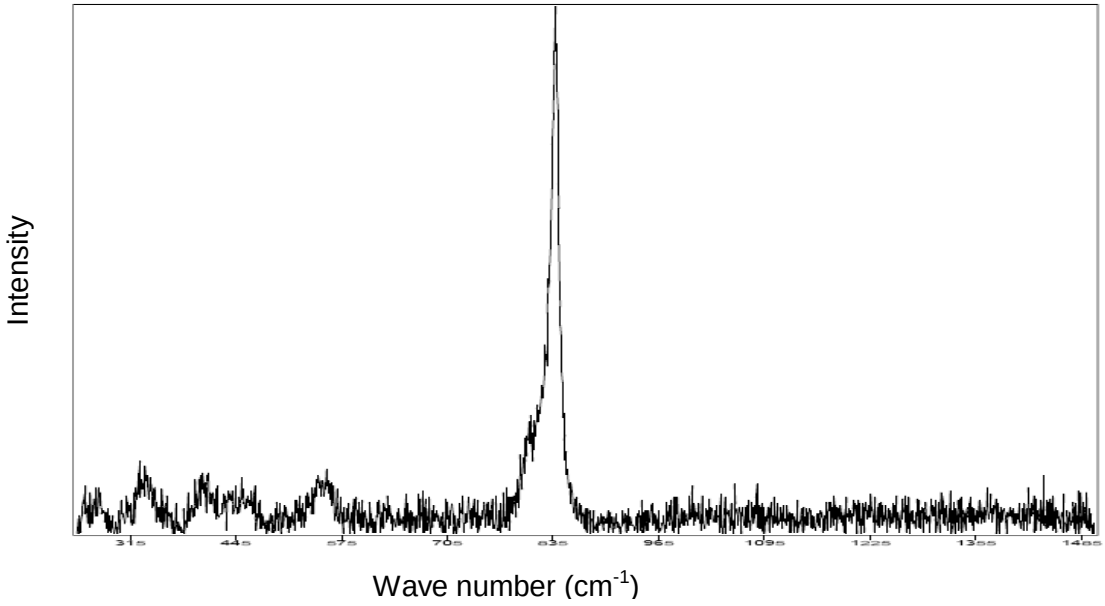

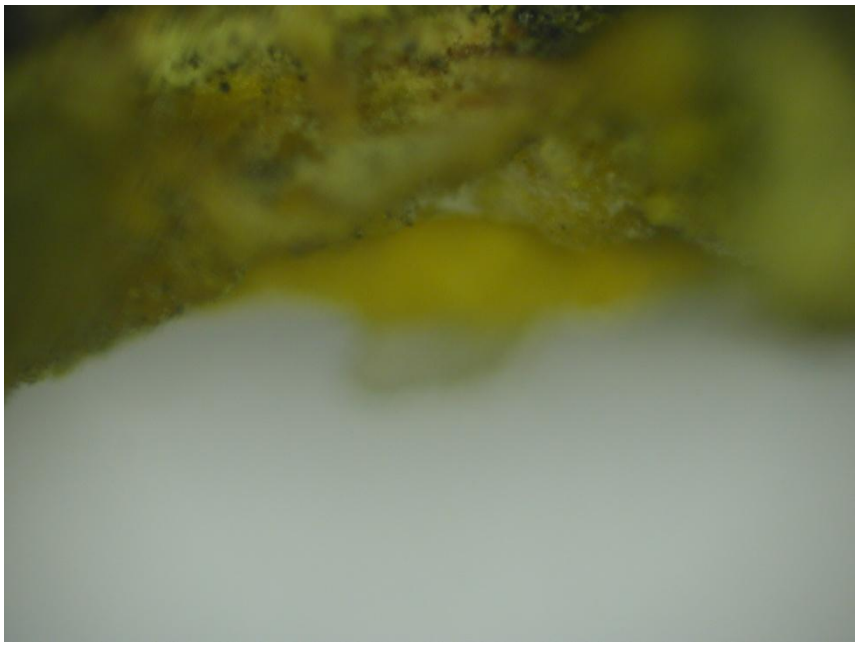

Figure A-12: Raman spectrum of sample (4B-5) above, and its image below.

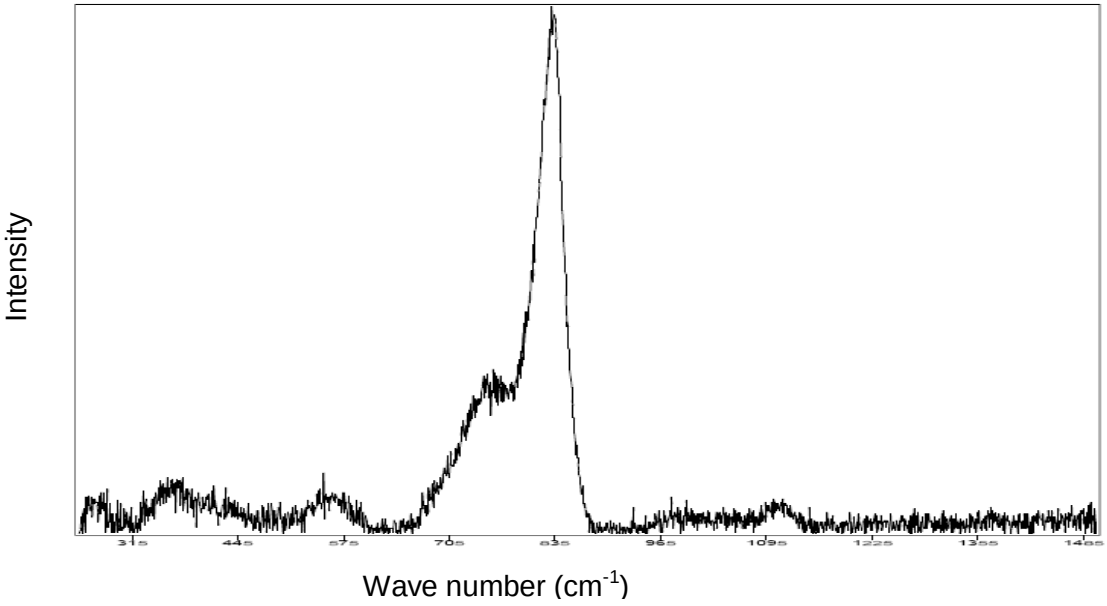

Figure A-13: Raman spectrum of sample (4C-1).

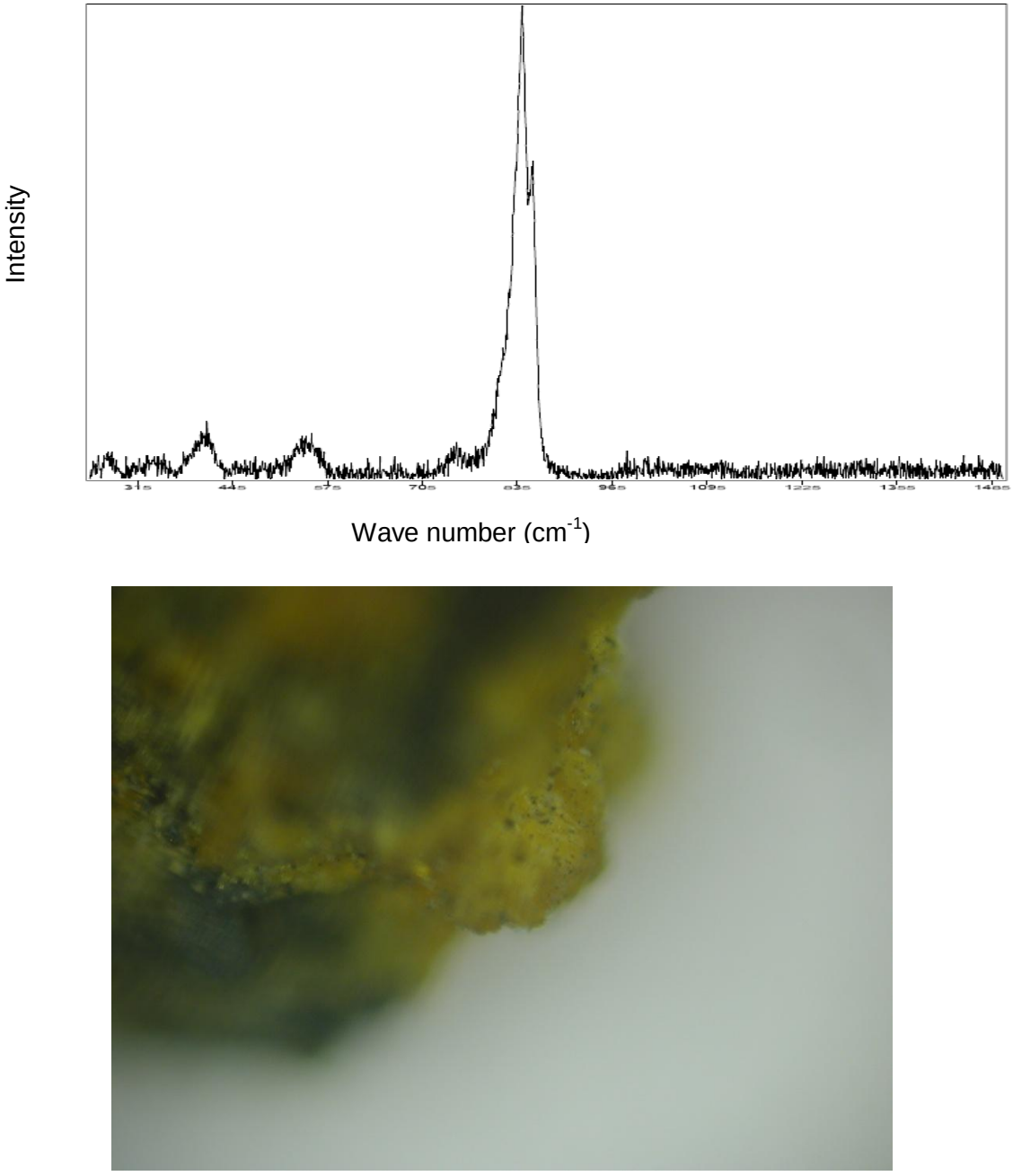

Figure A-14: Raman spectrum of sample (4C-2) above, and its image below.

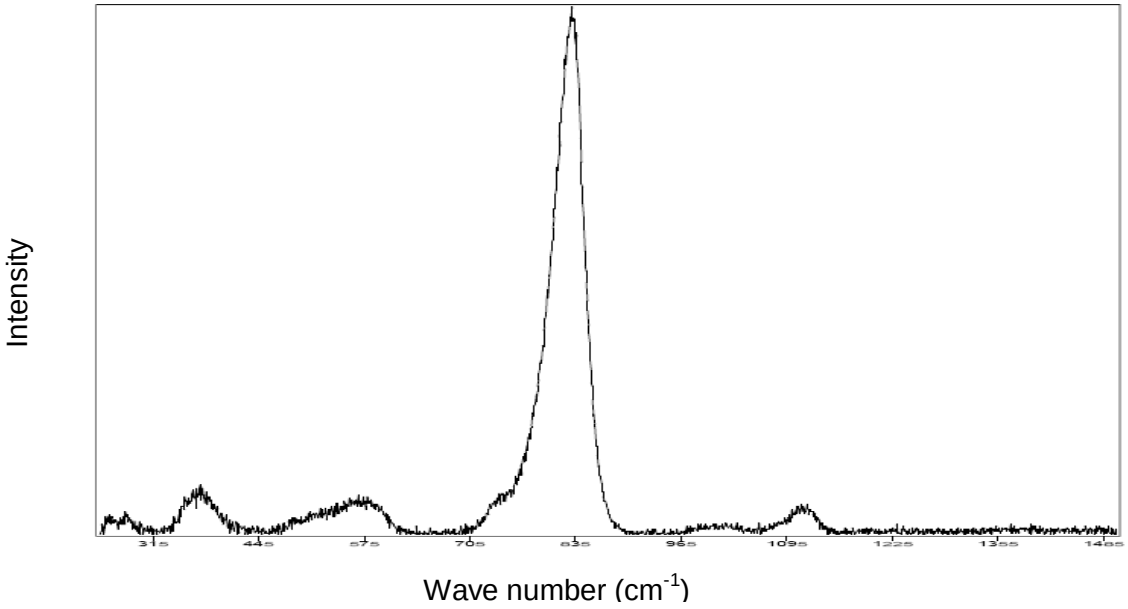

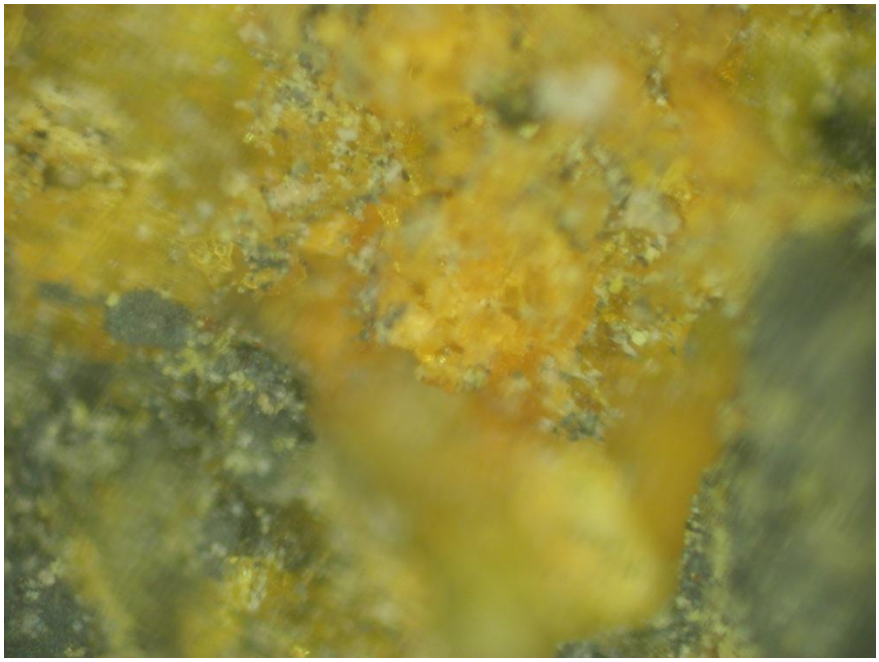

Figure A-15: Raman spectrum of sample (4C-3) above, and its image below.

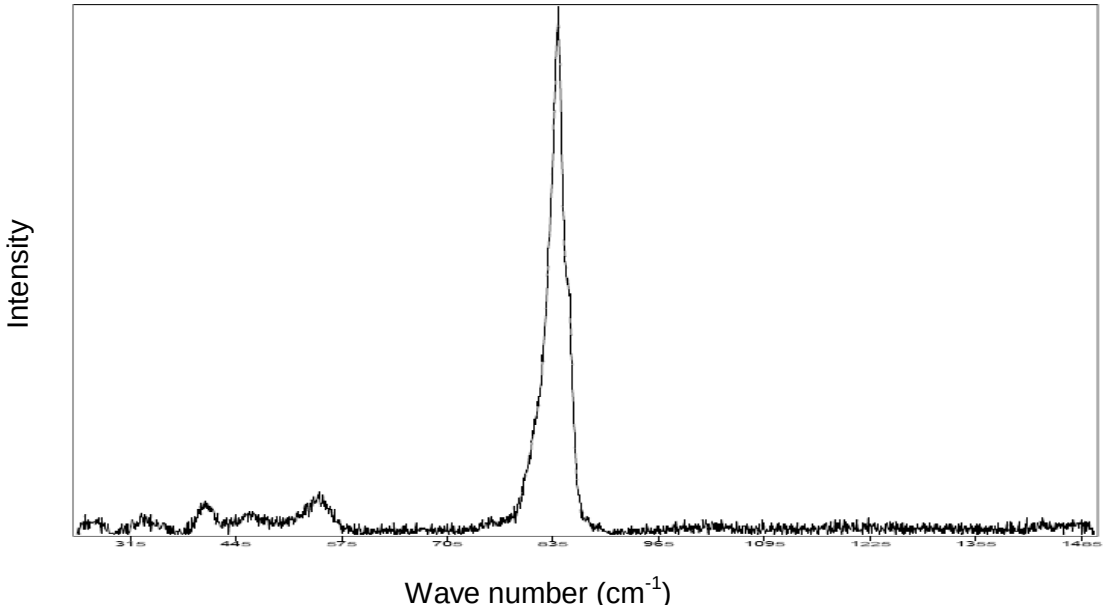

Figure A-16: Raman spectrum of sample (4C-4) above, and its image below.

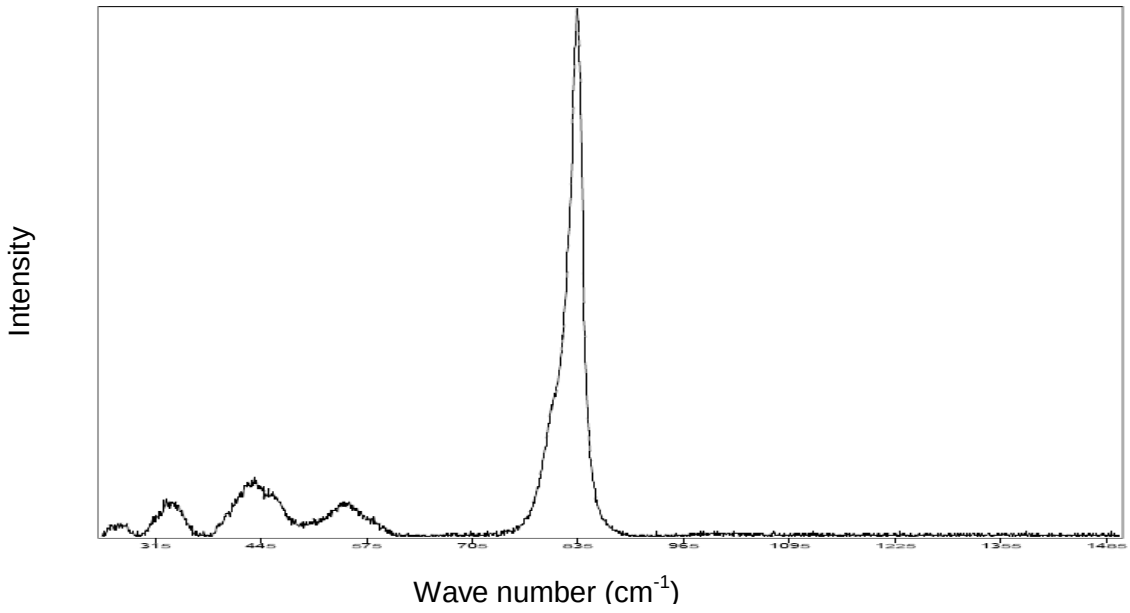

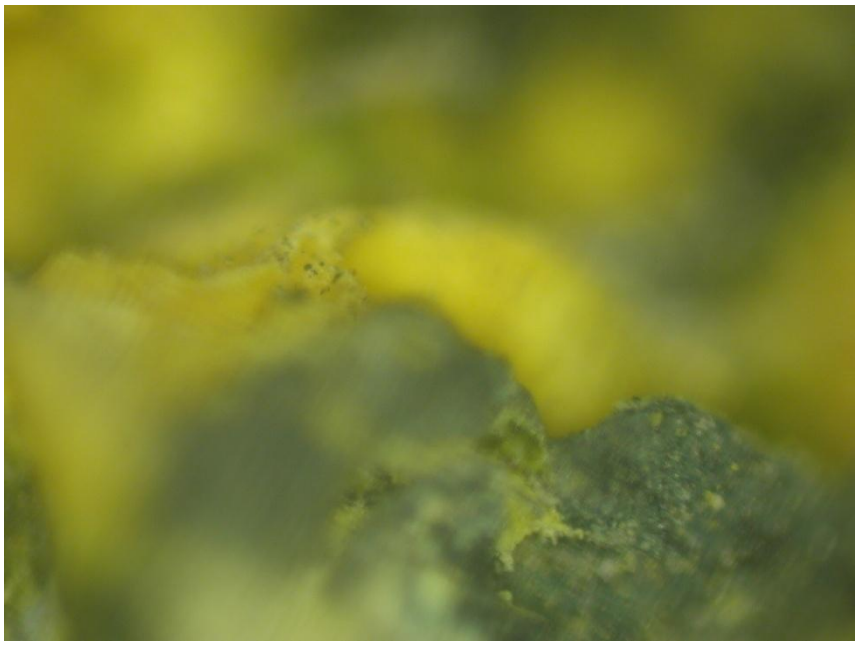

Figure A-17: Raman spectrum of sample (4C-5) above, and its image below.

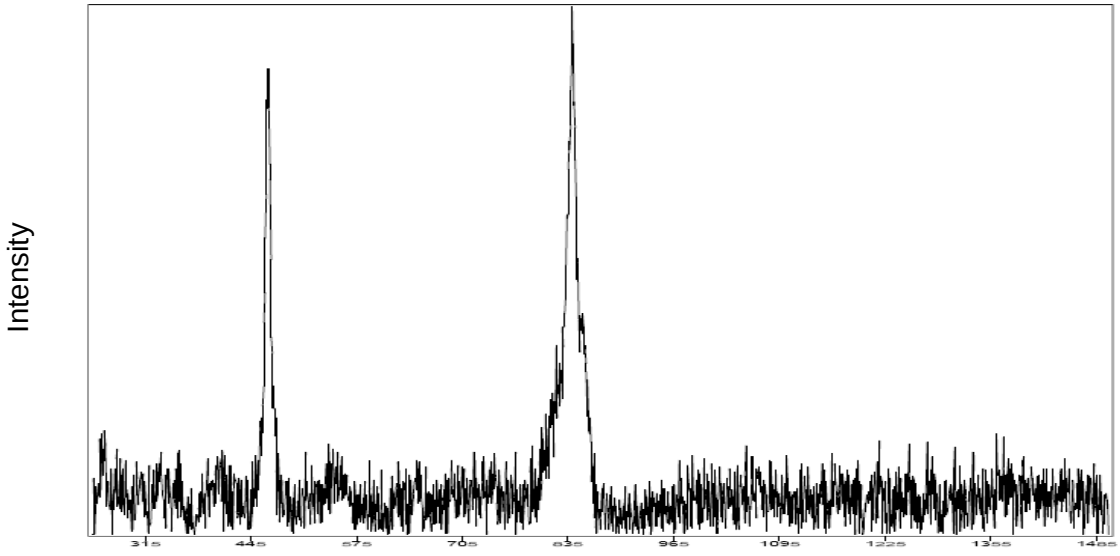

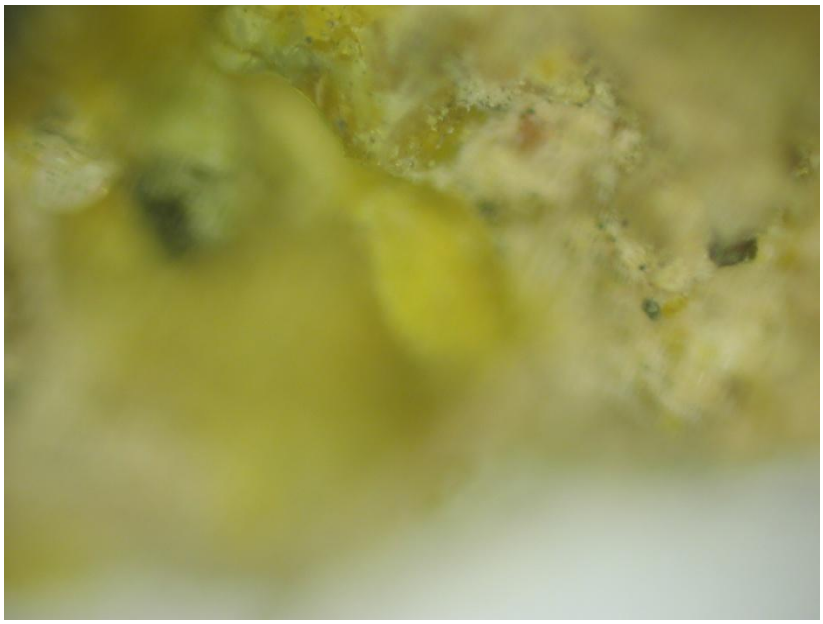

Figure A-18: Raman spectrum of sample (4D-1) above, and its image below.

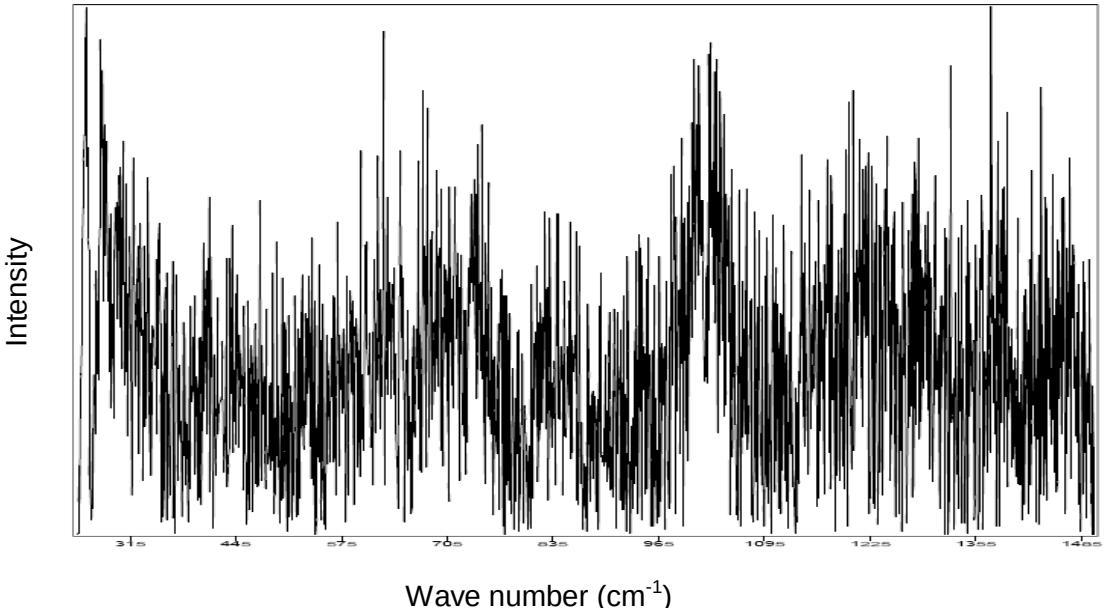

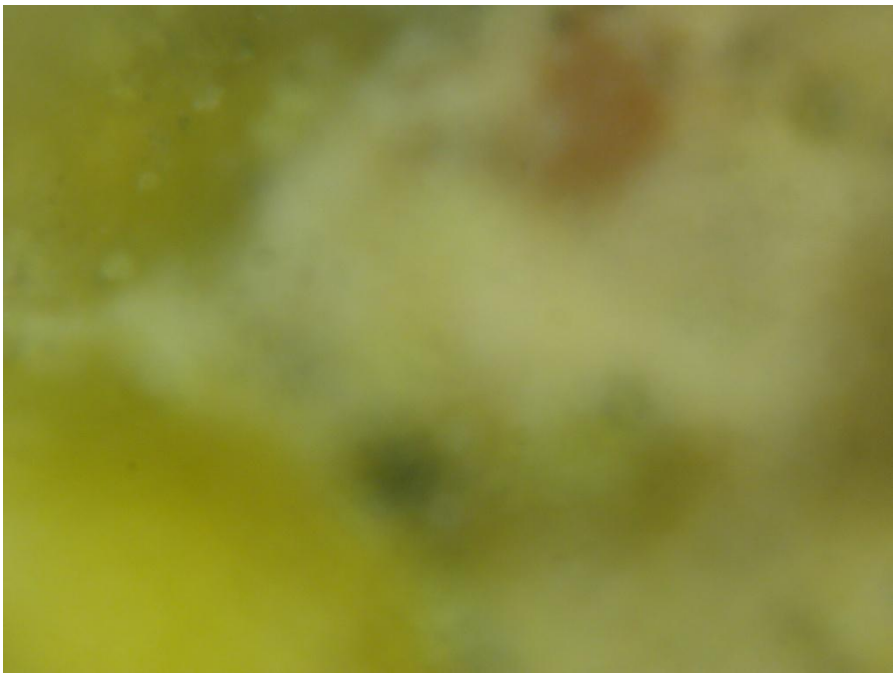

Figure A-19: Raman spectrum of sample (4D-2) above, and its image below.

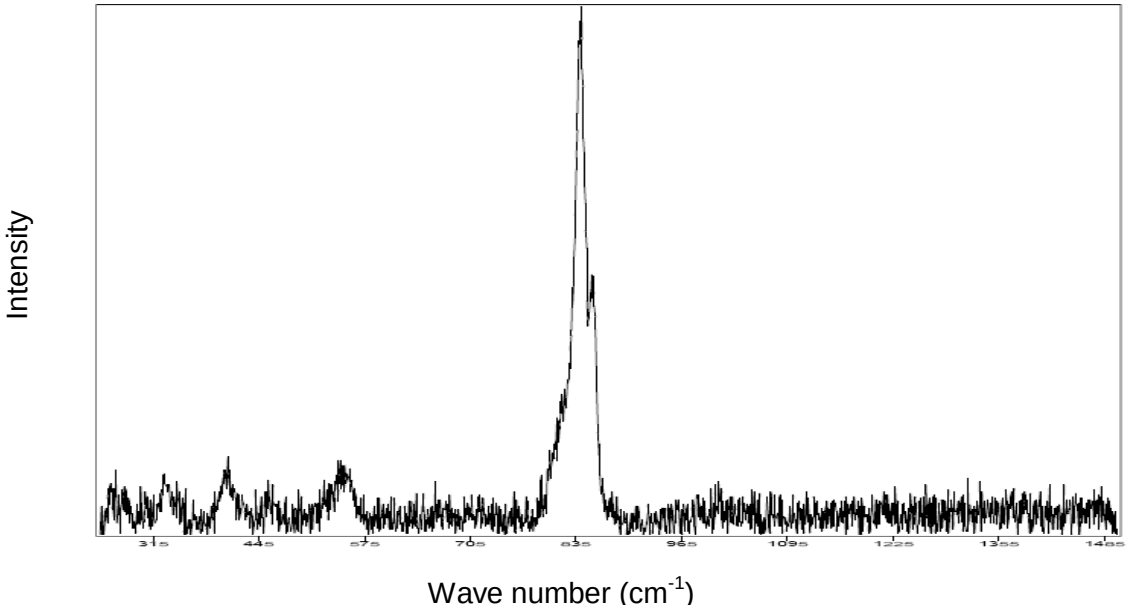

Figure A-20: Raman spectrum of sample (4D-3).

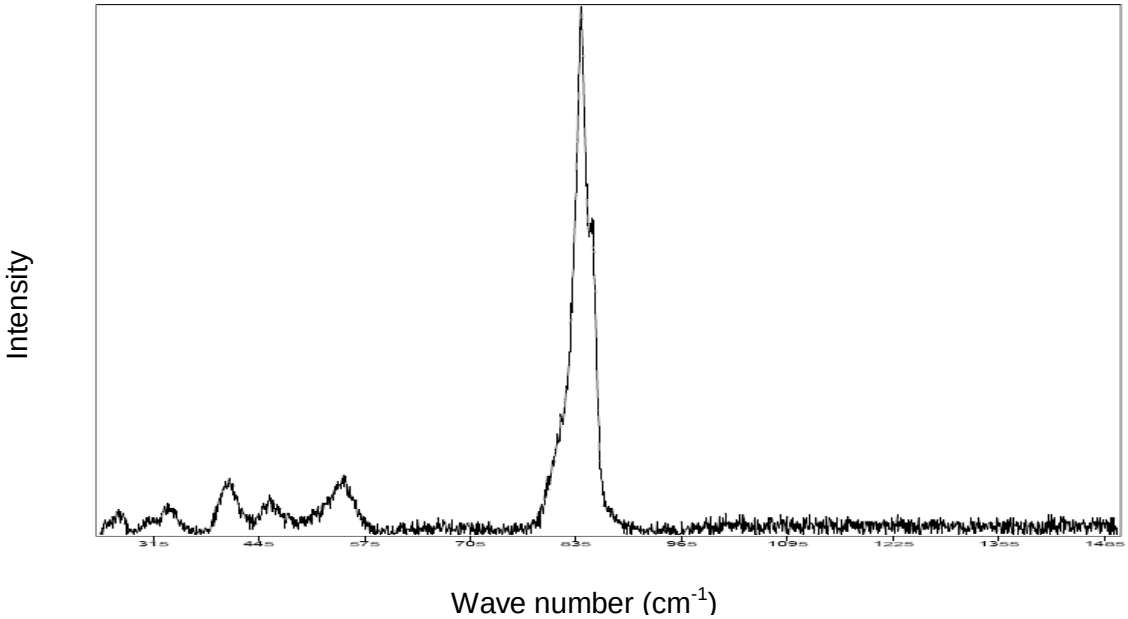

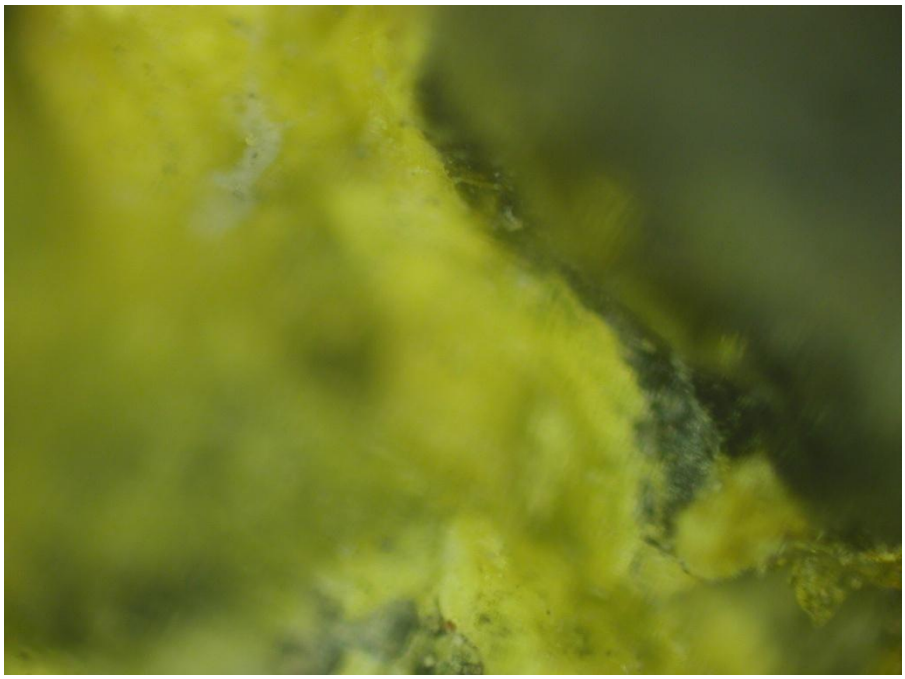

Figure A-21: Raman spectrum of sample (4D-4) above, and its image below.

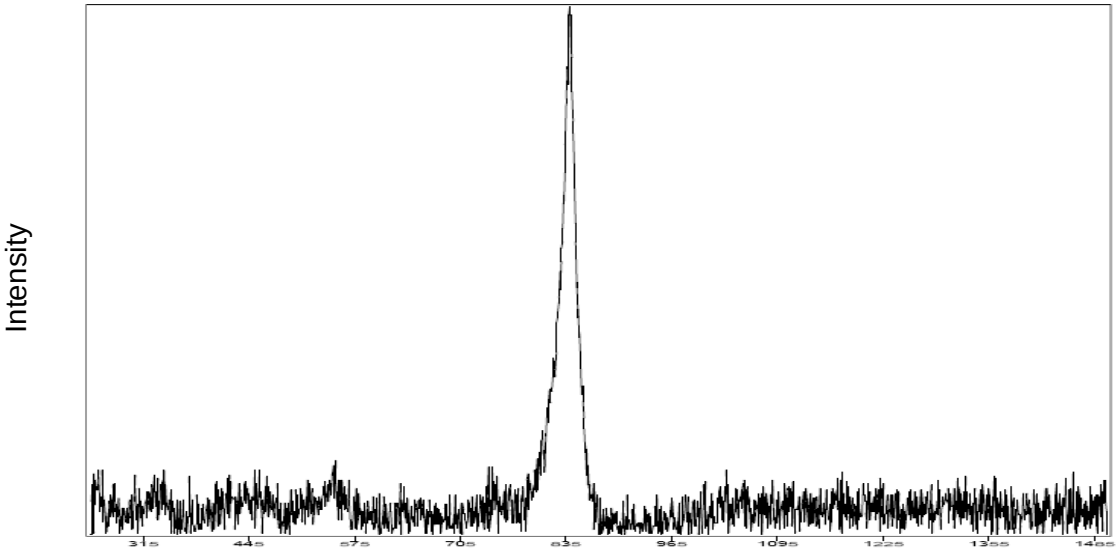

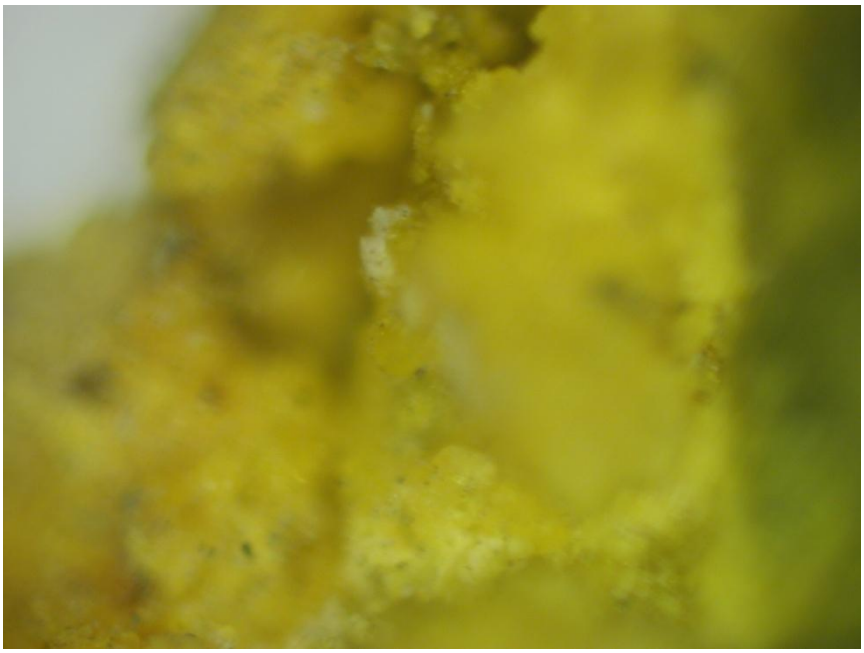

Figure A-22: Raman spectrum of sample (4D-5) above, and its image below.

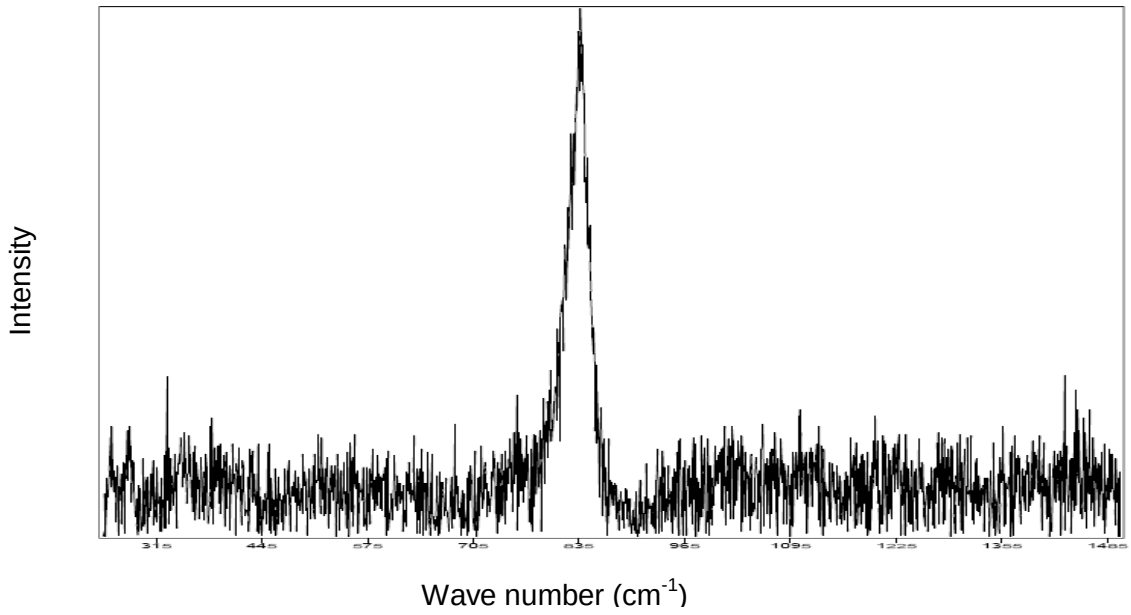

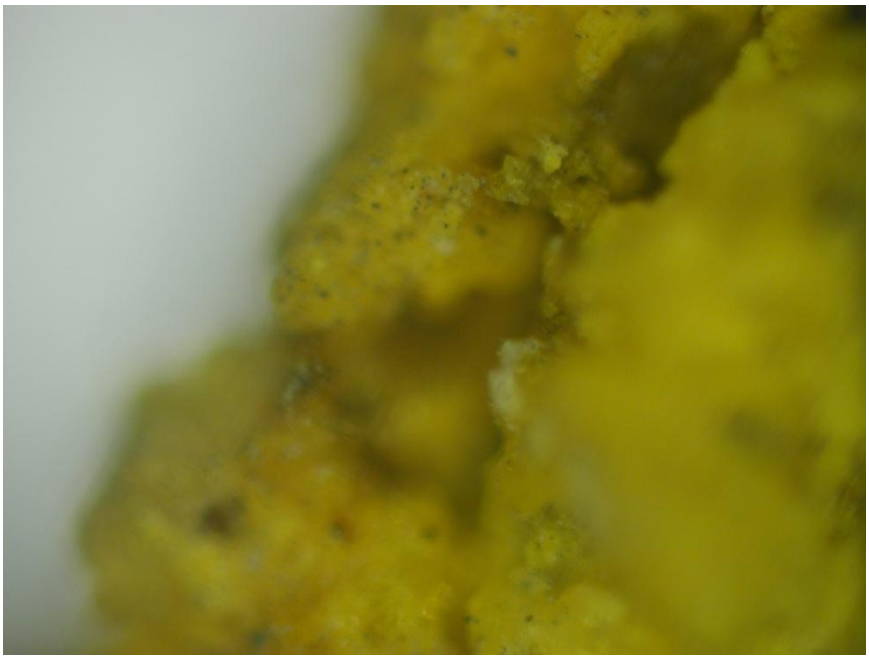

Figure A-23: Raman spectrum of sample (4D-6) above, and its image below.

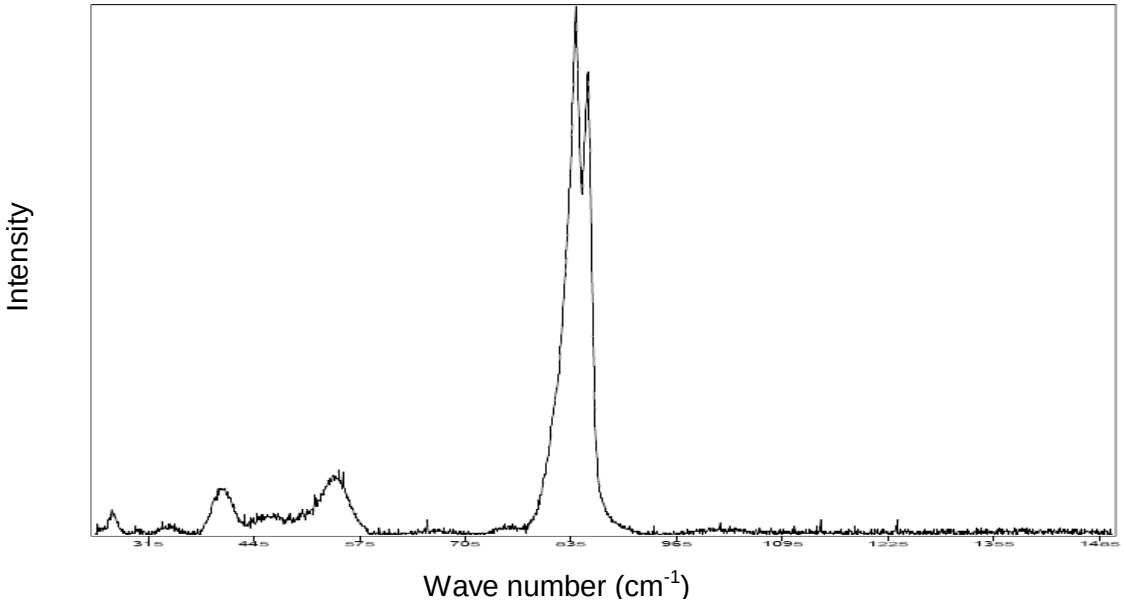

Figure A-24: Raman spectrum of sample (7A-1).

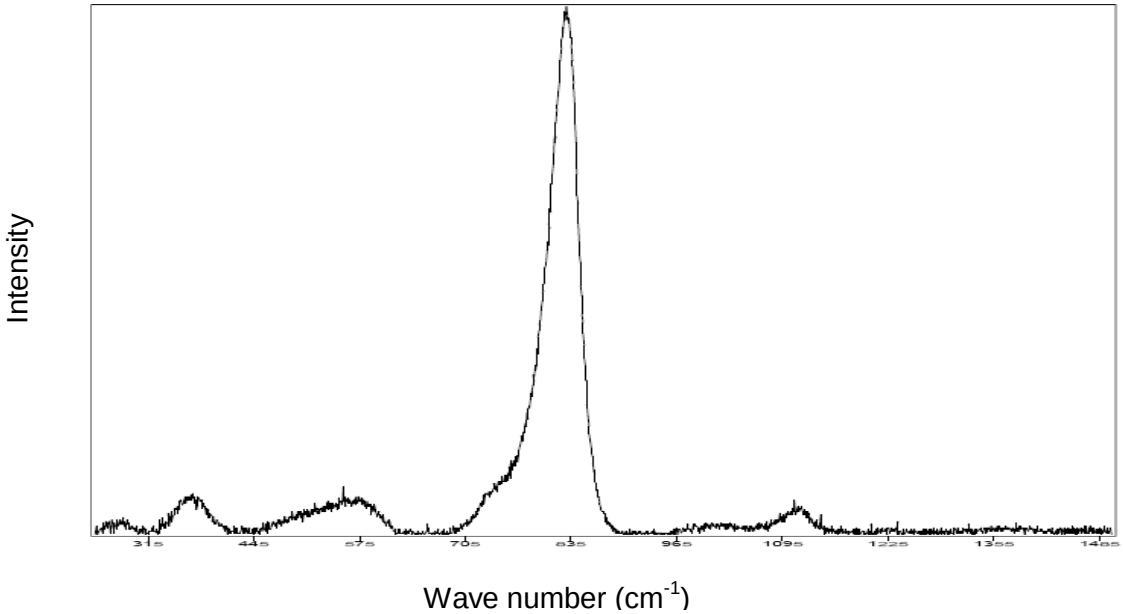

Figure A-25: Raman spectrum of sample (7B-1).

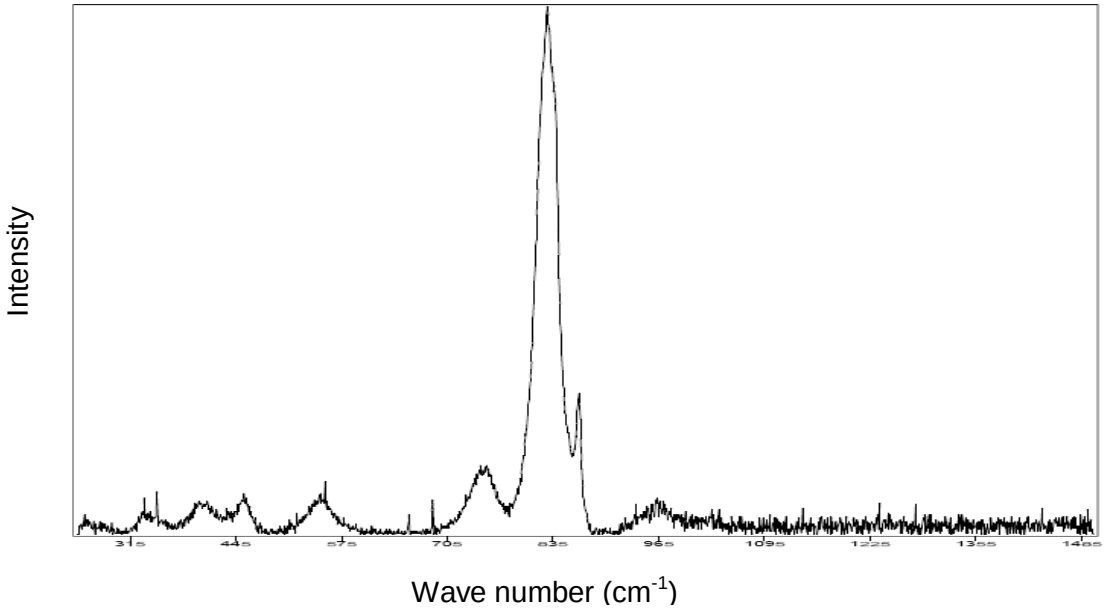

Figure A-26: Raman spectrum of sample (7C-1).

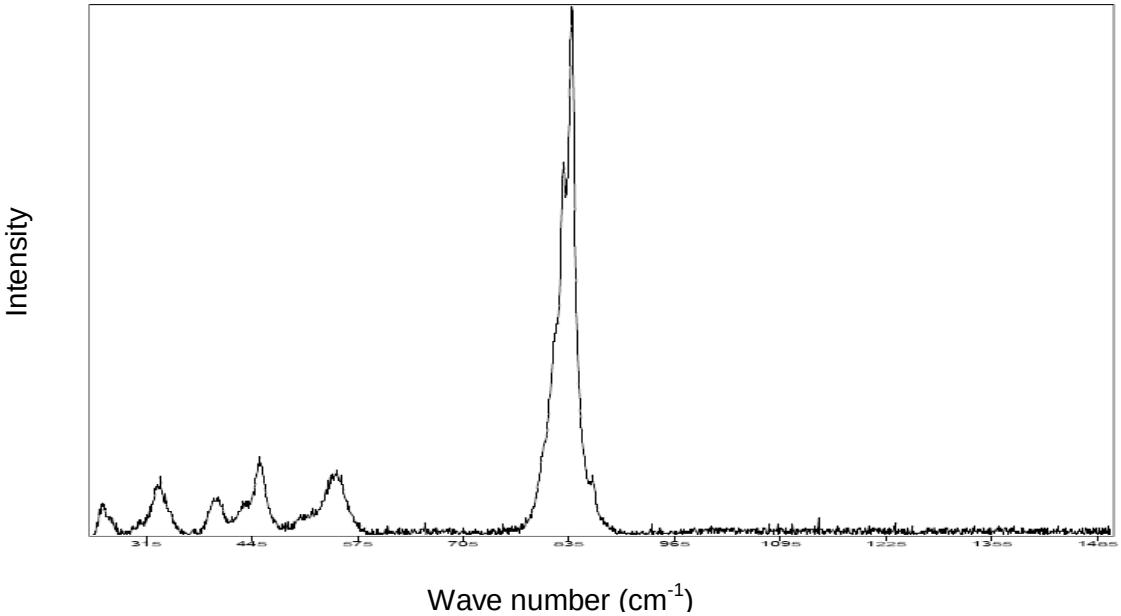

Figure A-27: Raman spectrum of sample (7C-2).

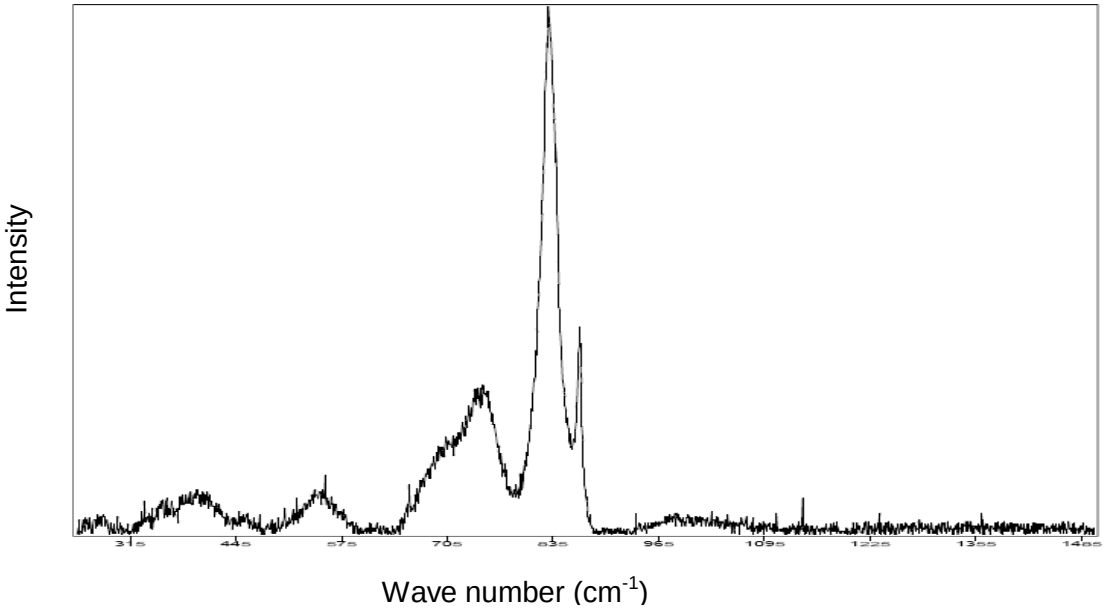

Figure A-28: Raman spectrum of sample (7C-3).

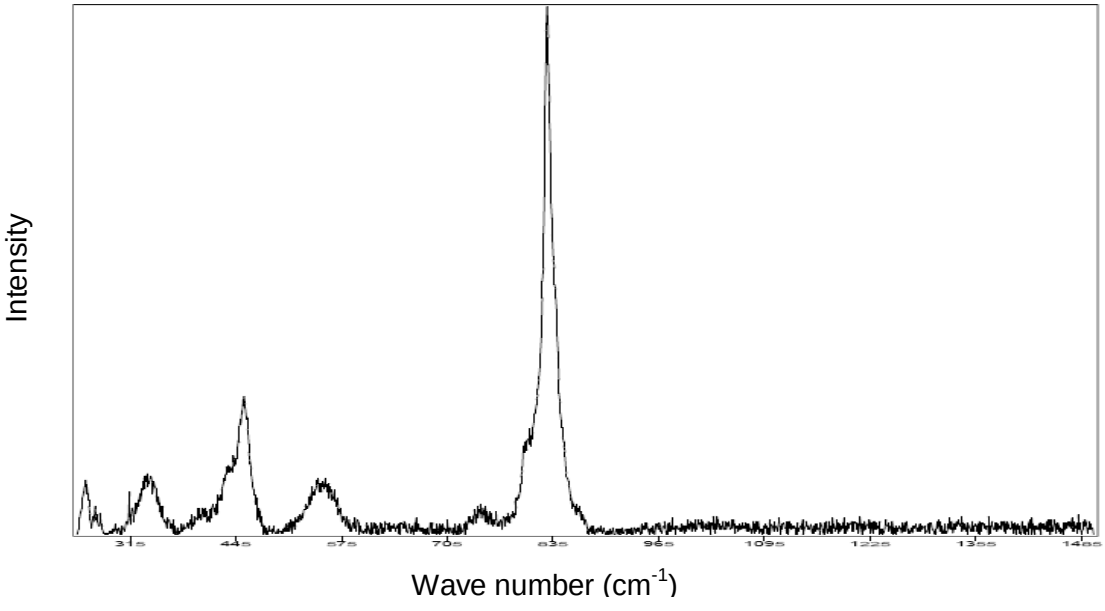

Figure A-29: Raman spectrum of sample (7D-1).

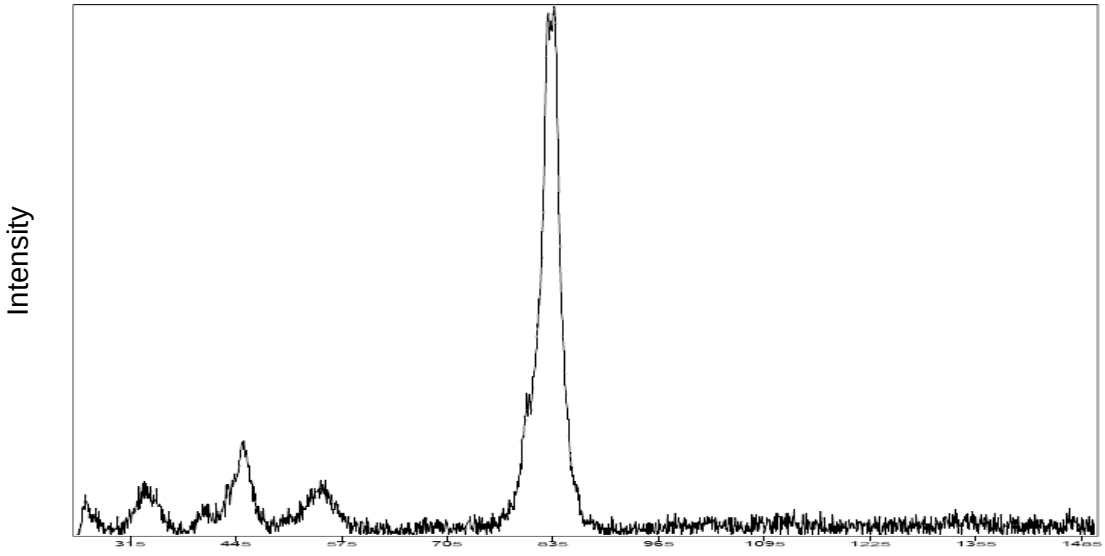

Figure A-30: Raman spectrum of sample (7D-2).

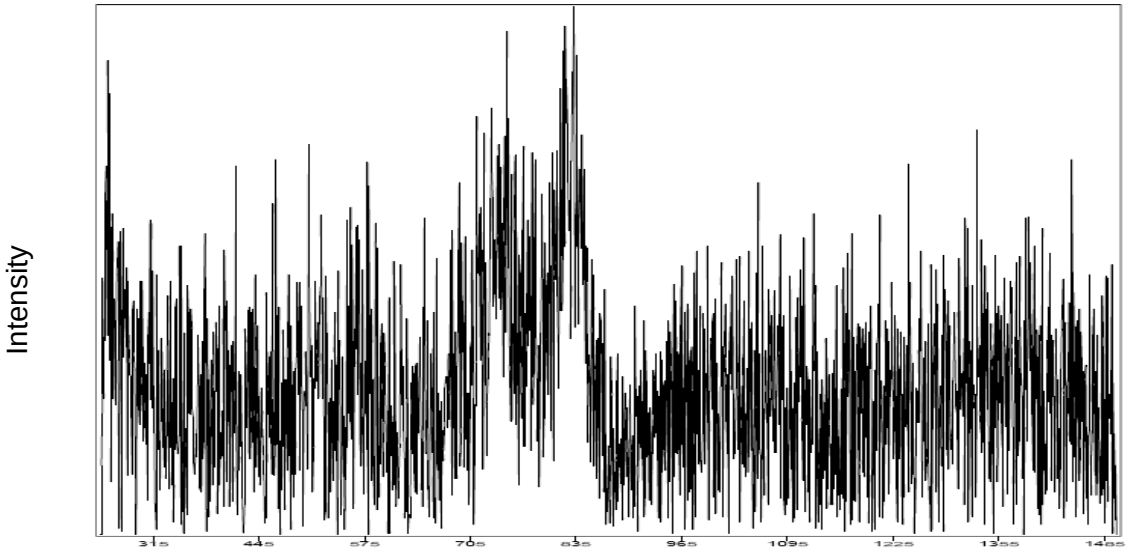

Figure A-31: Raman spectrum of sample (8A-1).

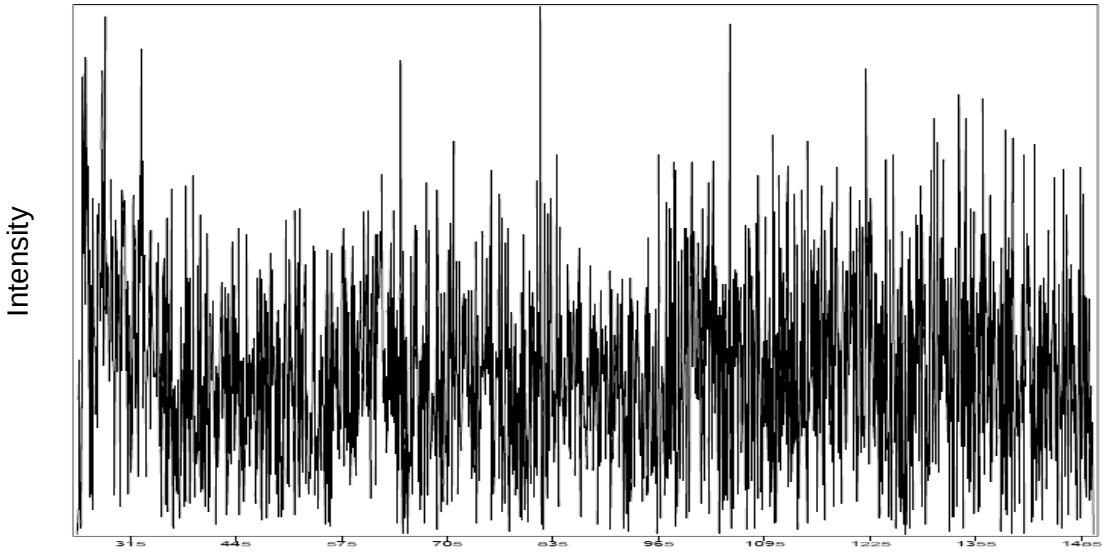

Figure A-32: Raman spectrum of sample (8A-2).

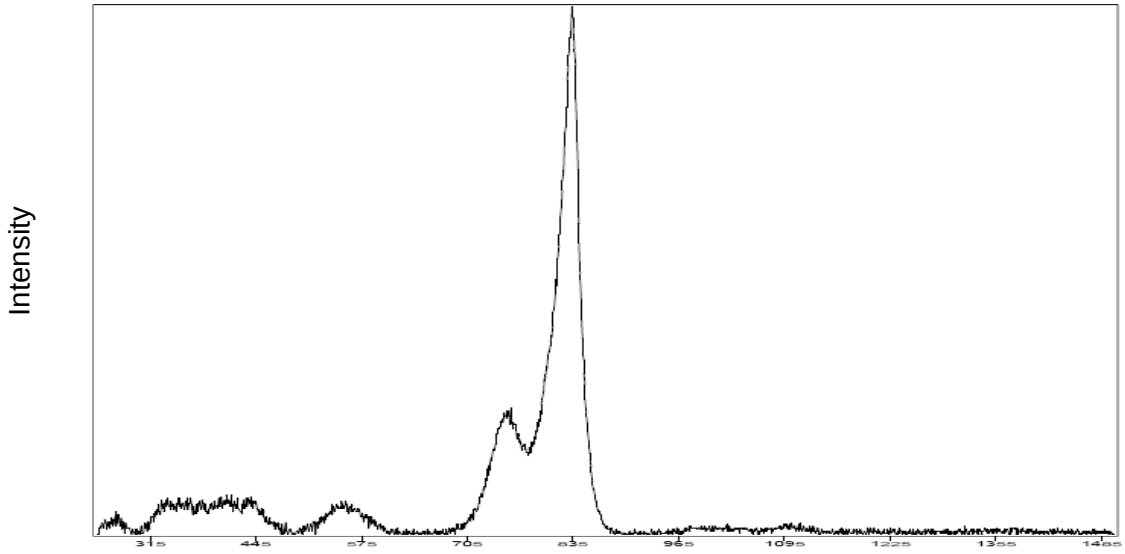

Figure A-33: Raman spectrum of sample (8B-1).

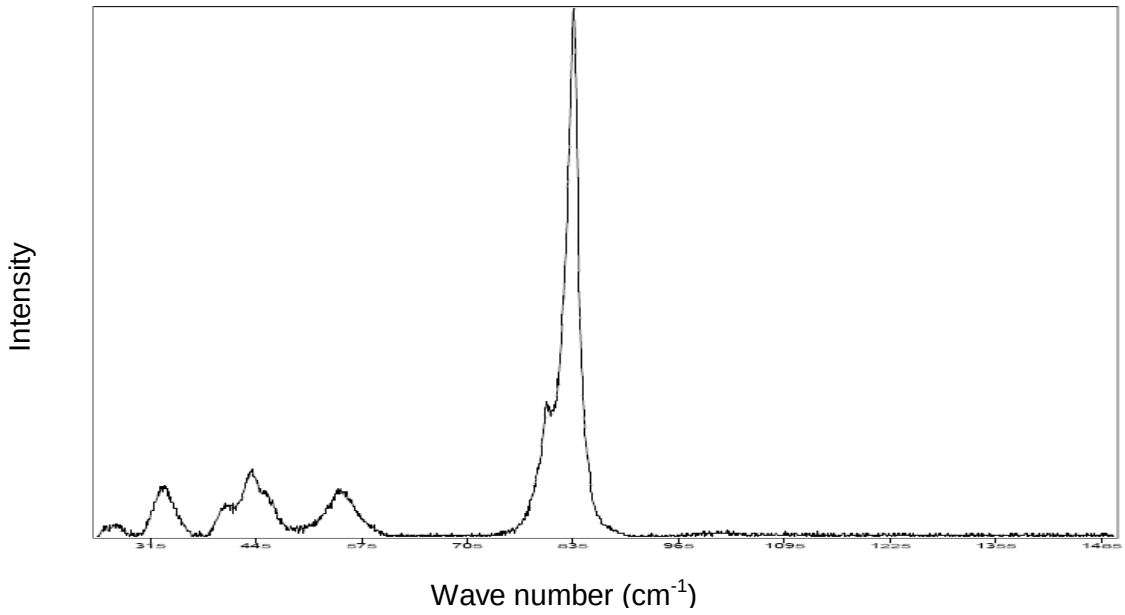

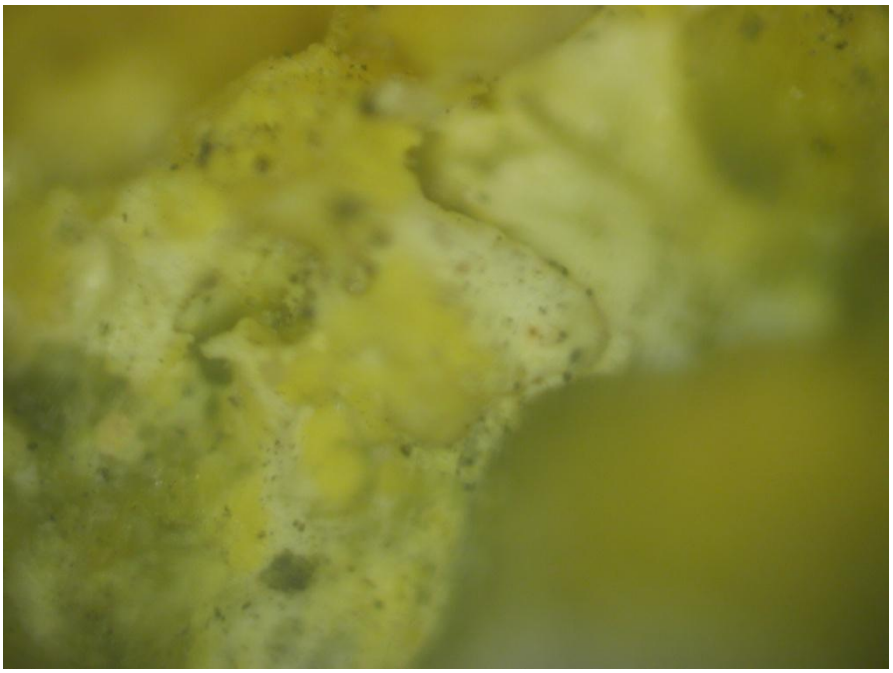

Figure A-34: Raman spectrum of sample (8B-2) above, and its image below.

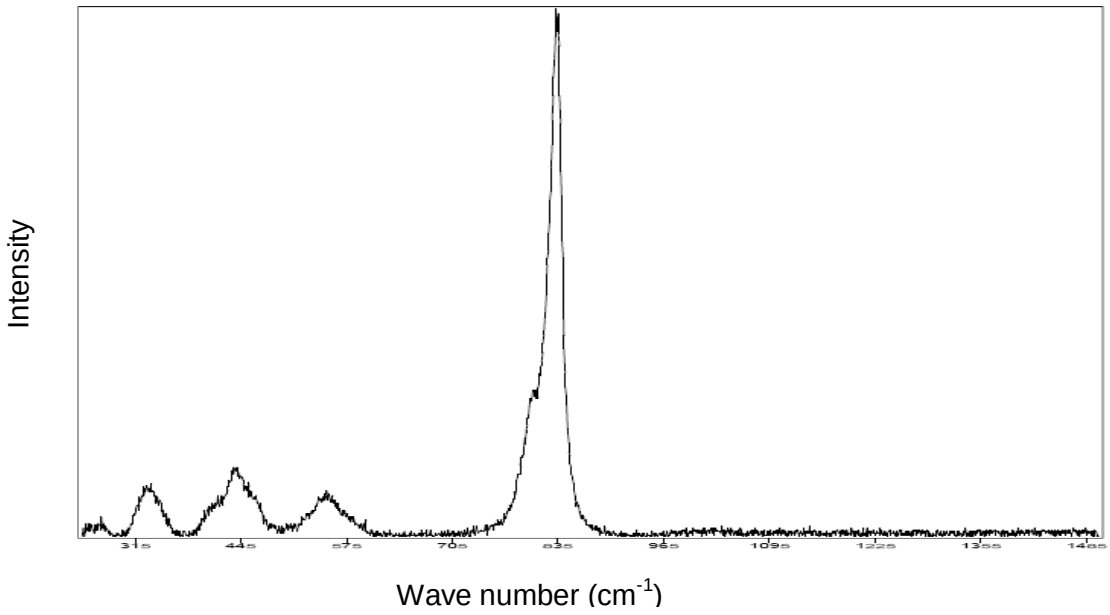

Figure A-35: Raman spectrum of sample (8B-3).

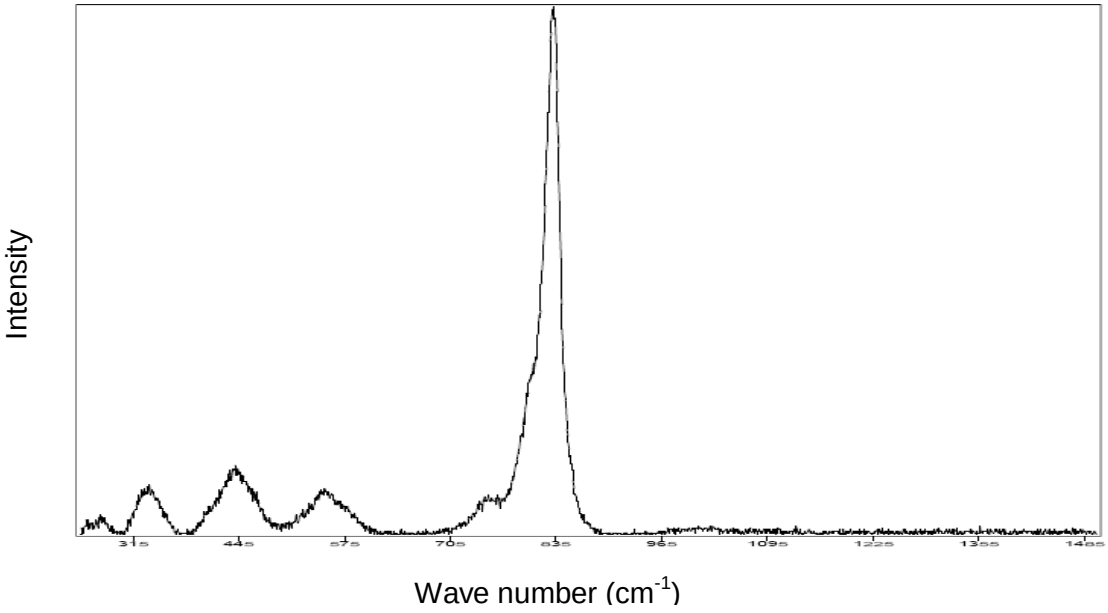

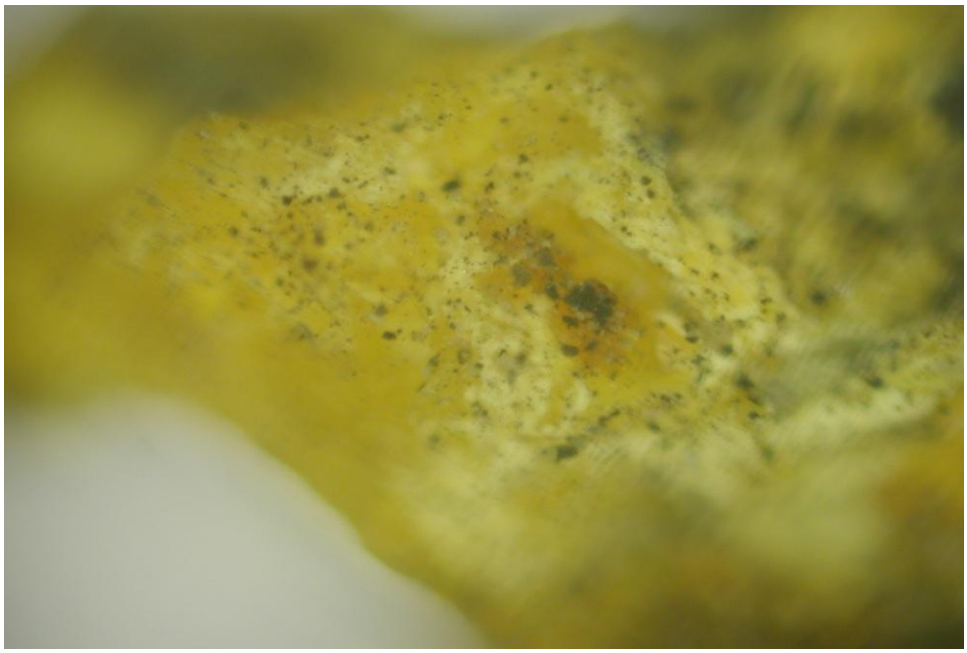

Figure A-36: Raman spectrum of sample (8B-4) above, and its image below.

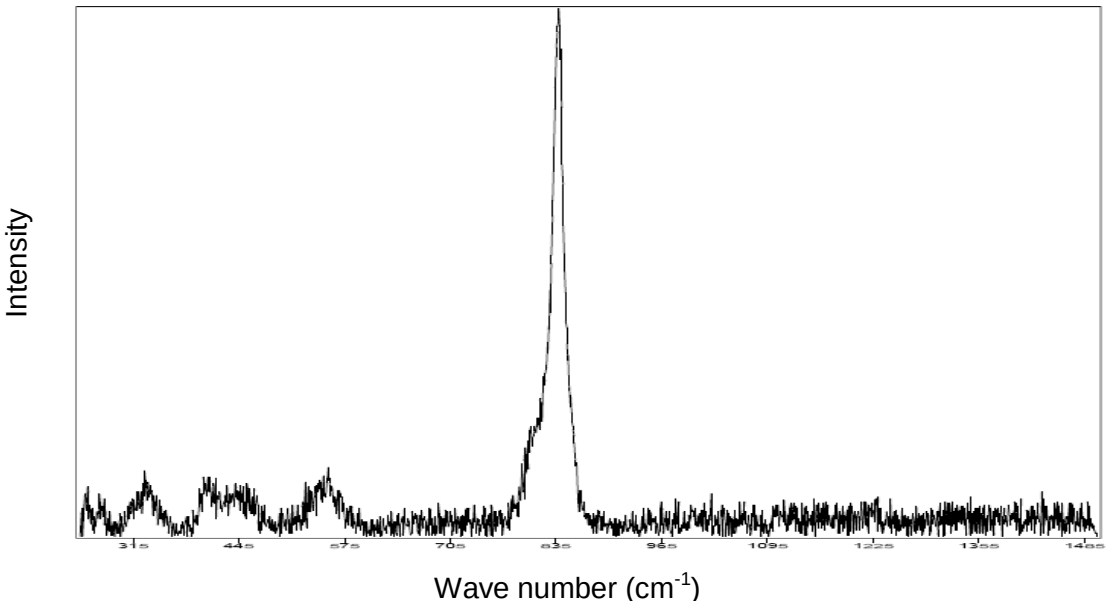

Figure A-37: Raman spectrum of sample (8C-1).

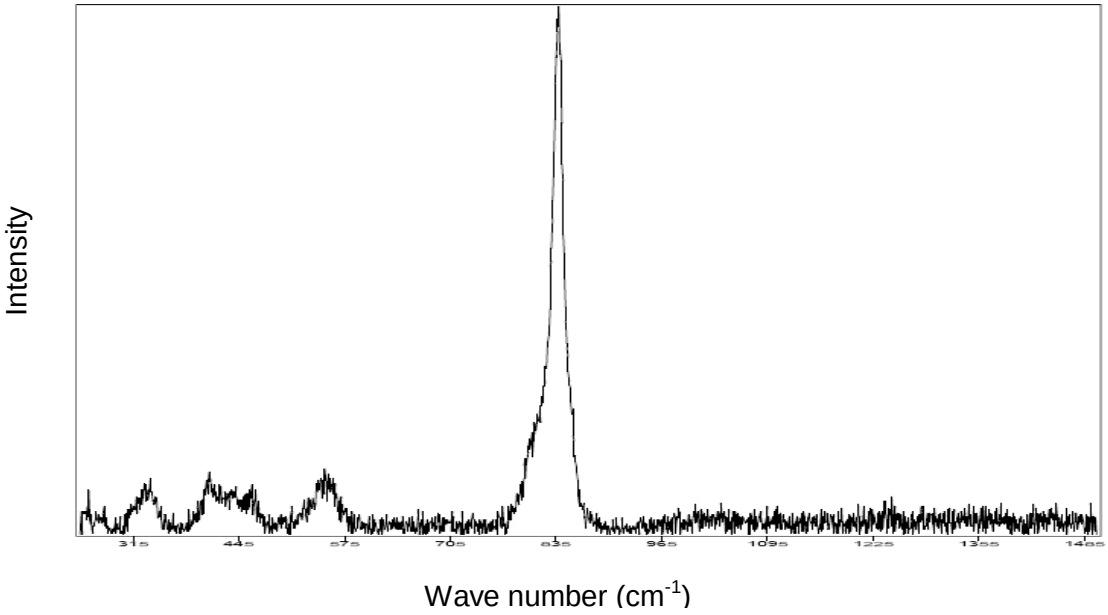

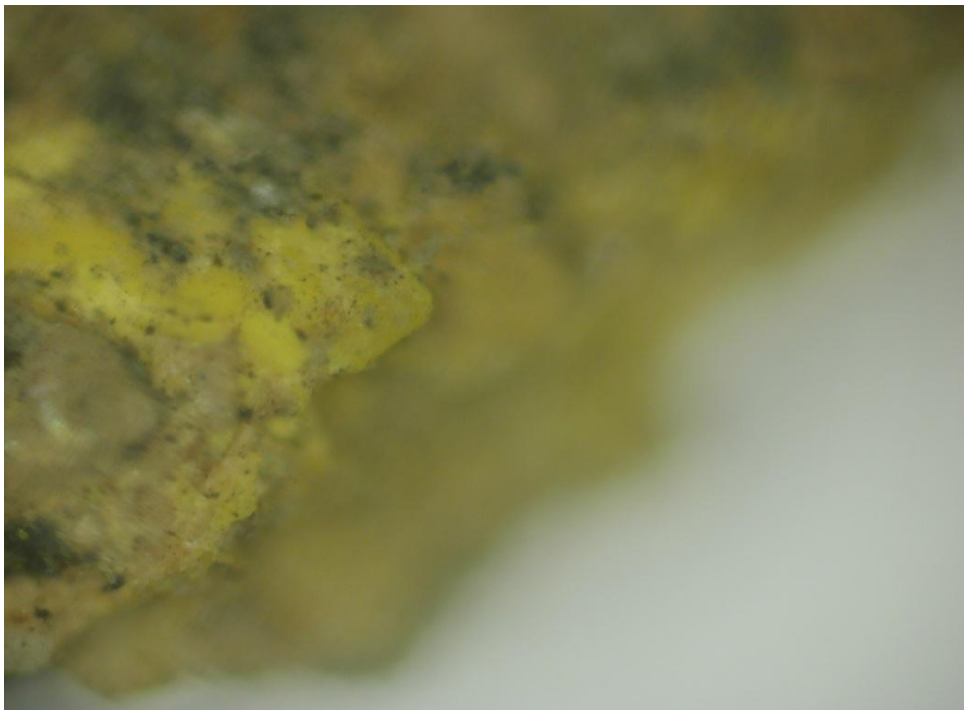

Figure A-38: Raman spectrum of sample (8C-2) above, and its image below.

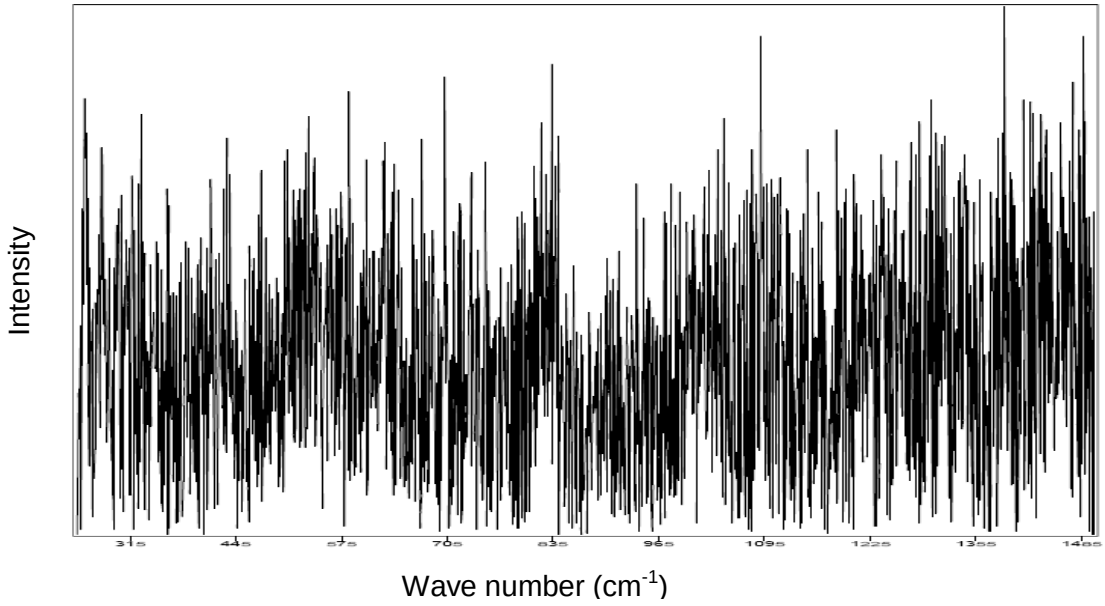

Figure A-39: Raman spectrum of sample (8C-3).

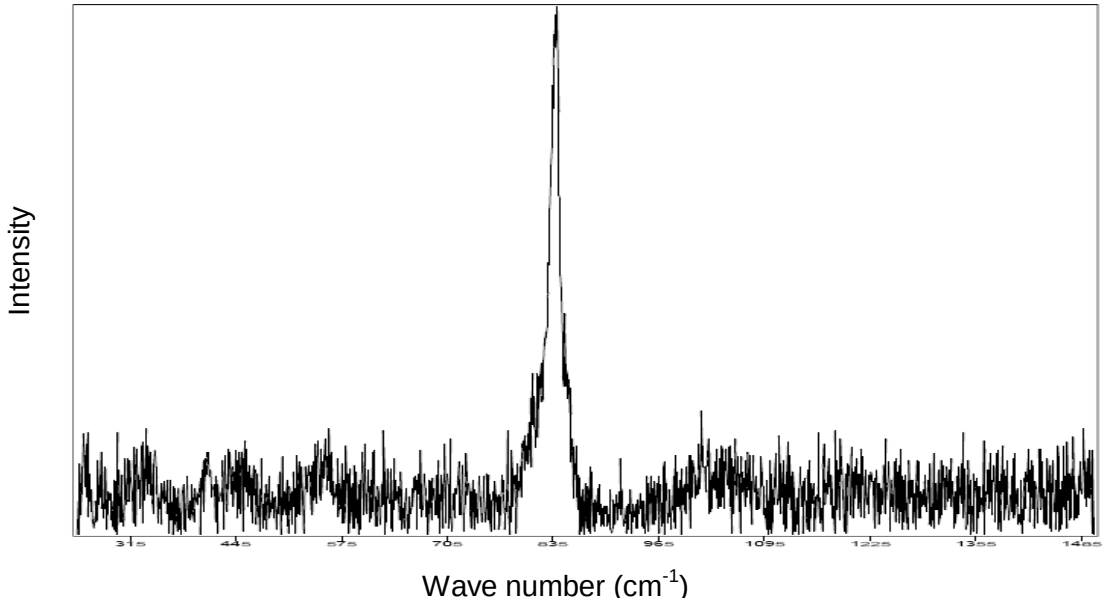

Figure A-40: Raman spectrum of sample (8C-4).

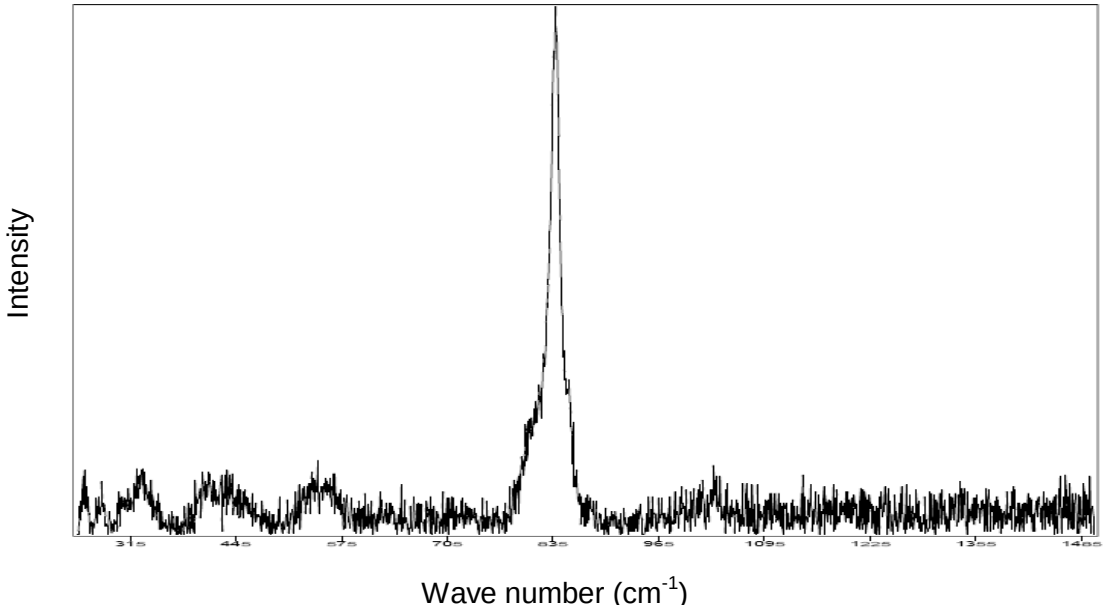

Figure A-41: Raman spectrum of sample (8C-5).

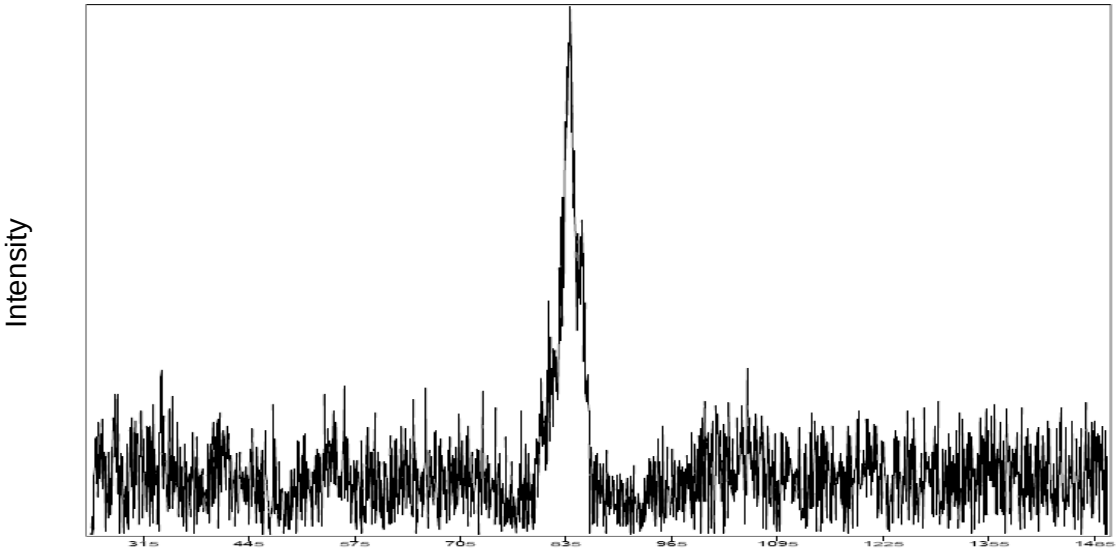

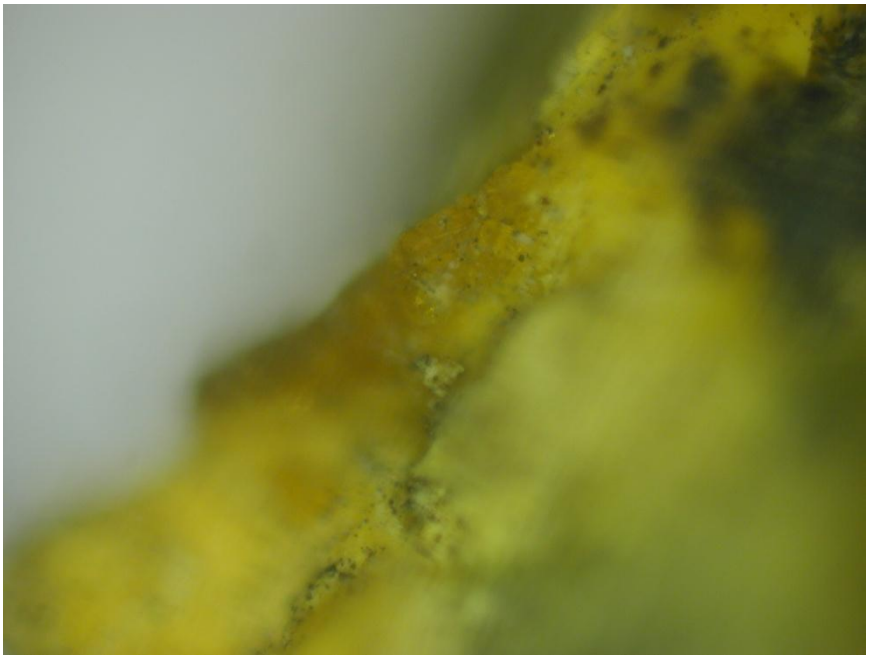

Figure A-42: Raman spectrum of sample (8C-6) above, and its image below.

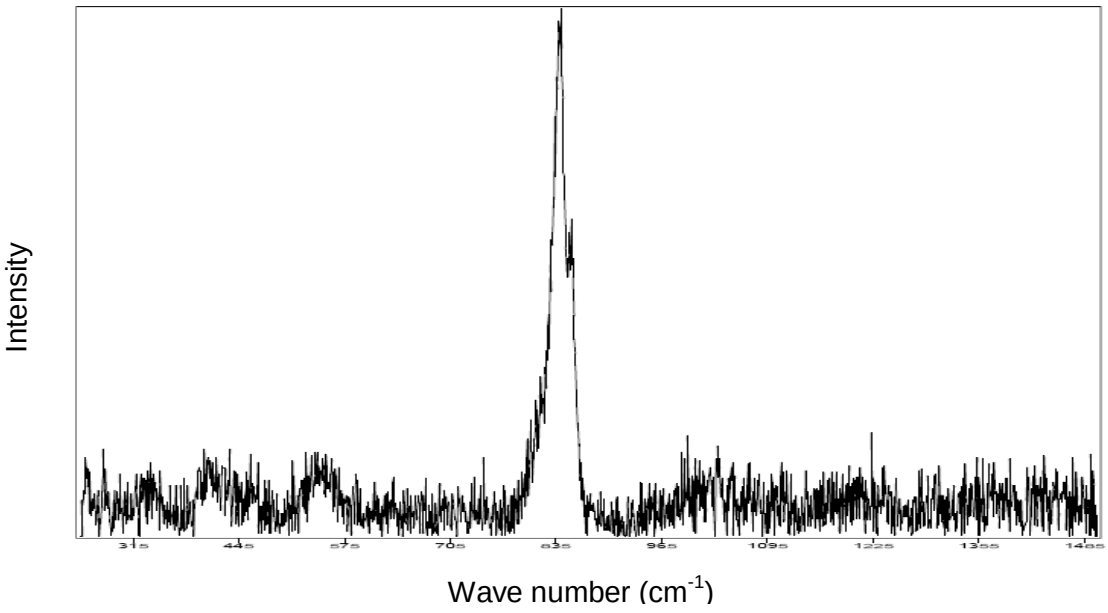

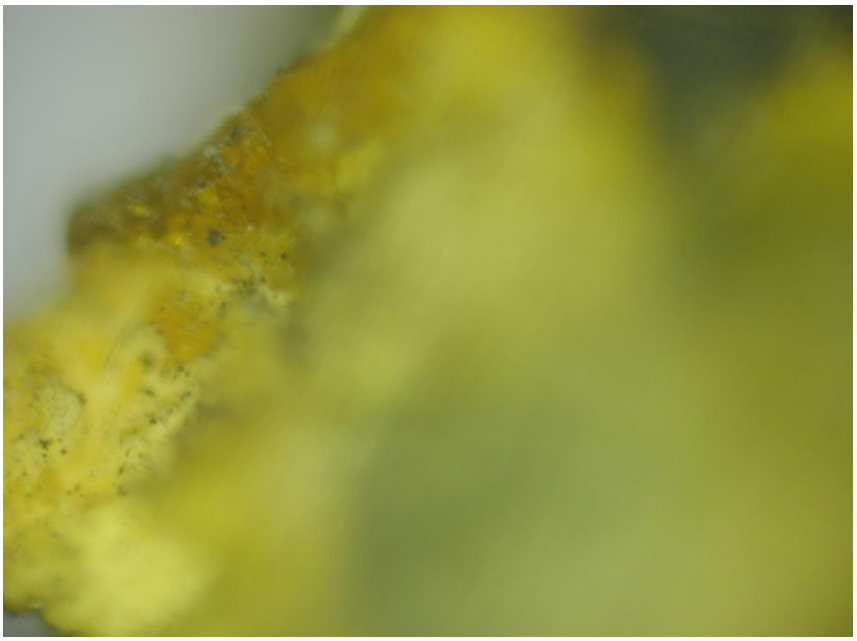

Figure A-43: Raman spectrum of sample (8C-7) above, and its image below.

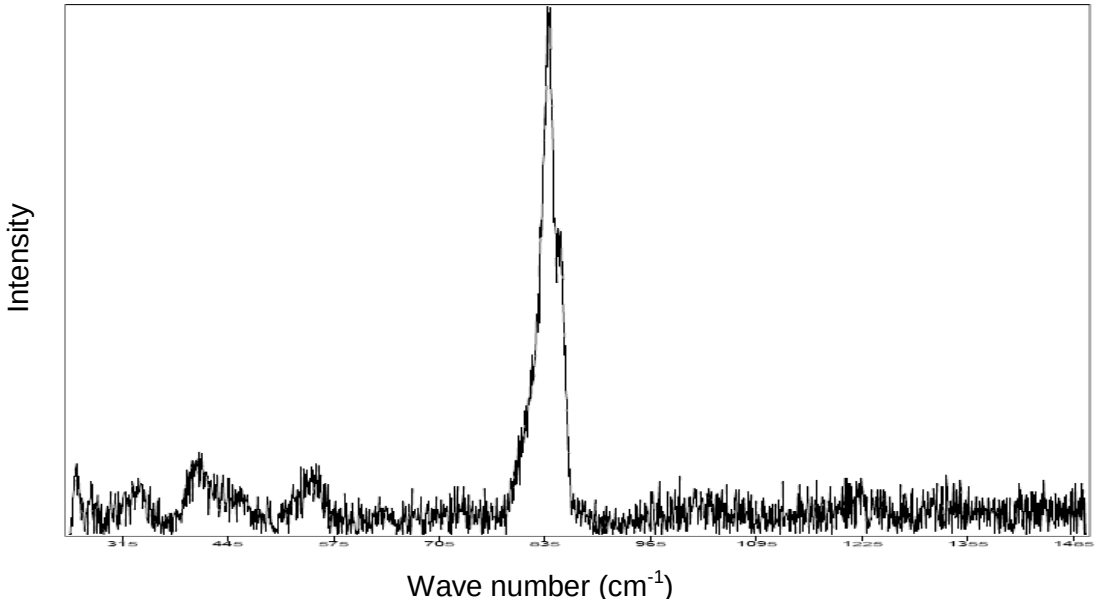

Figure A-44: Raman spectrum of sample (8C-8)

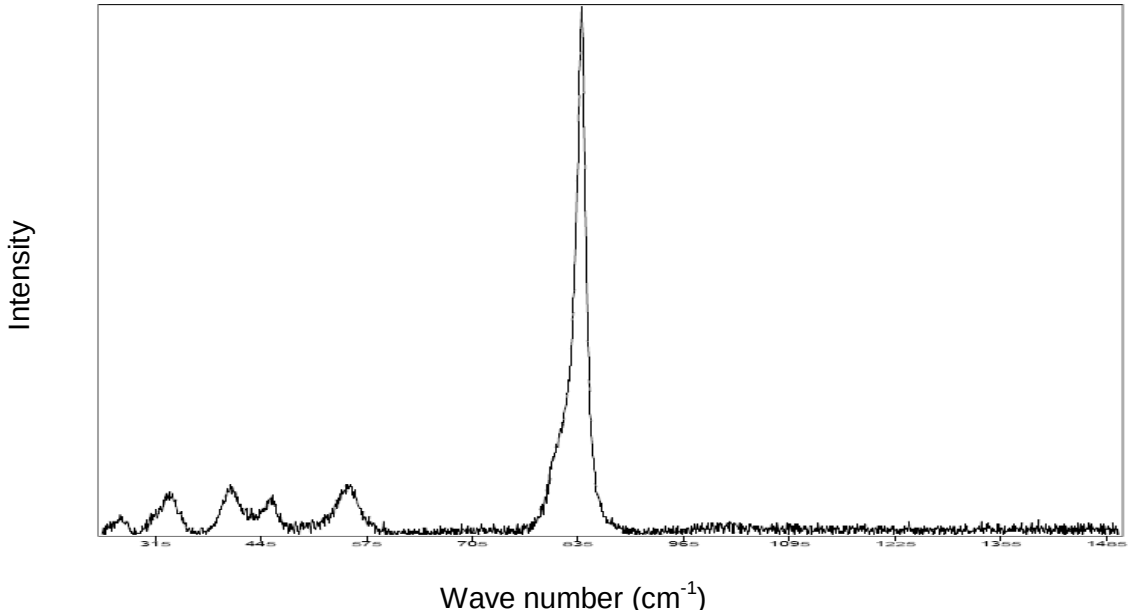

Figure A-45: Raman spectrum of sample (8D-1).

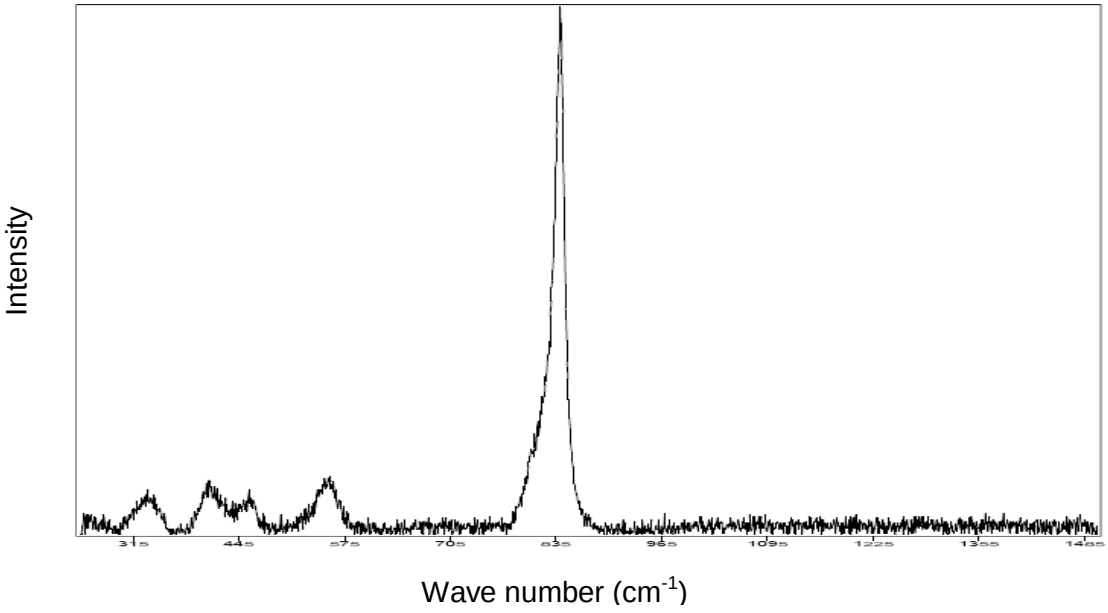

Figure A-46: Raman spectrum of sample (8D-2).

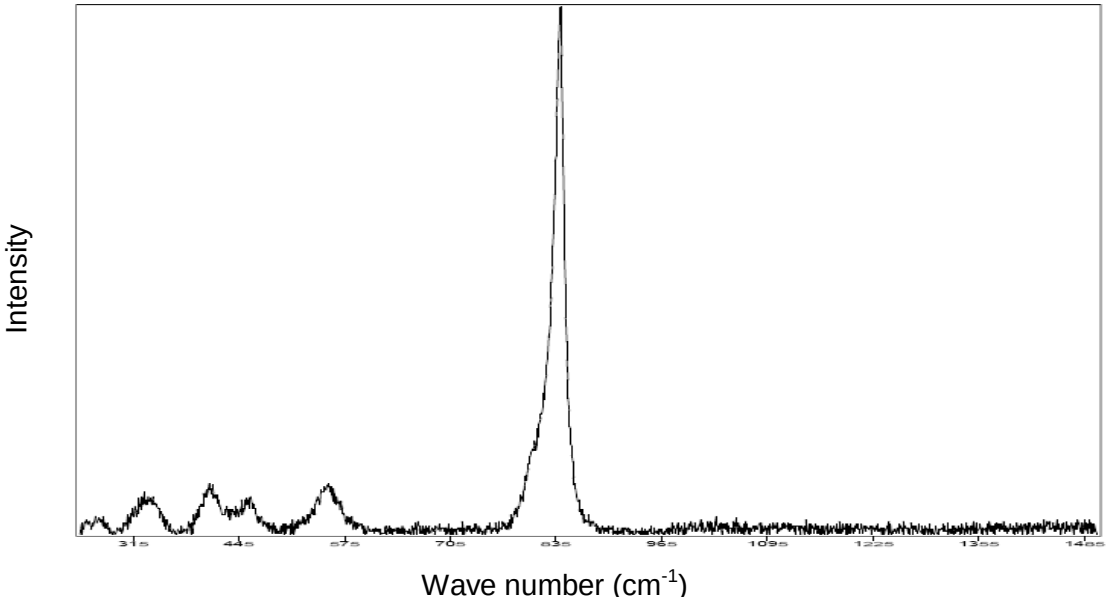

Figure A-47: Raman spectrum of sample (8D-3).

Appendix B: The scanning electron microscope results

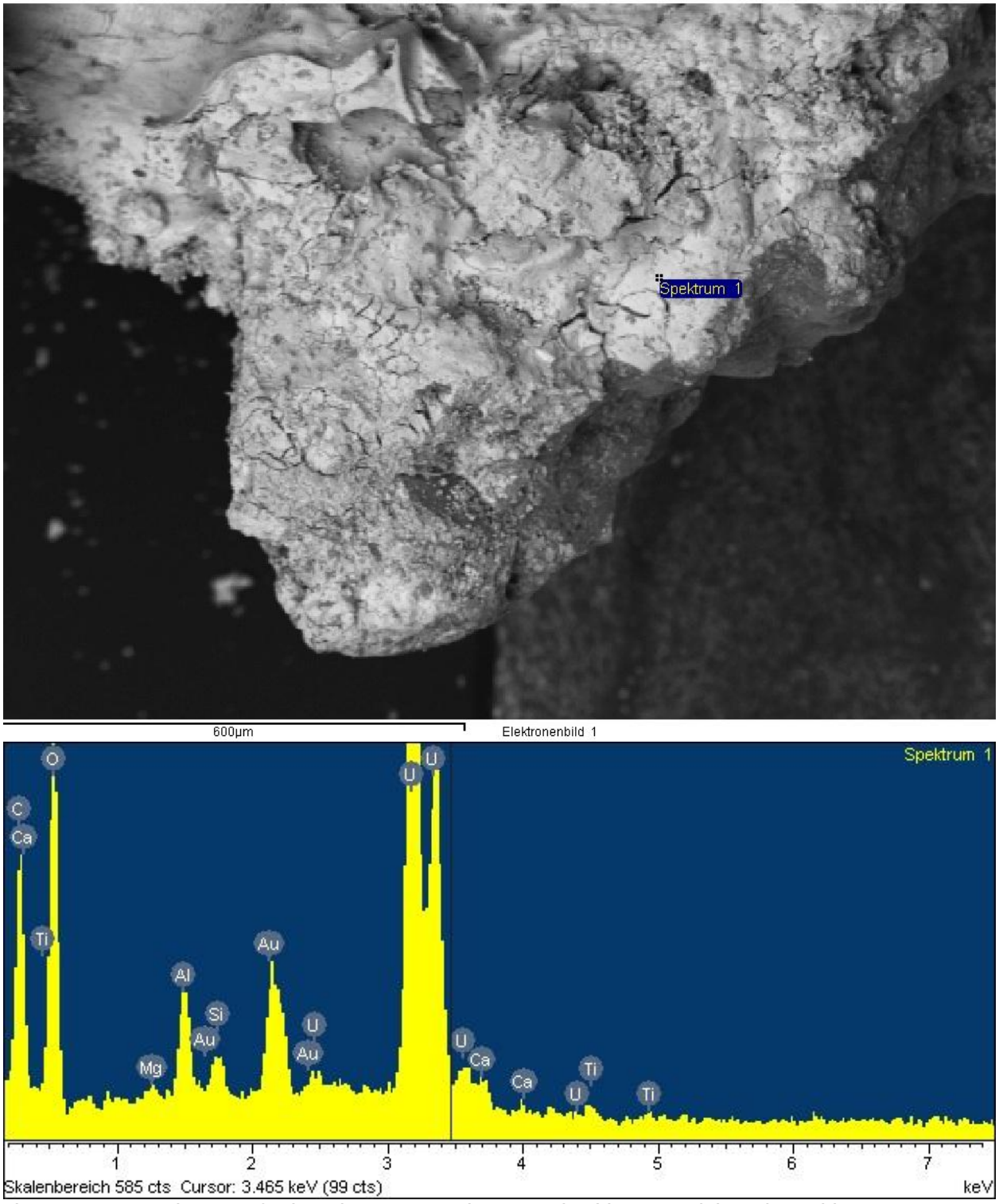

Figure B-1: BSE image of a location on sample 4 acquired by SEM (above), and its EDS spectrum (below).

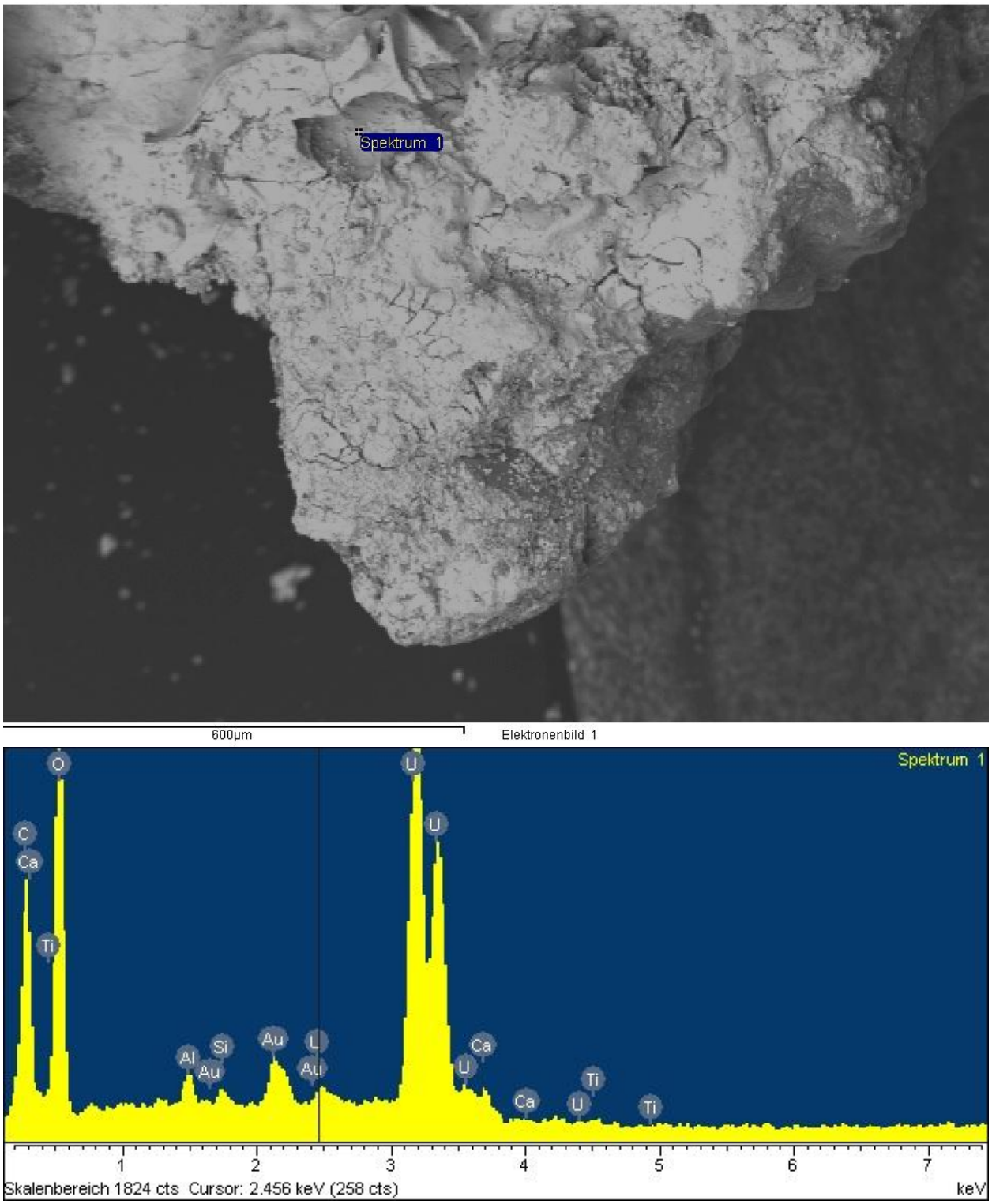

Figure B-2: BSE image of a location on sample 4 acquired by SEM (above), and its EDS spectrum (below).

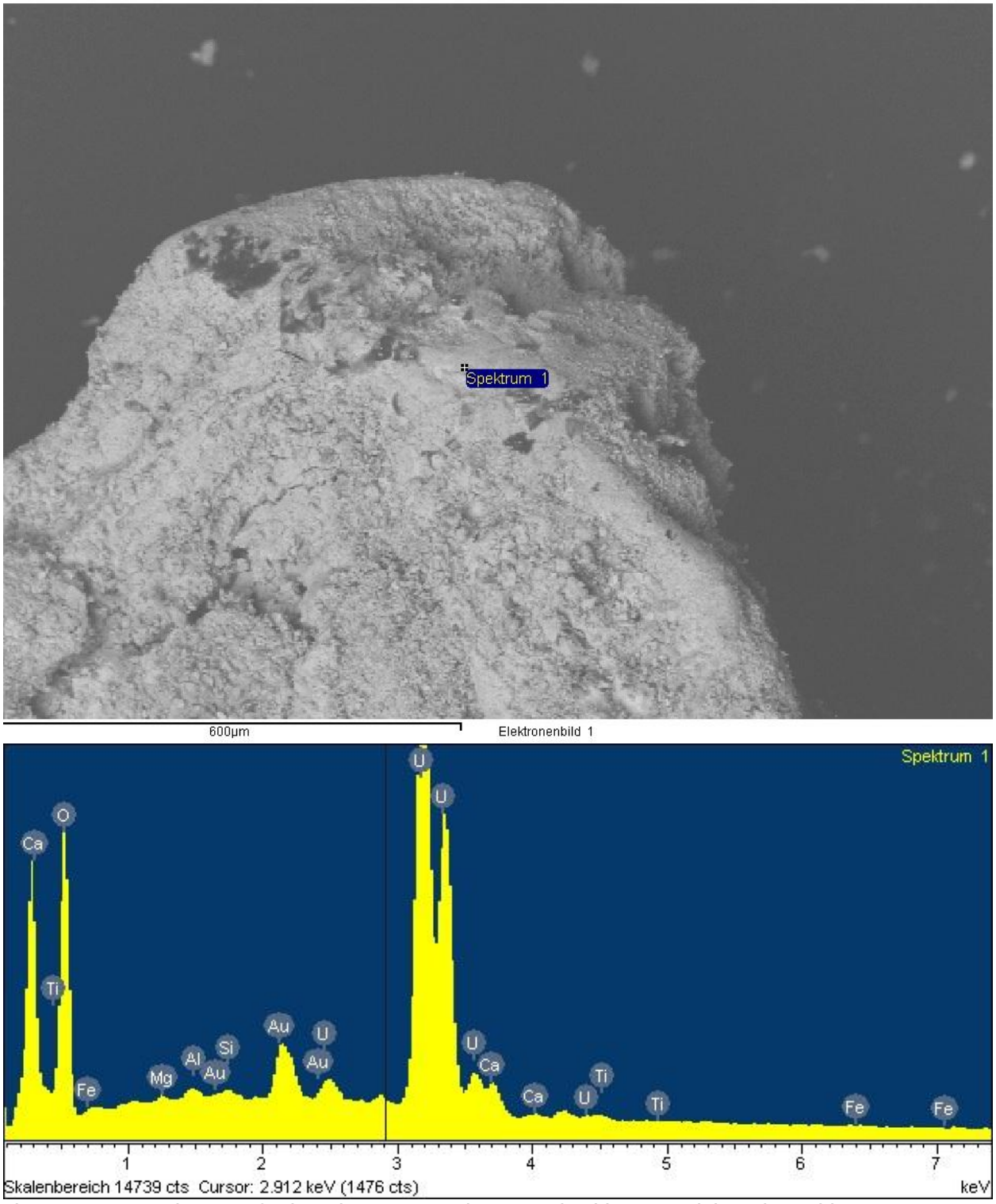

Figure B-3: BSE image of a location on sample 4 acquired by SEM (above), and its EDS spectrum (below).

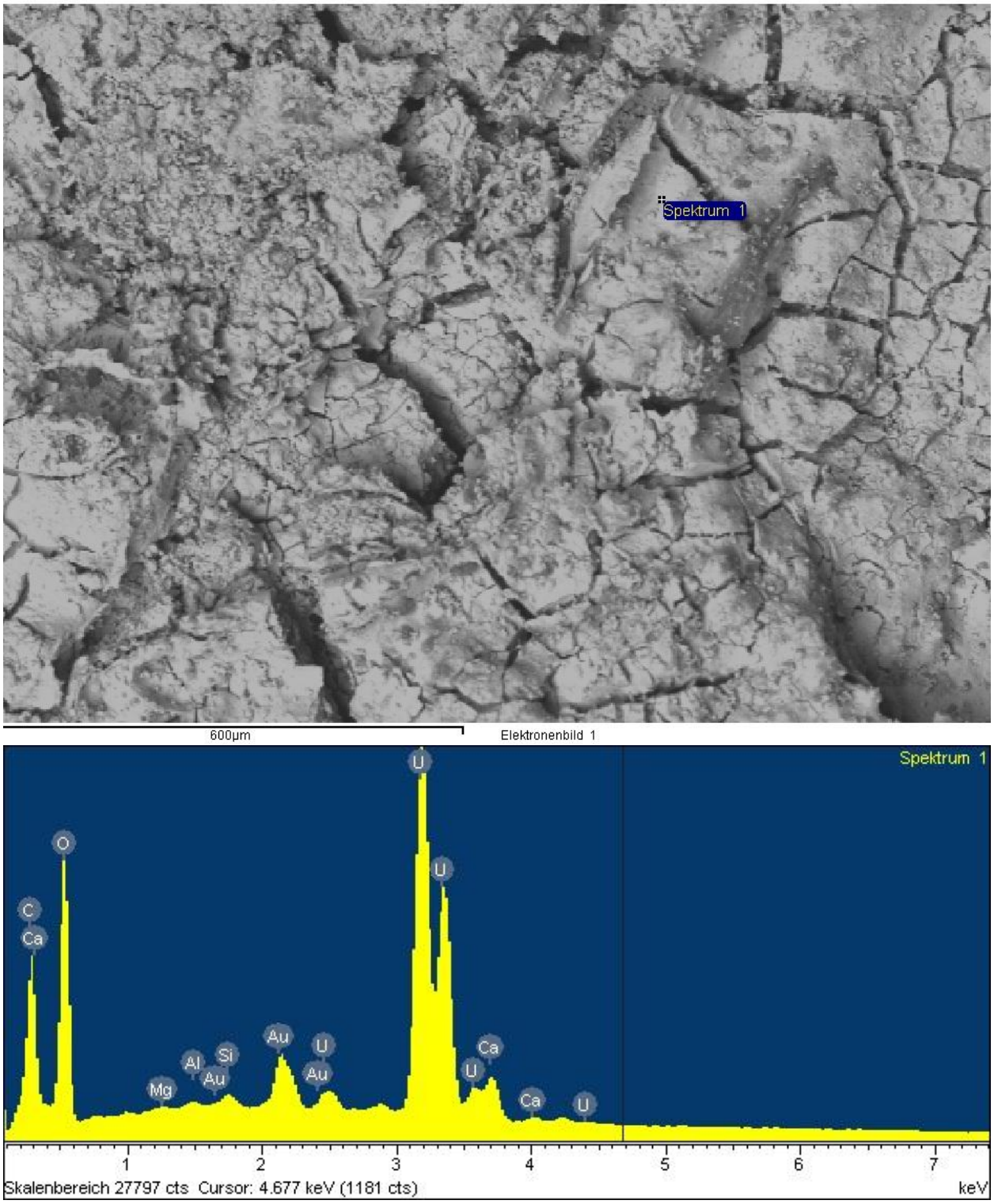

Figure B-4: BSE image of a location on sample 4 acquired by SEM (above), and its EDS spectrum (below).

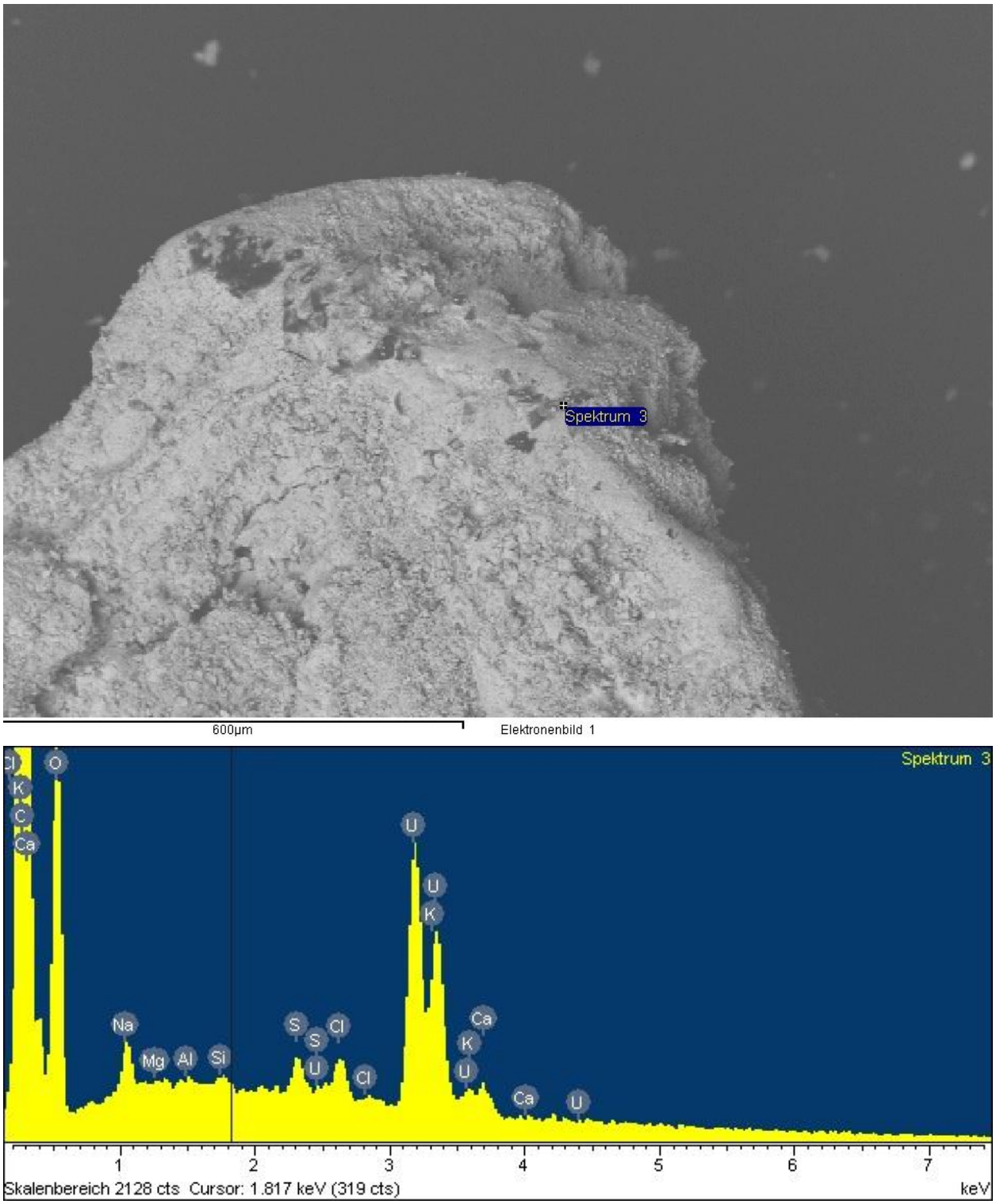

Figure B-5: BSE image of a location on sample 4 acquired by SEM (above), and its EDS spectrum (below).

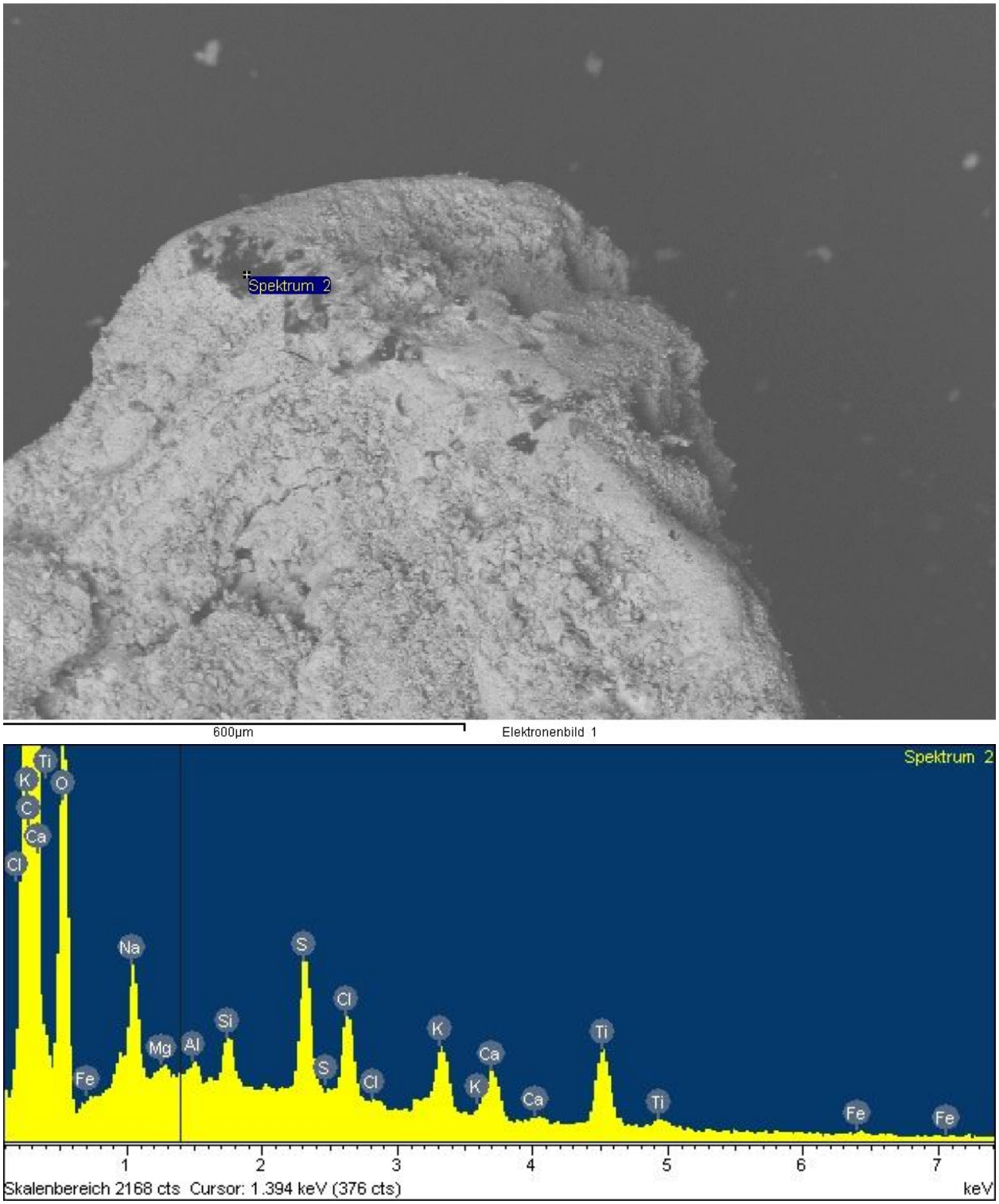

Figure B-6: BSE image of a location on sample 4 acquired by SEM (above), and its EDS spectrum (below).

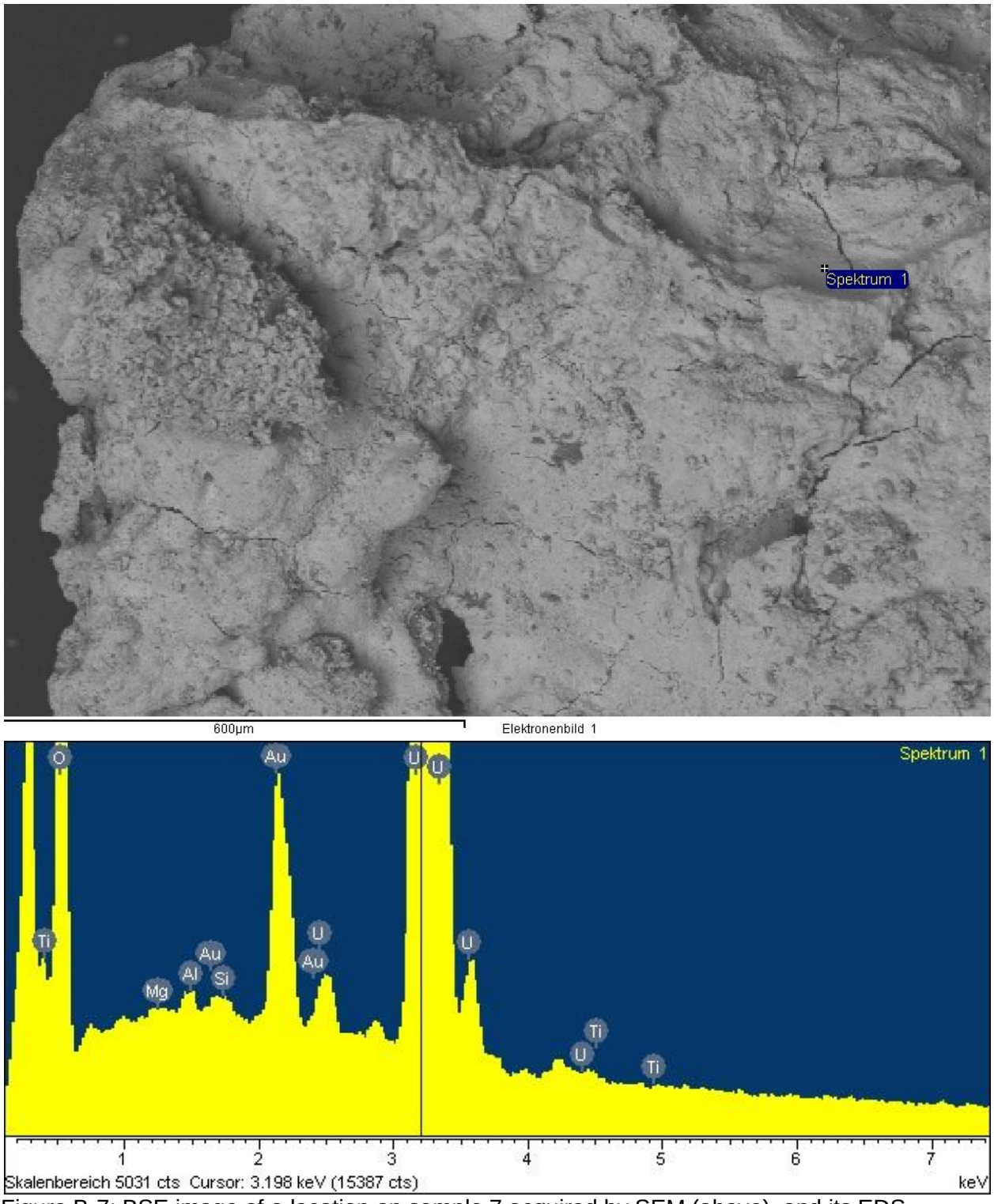

Figure B-7: BSE image of a location on sample 7 acquired by SEM (above), and its EDS spectrum (below).

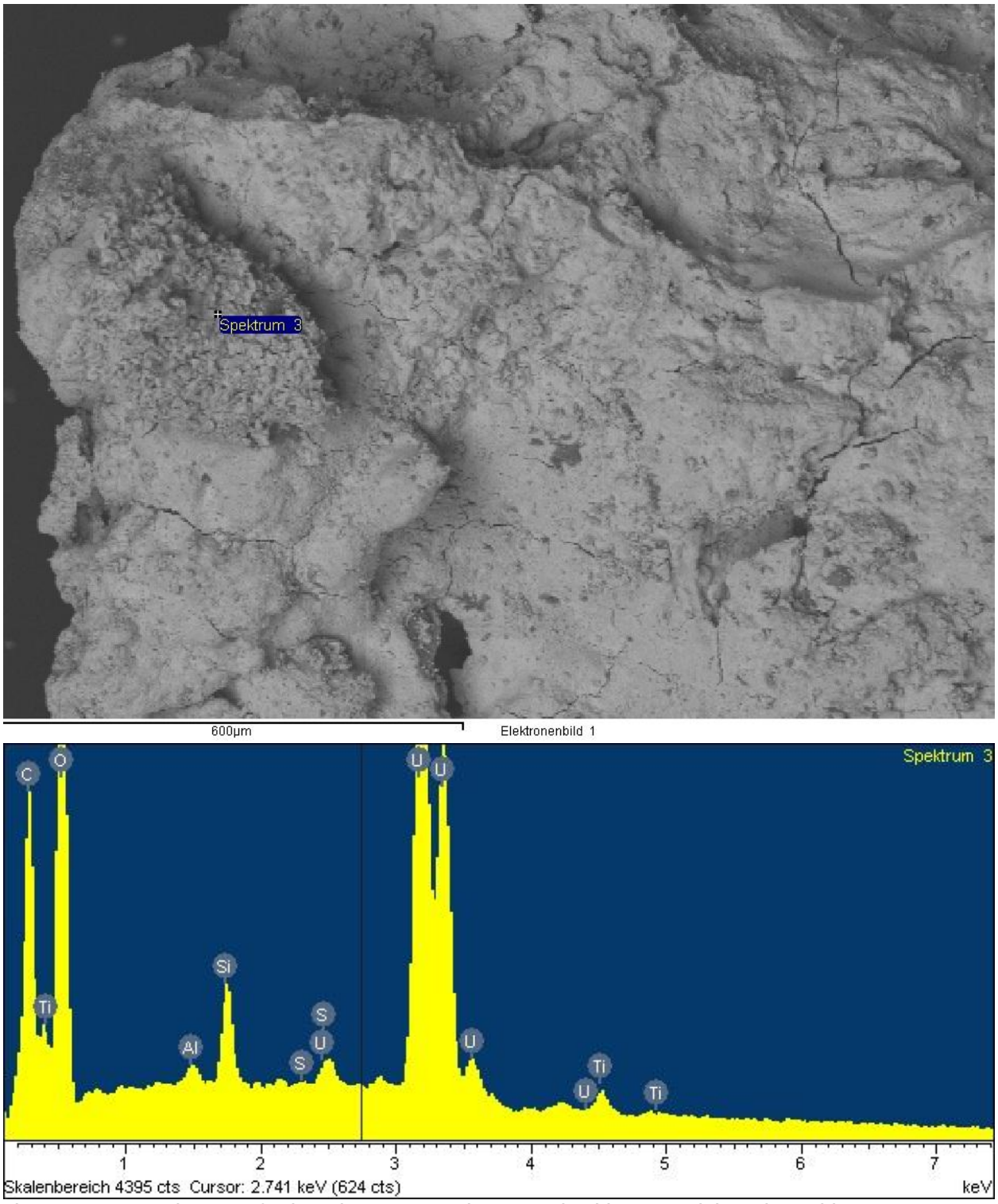

Figure B-8: BSE image of a location on sample 7 acquired by SEM (above), and its EDS spectrum (below).

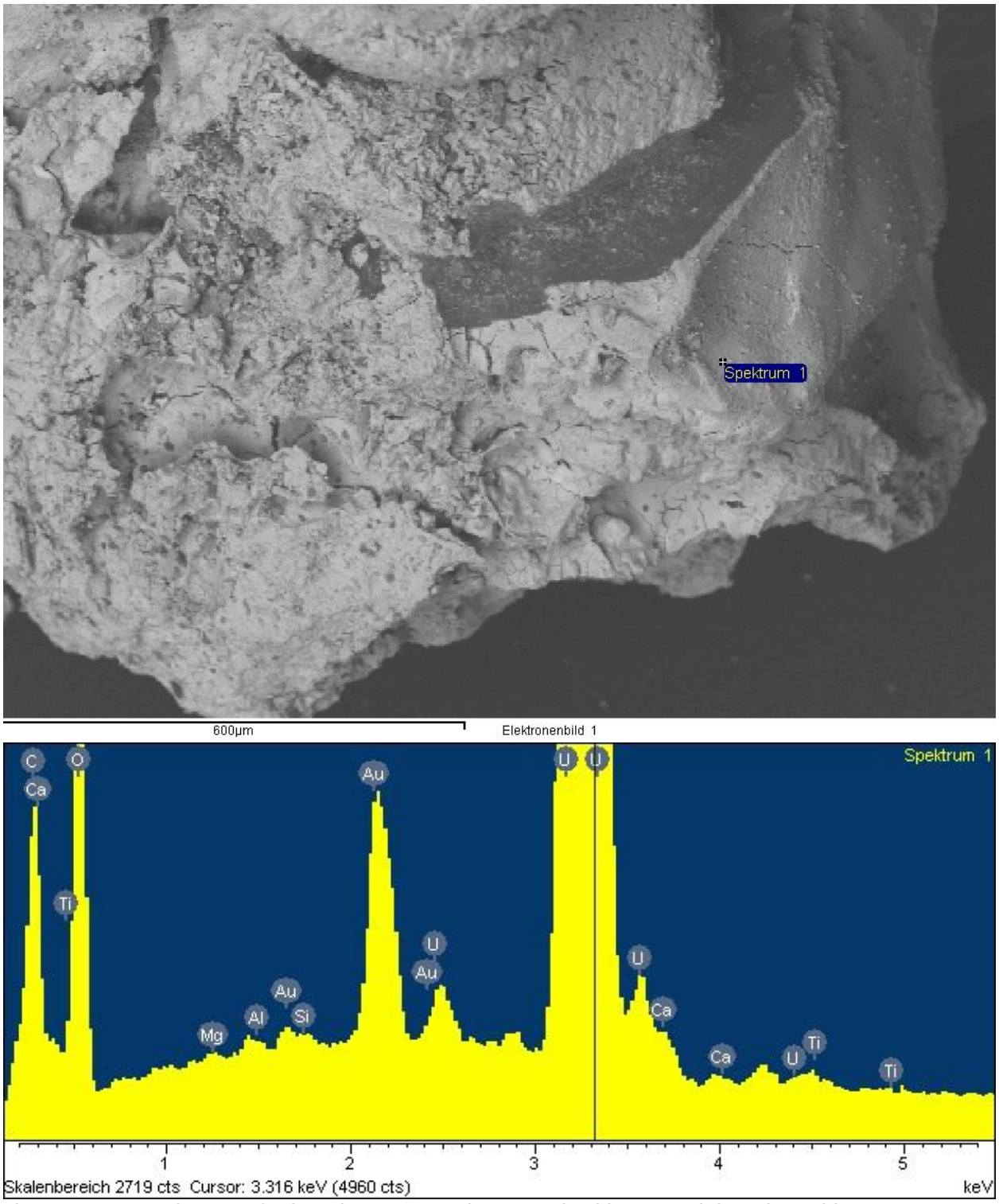

Figure B-9: BSE image of a location on sample 7 acquired by SEM (above), and its EDS spectrum (below).

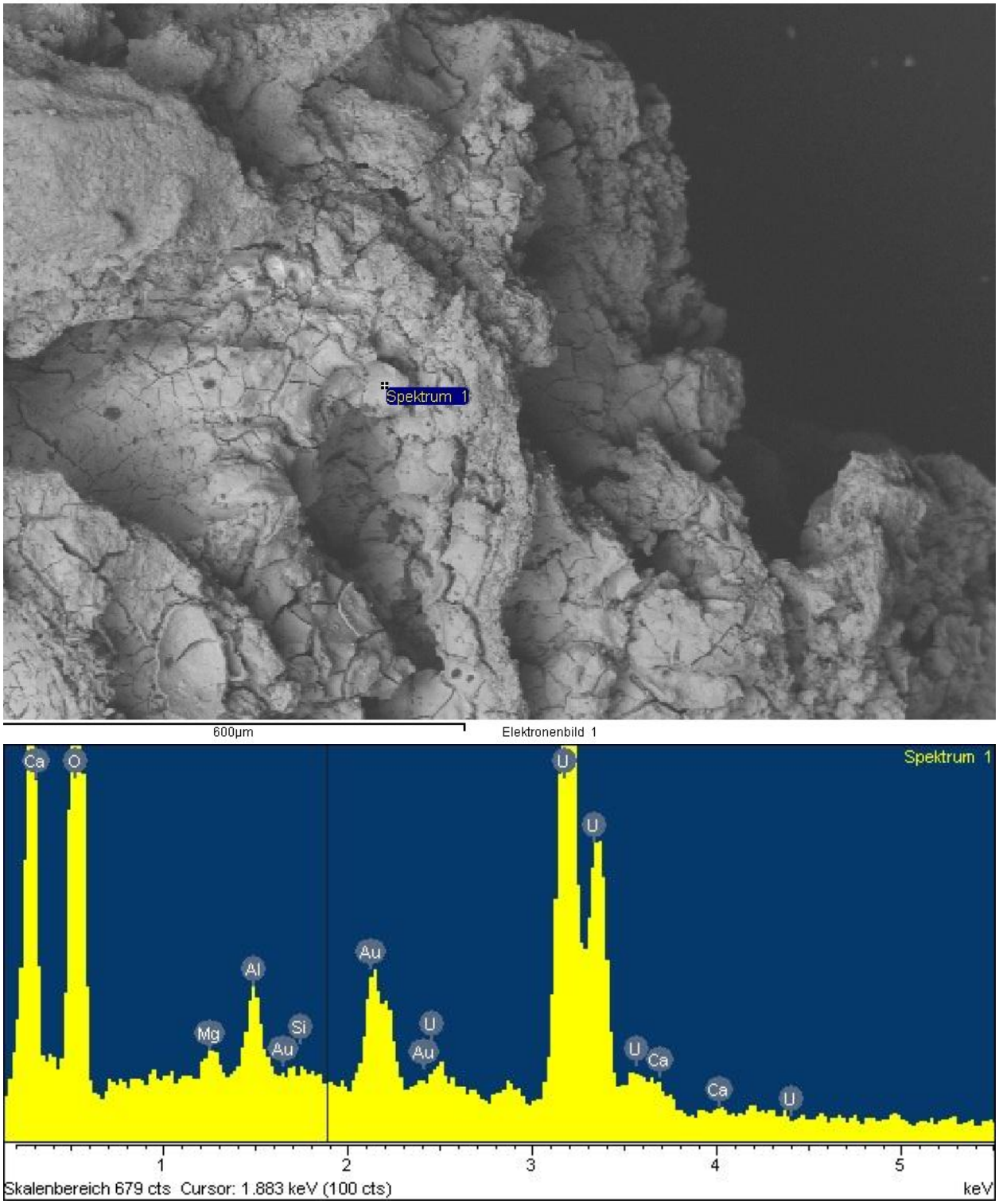

Figure B-10: BSE image of a location on sample 7 acquired by SEM (above), and its EDS spectrum (below).

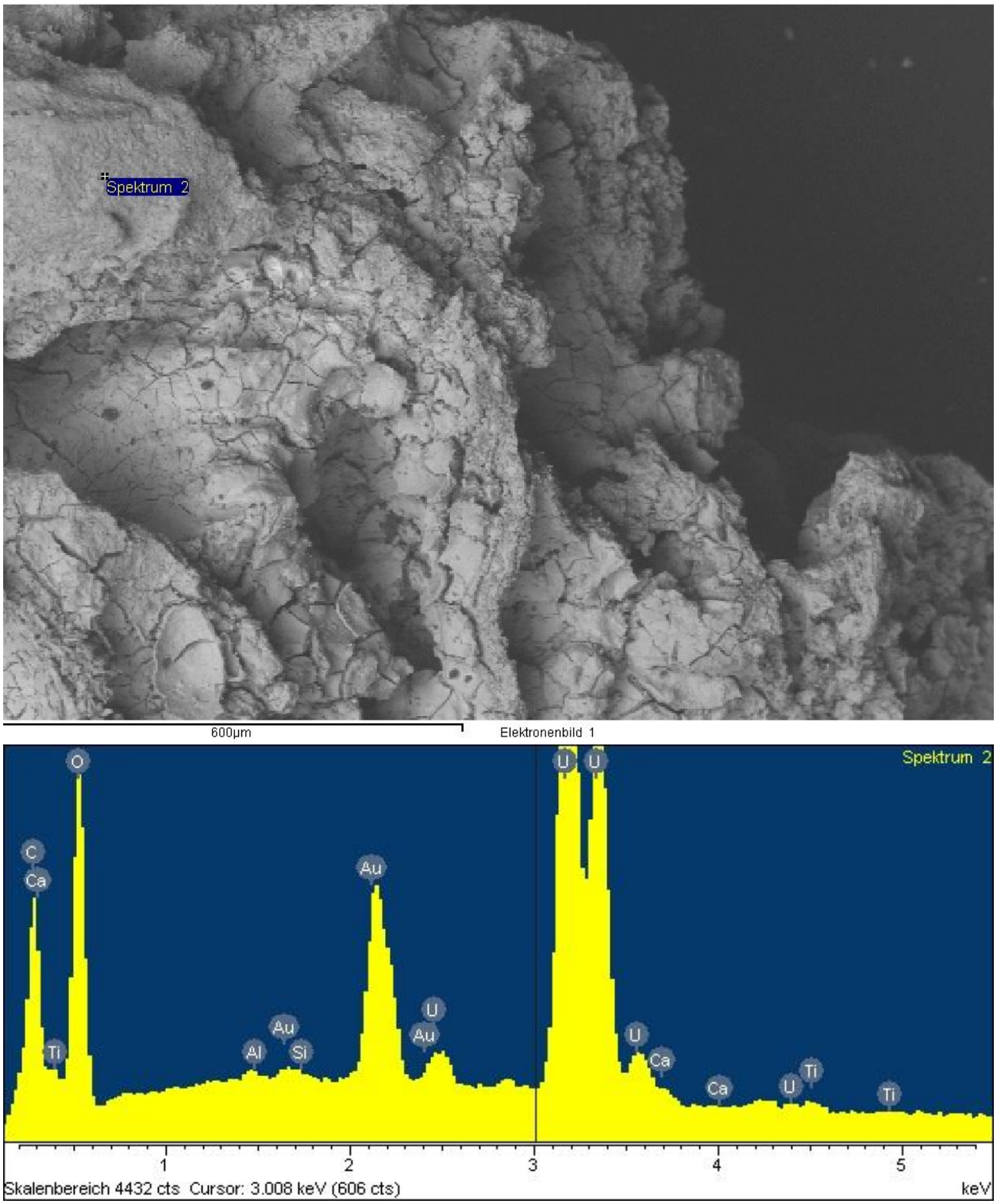

Figure B-11: BSE image of a location on sample 7 acquired by SEM (above), and its EDS spectrum (below).

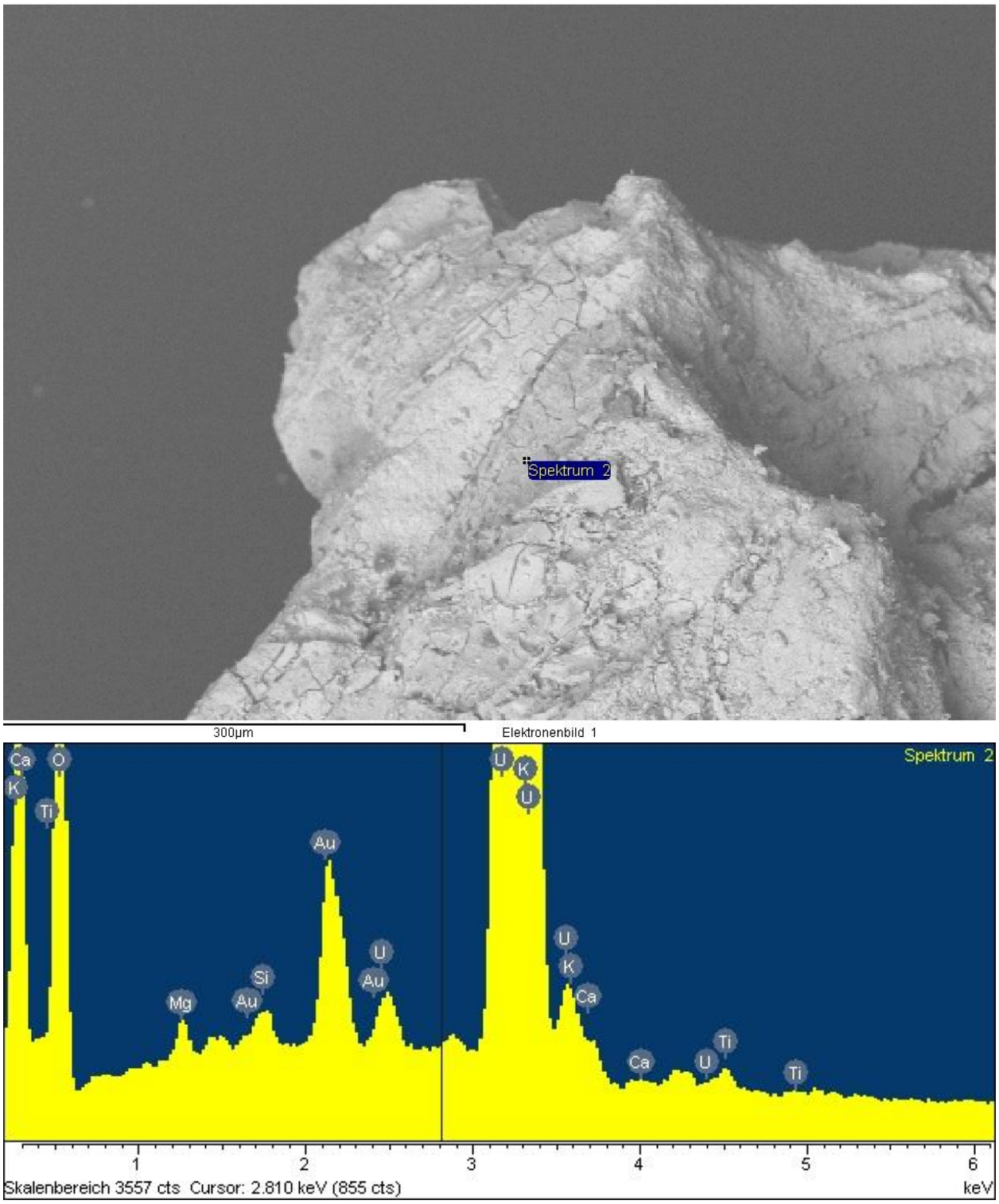

Figure B-12: BSE image of a location on sample 8 acquired by SEM (above), and its EDS spectrum (below).

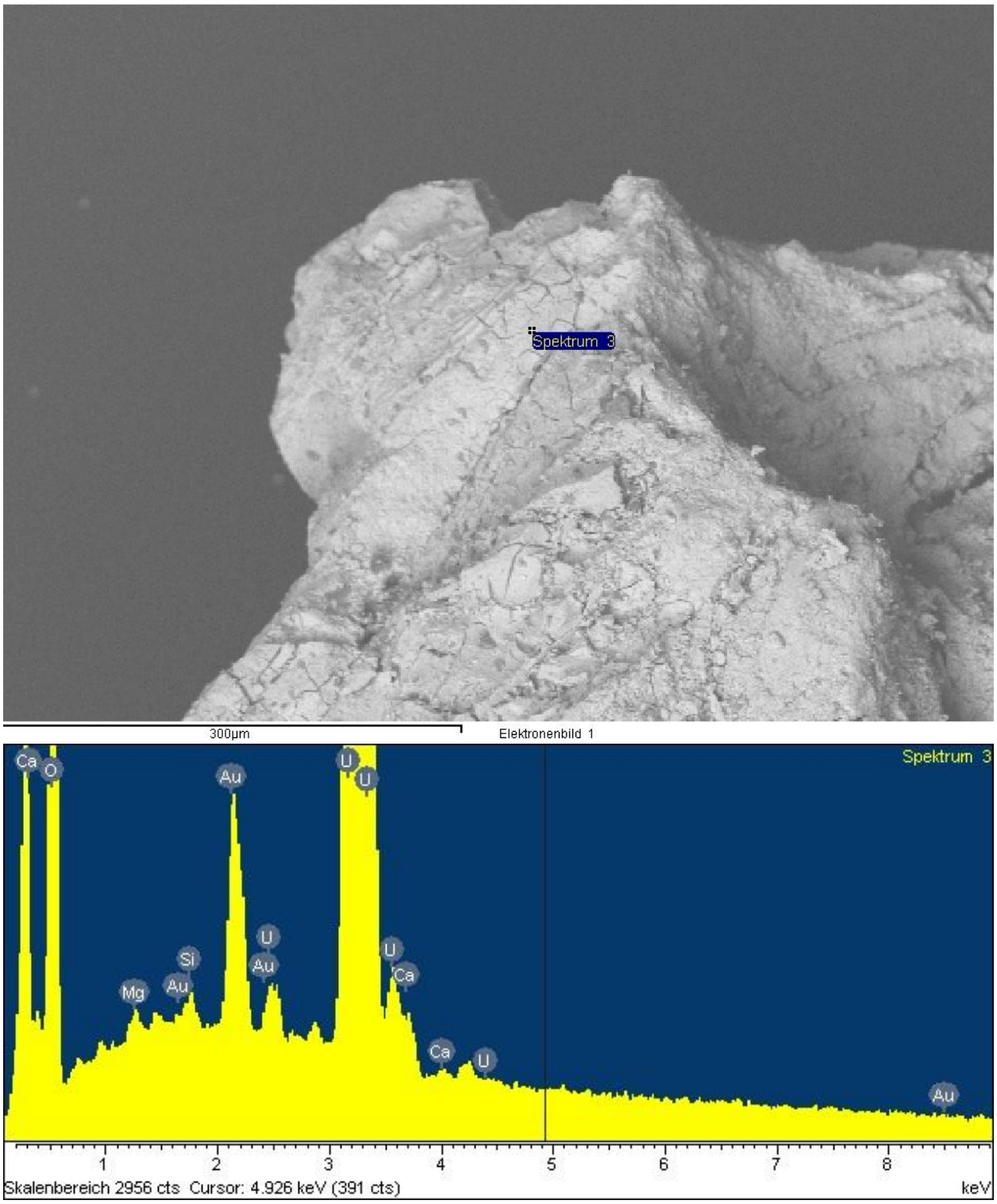

Figure B-14: BSE image of a location on sample 8 acquired by SEM (above), and its EDS spectrum (below).

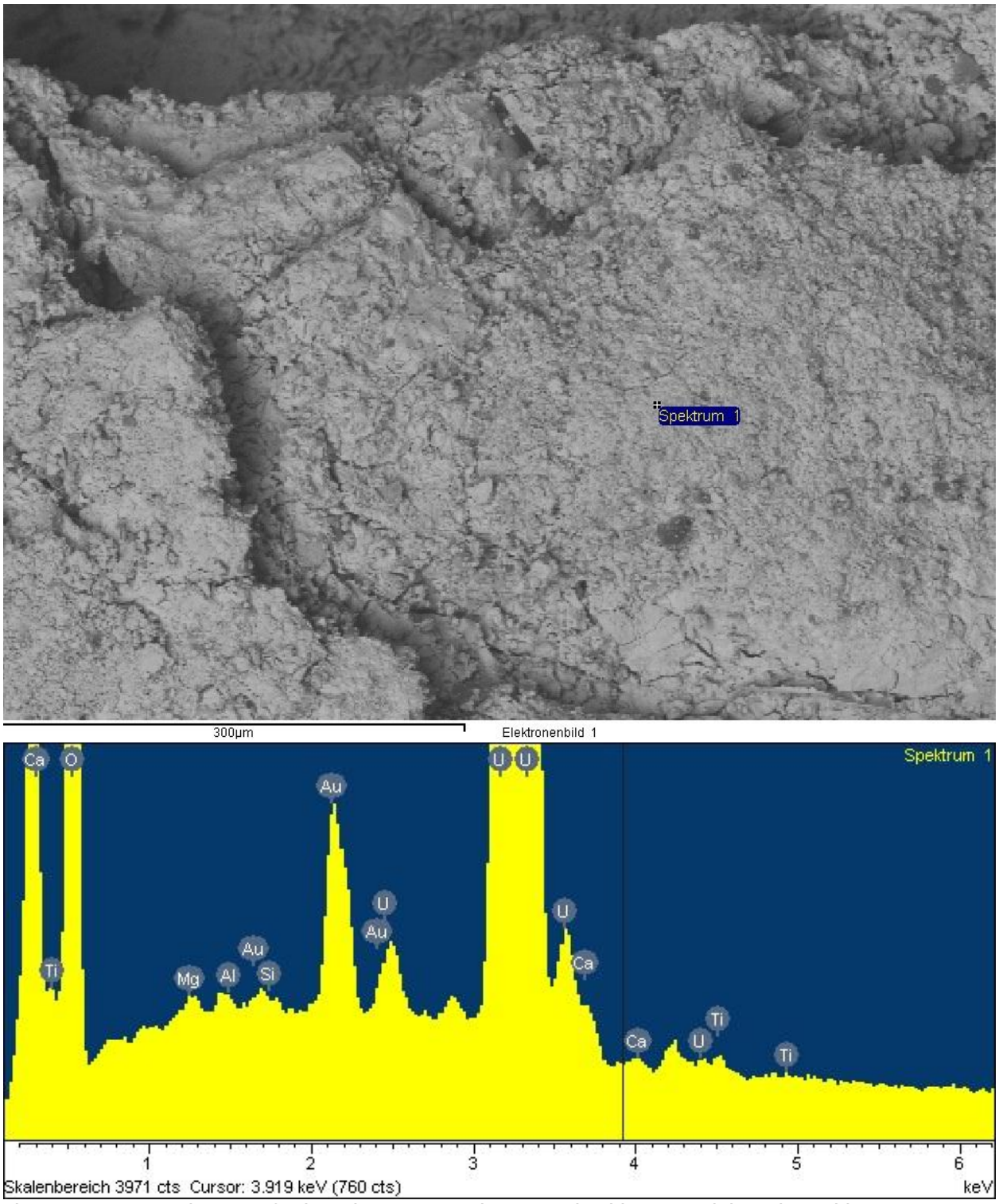

Figure B-14: BSE image of a location on sample 8 acquired by SEM (above), and its EDS spectrum (below).

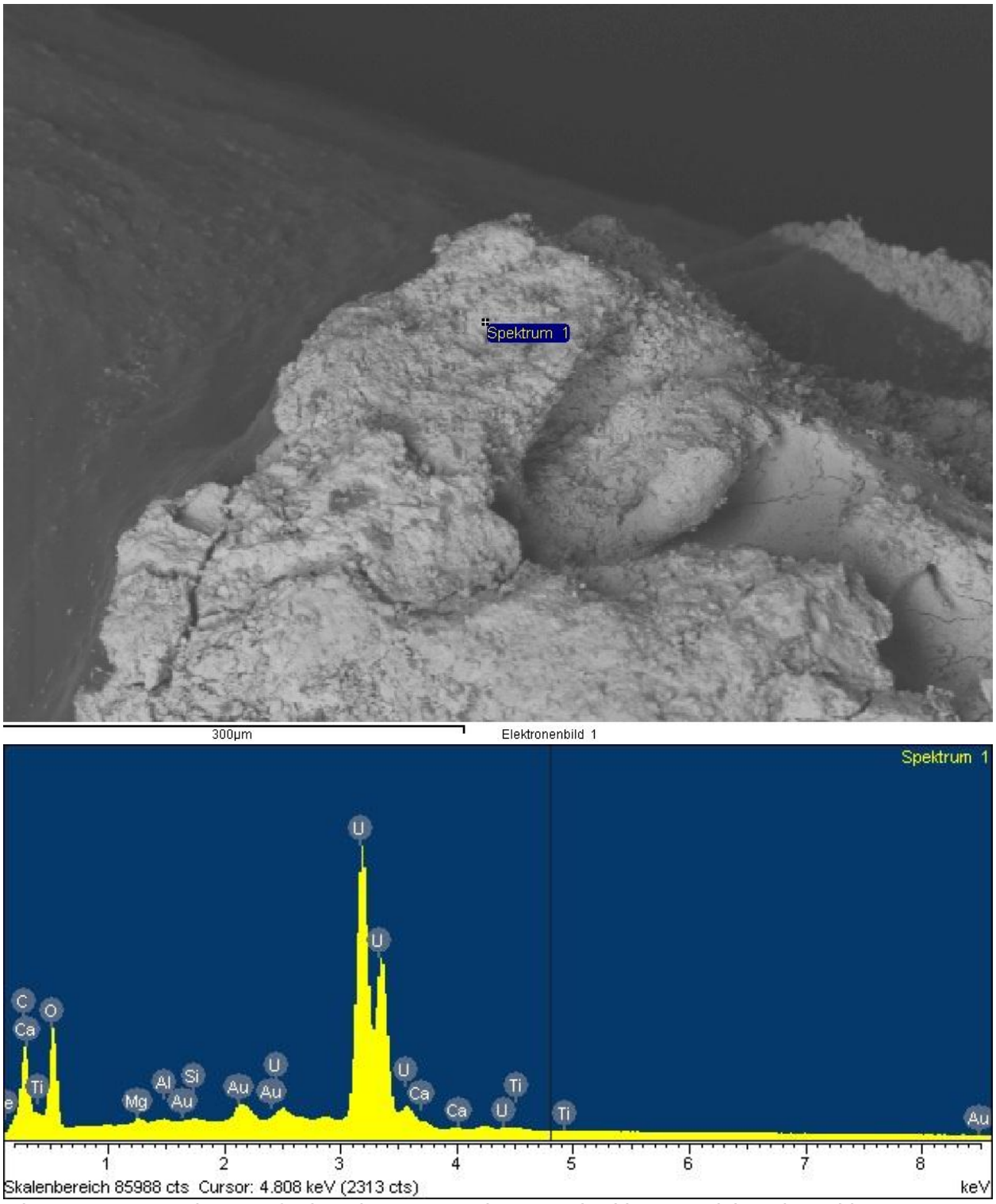

Figure B-15: BSE image of a location on sample 8 acquired by SEM (above), and its EDS spectrum (below).

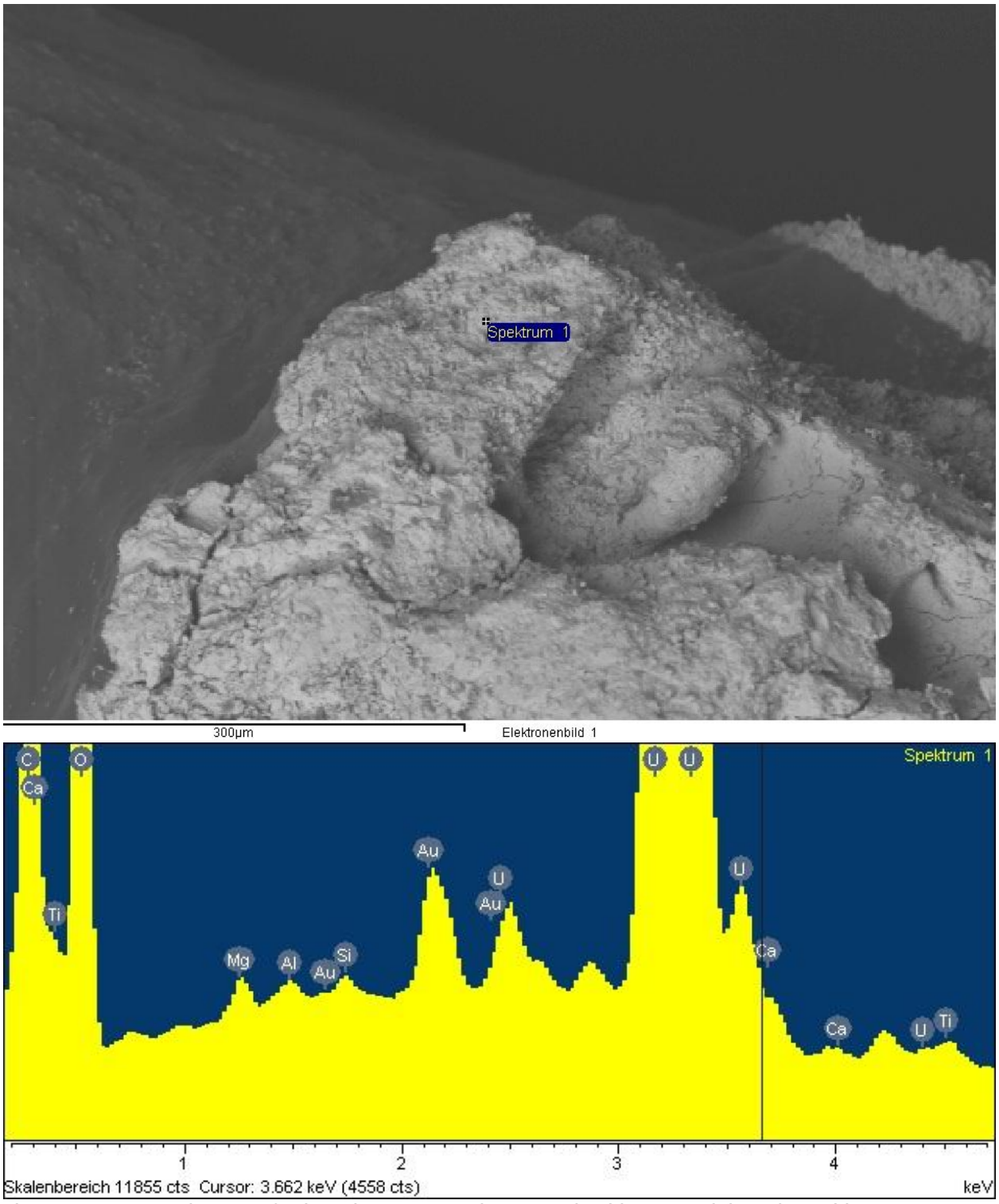

Figure B-16: BSE image of a location on sample 8 acquired by SEM (above), and its EDS spectrum (below).

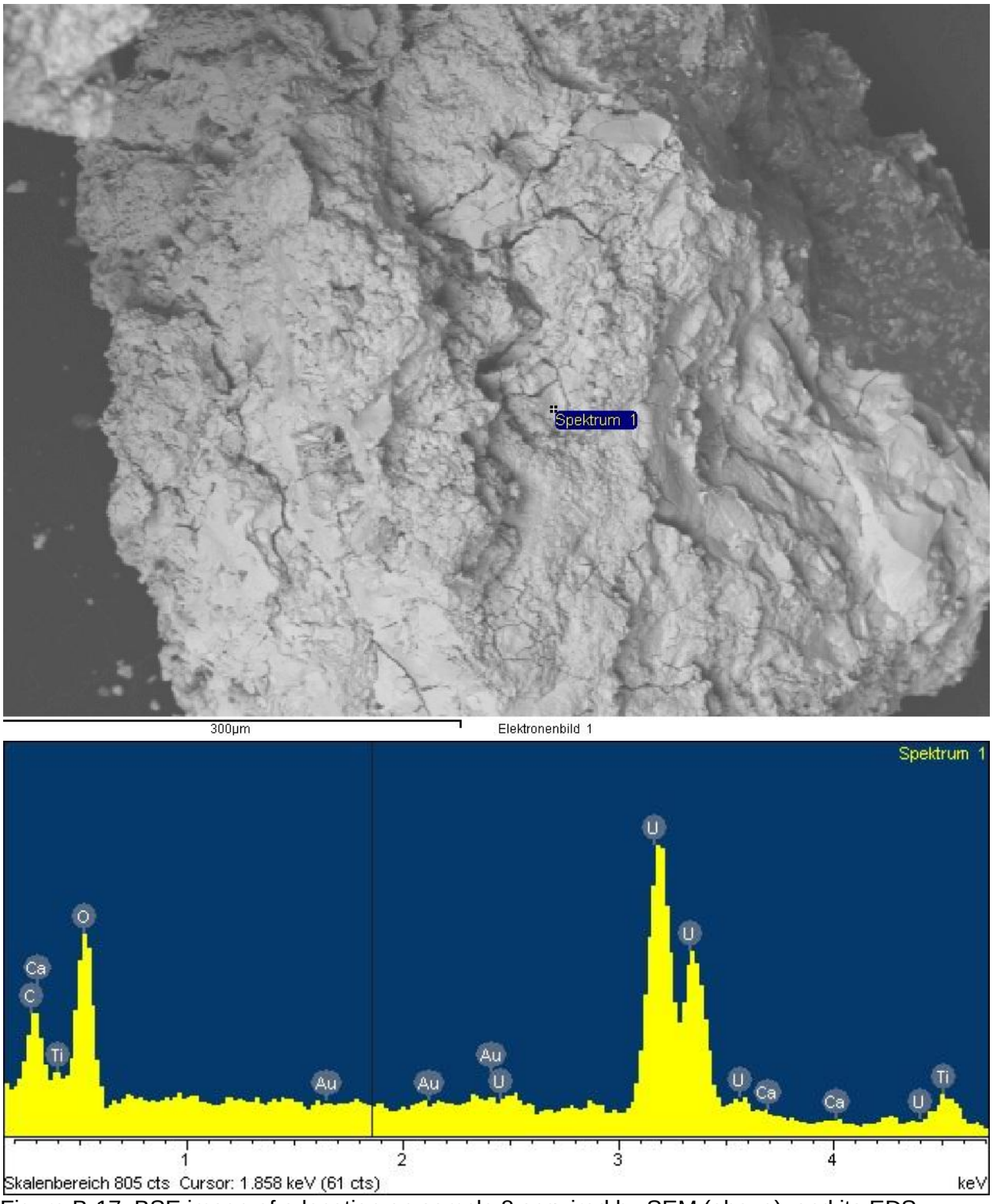

Figure B-17: BSE image of a location on sample 8 acquired by SEM (above), and its EDS spectrum (below).

Appendix C: A quantitative analysis performed via EMA showing the mass percentages for selected elements in the prepared resin block, the grains' symbols e.g. (1-1) refer to the grain number 1 in figure (2-11) and the number of measurement.

Reading #	Mg%	Al%	Ca%	Ti%	U%	Si%	P%	K%	Grain #
1	0.02	0.00	1.57	0.03	77.55	0.03	0.01	0.69	1-1
2	0.01	0.14	1.42	0.04	75.56	0.29	0.01	0.93	1-2
3	0.00	0.00	1.39	0.09	78.33	0.03	0.01	0.83	1-3
4	0.00	0.08	1.63	0.06	77.34	0.07	0.02	0.49	2-1
5	0.01	0.03	1.56	0.02	76.70	0.05	0.01	0.76	2-2
6	0.00	0.02	1.11	0.07	77.72	0.02	0.00	0.32	2-3
7	0.00	0.00	0.00	0.74	98.95	0.03	0.00	0.22	2-4
8	0.01	0.00	0.00	0.77	98.88	0.03	0.00	0.19	2-5
9	0.00	0.00	0.47	0.01	79.68	0.06	0.00	0.51	3-1
10	0.00	0.00	0.02	0.11	79.04	0.08	0.02	0.67	3-2
11	0.06	0.02	1.99	0.14	78.77	0.07	0.01	0.47	4-1
12	0.03	0.00	2.11	0.09	77.54	0.08	0.00	0.27	4-2
13	0.00	0.01	1.58	0.02	76.06	0.04	0.00	0.66	5-1
14	0.65	3.65	2.20	0.27	42.73	6.11	0.15	0.87	5-2
15	0.08	0.29	1.75	0.00	78.60	0.58	0.01	0.48	6-1
16	0.05	0.07	1.32	0.05	77.30	0.24	0.00	0.49	6-2
17	0.01	0.00	1.58	0.03	79.56	0.01	0.00	0.42	6-3
18	0.10	0.14	3.09	0.07	71.17	0.57	0.02	0.19	7-1
19	0.01	0.08	2.14	0.00	76.74	0.07	0.00	0.33	7-2
20	0.02	0.00	1.73	0.09	78.29	0.03	0.02	0.66	8-1
21	0.05	0.68	1.61	0.02	70.30	1.16	0.01	0.66	8-2
22	0.01	0.01	0.06	0.20	78.02	0.03	0.01	0.61	9-1
23	0.01	0.01	0.30	0.03	78.21	0.06	0.00	0.51	9-2
24	0.88	12.77	0.09	0.43	10.39	17.63	0.08	4.20	9-3
25	0.00	0.01	0.34	0.00	79.63	0.07	0.00	0.39	9-4
26	0.00	0.00	0.45	0.00	80.54	0.09	0.02	0.49	9-5
27	0.04	0.24	0.58	3.00	73.07	0.71	0.54	0.29	9-6
28	0.00	0.17	0.09	0.13	79.94	0.26	0.01	0.86	9-7
29	0.00	0.01	0.04	0.13	78.81	0.10	0.02	0.63	9-8
30	0.24	0.04	5.92	0.01	59.30	0.15	0.01	0.18	9-9
31	0.32	1.73	3.11	0.34	57.46	2.78	0.03	0.74	9-10
32	0.58	3.21	2.72	0.57	57.35	4.65	0.04	0.61	9-11
33	0.02	0.00	1.71	0.04	78.71	0.08	0.01	0.61	9-12
34	0.02	0.02	0.65	0.01	78.89	0.07	0.00	0.56	9-13
35	0.00	0.01	0.43	0.03	80.62	0.07	0.02	0.49	9-14
36	0.01	0.00	0.00	0.83	98.83	0.04	0.00	0.19	9-15
37	0.11	0.00	2.17	0.03	76.50	0.06	0.00	0.32	10-1
38	0.04	0.00	1.79	0.07	73.94	0.08	0.01	0.52	10-2
39	0.02	0.00	0.04	0.80	98.80	0.02	0.02	0.22	10-3
40	0.05	0.00	1.85	0.08	77.87	0.05	0.01	0.27	10-4
41	0.10	0.00	1.79	0.31	80.38	0.06	0.00	0.15	10-5

Appendix D: ICP-OES results

Table D-1: Ca calibration for ICP-OES.

Sample ID	Counts per second	RSD	Concentration mg/L
Calib Blank	214	1.25	0
Calib Std 1	30480	0.87	1
Calib Std 2	153663	1.71	5
Calib Std 3	308293	1.08	10

Table D-2: U calibration for ICP-OES.

Sample ID	Counts per second	RSD	Concentration mg/L
Calib Blank	495	4.34	0
Calib Std 1	6041	0.51	1
Calib Std 2	30795	1.65	5
Calib Std 3	61540	0.94	10

Table D-3: ICP-OES results for Ca without correction.

Sample ID	Analyte name	Counts per second	RSD	Concentration mg/L
4-1	Ca 315.887	47574	0.53	2.41
4-2	Ca 315.887	32657	0.78	1.65
4-3	Ca 315.887	46330	0.83	2.34
4-4	Ca 315.887	43865	1.51	2.22
4-5	Ca 315.887	37940	2.17	1.92
7-1	Ca 315.887	36288	1.66	1.84
7-2	Ca 315.887	31813	1.13	1.61
7-3	Ca 315.887	39422	0.62	2.00
7-4	Ca 315.887	39842	0.81	2.02
7-5	Ca 315.887	29299	1.31	1.48
8-1	Ca 315.887	51316	0.26	2.6
8-2	Ca 315.887	53877	2.34	2.73
8-3	Ca 315.887	62449	0.58	3.16
8-4	Ca 315.887	53284	1.22	2.70
8-5	Ca 315.887	48402	0.55	2.45
4-1	Ca 317.993	72673	0.04	2.36
4-2	Ca 317.993	50237	0.57	1.64
4-3	Ca 317.993	71809	1.05	2.34
4-4	Ca 317.993	68450	1.13	2.23
4-5	Ca 317.993	58831	1.75	1.92
7-1	Ca 317.993	56425	2.54	1.84
7-2	Ca 317.993	48948	0.18	1.60
7-3	Ca 317.993	58223	0.41	1.90
7-4	Ca 317.993	58999	0.14	1.92
7-5	Ca 317.993	45294	2.21	1.48
8-1	Ca 317.993	80010	0.41	2.60
8-2	Ca 317.993	84065	1.87	2.73
8-3	Ca 317.993	95806	0.84	3.11
8-4	Ca 317.993	83062	0.88	2.70
8-5	Ca 317.993	75214	0.68	2.45
4-1	Ca 396.847	5109244	1.33	2.29
4-2	Ca 396.847	3621159	0.75	1.63
4-3	Ca 396.847	5122966	0.21	2.30
4-4	Ca 396.847	4756503	1.24	2.13
4-5	Ca 396.847	4203960	0.54	1.89
7-1	Ca 396.847	3967785	1.65	1.78
7-2	Ca 396.847	3572667	0.86	1.60
7-3	Ca 396.847	4135218	1.13	1.86
7-4	Ca 396.847	4270647	1.64	1.92
7-5	Ca 396.847	3244899	1.19	1.46
8-1	Ca 396.847	5511780	1.24	2.47
8-2	Ca 396.847	5854837	0.21	2.63
8-3	Ca 396.847	6813055	1.77	3.06
8-4	Ca 396.847	5821611	1.37	2.61
8-5	Ca 396.847	5291485	0.15	2.37

Table D-4: ICP-OES results for U without correction.

Sample ID	Analyte name	Counts per second	RSD	Concentration mg/L
4-1	U 367.007	16608	0.70	6.73
4-2	U 367.007	6383	2.13	2.59
4-3	U 367.007	1056	0.61	0.43
4-4	U 367.007	554	12.24	0.22
4-5	U 367.007	225	14.70	0.09
7-1	U 367.007	3113	3.02	1.26
7-2	U 367.007	6701	1.65	2.71
7-3	U 367.007	9575	1.09	3.88
7-4	U 367.007	708	2.83	0.28
7-5	U 367.007	289	16.60	0.11
8-1	U 367.007	595	8.12	0.24
8-2	U 367.007	455	4.36	0.18
8-3	U 367.007	6139	0.83	2.49
8-4	U 367.007	196	1.27	0.08
8-5	U 367.007	671	6.31	0.27
4-1	U 385.958	43659	1.11	7.09
4-2	U 385.958	16160	1.81	2.63
4-3	U 385.958	2421	4.90	0.40
4-4	U 385.958	1095	6.21	0.19
4-5	U 385.958	476	7.26	0.08
7-1	U 385.958	7722	2.10	1.26
7-2	U 385.958	16713	1.31	2.72
7-3	U 385.958	22400	0.26	3.64
7-4	U 385.958	1677	2.07	0.28
7-5	U 385.958	565	10.30	0.10
8-1	U 385.958	1484	3.29	0.25
8-2	U 385.958	1052	6.00	0.18
8-3	U 385.958	15298	1.25	2.49
8-4	U 385.958	391	5.22	0.07
8-5	U 385.958	1731	1.13	0.29
4-1	U 409.014	47414	1.38	7.02
4-2	U 409.014	17733	1.21	2.63
4-3	U 409.014	2701	1.26	0.41
4-4	U 409.014	1324	1.98	0.20
4-5	U 409.014	405	17.80	0.07
7-1	U 409.014	8543	1.33	1.27
7-2	U 409.014	18527	0.78	2.75
7-3	U 409.014	24958	0.79	3.70
7-4	U 409.014	1909	11.09	0.29
7-5	U 409.014	507	16.03	0.08
8-1	U 409.014	1659	2.54	0.25
8-2	U 409.014	1209	5.55	0.18
8-3	U 409.014	16827	1.03	2.49
8-4	U 409.014	454	1.77	0.07
8-5	U 409.014	1869	1.34	0.28

Table D-5: ICP-OES results for Ca and U in mg/L after correction.

Sample ID	Ca 315.887	Ca 317.933	Ca 396.847	Ca average	U 367.007	U 385.958	U 409.014	U average
4-1	12.04	11.82	11.46	11.77	33.66	35.47	35.09	34.74
4-2	8.27	8.18	8.13	8.19	12.93	13.15	13.14	13.08
4-3	11.72	11.68	11.50	11.63	2.13	2.00	2.03	2.05
4-4	11.10	11.14	10.67	10.97	1.11	0.93	1.01	1.01
4-5	9.60	9.58	9.43	9.54	0.44	0.42	0.33	0.40
7-1	9.19	9.19	8.90	9.09	6.30	6.30	6.35	6.32
7-2	8.06	7.98	8.02	8.02	13.57	13.60	13.73	13.64
7-3	9.98	9.48	9.28	9.58	19.40	18.22	18.49	18.70
7-4	10.08	9.61	9.58	9.76	1.42	1.40	1.44	1.42
7-5	7.42	7.38	7.28	7.36	0.57	0.50	0.40	0.49
8-1	12.98	13.01	12.37	12.79	1.19	1.24	1.26	1.23
8-2	13.63	13.67	13.14	13.48	0.91	0.89	0.92	0.91
8-3	15.79	15.57	15.29	15.55	12.43	12.45	12.47	12.45
8-4	13.48	13.51	13.06	13.35	0.38	0.35	0.36	0.37
8-5	12.24	12.23	11.87	12.12	1.35	1.44	1.41	1.40

This section has been deleted in conformity with the rules stipulated by the internet publisher (ArchiMed). The Curriculum vitae is available in the print-version of this dissertation.

This section has been deleted in conformity with the rules stipulated by the internet publisher (ArchiMed). The Curriculum vitae is available in the print-version of this dissertation.